Structural Performance of Nuclear Power Plant Concrete Structures Affected by Alkali-Silica Reaction (ASR)

Task 2: Assessing Bond and Anchorage of Reinforcing Bars in ASR-Affected Concrete

Travis Thonstad
Jonathan M. Weigand
Fahim Sadek
Sorin Marcu
Timothy J. Barrett
Hai S. Lew
Long T. Phan
Adam L. Pintar

NIST

National Institute of
Standards and Technology
U.S. Department of Commerce

NIST Technical Note 2127

Structural Performance of Nuclear Power Plant Concrete Structures Affected by Alkali-Silica Reaction (ASR)

Task 2: Assessing Bond and Anchorage of Reinforcing Bars in ASR-Affected Concrete

Travis Thonstad
Jonathan M. Weigand
Fahim Sadek
Sorin Marcu
Timothy J. Barrett
Hai S. Lew
Long T. Phan
Engineering Laboratory
National Institute of Standards and Technology

Adam L. Pintar
Information Technology Laboratory
National Institute of Standards and Technology

February 2021

ACKNOWLEDGEMENTS

ABSTRACT

This report describes the results of Task 2 of a five-task comprehensive research program conducted at the National Institute of Standards and Technology (NIST) under the sponsorship of the U.S. Nuclear Regulatory Commission (NRC). The overall study aims to develop a technical basis for evaluating effects of Alkali-Silica Reaction (ASR), which occurs when the high pH concrete pore solution reacts with certain aggregate mineral phases to form expansive ASR gel and create internal expansive forces that cause cracking in concrete, on engineering properties and structural capacities of reinforced concrete structures. The report provides detailed information on experimental planning, measurements, testing, and computational modelling performed to achieve the objective of Task 2, assessing bond strength, development and lap-splice lengths of reinforcing bars in ASR-affected concrete. It presents experimental results and rigorous statistical analyses that quantify the effects of ASR-induced expansion, confinement provided by stirrups, and lap splice length on (1) the flexural performance and capacity of beams with lap spliced tensile reinforcement and (2) bond strength.

Keywords:

Alkali-silica Reaction; ASR; Bond Strength, Bond-slip, Compressive Strength; Concrete; Confinement; Expansion; Experimental; Finite Element Modeling; Flexural Strength; Lap Splice

PREFACE

The technical work reported herein is part of a comprehensive research program carried out by the Engineering Laboratory of the National Institute of Standards and Technology (NIST) on the structural performance of nuclear power plant concrete structures affected by alkali-silica reaction (ASR). The work is funded by the U.S. Nuclear Regulatory Commission (NRC) under Inter-agency agreement NRC-HQ-60-14-I-0004.

TABLE OF CONTENTS

LIST OF FIGURES

LIST OF TABLES

LIST OF ACRONYMS, ABBREVIATIONS, AND NOTATIONS

Acronyms

ACI	American Concrete Institute
ASR	Alkali-silica reaction
ASTM	American Society for Testing and Materials
CI	Cracking index
CCD	Central Composite Design
LASSO	Least absolute shrinkage and selection operator
NIST	National Institute of Standards and Technology
NPP	Nuclear power plant
NRC	Nuclear Regulatory Commission
RH	Relative humidity
RMS	Root mean square

Abbreviations

d	day
ft	foot
in	inch
kip	a force equal to 1,000 pounds
ksi	kip per square inch
lbf	pound force
min	minute
psi	pounds per square inch
s	second

Notation

A_b	Area of the reinforcement
A_c	Area of concrete cylinder or core
A_{st}	Cross-sectional area of one leg of a confining bar
A_{tr}	Total area of transverse reinforcement crossing the splitting plane
c_b	Minimum distance from center of the spliced reinforcement to the free surface of the beam or half the bar spacing
c_{max}	Maximum concrete cover
c_{min}	Minimum concrete cover
d_b	Nominal diameter of the reinforcement
d_c	Dimensions of concrete cross section bounded by reinforcing bars
E_c	Modulus of elasticity of concrete, psi
E_s	Modulus of elasticity of the steel reinforcement, psi
f'_c	Specified compressive strength of concrete
f_{cc}	Confined compressive strength of concrete
f_{cm}	Measured average compressive strength of concrete
f_{ct}	Measured average splitting tensile strength of concrete
f_{cu}	Average unconfined strength of concrete
f_{tm}	Mean value of the tensile strength of the reinforcing bars
f_{ym}	Mean value of the yield strength of the reinforcing bars
f_u	Ultimate tensile strength of reinforcement
f_y	Yield strength of reinforcement
K_{tr}	Density of transverse reinforcement, determined in accordance with the fib Model Code (2010) in Section 6.4.3; Transverse reinforcement index, determined in accordance with ACI318-19 elsewhere
k	Coverage factor
ℓ_d	Development length of the tensile reinforcement based on ACI318-19
ℓ_s	Tension reinforcement splice length
M_{max}	Maximum measured moment strength during testing
M_n	Nominal moment capacity of the beam section based on ACI318-19
n	Number of measurements in Chapter 4; number of reinforcing bars being spliced across the splitting plane elsewhere

n_t	Number of legs of confining reinforcement crossing a potential splitting failure surface at a section
N	Number of degrees of freedom
RH	Relative humidity
s	Stirrup spacing
u	Maximum average bond stress
u_c	Standard uncertainty
U	Uncertainty measure
β_i	Regression coefficient
δ	Bond slip
ϵ	Term representing random error
ε_{ASR}	ASR-induced linear expansion
$\varepsilon_{ASR\text{-}ult}$	Design ultimate expansion level of a concrete mixture
ε_{avg}	Average surface strain
ε_s	Strain in the reinforcement
ε_{su}	Ultimate strain of the reinforcing bar steel
ε_{sy}	Yield strain of the reinforcing bar steel
λ	Modification factor to reflect the reduced mechanical properties of lightweight concrete relative to normalweight concrete of the same compressive strength
μ_c	Mean value of a variable
ρ_v	Volumetric reinforcement ratio
$\rho_x,\ \rho_y,\ \rho_z$	Ratio of area of steel reinforcement to area of concrete in x, y, and z directions
σ_{avg}	Average stress in confined concrete
τ_b	bond stress, N/mm^2
τ_{bmax}	Maximum value of bond stress, N/mm^2
$\tau_{bu,split}$	Peak splitting bond resistance, N/mm^2
Σ_b	Perimeter of the reinforcement
ψ_e	Factor used to modify development length based on reinforcement coating
ψ_s	Factor used to modify development length based on reinforcement size
ψ_t	Factor used to modify development length for casting location in tension
Ω_y	Yielding modification factor

METRIC CONVERSION TABLE

To convert from	to	Multiply by
AREA AND SECOND MOMENT OF AREA		
square foot (ft^2)	square meter (m^2)	9.290 304 E–02
square inch (in.^{2})	square meter (m^2)	6.4516 E–04
FORCE		
kilogram–force (kgf)	newton (N)	9.806 65 E+00
kilopond (kilogram–force) (kp)	newton (N)	9.806 65 E+00
kip (1 kip=1,000 lbf)	newton (N)	4.448 222 E+03
kip (1 kip=1,000 lbf)	kilonewton (kN)	4.448 222 E+00
pound–force (lbf)	newton (N)	4.448 222 E+00
FORCE DIVIDED BY LENGTH		
pound–force per foot (lbf/ft)	newton per meter (N/m)	1.459 390 E+01
pound–force per inch (lbf/in.)	newton per meter (N/m)	1.751 268 E+02
LENGTH		
foot (ft)	meter (m)	3.048 E–01
inch (in)	meter (m)	2.54 E–02
MASS and MOMENT OF INERTIA		
kilogram–force second squared per meter (kgf · s^2/m)	kilogram (kg)	9.806 65 E+00
pound foot squared (lb · ft^2)	kilogram meter squared (kg · m^2)	4.214 011 E–02
pound inch squared (lb · in.^{2})	kilogram meter squared (kg · m^2)	2.926 397 E–04

To convert from	to	Multiply by
PRESSURE or STRESS (FORCE DIVIDED BY AREA)		
kilogram–force per square centimeter (kgf/cm^2)	pascal (Pa)	9.806 65 E+04
kilogram–force per square meter (kgf/m^2)	pascal (Pa)	9.806 65 E+00
kilogram–force per square millimeter (kgf/mm^2)	pascal (Pa)	9.806 65 E+06
kip per square inch (ksi) (kip/in.^{2})	pascal (Pa)	6.894 757 E+06
kip per square inch (ksi) (kip/in.^{2})	kilopascal (kPa)	6.894 757 E+03
pound–force per square foot (lbf/ft^2)	pascal (Pa)	4.788 026 E+01
pound–force per square inch (psi) (lbf/in.^{2})	pascal (Pa)	6.894 757 E+03
pound–force per square inch (psi) (lbf/in.^{2})	kilopascal (kPa)	6.894 757 E+00
psi (pound–force per square inch) (lbf/in.^{2})	pascal (Pa)	6.894 757 E+03
psi (pound–force per square inch) (lbf/in.^{2})	kilopascal (kPa)	6.894 757 E+00

EXECUTIVE SUMMARY

E.1   INTRODUCTION

Alkali-silica reaction (ASR) has long been recognized as a major cause of concrete internal cracking and deterioration (Stanton, 1940). This concrete deterioration mechanism begins with reaction between the alkali hydroxides in the cement paste and certain amorphous or micro-crystalline siliceous phases in the aggregates, which produces an alkali-silica gel that forms initially in the partially saturated pore space of the hardened cement paste. The alkali-silica gel is hygroscopic, absorbing moisture in the concrete matrix and expanding. This expansion will persist if moisture and other necessary conditions are present. Expansion of alkali-silica gel creates increasing internal pressure that leads to internal cracking and degradation of the mechanical properties of concrete (Hansen, 1944; Taylor, 1990).

The rate of ASR expansion is relatively slow and is a function of the reactivity of the mineral phases, the alkalinity of the pore solution, and the availability of moisture. Thus, the onset of ASR-induced cracking can take years or decades after construction to occur. However, once occurred, this deterioration at the material level may affect the bonding characteristics between the concrete and reinforcement and may further influence the overall capacity and service life of a reinforced concrete structural member or system.

At present, the industry solution is to identify the reactive aggregates and avoid using them through sourcing of materials for construction, and/or use fly ash pozzolan to control reactivity. Although this approach helps to avoid or mitigate ASR in new construction, it does not address the problem in existing structures. Given the current knowledge gaps on ASR effects and lack of consensus standards and code provisions to account for the effects of ASR on structural capacities, questions remain on how to (1) predict the progression of ASR-induced deterioration once initiated and (2) assess the residual material properties and in-situ structural capacity of the affected structures. These considerations are relevant for certain safety critical components of the nation's infrastructure (e.g., dams, bridges, and nuclear power plants). Reasonable predictions of the progression of ASR and future, residual structural capacities can provide critical support for decisions on whether the affected structures can continue to perform their safety functions without significant increase in risk to public safety.

This report describes work that is part of a comprehensive research program being conducted by the Engineering Laboratory of the National Institute of Standards and Technology (NIST) to study the effects of ASR on the structural performance of nuclear power plant concrete structures. The work is funded by the U.S. Nuclear Regulatory Commission (NRC) under Inter-Agency Agreement NRC-HQ-60-14-I-0004. The objective of this research program is to develop a technical basis for generic regulatory guidance for evaluation of ASR-affected nuclear power plant (NPP) concrete structures through its service life. Specifically, the program is intended to develop measurements for evaluation of (1) effects of ASR on structural performance and capability to perform intended function under design basis static and dynamic loads, and (2) characteristics of an aging management program to adequately monitor and manage aging effects of ASR degradation such that intended functions are maintained through the period of extended operation of renewed licenses. The intended outcome is a methodology for determining for an existing

ASR-affected structure (1) the in-situ structural capacity to resist design-basis static and dynamic loads and (2) future structural capacity.

The overall research program consisted of five tasks, intended to:

Task 1: Assess effects of ASR on in-situ mechanical properties of concrete

Task 2: Assess development and lap-splice lengths of reinforcing bars in ASR-affected concrete

Task 3: Evaluate seismic response characteristics of ASR-affected concrete structural members

Task 4: Estimate the degree of reaction in ASR-affected concrete and the corresponding expansion

Task 5: Predict future and ultimate ASR expansion in ASR-affected concrete

Specifically, this report describes the experimental planning, measurements and testing, data collection and data analysis, test results, and findings and conclusions that pertain to Task 2 of the overall research program conducted at NIST under the sponsorship of the NRC.

E.2 NIST TASK 2 EXPERIMENTAL PROGRAM

A series of 19 beam specimens, comprising 16 beams constructed with reactive aggregates using ASR 3 concrete mixture (see Section 2.2, Phan *et al.*, 2019, and Sadek *et al.*, 2021) and 3 reference beams (control specimens) constructed using the same reactive concrete mixture ASR 3 treated with a lithium nitrate solution to minimize/mitigate ASR (see Feldman *et al.*, 2020), were tested under four-point loading. The beams were all under-reinforced in order to induce flexural or tension-controlled failure mode in the beams and facilitate examination of effect of ASR on bonding characteristics between concrete and the reinforcements. The beams were stored in an environmental chamber prior to testing to accelerate ASR-induced expansion. The test program was designed as a rotatable central composite design (CCD, see Section 5.1) to facilitate examination of the effects of ASR-induced expansion, confinement provided by stirrups, and lap splice length on the flexural performance of beams with lap-spliced tensile reinforcement and on bond strength. In addition, the applicability of existing ACI code equations for the estimation of the bond strength and flexural capacity of reinforced concrete beams affected by ASR was assessed.

Specifically, the effects of the following three primary variables were investigated:

- ASR-induced expansion, $0 \leq \varepsilon_{ASR} \leq 0.22\,\%$, measured as averaged strain in the vertical and horizontal legs of stirrups;

- normalized splice length, $0.5 \leq \ell_s/\ell_d \leq 1.5$, where ℓ_s is the provided splice length and ℓ_d is the development length of the tensile reinforcement, determined in accordance with ACI 318-19 (ACI Committee 318, 2019); and

- confinement parameter, $0 \leq K_{tr}/d_b \leq 1.8$, where d_b is the nominal diameter of the spliced reinforcement and K_{tr} is the transverse reinforcement index, determined in accordance with ACI 318-19.

The influence of the above variables on the following response parameters was investigated:

- the normalized moment capacity, M_{max}/M_n, of the beams, where M_{max} is the maximum measured moment strength during testing and M_n is the nominal moment capacity of the beam section (see Section 4.5), computed in accordance with ACI 318-19;

- the normalized bond strength, $u/\sqrt{f_c'}$, where u is the maximum average bond stress measured during testing and f_c' is the compressive strength of the companion concrete cylinders tested at the same time as the respective beam specimens; and

- the beam failure mode, which indicated whether the specimen achieved the nominal flexural strength of the beam section (designated as Type B, see Section 4.5.2) or failed in bond splitting failure prior to achieving the nominal flexural strength of the beam section (designated as Type A, see Section 4.5.2).

The geometry and longitudinal reinforcement of the beams were selected to match beams previously tested by Rezansoff *et al*. (1991). Each beam had a cross section of 11.0 in × 13.0 in; a length between supports of 104.0 in; and a constant moment region, between loading points, of 44.0 in. The tensile reinforcement consisted of two No. 8 (1.0 in diameter) bars. Compression reinforcement, consisting of two No. 4 (0.5 in diameter) bars, was provided continuously along the beam's length to facilitate construction of the reinforcement cage. Closed No. 4 stirrups, with 135° hooks, were provided along the length of the beams. In the shear spans, the stirrup spacing was constant at 3 in. This dense arrangement of stirrups was selected to prevent spurious failure of the beam in shear. In the constant moment region, the stirrup spacing was varied between specimens, conforming to the levels of the confinement parameter, K_{tr}/d_b, specified in the experimental design. The clear concrete cover, between the outside of the stirrup and the beam face, was 1.0 in on all sides. This led to distances from the center of the outermost tensile bar to the side and bottom faces of the beams of 2.5 in and 2.0 in, respectively.

The beams were stored in an environmental chamber to accelerate the ASR reaction. For the first five months, the environmental chamber was kept at a temperature of roughly 80 °F and relative humidity above 95 %. After this initial period, the temperature in the chamber was increased to roughly 100 °F until approximately one year after casting, when all but one reactive beam had been tested. During this time, strains in the reinforcement were monitored for five of the beam specimens. The development of strain over time in the five beams was, for the most part, similar, despite varying stirrup spacings and lap splice lengths. Typically, strains in the longitudinal tensile reinforcement due to ASR-induced expansion were roughly half of the strains recorded in the stirrups at time of testing.

Although the target ASR expansion, measured as averaged strains in the vertical and horizontal legs of the beam stirrups, for the test program was 0.3 %, strains in the stirrups never achieved this level (see Section 4.4). Strains reached a value of 0.15 % expansion (half of the target expansion) after roughly 6 months, after which the increase slowed. The first two sets of specimens were tested at their intended

percent of target expansion values; however, beam specimens after this point were tested at roughly 3-month intervals. The maximum recorded strain in the stirrups was approximately 0.22 %.

A rigorous statistical analysis of the measured data (see Chapter 5) was conducted to quantify the influence of ASR-induced expansion, ε_{ASR}; normalized splice length, ℓ_s/ℓ_d; and the reinforcement confinement, K_{tr}/d_b, on the normalized maximum midspan moment, M_{max}/M_n, and the normalized bond strength, $u/\sqrt{f_c'}$. This analysis also assessed the applicability of existing ACI code equations for estimating the bond strength and flexural capacity of reinforced concrete beams affected by ASR and permitted quantification of the uncertainty due to sampling variability using a parametric bootstrap algorithm.

High-fidelity finite element models of seven of the tested beams were developed and validated against the test data (see Chapter 6). Four of the modeled beams were constructed with reactive ASR 3 concrete and were tested at two levels of ASR expansion. The variables examined in the modeling study were the degree of ASR expansion and the presence of continuous or spliced tensile reinforcement. These models utilized the measured concrete and steel properties and accounted for ASR expansion, degradation in material properties, and bond-slip in the reinforcement splice region.

E.3   FINDINGS

This section summarizes the findings from the experimental and computational program.

- Concrete cylinders cast at the same time as the reactive beams showed a decrease in mechanical properties over time (with increasing ASR-induced expansion). The maximum reductions, compared to the 28-day values, were roughly 15 %, 60 %, and 13 % for the compressive strength, modulus of elasticity, and splitting tensile strength, respectively. Unreinforced prism specimens, made with the same ASR 3 concrete and kept in the same environment as the beams and cylinders, had linear expansions over the same period of roughly 0.3 %. These reductions in the mechanical properties were consistent with the findings of the Task 1 study (Sadek *et al.*, 2021).

- The relationship between the concrete modulus of elasticity and the compressive strength of normalweight concrete recommended by ACI 318-19 overpredicted the compressive modulus of the reactive concrete cylinders by up to 50 %. This was particularly evident at higher expansion values and is consistent with the findings of the associated Task 1 study (Sadek *et al.*, 2021).

- The relationship between the splitting tensile strength and the compressive strength of normalweight concrete suggested by ACI 318-19 was found to be in good agreement with the measurements for the reactive concrete mixture used in the study; within 20 %, throughout the testing period.

- Significant surface cracking was observed on all of the reactive beam specimens prior to testing, and exudation of presumed ASR gel was also observed on the surface of the beams at the crack locations. The observed cracking pattern was randomly oriented; none of the observed cracks appeared to be preferentially aligned with the embedded reinforcement, and no discoloration was observed that would suggest corrosion of the reinforcement cages. The maximum crack width observed before testing was roughly (0.020 ± 0.004) in.

- For beams with ASR-induced expansions, $\varepsilon_{ASR} \geq 0.14$ %, visible cambering (upward deflection) of the beams was observed. The maximum camber observed before testing was (0.38 ± 0.06) in.

- Beams constructed with continuous tensile reinforcement failed through compressive failure of the concrete in the compression zone following flexural cracking and yielding of the tensile reinforcement. This behavior was expected as the beam sections were under-reinforced.

- For beams constructed with spliced tensile reinforcement, damage typically progressed from the formation of flexural cracks at the ends of the reinforcement splice, progressive widening of these cracks as midspan displacements increased, and finally bond splitting failure on the underside of the beam and a precipitous drop in capacity with increasing displacement. Two beams with code compliant lap splice lengths had damage progressions similar to the beams with continuous reinforcement.

- Beam deflections were generally symmetric about midspan; section rotations were generally largest at the ends of the splice region; strain increments in the tensile reinforcement due to loading were largest at the ends of the splice; and strain increments at mid-splice due to loading were roughly half the value at the ends of the splice.

- Within the range of ASR expansion examined in this test program ($\varepsilon_{ASR} \leq 0.22$ %), the stiffness of the beams did not appear to decrease due to ASR-induced expansion (or reduction of compressive concrete modulus) and the development of strain in the longitudinal reinforcement did not appear to be significantly influenced by the normalized splice length or confinement provided by the stirrups.

- Through a statistical analysis of the load test results, ASR-induced expansion was not found to decrease either the normalized moment strength or the normalized bond strength in the range of the parameters experimentally studied.

- For normalized lap splice lengths, $\ell_s/\ell_d \geq 1.3$ (complying with the code specified minimum lap splice length) and in the range of the confinement parameter, $0.5 \leq K_{tr}/d_b \leq 1.5$, the normalized bond strength relationship implied by the ACI 318-19 code equation for development length (Equation 1.7 in this report) and the recommended equation proposed by ACI Committee 408 for development length (Equation 1.9) were found to be conservative estimates (i.e., underpredict the bond strength) of the regression model fitted to the measured bond stress.

- The finite-element models were successful at estimating the upward cambering and strains in the reinforcement due to ASR-induced expansion as well as the load-deflection behavior of the beams during structural loading. The models also provided useful insights into the behavior of the beams, including the distribution of forces in the reinforcing bars and stresses in the concrete, preceding the failure of the beams.

E.4   CONCLUSIONS

This study investigated the behavior of ASR-affected beams with under-reinforced sections, asymmetric top and bottom reinforcement, spliced tensile reinforcement, and closed stirrups in the splice region. The

beams were designed to fail in flexure in the constant moment region. Spurious failure in shear was prevented through providing closely spaced stirrups in the shear spans. The conclusions presented below should be interpreted within the scope of the experimental program conducted and the ranges of experimental variables examined.

E.4.1 Statistical Analysis of Measured Data

From the analysis of the measured test results, the following conclusions were reached:

- There is no evidence that the mean normalized moment capacity, M_{max}/M_n, or the stiffness of the beams was reduced by the effects of ASR in the range of expansions studied, despite a reduction in the concrete compressive strength of up to 15 % and compressive elastic modulus up to 60 %.

- The normalized moment capacity, M_{max}/M_n, increased with increasing normalized splice length, ℓ_s/ℓ_d, within the range of the normalized splice length, $0.5 \leq \ell_s/\ell_d \leq 1.5$, used in this study.

- Beams constructed with normalized splice lengths, $\ell_s/\ell_d \geq 1.3$ (i.e., complying with the ACI 318-19 specified splice length), achieved or exceeded the nominal flexural strength of the section ($M_{max}/M_n > 1$) regardless of the degree of ASR-induced expansion when compared to the 90 % lower confidence bounds for the range of ASR-induced expansions considered ($\varepsilon_{ASR} \leq 0.22$ %).

- The measured increase in the normalized moment capacity, M_{max}/M_n, as a function of the normalized splice length, ℓ_s/ℓ_d, was generally consistent with the relationship predicted using section analysis based on the nominal strengths of the concrete and reinforcement (i.e., assuming no degradation in material properties due to ASR).

- For beams with normalized splice lengths $\ell_s/\ell_d \geq 1.3$ (i.e., complying with the ACI 318-19 specified splice length), the nominal beam moment strength M_n, computed using ACI 318 section analysis and nominal strengths of the concrete and reinforcement (i.e., assuming no degradation in material properties due to ASR) was a reasonable lower bound estimate for beam moment capacity (i.e., $M_{max}/M_n \geq 1.0$), regardless of degree of ASR expansion (up to 0.22 %).

- The mean normalized bond strength, $u/\sqrt{f_c'}$, was not found to be reduced by ASR-induced expansion, in the range of expansions studied ($\varepsilon_{ASR} \leq 0.22$ %). It should be noted that the measured compressive strength at the time of testing was used for this normalization.

- For beams with confinement parameters, $0 \leq K_{tr}/d_b \leq 1.8$, and a normalized splice length, $\ell_s/\ell_d = 1.3$ (i.e., the ACI 318-19 specified splice length), the normalized bond strength relationship implied by the ACI 318-19 code equation for development length (Equation 1.7) and the recommended equation proposed by ACI Committee 408 for development length (Equation 1.10) were reasonable lower bound estimates for the normalized bond strength, $u/\sqrt{f_c'}$ measured for ASR-affected concrete beams in this study; 99.8 % of the bootstrap replicate curves were completely above the bond strength implied by the ACI Committee 408 equation and 87.0 % of the curves were completely above the bond strength implied by the ACI 318-19 equation.

E.4.2 Computational Modeling and Analysis of Beams

The computational models investigated the influence of two primary variables:

- ASR-induced expansion, $\varepsilon_{ASR} = 0\,\%, 0.15\,\%, 0.22\,\%$, considered as the unconfined linear expansion of the concrete and

- The splice condition of the tensile reinforcement, which was either continuous or spliced.

The confinement parameter was held constant in each of the models, $K_{tr}/d_b = 1.0$. The normalized splice length in the models containing splices was also constant, $\ell_s/\ell_d = 1.0$.

From the results of the numerical models, the following conclusions were developed:

- The model developed by Saouma and Perotti (2006) and Saouma (2014) for predicting the progression of ASR-induced expansion was able to predict the upward deflection and strains on reinforcing bars within the expanded uncertainty of the measurement for beams at the 0.15 % expansion level.

- For beams at the 0.22 % expansion level, the model underestimated the upward deflection by up to 39 % and the strains on reinforcing bars by up to 21 %. It should be noted that the material formulation used in the beam models did not include the effects of creep.

- For beams with continuous reinforcement, models that incorporated the bond-slip relationship proposed by the *fib* Model Code for Concrete Structures 2010 (*fib* 2013) predicted the peak strength of the beams and the corresponding deflections within 5 %. The predicted forces in the reinforcing bars closely matched the forces based on strain measurements during testing.

- In order to capture the force-deflection behavior of the tested beam specimens with lapped spliced reinforcement, reduction in the bond strength in the relationship proposed by the *fib* Model Code for Concrete Structures 2010 was required in the region of the splice. For beams with ASR induced expansions of 0 %, 0.15 %, and 0.22 %, this reduction was 25 %, 22 %, and 5 %-10 %, respectively. This supports an increase in the bond strength with increasing ASR-induced expansion for the modeled specimens. Models of the tested beams with the reduced peak bond strengths predicted the peak strength of the beams and the corresponding deflections within 5 %, however the forces in the reinforcement based on measured strains in spliced bars were underestimated.

Chapter 1
INTRODUCTION

1.1 BACKGROUND

Alkali-silica reaction (ASR) is a concrete deterioration mechanism derived from the chemical degradation of coarse aggregates which can lead to material damage through an affected structure. ASR occurs most frequently in siliceous aggregates which undergo dissolution in the highly alkaline pore solution of the concrete. The result is the formation of a silica gel that, together with excess calcium from cement hydration, forms a hygroscopic gel that absorbs available water in the pore network. Upon the uptake of water, the silica gel undergoes a substantial volume increase which can cause local cracking, bulk expansions in the concrete, and degradation of its mechanical properties.

ASR in concrete structures was first identified by Stanton (1940), and considerable research on this topic has been conducted to date, including investigation of the in-situ mechanical properties of reactive mixtures in service (e.g., Clark, 1989; McLeish, 1990; Deschenes *et al.*, 2009; Smaoui *et al.*, 2006), methods to manage the effects of ASR in existing structures (e.g., Fournier *et al.*,2004; Fournier *et al.*, 2010; Charlwood *et al.*, 2012; Bérubé *et al.*, 2002a; Bérubé *et al.*, 2002b; Drimalas *et al.*, 2012) methods to prevent ASR in new structures (e.g., McCoy and Caldwell, 1951; Jensen *et al.*, 1984; Pleau *et al.*, 1989; Lane and Ozyildirim, 1995; Lane and Ozyildirim, 1999; Mather, 1999; Folliard *et al.*, 2006; Bektas *et al.*, 2006; Carles-Gibergues *et al.*, 2008; Thomas *et al.*, 2008; Thomas *et al.*, 2012c; Thomas *et al.*, 2012d) and methods for simulating the effects of ASR on structural components and structures (e.g., Bažant and Steffens 2000; Ulm *et al.*, 2000; Bangert *et al.*, 2004; Saouma and Perotti, 2006; Pesavento *et al.*, 2012; Saouma, 2014)

Of particular importance for the present study are investigations into the structural performance of flexural members, specifically those which studied the bond between ASR-affected concrete and deformed bar reinforcement.

1.1.1 Bond Mechanism

Independent of the presence of ASR, the transfer of forces from steel reinforcement to concrete is required for the two materials to act compositely. This transfer of forces occurs primarily through bearing of the reinforcement bar deformations, "lugs", on the surrounding concrete and is largely controlled by the fracture energy required to split the concrete along the bar's length. The energy required to produce and propagate this splitting crack depends on numerous factors, including the embedment length of the reinforcement, the passive confinement of surrounding concrete, the presence of transverse reinforcement, and stresses transverse to the splitting plane created by structural loads.

In practice, it is often convenient to visualize the bond of reinforcement as a frictional phenomenon, where an equivalent frictional average bond stress, u, acts uniformly over the exterior surface of the reinforcement, often treated as circular in cross section. In this instance, for an infinitesimal segment of

steel reinforcement with length, Δx, the change in axial stress from one end of the segment to the other, $\Delta f/\Delta x$, is given by:

$$\Delta f/\Delta x = \Sigma_b u/A_b = 4u/d_b, \tag{1.1}$$

where A_b, Σ_b, d_b are the area, perimeter, and diameter of the reinforcement, respectively.

To reach the yield stress of the steel, f_y, the reinforcement must be embedded in the concrete element for a minimum development length, ℓ_d, computed as:

$$\ell_d = d_b f_y/4u . \tag{1.2}$$

The critical parameter in the resulting expression is the value for the equivalent average bond stress, u, which has historically been determined empirically. ACI 318-63, with limited testing information, prescribed a value for the maximum allowable bond stress of:

$$u = 9.5 \sqrt{f_c'}/d_b \leq 800 \text{ psi}, \tag{1.3}$$

where f_c' is the 28-day specified concrete compressive strength in psi. This expression led to the resulting expression for the required development length, meant to achieve 125 % of the yield stress of the steel, adopted in ACI 318-71:

$$\ell_d = 0.04 A_b f_y/\sqrt{f_c'}, \tag{1.4}$$

Later, Orangun *et al.* (1977) developed an empirical value for the maximum average bond stress based on a statistical analysis of the available data (the equation is reproduced here with minor modification for convenience in notation):

$$u/\sqrt{f_c'} = 1.2 + 3(c_b/d_b - 0.5) + 50\,d_b/\ell_s + 4.8\,K_{tr}/d_b, \tag{1.5}$$

where c_b is the minimum distance from center of the spliced reinforcement to the free surface of the beam or half the bar spacing, ℓ_s is the splice length, $K_{tr} = 40\,A_{tr}/sn$ is the transverse reinforcement index that describes the confinement provided by the stirrups, A_{tr} is the total area of transverse reinforcement crossing the splitting plane assumed by the selection of c_b, s is the stirrup spacing, and n is the number of bars being spliced across the splitting plane. Rearranging and simplifying Equation 1.5 led to the expression for the development length prescribed in ACI 318-95, given in Equation 1.6, that has persisted in ACI 318 since:

$$\ell_d/d_b = (3/40) \left(f_y/\lambda\sqrt{f_c'}\right) \psi_t\psi_e\psi_s/\left(\frac{c_b+K_{tr}}{d_b}\right), \tag{1.6}$$

where ψ_t, ψ_e, ψ_s, and λ are correction factors pertaining to casting location, reinforcement coating, reinforcement diameter, and the use of lightweight concrete. For normalweight concrete and Grade 60, uncoated, deformed bar reinforcement in good casting position with a diameter of 1.0 in, the correction factors are all 1.0.

This development length would imply an average bond strength, u, based on Equation 1.2 of:

$$u = (10/3)\lambda\sqrt{f_c'}\left(\frac{c_b+K_{tr}}{d_b}\right)/\psi_t\psi_e\psi_s \tag{1.7}$$

ACI 318-19 specifies that if two bars are to be joined through a lap-splice, the ends of the bars must overlap for at least a distance of 130 % of the development length calculated using Equation 1.6 (Class B splice) to develop the yield stress of the steel. In cases where the stress in the reinforcement at the design load is less than, or equal to, 50 % of the yield stress in the steel and less than half of the bars in tension are being spliced over any given length, the bars can be overlapped for only 100 % of the development length (Class A splice).

Since 1997, ACI Committee 408 has maintained a formal database of bond and splice tests, now with over 600 entries. A portion of this database was the basis for the empirical relationships developed by Orangun *et al*. (1997) and adapted for ACI 318. In 2005, the committee published recommended design expressions based on a statistical analysis of this database. This recommended expression for the development length was given by (the equation is reproduced here with minor modification for convenience in notation):

$$l_d/d_b = (1/62)\left(f_y/f_c'^{1/4} - 2000\right)\psi_t\psi_e\lambda/(c_b/d_b + K_{tr}\sqrt{f_c'}/80\,d_b), \qquad (1.8)$$

for conventional reinforcement with a diameter of 1.0 in, assuming equal cover on all sides of the reinforcement.

This development length would imply an average bond strength, u, based on Equation 1.2 of:

$$u = 15.5\left(c_b/d_b + K_{tr}\sqrt{f_c'}/80\,d_b\right)/\left(1/f_c'^{1/4} - 2000/f_y\right)\psi_t\psi_e\lambda \qquad (1.9)$$

While the equations above have different forms, the influence of the parameters is consistent between each of the expressions. To increase the bond strength, and thus decrease the required development length, one should increase the bar cover, c_b/d_b; add stirrups or confinement steel around the longitudinal reinforcement, K_{tr}/d_b; or increase the design strength of the concrete, f_c'.

1.1.2 Rezansoff *et al*. (1991)

One test set in the ACI Committee 408 database is the work of Rezansoff *et al*. (1991). This test series is described briefly here, because it informs the experimental design described in Chapter 2. Rezansoff *et al*. (1991) tested 40 simply supported beams with lap-spliced tensile reinforcement under four-point loading. The study was conducted to investigate the influence of confinement of the splice region (in excess of the limit prescribed in ACI 318-89) on the splice performance. The variables examined were the beam size (scale effects), bar size, concrete strength, stirrup spacing, and splice length. Of the beams tested, 21 of the beams measured 11 in × 13 in in cross section and had depths to the lapped 1.0 in diameter tensile reinforcement between 11 in and 11.5 in. The beams were tested with a constant moment region, between central loading points, of 44 in and shear spans of 30 in.

Table 1.1 summarizes the specimen details and bond stress results for 12 of these beam tests in terms of several key normalized quantities. It should be noted that the variables presented in Table 1.1 were recomputed based on expressions in ACI 318-19, and therefore differ slightly from the original paper. The average bond strength, u, was computed using the reported splice length and maximum stress in the reinforcement during testing, which exceeded the yield stress of the steel, 65.5 ksi, in all but three cases (Beam 20-8-7, Beam 20-8-8, and Beam 20-8-9). The computed bond stress was normalized by the square root of the compressive strength of the concrete, which varied between 4200 psi and 5700 psi. In all cases, the beams failed by a bond-splitting failure, with splitting cracks developing on the bottom surface of the

beams, starting from the end of the splice. Confinement in excess of the limits specified by the code equations improved the bond without producing pullout failures and confinement provided by concrete cover was found to be slightly less effective than confinement provided by reinforcement for improving bond.

Table 1.1. Specimen details and test results (data from Rezansoff et. al 1991)

Beam	K_{tr}/d_b	c_b/d_b	ℓ_s/ℓ_d	$u/\sqrt{f_c'}\ (\sqrt{psi})$
20-8-1	2.2	1.5	1.0	13.9
20-8-2	1.6	1.5	1.0	10.2
20-8-3	1.1	1.5	1.0	8.9
20-8-4	2.2	1.5	0.9	15.1
20-8-5	1.6	1.5	0.9	13.1
20-8-6	1.1	1.5	1.0	10.8
20-8-7	0.5	2.0	0.9	9.0
20-8-8	1.0	2.0	0.9	10.7
20-8-9	1.5	2.0	0.9	12.8
20-8-10	2.5	2.0	0.9	16.5
20-8-11	2.5	1.5	0.9	17.7
20-8-12	2.1	2.0	0.9	15.4

1.1.3   Literature Survey on the Influence of ASR on Flexural Performance and Bond

Clark (1989) summarized the results of beam tests performed up to that time, mainly from Japan but also from Denmark. These tests were conducted on under-reinforced beam specimens with continuous reinforcement, ranging in height from 7 in to 19.7 in. From this survey of results, Clark observed that the flexural stiffness of the beams was not reduced by ASR, shear failure became less likely with increasing ASR expansion, and the capacities of ASR-affected beams were between 93 % and 147 % of nominally identical beams constructed with non-reactive aggregates. These observations were largely attributed to prestressing caused by the ASR-induced expansion, which occurred in the laboratory specimens under accelerated aging conditions. It was suggested that this prestressing may be absent under field conditions due to slower reaction rates and time-dependent effects such as creep.

Swamy and Al-Asali (1989, 1990) tested seven beam specimens under four-point loading with continuous, high-strength reinforcement (yield stress of 81 ksi or 560 MPa) at a depth to reinforcement of 3 in. The beams did not contain compression steel or stirrups in the constant moment region and had a longitudinal reinforcement ratio of roughly 1.8 %. Four of the beams were constructed with fly ash in order to study its effect on decreasing expansion and damage due to ASR. The results of the tests showed between a 15 % and 26 % reduction in strength due to ASR. Strength degradation was effectively mitigated in the beams constructed using fly ash (roughly a 5 % reduction in strength). The reduction in strength for these specimens, in comparison to previously tested specimens, was attributed to the reinforcement ratio used

in the beam specimens by Clark (1989). The sections tested by Swamy were over-reinforced, and therefore the compressive behavior of the concrete played a much more significant role in the beam response.

Chana (1989) and Chana and Korobokis (1992) examined the influence of ASR on the bond of deformed reinforcement, plain (smooth) bar, and square twisted bars. In total, the two studies comprised 120 pull tests. The beam and pullout specimens were constructed with varying bar cover, casting position, and stirrup confinement. After accelerated aging, the longitudinal surface expansion at the location of the bars was between 0.2 % to 0.3 % and the lateral surface expansion was between 0.5 % to 0.8 %. For specimens without stirrups and a cover of less than four bar diameters, ASR-induced expansion generally led to a decrease in the bond strength, independent of the reinforcement type, by up to 40 %. Specimens that contained stirrups or had reinforcement with cover greater than 4 bar diameters, showed no significant reduction in strength.

Chana and Korobokis (1992) also tested 8 beams and 16 slab sections under four-point loading. The beams had no stirrups or compression steel, a depth to reinforcement of 7.1 in, and a reinforcement ratio of 0.32 %. After accelerated aging, the longitudinal surface expansion at the level of tension reinforcement was roughly 0.2 %. The slab sections were constructed with either plain (smooth) or deformed bars; lap-spliced tensile reinforcement, with a splice length of 12.5 bar diameters in the shear span of the test specimens; and depths to reinforcement of 3 in. After accelerated aging, the longitudinal surface expansion at depth of reinforcement was roughly 0.09 % and 0.07 % for plain and deformed bars, respectively. For the beam test series, ASR-induced expansion resulted in a roughly 4 % reduction in moment strength. For the slab test series, ASR-induced expansion did not change the failure modes of the reactive specimens (bar pullout for plain bars and loss of bond in the splice for deformed bars) compared with their non-reactive counterparts. In addition, the effects of ASR led to a 17 % reduction in flexural strength and a 10 % reduction in anchorage force.

Fan and Hanson (1998) tested six beams, three of them with reactive aggregates. The beams had no stirrups in the constant moment region, were reinforced with continuous tensile reinforcement at a depth to reinforcement 8.2 in, and had continuous compression steel. The reinforcement ratios for the tested specimens were 0.44 % and 1.3 %. After nearly one year in an alkali bath, the beam specimens had longitudinal surface expansions of roughly 0.08 % at the level of the bars and a transverse surface expansion of 0.1 %. Despite significant cracking, there was no observed decrease in load carrying capacity of the beams.

Ahmed *et al*. (1998) tested 16 beam specimens, four of them constructed with reactive aggregates. Beams were reinforced with "high-tensile" bars, with an assumed 80 ksi yield strength, at a depth to reinforcement of 4.18 in and a reinforcement ratio 1.3 %. The tests investigated the effects of stirrup spacing, end anchorage condition, and the influence of repeated loads. The beam specimens were cured in a water bath for five months, after which the longitudinal surface expansion of the specimens at the location of the tensile reinforcement was roughly 0.2 %, lateral surface expansion was roughly 0.5 %, which varied depending on whether stirrups were present in the beams or not. In these tests, ASR-induced expansion decreased the probability of shear failure, produced an increase in beam capacity of roughly 10 %, and led to a larger number of cycles to failure under repeated loads.

Ahmed *et al*. (1999) tested 24 beams with different lap splices under static and cyclic loads. The tested beams had no stirrups or compression steel in the constant moment region, depths to the tensile reinforcement of 2.67 in, reinforcement ratios of 1.2 %, and splice lengths ranging from 5 to 32 bar

5

diameters. The beam specimens were cured in a water bath for five months, after which the longitudinal surface expansion at the location of the tensile reinforcement was roughly 0.2 % and the lateral surface expansion was at least 0.5 %. Lap splice length did not affect expansions; however, smaller expansion was observed for beams with continuous reinforcement. In this test series, ASR-induced expansion led to a reduction in strength ranging from about 5 % to 22 % for beams with lap splices of 5 to 20 bar diameters, respectively.

Monette *et al*. (2002) tested 15 beam specimens, eight of them with reactive aggregates. The beams were constructed with stirrups over their entire length, a depth to reinforcement of 3.94 in, a reinforcement ratio 1.1 %, and no compression steel. The beams were cured in an Alkali bath for either 147 or 161 days. The beams experienced a large gradient in longitudinal surface expansion: roughly 0.4 % at the top of the section and 0.05 % at the bottom, where the reinforcement was located. For this test series, ASR-induced expansion did not reduce the flexural strength or stiffness of the reinforced concrete beams.

Mutlon *et al*. (2005) and Morenon *et al*. (2019) tested five beams, three of them with reactive aggregates. One reactive beam was completely unreinforced, and the others were constructed with continuous tensile and compression reinforcement; stirrups throughout the constant moment region; depths to tensile reinforcement of 16.5 in and 17.75 in; and reinforcement ratios of 0.4 %, and 1.5 %. The sides of the beams were sealed and the top and bottom of the beams were subjected to different moisture conditions to provide data needed to calibrate multiphysics models. After accelerated aging, the transverse surface expansion was roughly 0.2 % and the longitudinal surface expansion varied from around 0.2 % at the level of reinforcement to -0.05 % at the top of the beam. ASR-induced expansion led to a roughly 30 % degradation in stiffness and strength of unreinforced beam and no reduction in strength or stiffness of the reinforced beams.

Bracci *et al*. (2012) tested eight large-scale column specimens with lap-splices, six of them with reactive aggregates. Specimens were tested horizontally in four-point and three-point bending, and axial loads were simulated with post-tensioned strands. The specimens were cured outdoors with supplementary water from a sprinkler system for a duration between 2 and 3 years. The specimens were constructed with lap splice lengths of 108 in (77 bar diameters), and depths to reinforcement of 20.7 in. After aging outdoors, the strain in the longitudinal reinforcement was between 0.02 % and 0.1 % and the transverse surface expansion was between 0.1 % and 0.9 %. Internal strain measurements and strains in reinforcement were roughly 50 % of the measured surface expansion. In this test series, ASR-induced expansion did not have a significant impact on the strength of the specimens.

Numerous other studies have included structural testing of ASR-affected concrete members (e.g., Kobayashi *et al*., 1987; Bach *et al*., 1993; Deschenes *et al*., 2009; Mander *et al*., 2015; Habibi *et al*., 2018) but are not discussed here. In general, the flexural strength of over-reinforced sections and the bond properties for beams without stirrups are reduced due to the reduction in material properties caused by ASR, which can be significant (up to a 50 % reduction in elastic modulus and tensile strength). Conversely the ASR-induced expansion, which prestresses the concrete element, has been found to improve the shear strength of flexural elements and, in the presence of stirrups, improves bond between the steel reinforcement and the concrete.

In 2013 NIST performed a scoping study to determine existing knowledge gaps and support future activities to evaluate the effects of ASR on structural capacity (Snyder and Lew, 2013). Identified in this study was the need to assess the applicability of existing design expression for reinforcement bond found

in ACI 318 and ACI 349 to structures affected by ASR. Although several previous studies have investigated bond in ASR affected structures (e.g., Chana, 1991; Ahmed *et al*., 1999), these tests were insufficient to span the potential parameter space, especially in regard to stirrup spacing and the resulting confinement, which was held constant in previous test series.

1.2   SCOPE OF THE STUDY

This experimental program was conducted to examine the influence of ASR on the bond and flexural strength of beam members with lap-spliced reinforcement. In particular, the research program aimed to assess the applicability of existing design expression for reinforcement bond strength found in ACI 318 to structures affected by ASR.

A series of 19 beam specimens were constructed and tested under four-point bending. The test series was designed to facilitate examination of the effects of the following three variables on beam performance:

- the degree of ASR-induced expansion, measured as the maximum strain induced in the stirrups confining the splice during curing;
- the degree of splice confinement, varied as the confinement ratio K_{tr}/d_b, where K_{tr} is the transverse reinforcement index and d_b is the reinforcing bar diameter; and
- The ratio of the lap splice length of the tensile reinforcement, ℓ_s, to the development length, ℓ_d, determined in accordance with ACI 318-19.

The experiment was designed to limit cross-correlation, capture interactions, and capture second order effects in this parameter space.

1.3   REPORT OUTLINE

The focus of this report is to present the results of the experimental program and to describe subsequent numerical simulations, which aimed to capture the major features of the observed experimental response.

- Chapter 2 presents the details of the experimental program including the design of the test specimens, accelerated aging method, experimental test setup, and instrumentation.

- Chapter 3 presents the observed damage of the test specimens, including cracking due to ASR, and damage observed during testing.

- Chapter 4 presents the measured response of the test specimens including measured material properties, expansion during the accelerated aging process, and measurements during testing.

- Chapter 5 presents a statistical analysis of the measured data including the flexural strength of the beams, bond strength, and beam failure type.

- Chapter 6 presents finite element models of select specimens and compares the predicted and measured responses.

- Chapter 7 summarizes the testing program and presents findings and conclusions based on the analysis of the observed and measured data.

Chapter 2
EXPERIMENTAL PROGRAM

2.1 DESIGN OF TEST SPECIMENS

To achieve the objective of this Task as described in Section 1.2, tests were conducted to investigate the flexural performance of reinforced concrete beams with lap-spliced reinforcement that were made with reactive coarse and fine aggregates. The geometry and longitudinal reinforcement of the beams were selected to match beams previously tested by Rezansoff *et al.* (1991), see Section 1.1.2. This test series was selected because it was included in the experimental database developed for ACI 408R-03, which was used to develop the existing development length equations specified by ACI 318-19. Aligning the present experimental program to these tests also allowed for comparison of the behavior of the ASR-affected beams to that with sound, non-ASR-affected concrete and an evaluation of the applicability of the ACI development length equation for ASR-affected concrete structures.

The beam geometry and cross section are shown in Figure 2.1 and Figure 2.2, respectively. Each beam had a nominal cross section of 11.0 in × 13.0 in; a length between supports of 104.0 in; and a constant moment region, between loading points, of 44.0 in. The tensile reinforcement consisted of two No. 8 (1.0 in diameter) bars. Compression reinforcement, consisting of two No. 4 (0.5 in diameter) bars, was provided continuously along the beam's length to facilitate construction of the reinforcement cage. All reinforcement was ASTM A615 Gr 60 (ASTM A 615/A 615M, 2020). Closed No. 4 (0.5 in diameter) stirrups, with 135° hooks, were provided along the length of the beams. In the shear regions, the stirrup spacing was constant at 3.0 in. This dense arrangement of stirrups was selected to avoid any possibility of failure in the shear region. In the constant moment region, the stirrup spacing was varied between tests. The clear cover, between the outside of the stirrup and the beam face, was 1.0 in on all sides. This led to distances from the center of the outermost tensile bar to the side and bottom faces of the beams of 2.5 in and 2.0 in, respectively.
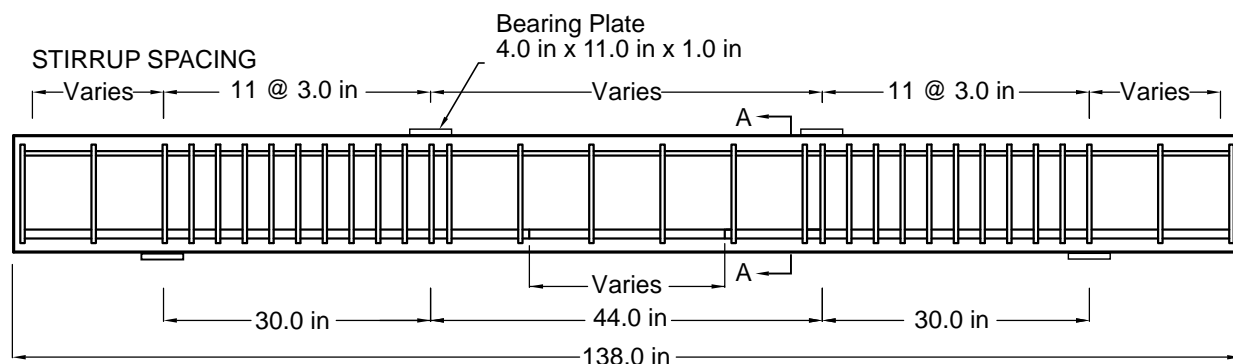
Figure 2.1. Typical elevation of beams with lap splices
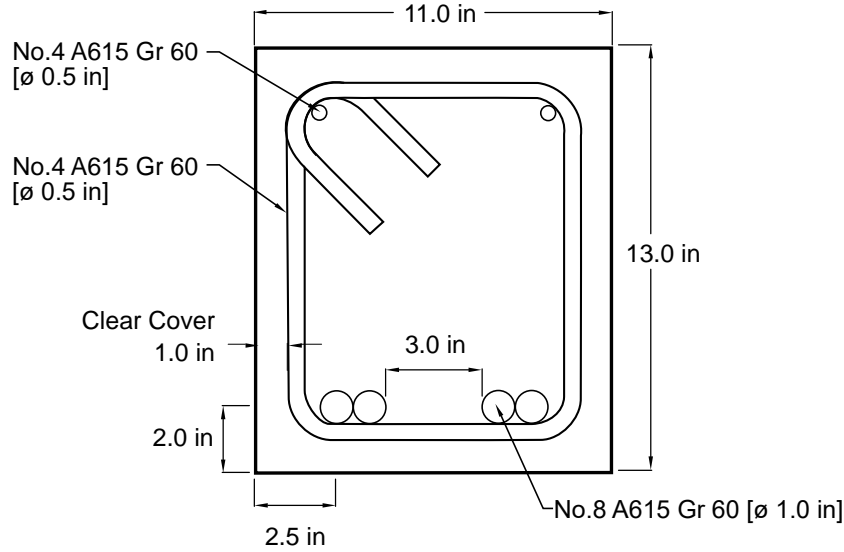
Figure 2.2 Typical cross section of beams with lap splices

Table 2.1 lists the parameters varied in the test series. A total of 19 simply supported beams were tested under symmetric four-point bending. Of these, 17 contained lap splices and three were constructed with concrete treated with a lithium nitrate solution to limit the reaction of the aggregates. The test series considered the influence of the following variables on the flexural capacity of ASR-affected, reinforced concrete beams:

- The target level of ASR expansion at testing, ε_{ASR}, measured as the maximum strain in the stirrups relative to the design ultimate expansion level $\varepsilon_{ASR\text{-}ult}$ of 0.3 % for ASR 3 concrete mixture. For example, Beam 1, with a testing target of 25 %, was planned to be tested when the ASR-induced expansion had resulted in a nominal strain in the stirrups of ε_{ASR} = 25 % × $\varepsilon_{ASR\text{-}ult}$ = 0.25 × 0.3 % = 0.075 %;
- The degree of confinement in the constant moment region, represented by the confinement parameter K_{tr}/d_b, where K_{tr} is the transverse reinforcement index and d_b is the reinforcing bar diameter; and
- The ratio of the lap splice length of the tensile reinforcement, ℓ_s, to the development length, ℓ_d, calculated according to ACI 318-19.

Note that the ultimate expansion for this concrete mixture (ASR 3) was 0.5 %, based on measurements taken from standard prisms in accordance with ASTM C1293 (ASTM C1293, 2020), see Feldman *et al*. (2020) and Section 4.3 of this report. However, due to size effects, confinement effects, and different environmental conditions from those used for the standard prisms, the measured ultimate expansions on the reinforcement used in block specimen ASR 3 of Task 1 (Sadek *et al*., 2021) were in the range of 0.25 % to 0.35 %. As a result, a design ultimate expansion level $\varepsilon_{ASR\text{-}ult}$ of 0.3 % was deemed reasonable for this testing program.

A rotatable central composite design (CCD, see Box *et al*., 2005) was used for the design of experiments, considering the above parameters. This design includes an embedded factorial design with additional points that allow for the estimation of curvature in the region of interest. The design was centered around the point (50 %, 1.0, 1.0) in the design space (ε_{ASR}, K_{tr}/d_b, ℓ_s/ℓ_d). Additional beams were added to the design, including two beams without spliced reinforcement, as reference specimens.

Beams were constructed with varying confinement and lap-splice lengths (K_{tr}/d_b and ℓ_s/ℓ_d in Table 2.1). Some beams were constructed with code compliant Class B splices (Beams 2, 4, 6, and 8); however, many were deliberately designed with insufficient lap splice lengths for the purpose of studying the maximum bond stress achievable prior to bond splitting failure. To investigate the influence of confinement, one beam (Beam 13) was designed with no stirrups in the splice region, while other beams were designed with closely spaced transverse stirrups, in excess of the maximum amount considered to be effective for decreasing development length under static loading per ACI 408R-03.

Table 2.1. Beam test matrix based on a rotatable central composite design

Beam	Testing Target (% of $\varepsilon_{ASR-ult}$)	K_{tr}/d_b	ℓ_s/ℓ_d
1	25	0.5	0.7
2	25	0.5	1.3
3	25	1.5	0.7
4	25	1.5	1.3
5	75	0.5	0.7
6	75	0.5	1.3
7	75	1.5	0.7
8	75	1.5	1.3
9	50	1.0	1.0
10	50	1.0	N/A[‡]
11	0*	1.0	1.0
12	100	1.0	1.0
13	50	0.0[†]	1.0
14	50	1.8	1.0
15	50	1.0	0.5
16	50	1.0	1.5
17	0*	1.0	1.0
18	0*	1.0	N/A[‡]
19	100	1.0	1.0

* Beam constructed with ASR Mix 3 concrete but treated with lithium nitrate solution to prevent expansion

[†] Beam had no stirrups in the constant moment region

[‡] Beam had continuous tensile reinforcement

2.2 CONCRETE MIXTURE

Table 2.2 summarizes the mixture design used in the beam specimens. ASR Mix 3 concrete described in the Task 1 study (Sadek *et al*., 2021) was used for all 19 of the beam specimens. The target 28-day strength of the mixture was 5000 psi based on the measured strengths in the Task 1 study. The Placitas gravel and Jobe sand conformed to ASTM C33 (ASTM C33/C33M, 2018) gradation requirements #6 coarse aggregate and fine aggregate, respectively.

Table 2.2. ASR Mix 3 Concrete Proportions

Constituent	Design proportions by weight (lb/yd^3)
Type I/II, high alkali (0.89 % Na_2O_e) cement	588
Placitas coarse aggregate	1767
Jobe fine aggregate	1185
Water	293
Sodium Hydroxide (NaOH)	4

Two of the tested specimens (Beam 17 and Beam 18) were cast separately from the rest of the beams. For these specimens, no sodium hydroxide was added to the mix and a 30 % lithium nitrate solution was added at a dosage of 3.2 gal/yd^3. This corresponds to 110 % of the recommended dosage by the lithium nitrate manufacturer for the mix design (without the addition of sodium hydroxide) presented in Table 2.2.

2.3 FABRICATION OF TEST SPECIMENS

Figure 2.3 shows the beam reinforcement and formwork prior to casting. The reinforcement cages were fabricated using jigs and placed into the formwork. To ensure consistent spacing between the tensile bars and formwork bottom, plastic-tipped slab bolsters were used to support the cage at the ends of the beam and just outside the constant moment region.

Figure 2.3. Formwork, reinforcement, and instrumentation of beam specimens

The first 17 beams (Beams 1-16 and Beam 19) were cast on February 6, 2018. Batching and mixing of concrete were carried out at the NIST campus in Gaithersburg, MD. The coarse and fine aggregates, along with the cement and water, were loaded to a concrete volumetric truck mixer that was used as a batching plant (Figure 2.4). The volumetric truck contents were then loaded via a conveyer belt into a concrete mixer truck (Figure 2.5), where the sodium hydroxide was added as a 3 M solution. After mixing, the concrete was discharged from the concrete mixer onto the belt, which conveyed and placed concrete into the beam formwork. The concrete was consolidated using vibrators (Figure 2.6).

Figure 2.4. Loading of aggregates into volumetric truck mixer

Figure 2.5. Loading the volumetric truck contents to a concrete mixer truck via a conveyer belt (telebelt)

Figure 2.6. Concrete placement into beam's formwork and consolidation using vibrators

Since Beam 11 was intended to serve as a control specimen and to be tested at 0 % target expansion (see Table 2.1), a lithium nitrate solution was added to the concrete mixer prior to casting Beam 11 (the last beam to be cast) to mitigate ASR effects. Because the remaining volume of concrete in the mixer could not be determined, the precise dosage of lithium nitrate solution could not be quantified.

The remaining two beams (Beam 17 and Beam 18) were cast on August 23, 2019. This separate cast was conducted to more accurately dose the lithium nitrate solution. Batching and mixing of concrete were also carried out at the NIST campus in Gaithersburg, MD. The coarse and fine aggregates, along with the cement and water, were directly loaded by a telescoping forklift into a concrete mixer truck (Figure 2.7). Prior to placing the concrete, a 30 % lithium nitrate solution was added to the mixture at a dosage of 3.2 gal/yd^3 of cement). After additional mixing, the concrete was discharged from the mixer into a hopper, which was used to place concrete into the beam formwork. The concrete was consolidated using vibrators.

15

Figure 2.7. Loading of aggregates into concrete mixer truck

In addition to casting the beams, companion concrete specimens were prepared for both placements. These included 3 in × 3 in × 11.25 in standard prisms for monitoring of ASR expansion (Section 4.3) and 4 in × 8 in cylinders for mechanical properties testing (Section 4.1).

2.4   CURING

Immediately after completion of concrete placement and finishing, each beam was covered with wet burlap and plastic sheets to prevent loss of moisture and minimize the potential for developing drying shrinkage cracks during the hydration process. Water was sprayed onto the burlap on a daily basis. After removal of the formwork seven days after the placement of concrete, the first set of beams (Beam 1-Beam 16 and Beam 19) were moved to the environmental chamber and kept at a temperature of roughly 80 °F with a relative humidity (RH) in the range of 95 % to 100 %. After roughly 160 days in this environment, the temperature in the chamber was increased and kept in the range of 100 °F to 110 °F, as shown in Figure 2.8. This curing condition was maintained until roughly 400 days after casting, after which the remaining untested beam (Beam 12) was kept at ambient conditions (relative humidity in the range of 50 % to 75 % and temperature in the range of 75 °F to 90 °F) until testing. The second set of beams

(Beam 17 and Beam 18) were kept at ambient conditions after removal of the formwork until testing (78 days after casting).
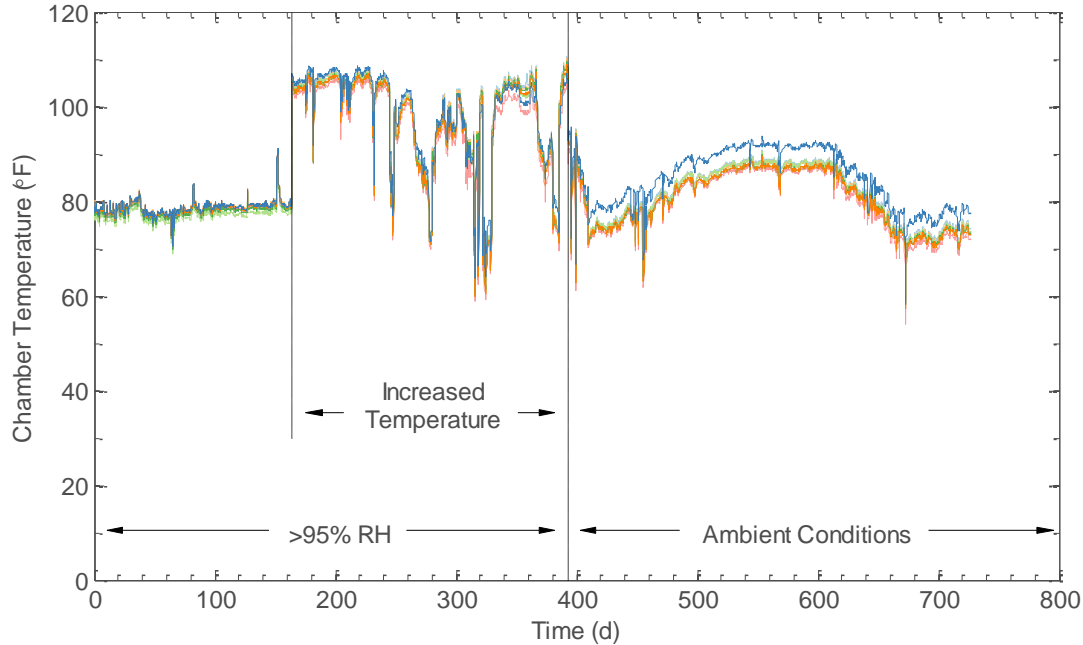
Figure 2.8. Measured temperatures inside the environmental chamber

2.5   TEST SETUP

The beams were simply supported and subjected to static, four-point bending as shown in Figure 2.9. Increasing vertical displacements were applied to the center of the beam by a servo-hydraulic actuator at a constant displacement rate of 0.06 in/min. The total force required to maintain the imposed displacement was recorded by a load cell integral to the actuator. A spreader beam was used to divide the actuator force into two equal loads on the beam specimens.

Both contact points on the beam top surface consisted of 2.0 in diameter steel cylinders, connected to the spreader beam, bearing on a 1.0 in thick plate that was as wide as the top surface of the beam and 4.0 in in length along the beam's span, as shown in Figure 2.10. A 0.125 in thick piece of medium-density fiberboard was placed beneath the steel bearing plate to evenly distribute load on the beam's top surface, which was ground flat at the loading points prior to testing.

Figure 2.9. Beam test setup

The beams were supported on sliding-rocker assemblies, as shown in Figure 2.11. These supports comprised a greased polytetrafluoroethylene-stainless steel sliding surface, a 3.0 in diameter steel cylinder rocker, and a 1.0 in thick bearing plate that was as wide as the bottom surface of the beam and 4.0 in in length along the beam's span. The beam end was allowed to rotate about the centerline of the cylinder and slide horizontally at the stainless steel interface. The minimal friction in the sliding-rocker assembly prevented instability of the system while reducing any axial forces caused by the vertical deflection of the beam. A 0.125 in thick piece of medium-density fiberboard was used to evenly distribute load from the bearing plate on the beam's bottom surface. Deformation of the fiberboard, which would act to increase the apparent deflection of the beam specimen, was not observed in the tests.
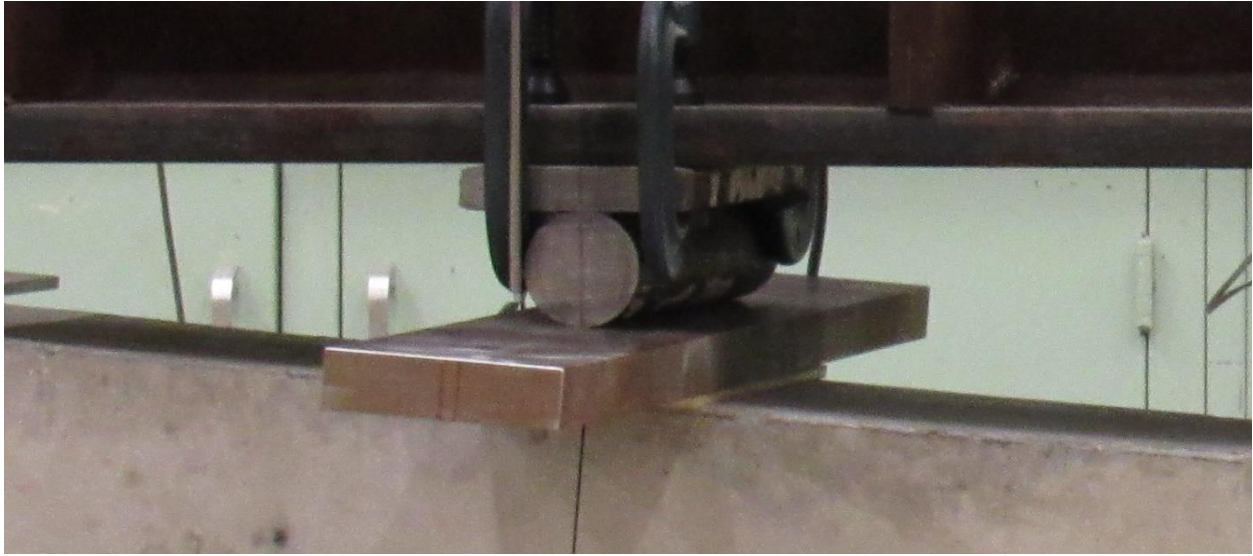
Figure 2.10. Beam loading point

Figure 2.11. Beam vertical support

2.6   INSTRUMENTATION

The applied load, beam deflection, and rotation of the beam were monitored during testing. In addition, strain gages applied to the tensile and transverse reinforcement prior to placing the concrete, monitored the development of strains in the reinforcement in the spliced region during both curing and testing.

Figure 2.12 shows the location of beam displacement potentiometers which were used to measure the beam deflection during testing. Beam deflections were measured at midspan, the two loading points, and halfway between each loading points and its adjacent support. Deflections were measured on either side of the beam specimen, as shown in Figure 2.12. The potentiometers spanned between aluminum square

tube sections fixed to the loading frame and steel plates, which extended from the top surface of the beam and were adhered to the concrete using hot-melt adhesive, as shown in Figure 2.13.
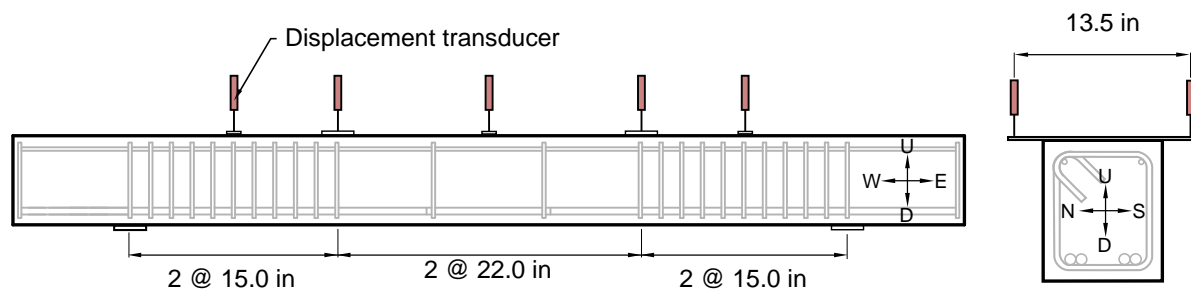
Figure 2.12. Beam displacement potentiometer locations
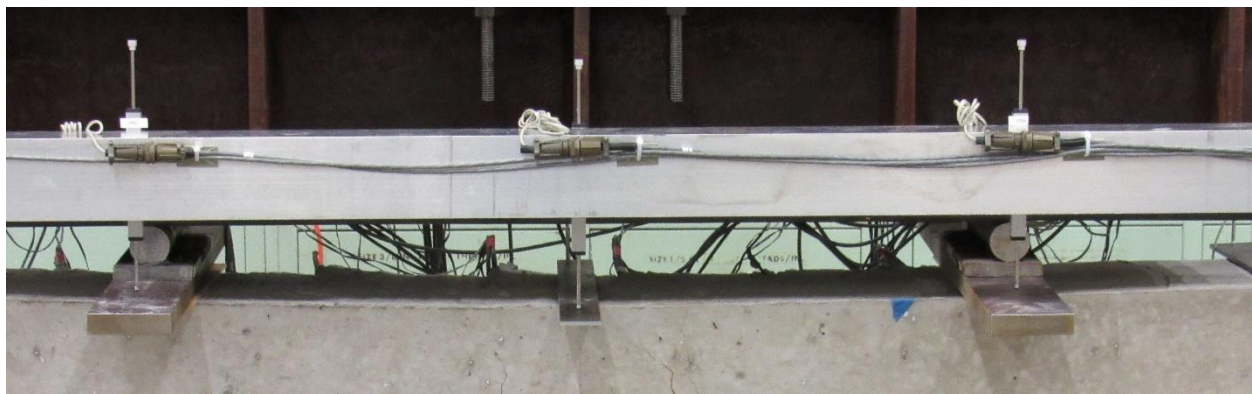
Figure 2.13. Beam displacement potentiometers

Figure 2.14 shows the nominal location of section rotation measurements during the tests. Prior to casting the beams, threaded rods were passed, horizontally, through the formwork walls and the reinforcement cage. Displacement transducers, shown in Figure 2.15, were affixed to the rods and used to measure the relative deformation between successive rod locations during static loading. Section rotations were computed by subtracting the displacement reading from the top instrument from the displacement reading from the bottom instrument and dividing by the measured separation between the instruments.
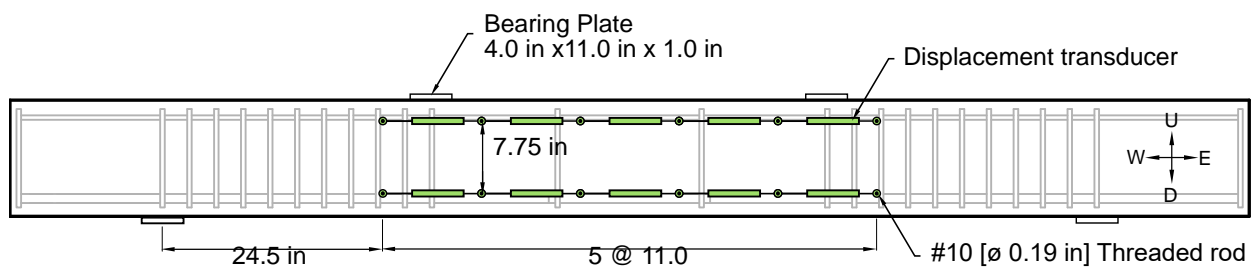
Figure 2.14. Section rotation measurement locations
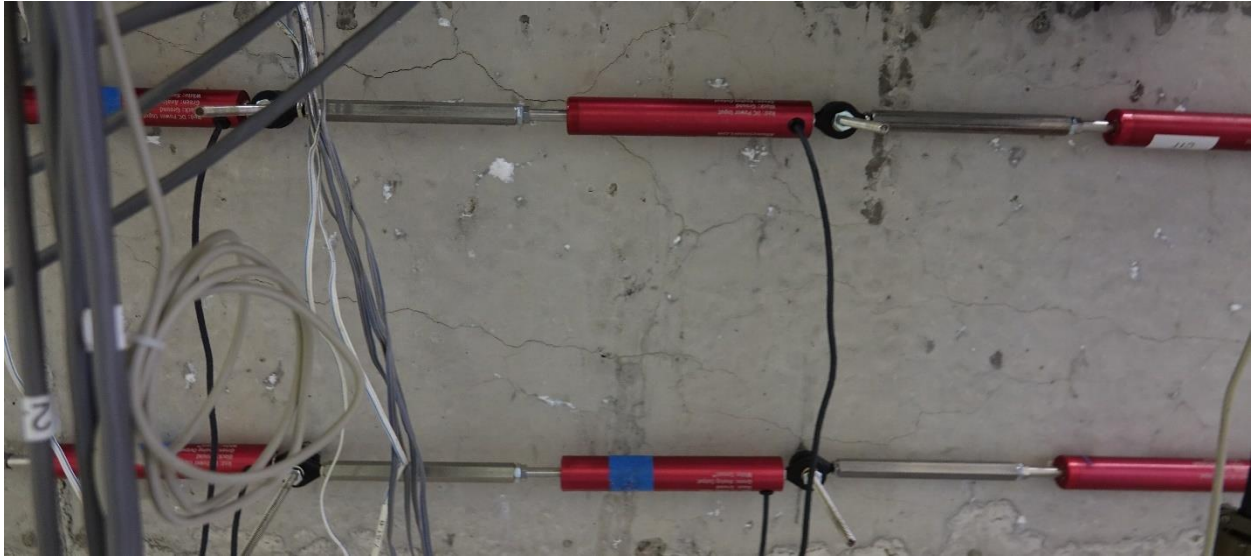
Figure 2.15. Displacement transducers used to measure section rotation

Figure 2.16 shows inclinometers that were used to measure the rotation of the beam at the supports. Inclinometers were affixed to the beam surface at mid-height using hot-melt adhesive.

Figure 2.16. Inclinometers used to measure beam end rotation

Figure 2.17 shows the relative location of strain gages. Gages were applied on both sides of the tensile bars at mid-splice and just outside the splice region. Gages were also applied on the bottom and south leg of four stirrups in the constant moment region. Because the lap splice length and the stirrup spacing varied between beams, the absolute location of the gages varied as well. The location of the strain gages for each beam test is given in Appendix B.
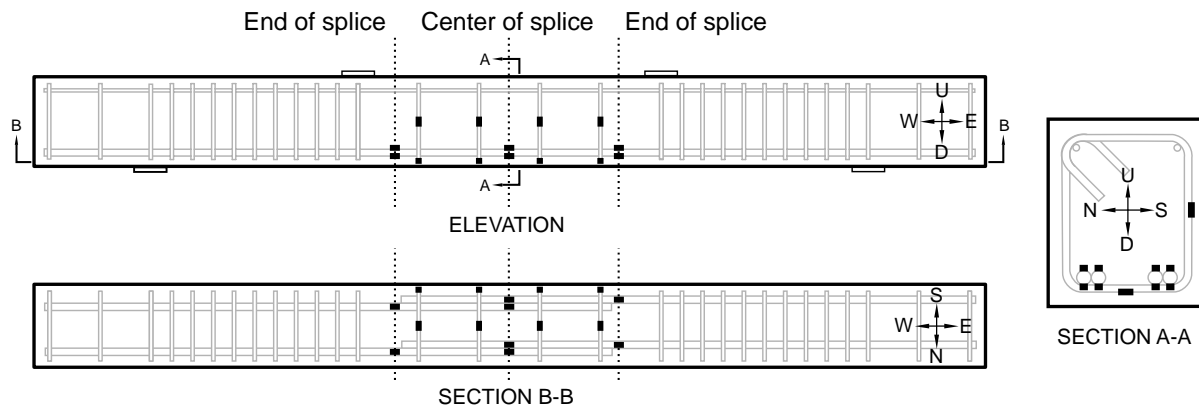
Figure 2.17. Location of strain gages on beam reinforcement

Figure 2.18 shows the typical installation of a foil resistance strain gage on a longitudinal reinforcement bar. The bars were prepared using a belt sander to remove their mill scale and achieve the required flatness in the gage area. Bars were further prepared using a fine grit sandpaper and cleaned using a chemical degreaser, prior to gage installation. Gages were adhered to the bar using a two-component epoxy system and the gage installation was protected from the highly alkaline concrete environment using a two-part polysulfide liquid polymer compound, as shown in Figure 2.19.

Figure 2.18. Strain gage application on longitudinal reinforcement

Figure 2.19. Strain gage protective coating on beam stirrups

Strains on five of the 19 beam specimens were monitored during curing in the environmental chamber to measure the ASR-induced expansion. These were Beams 6, 8, 10, 12, and 14. The monitored beams were selected with different splice length and stirrup arrangements to investigate any potential difference in the ASR-induced expansion.

Figure 2.20 shows the location of a high-resolution camera, relative to the beam specimen, that was used to capture video of each test. This video was synchronized to the test data using a digital indicator visible in the camera's frame. This video was subsequently used to track the progression of damage (e.g., cracking, spalling, and crushing) throughout the tests.

Figure 2.20. High-resolution camera position, relative to beam specimen

Chapter 3
OBSERVED RESPONSE

This Chapter describes the cracking that was observed in the beams due to the effects of ASR-induced expansion prior to structural loading and the progression of damage that was observed in the beams during structural testing. In many instances, it is convenient to refer to sides or faces of the beam specimens in terms of cardinal directions (north, east, south, west), which correspond to the directions in the tested orientation. Figure 3.1 presents this nomenclature for a typical beam specimen.
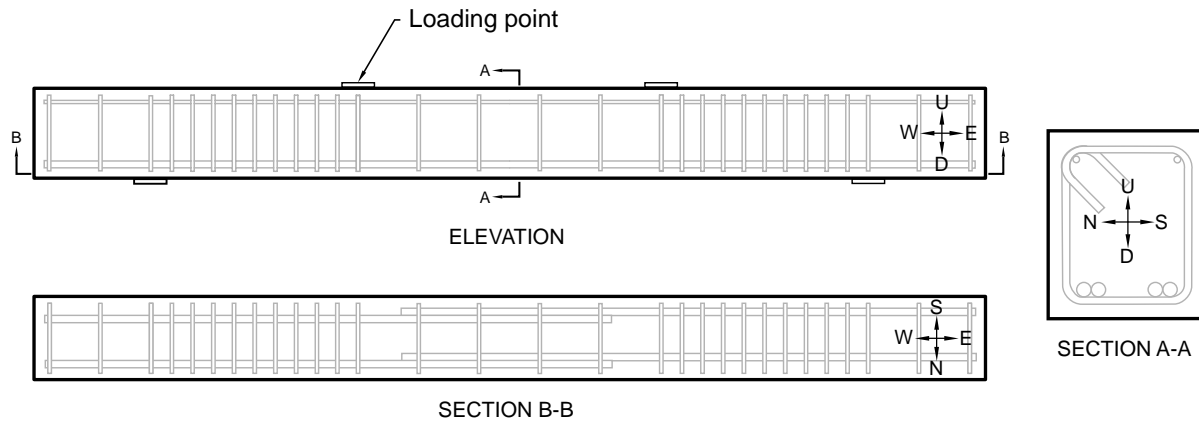
Figure 3.1. Nomenclature for beam faces

3.1 ASR-INDUCED EXPANSION

Prior to testing, the beams remained in the environmental chamber, which was kept at the RH and temperature outlined in Section 2.4. Figure 3.2 shows the beams in the environmental chamber after approximately 6 months of accelerated reaction.

Figure 3.2. Beam specimens in environmental chamber

Beams were removed from the chamber on the day of the test and placed into the testing frame. Visual observations of the condition of the concrete were recorded and then the beam was tested. The entire process took less than 8 hours.

Figure 3.3 shows a closeup view of the north face of Beam 6, which was tested at an expansion of 75 % of design ultimate expansion $\varepsilon_{ASR-ult}$ (0.3 %). In general, significant cracking (consisting of randomly oriented surface cracks) was observed on all of the reactive beam specimens prior to testing. Exudation of a white substance, from the cracks, was also observed. It is presumed that this substance was ASR gel, however no chemical analyses were performed to confirm this assumption. As anticipated, beams that were tested earlier in the experimental program tended to have less pronounced surface cracking and smaller crack widths than beams that were tested at higher levels of expansion. The maximum crack widths observed for Beam 2, Beam 10, and Beam 7 (tested at 25 %, 50 % and 75 % of the $\varepsilon_{ASR-ult}$) were approximately (0.008 ± 0.004) in, (0.016 ± 0.004) in, and (0.02 ± 0.004) in, respectively. Surface cracking tended to be more significant at the ends of the beams, with 5 faces exposed to the environment, than over interior portions of the beams.

The observed cracks did not appear to be preferentially aligned with the embedded reinforcement, and no discoloration was observed that would suggest corrosion of the reinforcement cages.

Figure 3.3. Beam 6 concrete condition prior to testing (with the surface of the beam wetted with rag to improve contrast)

A visual crack mapping procedure was performed to quantify the degree of surface cracking present on the beam specimens prior to testing. This approach was based on the cracking index (CI) method that was developed, and is used extensively, by the Federal High Administration (Fournier *et al.*, 2010). This method was also used to measure surface expansion on the reactive block specimens in the Task 1 study (Sadek *et al.*, 2021). The CI has been used to judge the extent of surface damage to the concrete due to ASR, based on the implicit assumption that external damage is proportional to internal damage; thus, the higher the CI, the higher the assessed level of damage of the concrete element under investigation.

The crack mapping procedure employed in the present study included measurement and summation of crack widths along a set of lines drawn vertically on the North face of the beam specimens. These vertical lines were drawn at each of the four loading points and halfway between each loading point, as shown in Figure 3.4. The purpose of performing surface crack measurements, prior to testing the beams, was to determine if any correlation existed between the CI value and the internal strains recorded in the stirrups (as described in Section 2.6, strains in the reinforcement were measured during the accelerated reaction on the bottom reinforcing bars and the vertical legs and bottom of the stirrups).
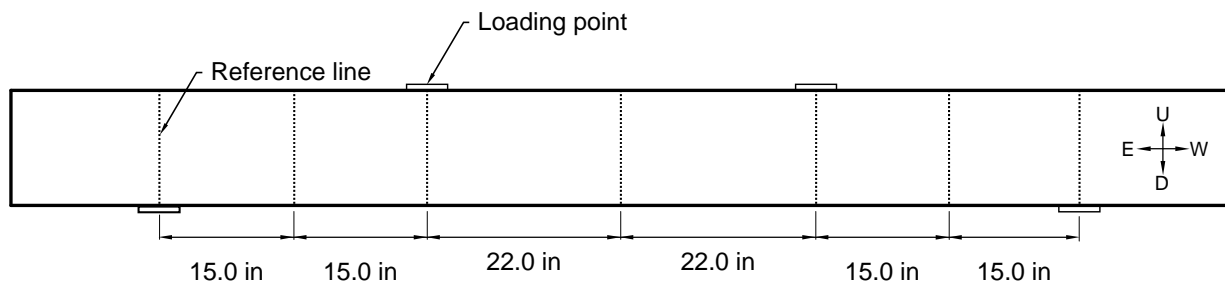
Figure 3.4. Locations of reference lines on beam specimens

The width of all cracks that crossed each of the vertical lines were measured using a handheld optical microscope, with 20× optical magnification and a measuring reticle graduated in 0.1 mm increments. Crack widths were estimated between divisions with a resolution of 0.05 mm. The cracking index was calculated as the summation of all crack widths along a given grid line, divided by the height of the North side of the beam, measured at midspan. Cracks smaller than 0.1 mm were observed and recorded but were not used in calculation of the CI.

Table 3.1 gives the average CI over the three vertical reference lines in the constant moment region for several representative beams prior to testing. In general, the crack index in the constant moment region did appear to increase with ASR-induced expansion, however significant variation did exist among beams tested at the same target expansion.

Table 3.1. Average cracking index for representative beam specimens prior to testing

Beam	Testing Target (% of $\varepsilon_{ASR\text{-}ult}$)	Cracking Index (in/in)
2	25	0.0003
4	25	0.0007
9	50	0.0011
10	50	0.0008
6	75	0.0012
8	75	0.0018

The beams were observed to have noticeable camber (upward deflection) prior to testing. Figure 3.5 shows an example of the camber measured prior to testing for Beam 19. The camber values were estimated using a laser level and tape measure, as shown in Figure 3.5. The laser level was fixed on both lower, or upper, corners of the beam, while the location of the surface of the beam at midspan, relative to the laser level, was recorded. For beams where the camber was estimated at the top surface of the beam, the estimate was adjusted for the slight variation in beam height from one end of the beam to the other (assuming the form flat bottom surface was the most appropriate datum). The development of camber is attributed to the non-symmetric reinforcement of the beam (larger tension reinforcement than compression reinforcement), which led to non-symmetric restraint of the ASR-induced expansion.

Figure 3.5. Beam 19 camber prior to testing

The observation of camber in beam specimens which have undergone ASR-induced expansion is common in the literature (e.g., Swamy and Al-Asali 1989, Ahmed *et al*. 1998, Fan and Hanson 1998, and Multon *et al* 2005). Table 3.2 gives the estimated camber present in several representative beams prior to testing.

Table 3.2. Estimated camber in beam specimens prior to testing

Beam	Testing Target (% of $\varepsilon_{ASR\text{-}ult}$)	Observed Camber (in)
2	25	*
4	25	*
9	50	0.15 ± 0.06
10	50	0.16 ± 0.06
12	100	0.38 ± 0.06
19	100	0.31 ± 0.06

* No visually perceivable camber was present prior to these tests

3.2 STRUCTURAL TESTING

Figure 3.6 shows the shear region of Beam 12 after testing. As shown in the figure, the region between the loading point (third vertical line from left) and the support remained essentially undamaged. Damage in the beam specimens was confined to the constant moment region between the central loading points. The damage progression during structural testing consisted of flexural cracking, a progressive widening of flexural cracks, followed by either compressive failure of the concrete compression zone of the section and/or bond-splitting failure at the tensile reinforcement splice. No evidence of shear or bearing failure was observed in any of the beam tests.

Figure 3.6. Beam 12 shear span and bearing regions at end of testing

3.2.1 Compressive Failure of the Concrete Compression Zone of the Section

Two beams (Beams 10 and 18, tested at 50 % and 0 % of $\varepsilon_{ASR\text{-}ult}$, respectively) were tested with continuous reinforcement as references for the remainder of the beams in the experimental program. The damage progression for these beams consisted of flexural cracks forming near midspan, followed by yielding of the tensile reinforcement, and finally compressive failure of the concrete compression zone of the section.

29

Figure 3.7 shows the crack pattern on the north face of Beam 18 at the end of testing. The damage progression for Beams 10 and 18 was similar. Flexural cracks formed near midspan of the beam, between the loading points. The reinforcement yielded and, after additional deflection, compressive failure of the concrete compression zone occurred at midspan and the load dropped precipitously.
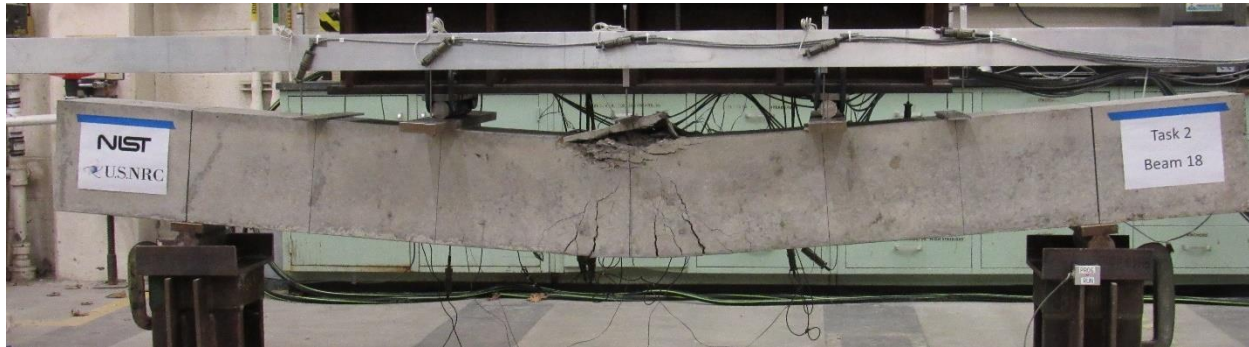
Figure 3.7. Beam 18 crack pattern at the end of testing

The progression of damage for Beam 8 (tested at 75 % of $\varepsilon_{ASR\text{-}ult}$), with a code compliant (Class B) splice as designated by ACI 318-19, and Beam 16 (tested at 50 % of $\varepsilon_{ASR\text{-}ult}$), with a splice length exceeding that specified by the ACI 318-19, were similar to that of the beams with continuous reinforcement. Figure 3.8 shows the crack pattern of Beam 8 at failure. The location of damage was different from the beams with continuous reinforcement, however. Deformations and damage were concentrated at the west end of the reinforcement splice, corresponding to the right side of the constant moment region in Figure 3.7.

Figure 3.8. Beam 8 crack pattern at the end of testing

3.2.2   Bond Splitting Failure

The remaining 15 beams failed due to bond splitting failure in the splice region. Beams 2, 4, 6 ,12, 14, and 19 achieved their nominal flexural strengths, calculated in accordance with ACI 318-19, prior to the loss of confinement of the splice due to concrete and bonding failure in the splice region.

Figure 3.9 shows the crack pattern at the end of testing for Beam 6, tested at 75 % of $\varepsilon_{ASR\text{-}ult}$. The damage progression for the remaining beam specimens was similar. Vertical, flexural cracks first formed in the constant moment region at the ends of the splice region, followed by longitudinal splitting cracks on the bottom surface of the beam as shown in Figure 3.10 for Beam 6. In certain cases, additional splitting cracks formed on the sides of the beam, adjacent the spliced bars, after additional beam deflection.

Figure 3.9. Beam 6 crack pattern at the end of testing
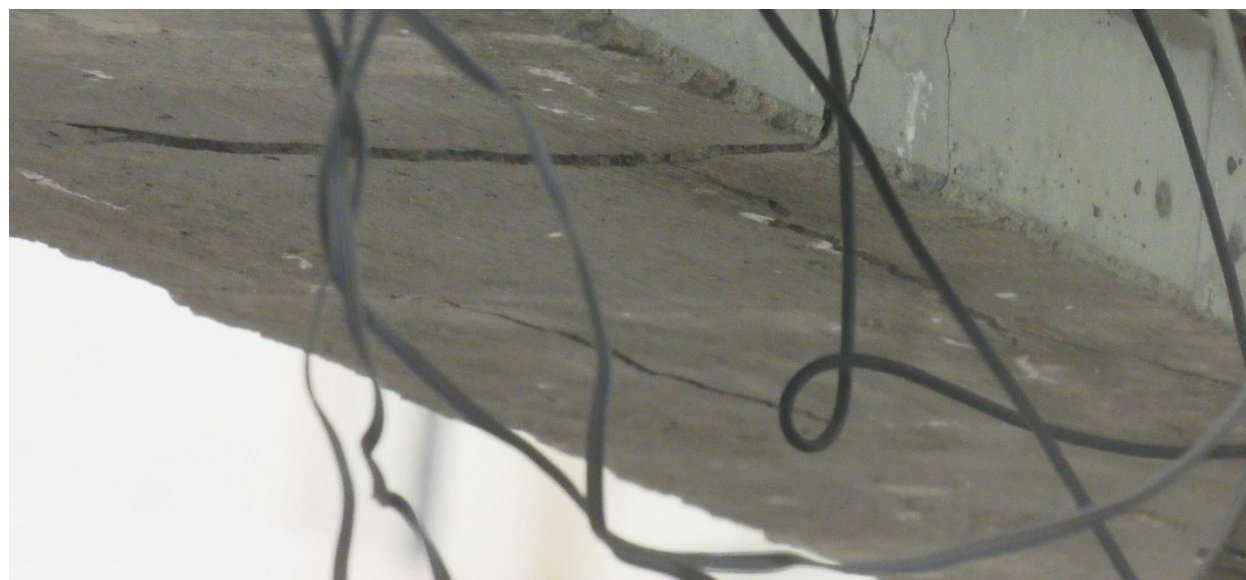
Figure 3.10. Beam 6 splitting cracks during loading

After bond splitting cracks formed, the resistance of the beams began to drop, presumably because the spliced deformed bar reinforcement began slipping relative to one another. The loading was continued until an actuator displacement of 1.5 in was reached, to capture the complete softening response of the beam specimen. During this post-peak loading, compressive failure of the concrete compression zone of the section occurred vertically above the tensile reinforcement splice.

31

Figure 3.11 shows the underside of Beam 6 after testing. The beam has been flipped upside-down in the photograph (the North side of the beam is still pictured). In addition to the flexural cracks, splitting cracks on the bottom of the beam, at the location of and along the tensile reinforcement splice, were observed. These cracks extended from vertical flexural cracks that formed at either end of the splice region. Additionally, horizontal cracks on the North face of the beam at the elevation of the tensile reinforcement were also observed, extending partially through the splice region.

Figure 3.11. Beam 6 failure pattern (taken after testing with the beam flipped upside-down)

Chapter 4
MEASURED RESPONSE

This chapter describes the measured response of the beam specimens. Material tests performed on standard test specimens are also presented.

- Section 4.1 gives the measured mechanical properties of concrete cylinders cast with the same concrete as the beam specimens.
- Section 4.2 presents the measured mechanical properties of the steel reinforcement used to construct the beam specimens
- Section 4.3 describes the length change of standard expansion prisms cast with the same concrete as the beam specimens throughout the testing program
- Section 4.4 presents the strains measured in the beam reinforcement during ASR-induced expansion.
- Section 4.5 describes the response of the beam specimens under structural loading.

Each value reported in the sections that follow is denoted by mean value μ_c which was typically averaged from at least three independent measurements, followed by +/- uncertainty U. Unless otherwise noted, the uncertainty is reported as the expanded uncertainty associated with the mean, which is determined for n independent measurements by $U = (k\,u_c)/\sqrt{n}$ from the combined standard uncertainty u_c (i.e., estimated standard uncertainty in the mean from an uncertainty analysis) with a coverage factor of k determined by the two-tailed Student's t distribution at probability p = 95 % (i.e., at the 95th percentile) with $N = n - 1$ degrees of freedom. Assuming that the unknown true value being measured (for example, the compressive strength, elastic modulus, or tensile strength) is approximately normally distributed with standard deviation u_c, the reported mean value lies within the interval defined by $\pm U$ with a level of confidence of 95 %. For each plot in this section, markers correspond to mean values and the error bars correspond to $\mu_c \pm U$.

4.1 CONCRETE MECHANICAL PROPERTIES

The compressive strength, modulus of elasticity, and splitting tensile strength of the beam concrete were determined through tests on the companion cylinders prepared during casting of the beams. Testing was conducted in accordance with ASTM C39 Standard Test Method for Compressive Strength of Cylindrical Concrete Specimens (ASTM C39, 2020), ASTM C469/469M-14 Standard Test Method for Static Modulus of Elasticity and Poisson's Ratio of Concrete in Compression (ASTM C469/469M, 2014), and ASTM C496/496M Standard Test Method for Splitting Tensile Strength of Cylindrical Concrete Specimens (ASTM C496/496M, 2017), respectively.

The development of these concrete mechanical properties over time was captured by testing cylinders at 7 days, 14 days, 28 days, and 90 days and before and after each round of beam testing. In the following subsections, values presented for testing periods, corresponding to target levels of ASR expansion, are shown as the average values for both test days, immediately preceding and following beam tests.

4.1.1 Uniaxial Compressive Strength

Table 4.1 provides the measured compressive strength of the 4 in × 8 in reactive concrete cylinders throughout the testing period. Table 4.2 provides the compressive strength of cylinders made with concrete treated with lithium nitrate used to construct Beam 17 and Beam 18, which served as reference specimens.

Table 4.1. Compressive strength of reactive concrete mixture

Time	Compressive Strength (psi)
7 d	3870 ± 210
14 d	4340 ± 420
28 d	4450 ± 700
90 d	4560 ± 130
99 d (25% of $\varepsilon_{ASR\text{-}ult}$ Testing)	4000 ± 360
195 d (50% of $\varepsilon_{ASR\text{-}ult}$ Testing)	3770 ± 450
293 d (75% of $\varepsilon_{ASR\text{-}ult}$ Testing)	3960 ± 500
388 d (100% of $\varepsilon_{ASR\text{-}ult}$ Testing)	4180 ± 620
648 d (Beam 12 Testing)	4920 ± 1030

Table 4.2. Compressive strength of lithium-nitrate treated mixture

Time	Compressive Strength (psi)
7 d	3900 ± 200
28 d	4510 ± 220
78 d (date of tests)	5090 ± 240

Figure 4.1 shows the compressive strength of the beam concrete for both the reactive mixture (blue line) and the lithium-nitrate treated mixture (orange line) plotted against time, measured in days after casting. In the figure, the marker represents the average value of the compressive strength, while the error band at each time corresponds to the expanded uncertainty. The cylinders continued to gain strength until roughly 90 days. For specimens tested after 90 days, the compressive strength was roughly 10 % less than the 28-day compressive strength. The final measurement, at 648 days, was somewhat anomalous. The average compressive strength was somewhat larger than the 28-day value, however the expanded uncertainty for this measurement was also considerably larger, in comparison to the expanded uncertainty of measurements taken a year earlier.
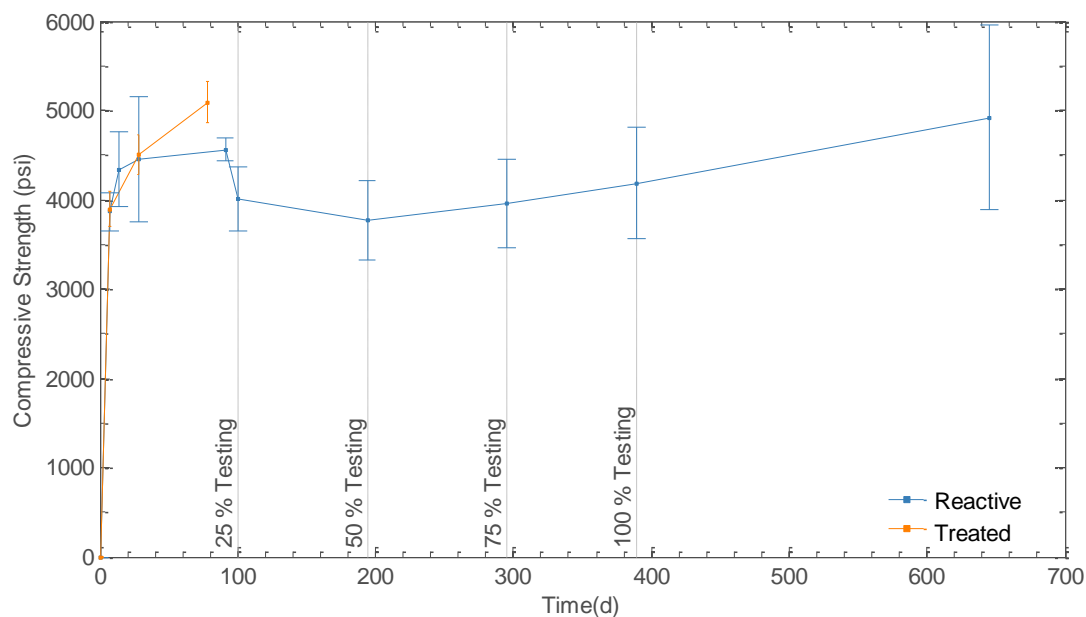
Figure 4.1. Concrete compressive strength

4.1.2 Modulus of Elasticity

Table 4.3 provides the measured modulus of elasticity of 4 in × 8 in reactive concrete cylinders throughout the testing period. Table 4.4 provides the modulus of elasticity of cylinders made with concrete treated with lithium nitrate used to construct Beam 17 and Beam 18.

Table 4.3. Modulus of elasticity of reactive concrete mixture

Time	Modulus of Elasticity E_c (ksi)
7 d	3840 ± 2520
14 d	3900 ± 700
28 d	4120 ± 560
91 d	2440 ± 970
99 d (25% of $\varepsilon_{ASR-ult}$ Testing)	2320 ± 150
293 d (75% of $\varepsilon_{ASR-ult}$ Testing)	1750 ± 290
388 d (100% of $\varepsilon_{ASR-ult}$ Testing)	2155 ± 220
648 d (Beam 12 Testing)	2320 ± 1300

35

Table 4.4. Modulus of elasticity of lithium-nitrate treated mixture

Time	Modulus of Elasticity E_c (ksi)
7 d	4310 ± 150
28 d	4630 ± 10
78 d (date of tests)	4680 ± 500

The compressive modulus was determined as the slope of the linear regression of the measured stress and strain up to 40 % of the compressive strength of the cylinder. This approach, unlike the ASTM C469 secant stiffness method, reduced the influence of the initial nonlinearity of the compressive stress-strain response that is often seen in ASR-affected concrete cylinders. Calculation of the values of compressive modulus as the slope obtained from linear regression more robustly captured the basic features of this nonlinearity; however, as was described the in the Task 1 study (Sadek *et al.*, 2021), the choice of calculation method had only a minimal effect on the reported compressive modulus values.

Figure 4.2 shows the compressive modulus of both the reactive cylinders (blue line) and the lithium-nitrate treated mixture (orange line) plotted against time, measured in days after casting. For the reactive concrete cylinders, the compressive modulus at 28 days was (4120 ± 560) ksi, roughly $62\,000\sqrt{f_c'}$, within 10 % of the 3800 ksi value ($57\,000\sqrt{f_c'}$) estimated using ACI 318-19 based on the 28-day compressive strength. The average value of the compressive modulus at 90 days was roughly 50 % of the 28-day compressive modulus. After 90 days, the measured elastic modulus remained relatively constant with time, at around 2000 ksi.
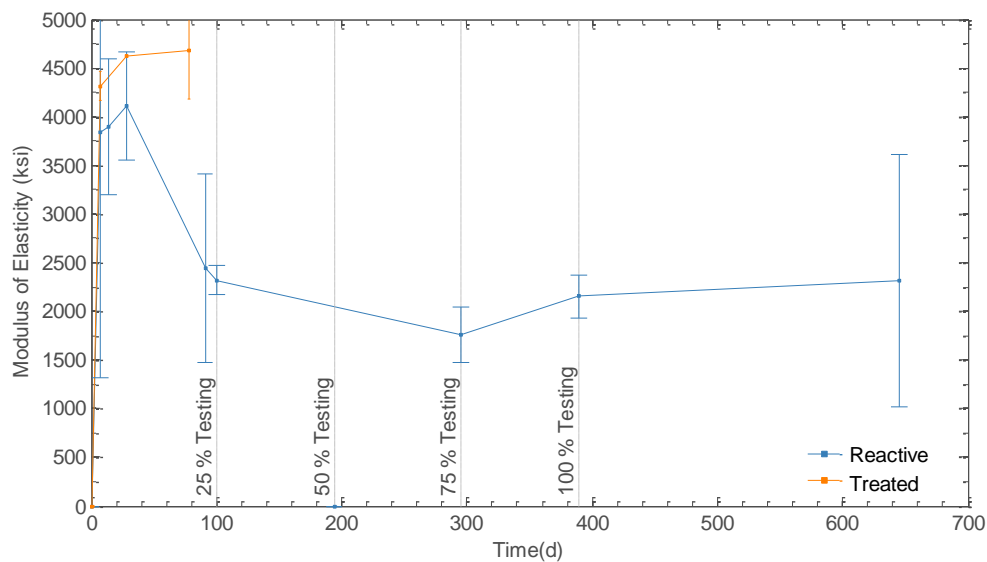
Figure 4.2. Concrete modulus of elasticity E_c

Figure 4.3 compares the measured elastic modulus to that predicted using Equation 19.2.2.1.b in ACI 318-19 for normalweight concrete. The solid line in the figure is the relationship given in ACI 318-19, the

dashed lines are the +/- 20 % bounds on the coefficient, and the horizontal axis is scaled with the square root of the compressive strength. For the non-reactive cylinders and the reactive cylinders tested before 90 days, the ACI 318-19 equation is in reasonable agreement with the measured values, within roughly 20 %. For the reactive cylinders tested after 90 days, the equation overpredicts the elastic modulus by as much as 50 %. Similar observations were made in the Task 1 study (Sadek *et al.*, 2021) for the reactive concrete mixes.
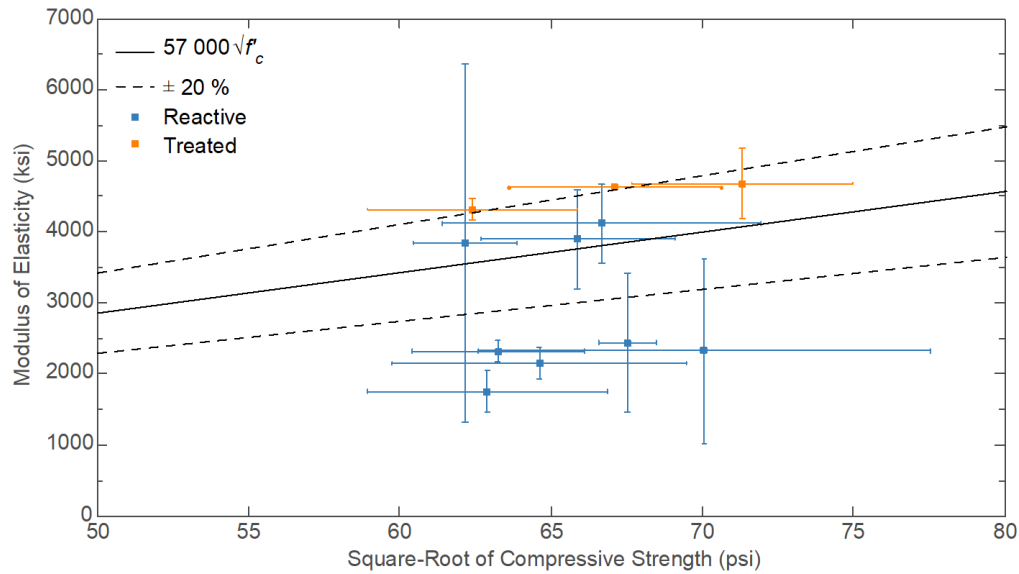
Figure 4.3. Concrete modulus of elasticity vs. the square root of compressive strength

4.1.3 Splitting Tensile Strength

Table 4.5 provides the measured splitting tensile strengths of 4 in × 8 in reactive concrete cylinders. Table 4.6 provides the splitting tensile strengths of cylinders made with lithium-nitrate treated concrete that was used to construct Beam 17 and Beam 18.

Table 4.5. Splitting tensile strength of reactive concrete mixture

Time	Tensile Strength (psi)
7 d	500 ± 110
14 d	480 ± 120
28 d	450 ± 10
91 d	430 ± 80
99 d (25 % of $\varepsilon_{ASR-ult}$ Testing)	390 ± 80
195 d (50 % of $\varepsilon_{ASR-ult}$ Testing)	440 ± 90
293 d (75 % of $\varepsilon_{ASR-ult}$ Testing)	520 ± 130
388 d (100 % of $\varepsilon_{ASR-ult}$ Testing)	410 ± 30
648 d (Beam 12 testing)	440 ± 80

Table 4.6. Splitting tensile strength of lithium-nitrate treated mixture

Time	Tensile Strength (psi)
7 d	420 ± 20
28 d	450 ± 50
78 d (date of tests)	450 ± 10

Figure 4.4 shows the splitting tensile strength of both the reactive cylinders (blue line) and the lithium-nitrate treated cylinders (orange line) plotted against time, measured in days after casting. For the reactive cylinders, the splitting tensile strength at 28 days was (450 ± 10) psi, within 1 % of the estimated value of 447 psi ($6.7\sqrt{f_c'}$) using ACI 318-19 based on the 28-day compressive strength. The average value of the splitting tensile strength remained, for the most part, constant with time, despite visible signs of distress and a reduction of the modulus of elasticity for the cylinders.
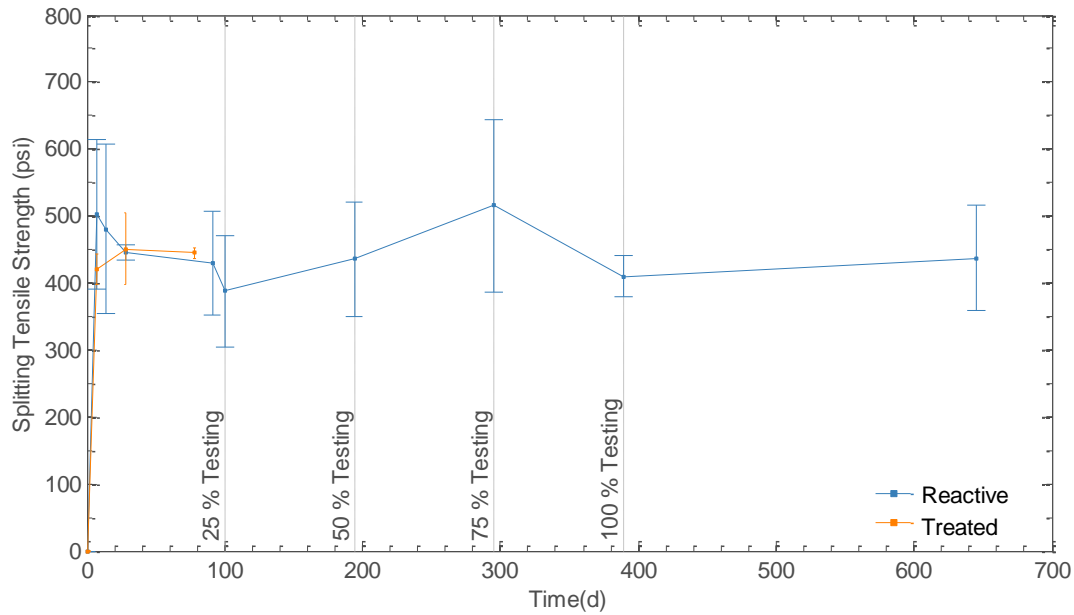
Figure 4.4. Concrete splitting tensile strength

Figure 4.5 compares the measured splitting tensile strength to that estimated using ACI 318-19, for normalweight concrete. The solid line in the figure is the relationship given in ACI 318-19, the dashed lines are +/- 20 % bounds on the coefficient, and the horizontal axis is the square root of the compressive strength.
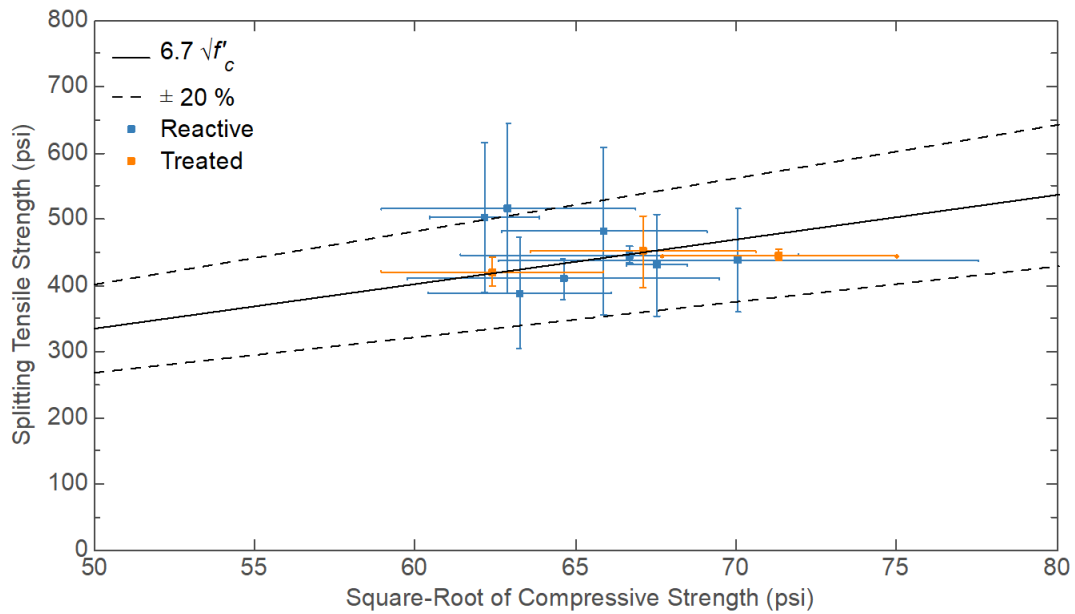
Figure 4.5. Splitting tensile strength vs. the square root of compressive strength

The measured values were in reasonable agreement with the relationship given in ACI 318-19, with all the mean values falling within the +/- 20 % bounds. This was expected, because neither the compressive strength nor the splitting tensile strength of the concrete was significantly affected by ASR. This is in contrast to the results of previous studies that have observed a significant decrease in the splitting tensile strength with increasing ASR damage, up to 40 % (e.g., Ahmed *et al.*, 1999; Fan and Hanson, 1998), however it is consistent with the measurements in the associated Task 1 study (Sadek *et al.*, 2021) for the same reactive mixture.

4.2   REINFORCEMENT MECHANICAL PROPERTIES

Figure 4.6 shows the engineering stress-strain relationships, obtained in accordance with ASTM A370-17a Standard Test Methods and Definitions for Mechanical Testing of Steel Products (ASTM A370, 2019), for the No. 4 and No. 8 reinforcing bars used as beam reinforcement. The reinforcement samples were prepared in a similar fashion to those used in the beam specimen. At the midpoint of the samples, the deformed bars were ground flat, chemically etched, and strain gages were affixed using cyanoacrylate adhesive. Engineering strains were also recorded using an extensometer meeting ASTM E83 B2 classification (ASTM E83, 2016) with a 2.0 in gage length. The extensometer was attached to the reinforcement at the location of the strain gage. The strain readings between the two methods were indistinguishable prior to reaching the strain capacity of the adhesive attaching the strain gage to the bar, which occurred at roughly 1 % strain; the engineering strains presented in Figure 4.6 were recorded by the extensometer. Nominal engineering stresses were calculated by dividing the force recorded by the load cell, integral to the testing machine, by the nominal area of the reinforcing bar. It should be noted that this procedure leads to an estimated elastic modulus different from the nominal modulus of the steel, since the area of the reinforcement sample has an effective area smaller than the nominal one. This is due to both the manufacturing process and gage installation. For example, the apparent modulus of the No. 8 (1.0 in diameter) tensile reinforcement, using the nominal bar area, was (25 100 ± 400) ksi, 13 % lower than the nominal elastic modulus of 29 000 ksi.
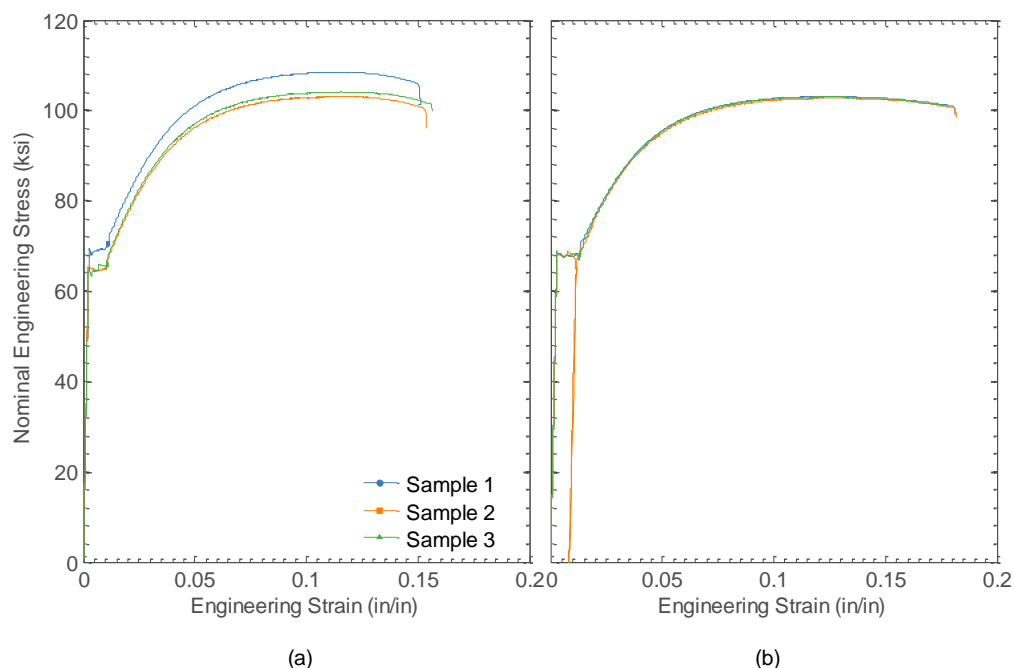
Figure 4.6. Engineering stress-strain curves for the rebars used in the beam: (a) No. 4 bars, (b) No. 8 bars

A summary of the reinforcement tests is presented in Table 4.7. The yield strength, f_y, was calculated as the upper yield point stress between a strain of 0.002 and 0.005, the tensile strength, f_u, was determined from the maximum load reading of the testing machine, and the ultimate tensile strain was determined as the strain corresponding to a 5 % decrease in the load from the peak value, prior to removal of the extensometer.

Table 4.7. Measured properties of reinforcement

	No. 4	No. 8
Yield Strength f_y (ksi)	66.6 ± 5.7	68.6 ± 0.8
Tensile Strength f_u (ksi)	105.2 ± 7.0	102.9 ± 0.4
Ultimate tensile strain (%)	15.4 ± 0.7	18.1 ± 0.5

4.3 EXPANSION PRISMS

The rate of ASR-induced expansion of the unreinforced companion specimens was estimated using the 3 in × 3 in × 11.25 in standard prisms, prepared using the same concrete as the reactive cylinders and beam specimens. While the measured length change of these prisms was not representative of the restrained ASR-induced expansion in the beams, it was indicative of the potential expansion of the concrete mixture and was useful information for scheduling the structural testing of the beam specimens.

41

Figure 4.7 shows the length change versus time for the standard prisms. One group of prisms, "Reference" in Figure 4.7, were suspended vertically over water in sealed containers and kept at a constant temperature of 100 °F throughout the duration of the study, in accordance with ASTM C1293 (ASTM C1293, 2020). The remaining prisms were exposed to the same conditions as the beam specimens in the environmental chamber, which had variations in temperature and humidity, as described in Section 2.4. One set of prisms, "Sealed" in Figure 4.7, were kept in sealed plastic bags in closed plastic containers within the chamber. The remaining group of prisms, "Chamber" in Figure 4.7, rested directly on the beam specimens.
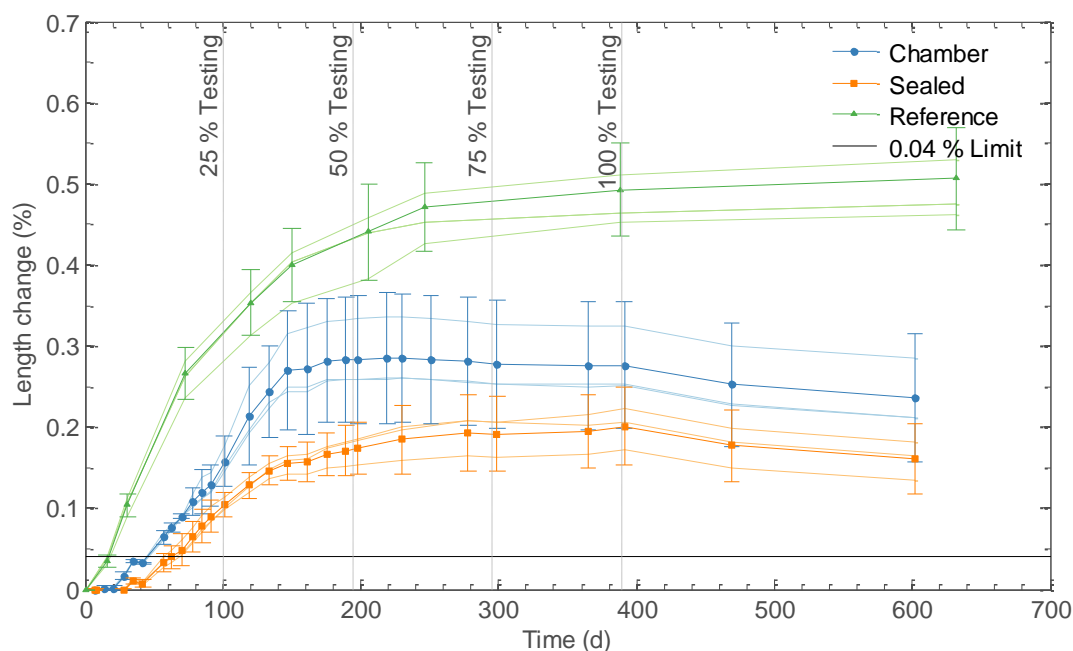
Figure 4.7. Measured length change for prisms

Prisms kept within the environmental chamber tended to expand at a slower rate, attributed to the lower initial temperature of the chamber and achieved smaller ultimate expansions than the "Reference" prisms. Until roughly 150 days, the chamber temperature was kept constant at roughly 80 °F, after which the temperature was increased to between 100 °F and 110 °F. After roughly 180 days the prisms stored with the beam specimens ("Chamber") ceased expanding, while the sealed and reference specimens did not.

Table 4.8 summarizes the expansion of the prisms kept with the beam specimens at the dates where beam testing occurred. At 365 days, the duration for the ASTM C1293 assessment, prisms that were sealed and placed in the environmental chamber ("Sealed") had the smallest length change of (0.19 ± 0.05) %, and prisms stored at 100 °F ("Reference") had the largest, with a length change of (0.49 ± 0.06) %. The prisms kept with the beam specimens ("Chamber") had a length change of (0.28 ± 0.08) %.

For both sets of prisms stored in the environmental chamber, the decrease in the length change after roughly 390 days is attributed to the change in temperature and humidity of the environmental chamber after it was returned to ambient conditions.

Table 4.8. Measured length change for expansion prisms kept in environmental chamber

Time (d)	Length change (%)		
	Chamber	Sealed	Reference
99 (25 % of $\varepsilon_{ASR-ult}$ Testing)	0.16 ± 0.03	0.10 ± 0.02	0.32 ± 0.04
195 (50 % of $\varepsilon_{ASR-ult}$ Testing)	0.28 ± 0.08	0.17 ± 0.03	0.43 ± 0.06
293 (75 % of $\varepsilon_{ASR-ult}$ Testing)	0.28 ± 0.08	0.19 ± 0.05	0.48 ± 0.06
365	0.28 ± 0.08	0.19 ± 0.05	0.49 ± 0.06
388 (100 % of $\varepsilon_{ASR-ult}$ Testing)	0.28 ± 0.08	0.20 ± 0.05	0.49 ± 0.06
648 (Beam 12 testing)	0.24 ± 0.08	0.16 ± 0.04	0.50 ± 0.06

4.4   STRAINS IN THE REINFORCEMENT DURING ASR-INDUCED EXPANSION

As indicated in Chapter 2, strains were monitored in five of the 19 beam specimens during ASR-induced expansion. Monitored beams were selected with different stirrup arrangements to investigate any potential difference in expansion. During ASR-induced expansion, strains in the stirrups and longitudinal reinforcement were measured and recorded every 12 to 14 minutes, on average. Strain data processing followed the procedure used in the Task 1 study (Sadek *et al.*, 2021) to average and stitch the data. After data collection, visual inspection of the time-history of each strain gage measurement was conducted to ensure that the gages produced meaningful data. If a gage showed erratic behavior (e.g., sudden upward or downward jumps, discontinuity, or behavior significantly inconsistent with surrounding gages), the strain data were removed, starting from the onset of erroneous behavior.

Figure 4.8 shows the strains in the reinforcement for the five monitored beams during ASR-induced expansion. In the figure, individual gages are shown as lighter lines and the averages are represented by the darker lines. The error bars in the figure display the expanded uncertainty of the mean based on the gage measurements. The gages are differentiated into two groups: longitudinal (in blue), which includes gages at both the ends and center of the reinforcement splice, and stirrup (in orange), which includes gages on both the bottom and vertical leg. It is assumed in this grouping that the lap splice length is sufficient to permit the full development of the longitudinal strain at mid splice. If the bond stress is constant and develops the yield stress of the reinforcement in one development length, then this assumption is valid until the reinforcement reaches half of the yield strain for a normalized splice length, ℓ_s/ℓ_d, of 1.0. Since the normalized lap splice length was greater than or equal to 1.0 for each of the monitored beam specimens and the measured strains in the longitudinal reinforcement were generally less than 1000 με, this assumption was deemed reasonable.
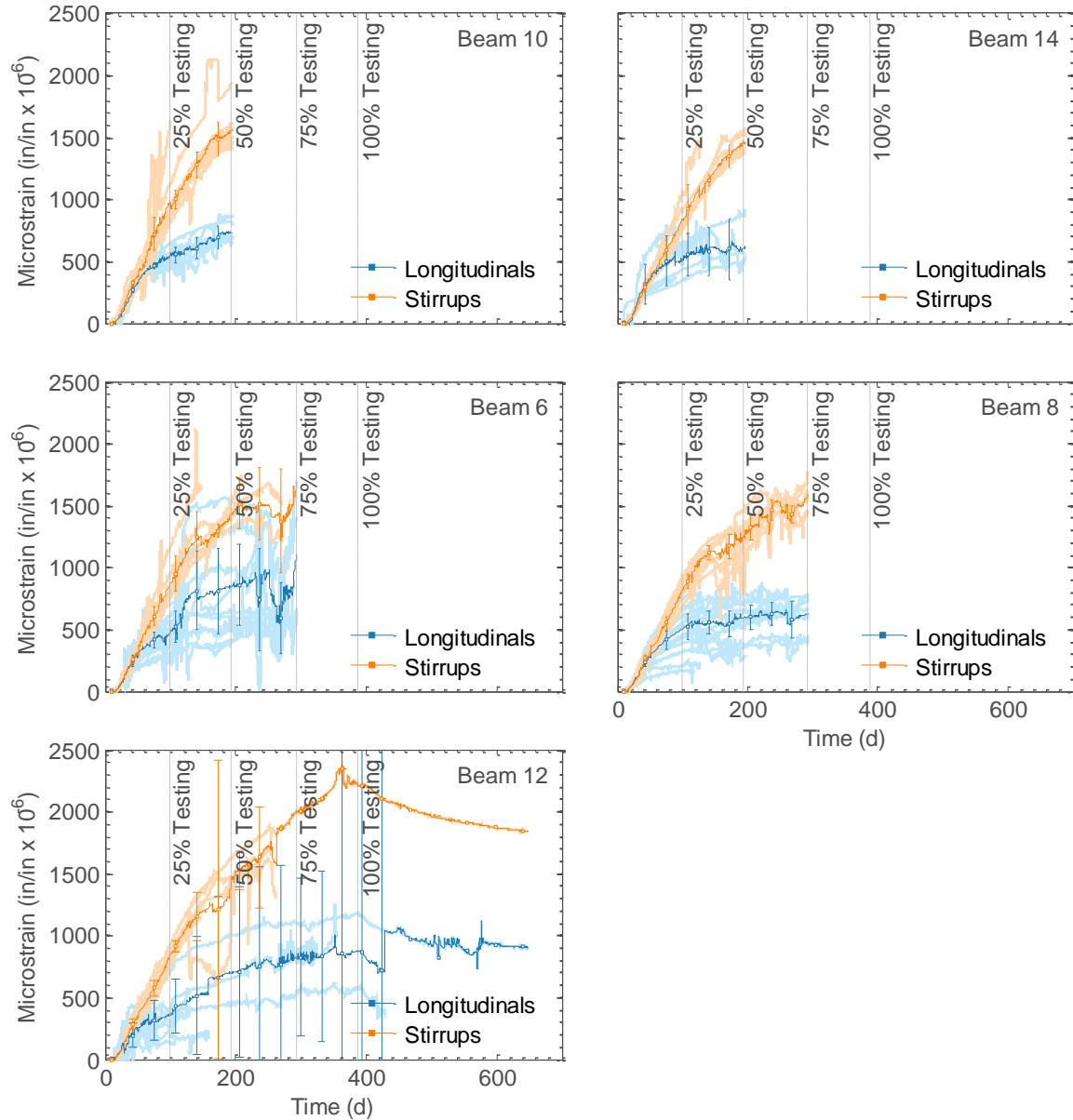
Figure 4.8. Strains in the reinforcement due to ASR-induced expansion

Figure 4.9 shows the average strains in the reinforcement for all five of the monitored beam specimens. Beams were monitored until being tested under quasi-static loads. As a result, the amount of data for later test dates (i.e., 25 % target expansion versus 75 % target expansion) was less than at earlier test dates. The error bars in the figure represent the expanded uncertainty in the mean. Because the number of monitored beam specimens decreased throughout the test program, the expanded uncertainties in the mean increased. After the 75 % target expansion testing, only one monitored specimen remained, and the uncertainty would have been theoretically infinite. This is indicated using a dashed line in the figure. This value should therefore be treated as a best estimate only.
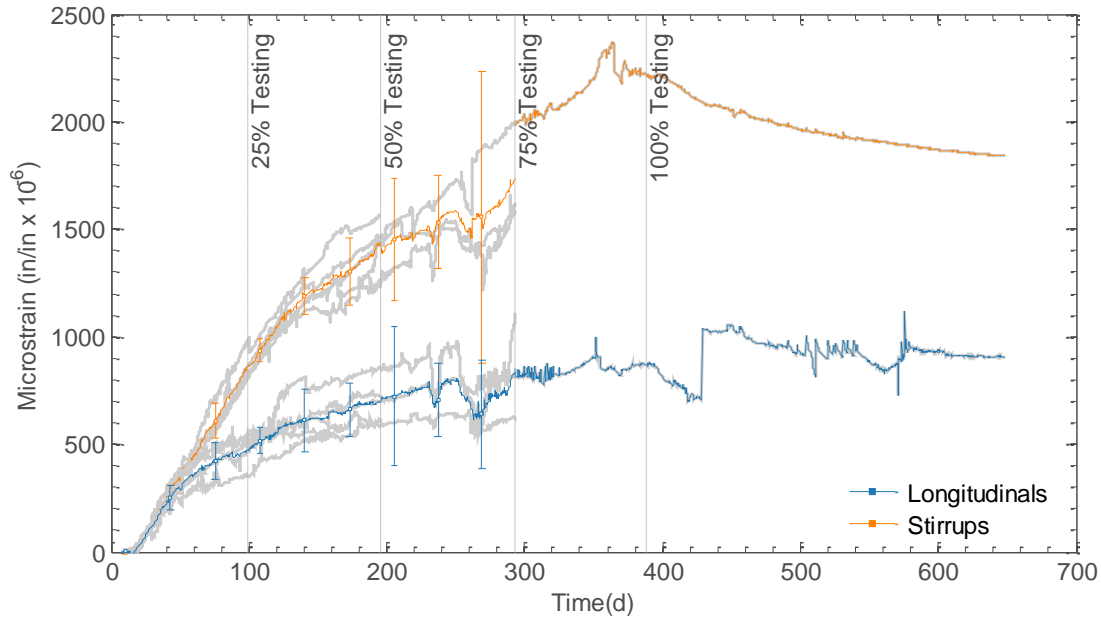
Figure 4.9. Average strains in the reinforcement due to ASR-induced expansion

After roughly 50 days, the strains in the stirrups and longitudinal tensile (bottom) reinforcement diverged. Despite the difference in stirrup arrangement, represented by the variation of the confinement parameter K_{tr}/d_b in the range of $0.5 \leq K_{tr}/d_b \leq 1.8$, no significant difference in stirrup strains was observed between the five specimens. This is consistent with previous studies (e.g., Mohammed *et al.*, 2003 and Multon *et al.*, 2005) which observed little reduction in transverse strains in the concrete due to the presence of stirrups.

From roughly 100 days onward, longitudinal strains in the tensile (bottom) reinforcement were about half of the strains recorded in the stirrups. This is attributed to the restraint provided by the longitudinal reinforcement on the concrete expansion and the cambering induced in the beam by the asymmetric reinforcement layout; the beam was reinforced with No. 4 [0.5 in diameter] compression steel versus No. 8 [1.0 in diameter] tensile reinforcement. Based on an elastic analysis of the beam section for the nominal modular ratio of the materials (the ratio of the steel and concrete moduli of elasticity), and assuming a free expansion strain of 0.15 %, the resulting mechanical strain in the tensile reinforcement was estimated to be 0.12 % (a 20 % reduction). If one includes the effects of creep, which could be significant, the strains in the tensile (bottom) reinforcement would be less (due to the compressive stresses induced by restraint of the expansion). Based on the camber measurements at the time of testing at 100 % of $\varepsilon_{ASR\text{-}ult}$, the difference between the strain at the centroid of the beam and the location of the tensile reinforcement was estimated to be roughly 0.07 %. This value is about half of the difference in strains measured between the stirrups and longitudinal reinforcement at that same time, estimated to be 0.13 % based on Table 4.9.

Table 4.9 presents the average strains in the stirrup (vertical and horizontal bottom legs) and longitudinal bars at the target levels of ASR expansion. The ultimate ASR-induced expansion for the concrete mixture was 0.5 % at 100 °F, based on the length change of unreinforced prisms from previous trial mixes (Feldman

45

et al., 2020 and Sadek *et al*., 2021). In the beam specimens, it was assumed that the passive confinement from the stirrups and longitudinal reinforcement would reduce this expansion, and based on the results of the Task 1 study (Sadek *et al*., 2021), it was estimated that this restrained expansion would produce strains in the stirrups of roughly 0.3 % for the concrete mixture used in this test series (see Section 2.1). Stirrup strains for beam testing of ε_{ASR} = 0 %, 0.08 %, 0.15 %, 0.23 %, and 0.30 % were determined based on percentages of the 0.3 % target value that were reported in Table 2.1 (0 %, 25 %, 50 %, 75 %, and 100 %)*.* After reaching the second target strain value of 0.15 %, expansion in the beams began to slow significantly and expansion in the companion prisms ceased entirely. Because of the reduced expansion rate, the remaining beams were tested at roughly 100-day intervals. Beam 12 was kept in the chamber until the remaining non-reactive specimens were cast and was therefore tested over 250 days after reaching 100 % testing target date.

Table 4.9. Average strains in the reinforcement due to ASR-induced expansion at the time of testing

Time (d)	Stirrup strain (%)	Tensile reinforcement (longitudinal) strain (%)
99 (25 % of $\varepsilon_{ASR\text{-}ult}$ Testing)	0.09 ± 0.01	0.05 ± 0.01
195 (50 % of $\varepsilon_{ASR\text{-}ult}$ Testing)	0.14 ± 0.02	0.07 ± 0.02
293 (75 % of $\varepsilon_{ASR\text{-}ult}$ Testing)	0.17 ± 0.06	0.09 ± 0.06
388 (100 % of $\varepsilon_{ASR\text{-}ult}$ Testing)	**0.22****	**0.09****
648 (Beam 12 Testing)	**0.18****	**0.09****

** Only one gage remained functional at this date (these values should be treated only as best estimates of the strain)

4.5 FLEXURAL BEHAVIOR

The measured response of the beam specimens during the four-point loading is presented in the following subsections. Where appropriate, only measurements for a characteristic beam are shown. Plots for the complete set of specimens can be found in Appendix C. Measured values presented in this section have expanded measurement uncertainties as specified in Appendix A, for each instrument and measurement type.

Table 4.10 summarizes the flexural behavior of the beam specimens in terms of the peak load strength and the corresponding midspan deflections at the peak load during testing.

Table 4.10. Measured peak load strength and corresponding midspan deflections

Beam	Testing Target (% of $\varepsilon_{ASR\text{-}ult}$)	ε_{ASR} (%)	K_{tr}/d_b	ℓ_s/ℓ_d	Peak load strength (kip)	Midspan deflection (in)
1	25	0.09 ± 0.01	0.5	0.7	52.0 ± 0.6	0.334 ± 0.006
2	25	0.09 ± 0.01	0.5	1.3	71.1 ± 0.6	0.424 ± 0.006
3	25	0.09 ± 0.01	1.5	0.7	42.8 ± 0.6	0.251 ± 0.006
4	25	0.09 ± 0.01	1.5	1.3	76.8 ± 0.6	0.783 ± 0.006
5	75	0.17 ± 0.06	0.5	0.7	52.5 ± 0.6	0.288 ± 0.006
6	75	0.17 ± 0.06	0.5	1.3	78.9 ± 0.6	0.791 ± 0.006
7	75	0.17 ± 0.06	1.5	0.7	49.5 ± 0.6	0.281 ± 0.006
8	75	0.17 ± 0.06	1.5	1.3	76.3 ± 0.6	0.908 ± 0.006
9	50	0.14 ± 0.02	1.0	1.0	58.6 ± 0.6	0.357 ± 0.006
10	50	0.14 ± 0.02	1.0	N/A‡	77.5 ± 0.6	0.999 ± 0.006
11	0*	*	1.0	1.0	59.2 ± 0.6	0.353 ± 0.006
12	100	0.22**	1.0	1.0	69.3 ± 0.6	0.489 ± 0.006
13	50	0.14 ± 0.02	0.0†	1.0	50.3 ± 0.6	0.275 ± 0.006
14	50	0.14 ± 0.02	1.8	1.0	71.0 ± 0.6	0.492 ± 0.006
15	50	0.14 ± 0.02	1.0	0.5	35.3 ± 0.6	0.197 ± 0.006
16	50	0.14 ± 0.02	1.0	1.5	77.2 ± 0.6	0.744 ± 0.006
17	0*	*	1.0	1.0	59.6 ± 0.6	0.42 ± 0.006
18	0*	*	1.0	N/A‡	76.0 ± 0.6	1.018 ± 0.006
19	100	0.18**	1.0	1.0	67.1 ± 0.6	0.385 ± 0.006

** Only one gage remained functional at this date (these values should be treated only as estimates of the strain)

* Beam constructed with concrete treated with lithium nitrate solution to prevent expansion

† Beam had no stirrups in the constant moment region

‡ Beam had continuous tensile reinforcement

4.5.1 Calculated Moment

Figure 4.10 shows the nominal shear and moment diagrams for the four-point bending arrangement used in the tests. A spreader beam was used to divide the actuator force equally to the central loading points. Moments were calculated as half of the recorded actuator force multiplied by the nominal shear span length of 30 in. The peak load strengths, P_{max}, for all 19 beam specimens, are given in Table 4.10. Measured values of the shear span length varied between tests but were within 1 % to 2 % of the nominal value used in the calculation of moments.
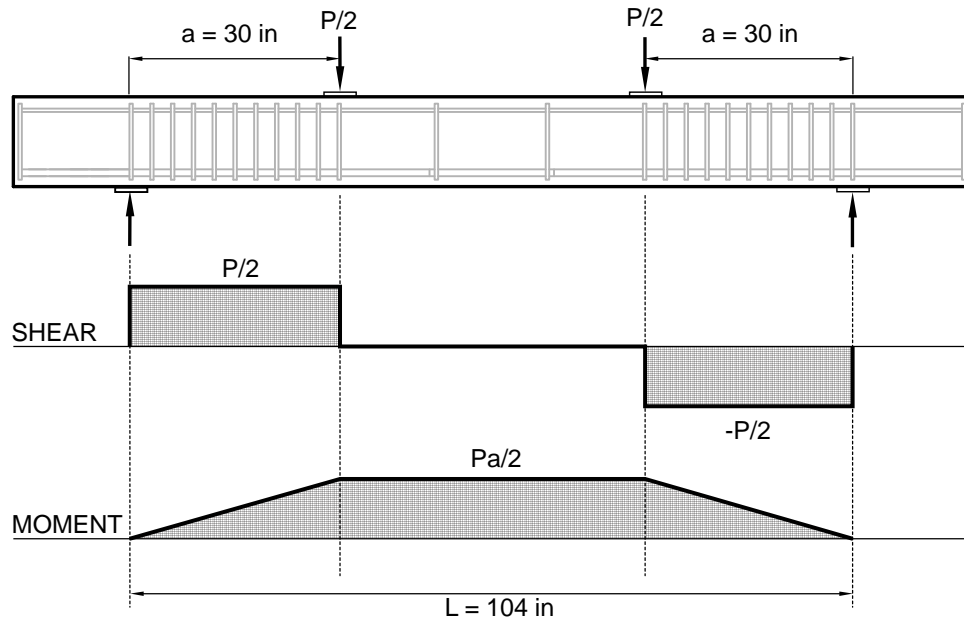
Figure 4.10. Shear and moment diagrams for testing configuration

Table 4.11 summarizes the maximum moment strengths, M_{max}, computed based on the measured peak loads for all 19 of the beam specimens. Table 4.11 also lists the ratio of the peak moment strength M_{max} to the nominal flexural strength of the beam section, M_n, calculated in accordance with ACI 318-19. The nominal flexural strength was calculated to be 940 kip-in assuming a concrete compressive strength of 4500 psi and a reinforcement yield strength of 60 ksi. A ratio $M_{max}/M_n \geq 1.0$ indicates the specimen achieved or exceeded the nominal flexural capacity of beam section during testing.

Table 4.11. Calculated maximum moment strengths

Beam	Testing Target (% of $\varepsilon_{ASR\text{-}ult}$)	ε_{ASR} (%)	K_{tr}/d_b	ℓ_s/ℓ_d	M_{max} (kip-in)	M_{max}/M_n
1	25	0.09 ± 0.01	0.5	0.7	775 ± 9	0.82
2	25	0.09 ± 0.01	0.5	1.3	1069 ± 9	1.13
3	25	0.09 ± 0.01	1.5	0.7	647 ± 9	0.68
4	25	0.09 ± 0.01	1.5	1.3	1158 ± 9	1.22
5	75	0.17 ± 0.06	0.5	0.7	785 ± 9	0.83
6	75	0.17 ± 0.06	0.5	1.3	1186 ± 9	1.25
7	75	0.17 ± 0.06	1.5	0.7	746 ± 9	0.79
8	75	0.17 ± 0.06	1.5	1.3	1143 ± 9	1.21
9	50	0.14 ± 0.02	1.0	1.0	879 ± 9	0.93
10	50	0.14 ± 0.02	1.0	N/A‡	1125 ± 9	1.19
11	0*	*	1.0	1.0	890 ± 9	0.94
12	100	0.22**	1.0	1.0	1040 ± 9	1.10
13	50	0.14 ± 0.02	0.0†	1.0	759 ± 9	0.80
14	50	0.14 ± 0.02	1.8	1.0	1030 ± 9	1.09
15	50	0.14 ± 0.02	1.0	0.5	516 ± 9	0.55
16	50	0.14 ± 0.02	1.0	1.5	1125 ± 9	1.19
17	0*	*	1.0	1.0	860 ± 9	0.91
18	0*	*	1.0	N/A‡	1106 ± 9	1.17
19	100	0.18**	1.0	1.0	1003 ± 9	1.06

** Only one gage remained functional at this date (these values should be treated only as estimates of the strain)

* Beam constructed with concrete treated with lithium nitrate solution to prevent expansion

† Beam had no stirrups in the constant moment region

‡ Beam had continuous tensile reinforcement

4.5.2 Failure Type

Table 4.12 summarizes the failure type for each beam specimen. The beams were divided into two failure types based on the calculated maximum moment strength for the beam, M_{max}, divided by the nominal flexural strength of the beam section, M_n:

> Type A: Beams that failed through bond splitting failure in the splice region prior to achieving the nominal flexural strength of the section ($M_{max}/M_n < 1.0$), and
>
> Type B: Beams that failed through compressive failure of the concrete compression zone of the section after yielding of tensile reinforcement or beams that failed through bond splitting failure in the splice region after reaching the nominal flexural strength of the beam ($M_{max}/M_n \geq 1.0$).

Satisfactory flexural performance could then be classified as beams with Type B failures.

Table 4.12. Failure types for the 19 beams

Beam	Testing Target (% of $\varepsilon_{ASR-ult}$)	ε_{ASR} (%)	K_{tr}/d_b	ℓ_s/ℓ_d	M_{max}/M_n	Failure Type
1	25	0.09 ± 0.01	0.5	0.7	0.82	A
2	25	0.09 ± 0.01	0.5	1.3	1.13	B
3	25	0.09 ± 0.01	1.5	0.7	0.68	A
4	25	0.09 ± 0.01	1.5	1.3	1.22	B
5	75	0.17 ± 0.06	0.5	0.7	0.83	A
6	75	0.17 ± 0.06	0.5	1.3	1.25	B
7	75	0.17 ± 0.06	1.5	0.7	0.79	A
8	75	0.17 ± 0.06	1.5	1.3	1.21	B
9	50	0.14 ± 0.02	1.0	1.0	0.93	A
10	50	0.14 ± 0.02	1.0	N/A‡	1.19	B
11	0*	*	1.0	1.0	0.94	A
12	100	0.22**	1.0	1.0	1.10	B
13	50	0.14 ± 0.02	0.0†	1.0	0.80	A
14	50	0.14 ± 0.02	1.8	1.0	1.09	B
15	50	0.14 ± 0.02	1.0	0.5	0.55	A
16	50	0.14 ± 0.02	1.0	1.5	1.19	B
17	0*	*	1.0	1.0	0.91	A
18	0*	*	1.0	N/A‡	1.17	B
19	100	0.18**	1.0	1.0	1.06	B

** Only one gage remained functional at this date (these values should be treated only as estimates of the strain)

* Beam constructed with concrete treated with lithium nitrate solution to prevent expansion

† Beam had no stirrups in the constant moment region

‡ Beam had continuous tensile reinforcement

In general, beams with normalized splice lengths, $\ell_s/\ell_d \geq 1.3$, (complying with ACI requirements) achieved the nominal flexural capacity of the beam section prior to bond splitting failures and thus were classified as having Type B failures. Beams with splices less than one development length, $\ell_s/\ell_d < 1.0$, failed through bond splitting failure prior to achieving the nominal flexural strength of the beam section and were classified as having Type A failures. Beams with splice lengths equal to one development length, $\ell_s/\ell_d = 1.0$, failed through bond splitting failures and did not achieve the nominal flexural capacity of the beam section except in the case of Beam 14, with tightly spaced stirrups in the splice region, and Beams 12 and 19, which were tested at an ASR-induced expansion of roughly, $\varepsilon_{ASR} = 0.2 \%$.

4.5.3   Deflections

Figure 4.11 shows the measured deflections during testing for a characteristic beam specimen on the north and south sides of the beam (the beam specimens were placed on supports spanning east to west). Deflections were measured at midspan, the two loading points, and halfway between each of the loading

points and the adjacent support. The measurements in the figure are labeled based on their locations along the beam span, with midspan serving as the origin (x=0). The actuator displacement is shown in grey for reference.
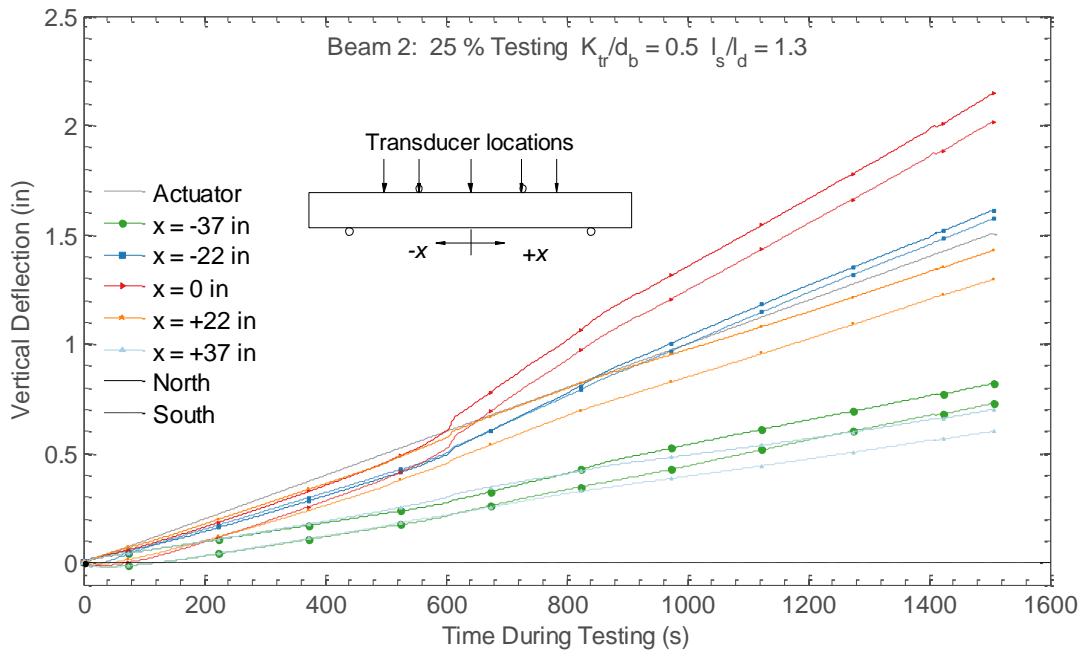

Figure 4.11. Measured deflections for Beam 2

In general, displacements measured on the north and south sides of the beam were within 20 % of one another. Offsets in the measured signals, as seen between the solid and dashed lines in Figure 4.11, were observed. These offsets were attributed to rotation of the beams about their longitudinal axes at small applied loads and displacements, which were necessary to produce even bearing on the bottom surface of the beams. This rotation was also observed in video recordings of the tests. Because the initial rotation produced nearly equal and opposite displacements on the two sides of the beams, the average of the North and South measurements was used to obtain the beam displacement in subsequent figures.

Figure 4.12 shows the displacement profile for a typical beam specimen that exhibited Type B failure at the maximum moment strength, M_{max}, and at several intermediate levels of applied moment corresponding to fractions of the ACI 318 nominal flexural strength of the beam section, M_n.
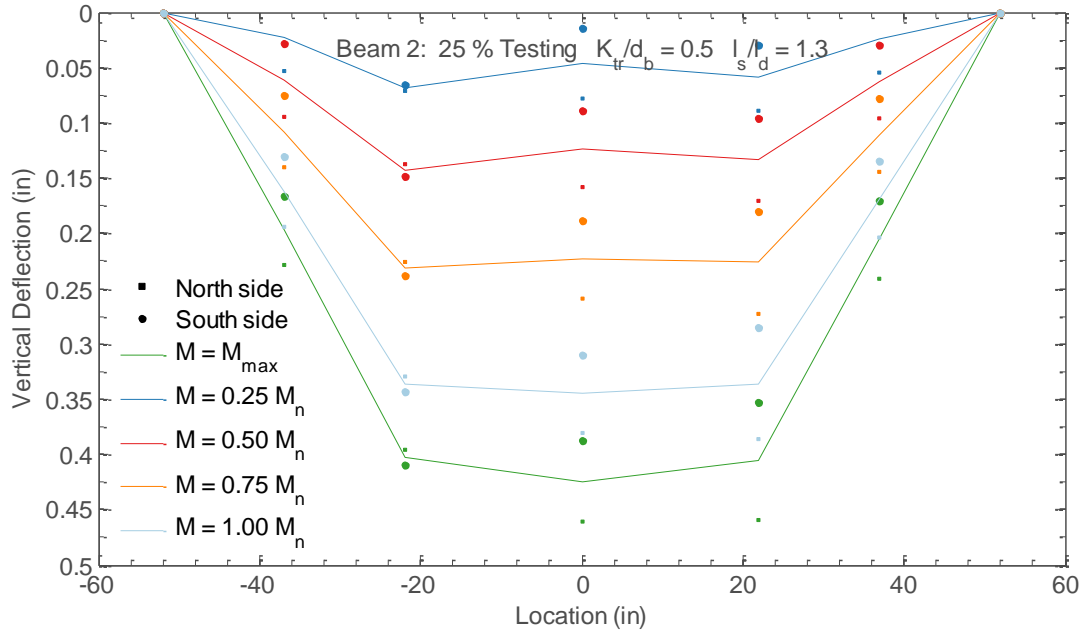
Figure 4.12. Measured deflection profiles for Type B failure mode

Vertical deflection of the beams was generally symmetric about midspan, however in some specimens, asymmetry in the deflections was observed, with larger deflections occurring on one side of midspan than the other (up to a roughly 15 % difference between the deflections at the loading points). This asymmetry was more pronounced at larger deflections and was consistent with observations of the flexural cracking of the beam specimens, which normally began at the ends of the reinforcement splices. After flexural cracks formed at the ends of the splice region, the crack widths typically increased asymmetrically, favoring one side of the splice region over the other. This produced concentrated rotations of the beam at the flexural crack, offset from the beam midspan, leading to asymmetric deflections of the beam specimens.

4.5.4 Force-Displacement Behavior

Figure 4.13 and Figure 4.14 show the load-midspan deflection curves for all 19 beam specimens. In both figures, the data is truncated after the measured load dropped below 80 % of the peak value.

In Figure 4.13, each pane separates the beam specimens by the six normalized splice lengths. Testing target expansion percentage and the confinement parameter, K_{tr}/d_b, are designated in the figure by line color and marker, respectively. For all of the beam specimens, the measured load increased roughly linearly until either bond splitting failure in the splice region and a corresponding drop in the measured load (e.g., $\ell_s/\ell_d = 0.7$), or yielding of the longitudinal reinforcement and a corresponding plateau in the measured load (e.g., $\ell_s/\ell_d = 1.5$). For beams with spliced reinforcement, after reaching this plateau in the load, the load remained near its peak value until bond splitting failure in the splice region occurred, which led to a precipitous drop in load (e.g., $\ell_s/\ell_d = 1.3$). In specimens with continuous reinforcement, the load remained near its peak value until compressive failure of the concrete compression zone of the section ("No splice" in the figure).

52

The panes show the influence of the normalized splice length, ℓ_s/ℓ_d , on the beam behavior. Small variations caused by ASR expansion and splice confinement can also be observed. For example, the vertical load capacity was found to increase by roughly 15 % when comparing the beams tested at 0 % and 100 % target expansions that were nominally identical except for the expansion due to ASR at the time of testing ($\ell_s/\ell_d = 1.0$).
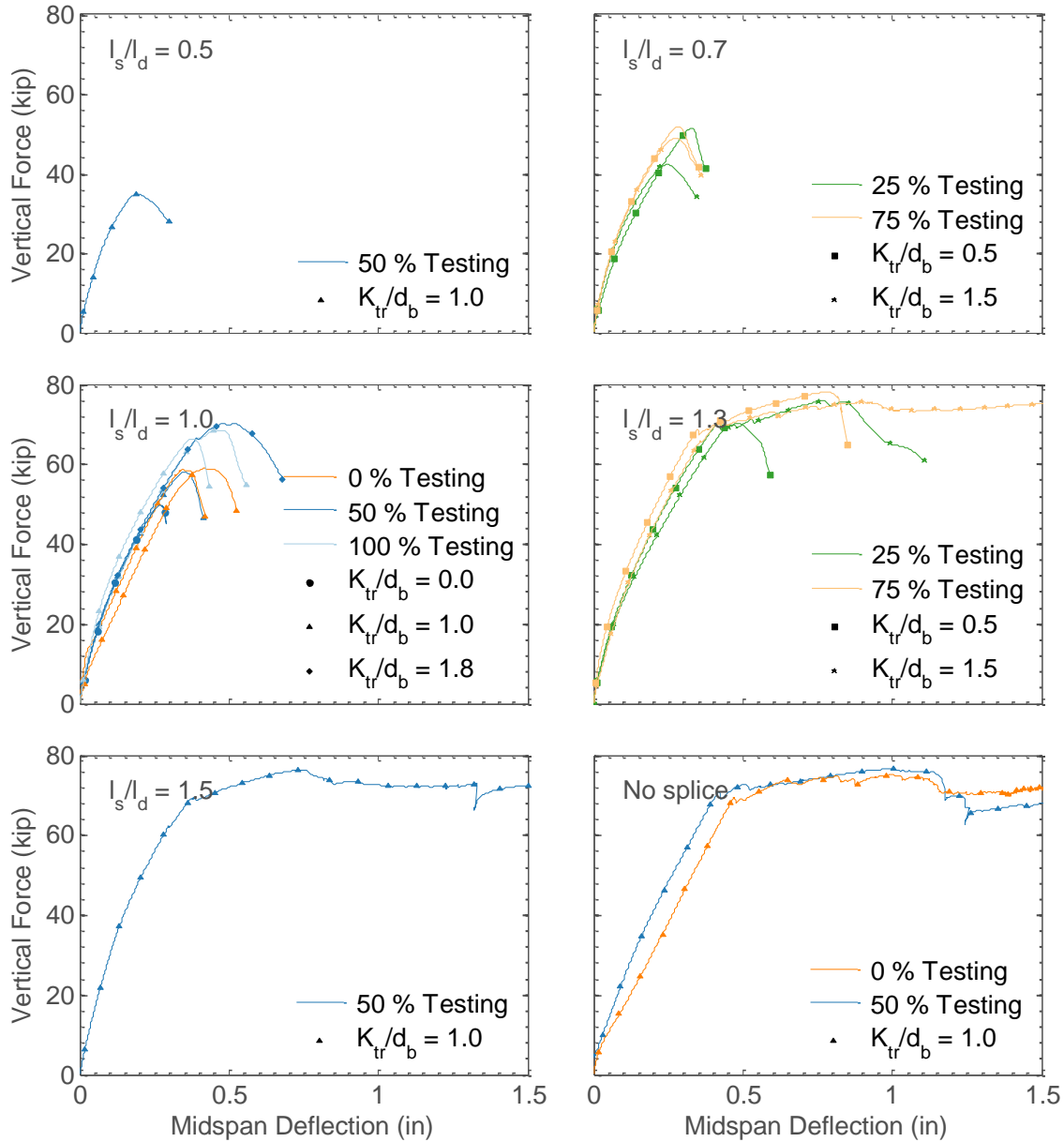

Figure 4.13. Load-midspan deflection behavior for 6 levels of normalized splice length

In Figure 4.14, each pane separates the beams by the five target expansion levels. The splice length ratio, ℓ_s/ℓ_d, and the confinement parameter, K_{tr}/d_b, are designated in the figure by line color and marker

53

type, respectively. Beams with code compliant splice lengths, $\ell_s/\ell_d \geq 1.3$, reached a load plateau at roughly 70 kip, corresponding to reinforcement yielding with a positive post yield stiffness. Beams with insufficient lap splices, conversely, were unable to achieve the nominal flexural strength of the section, corresponding to an applied load of 63.2 kip. The influence of confinement for beams with splice lengths equal to one development length (blue curves) can also be seen. Increasing the confinement level led to increases in the peak load capacity despite the shorter physical splice length provided at the higher confinement values.
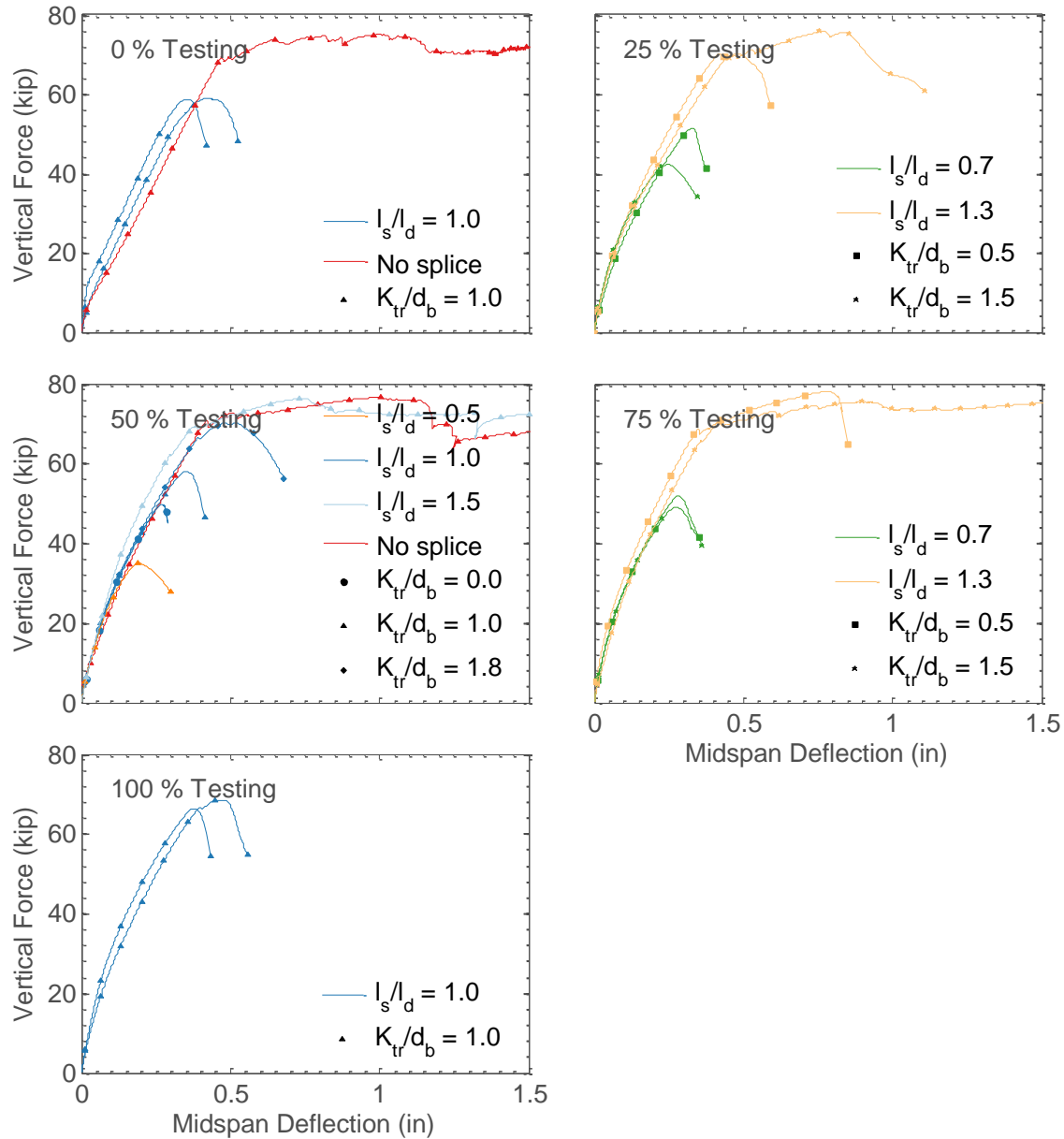
Figure 4.14. Load-midspan deflection behavior for 5 levels of target ASR expansion

4.5.5   Rotations

Figure 4.15 shows longitudinal deformations of a typical beam specimen measured by displacement transducers affixed to a series of embedded horizontal rods. As shown in Section 2.6, the transducers were placed in two rows, one near the top of the beam and one near the bottom. In the Figure, transducers located in the bottom row are shown with solid lines and those located in the top row with dashed lines. The instruments are identified based on the nominal location of the measurement along the beam's length with the beam's midspan serving as the origin. Since the transducers spanned between two successive rods, a position halfway between the rods was used to locate the measurement.
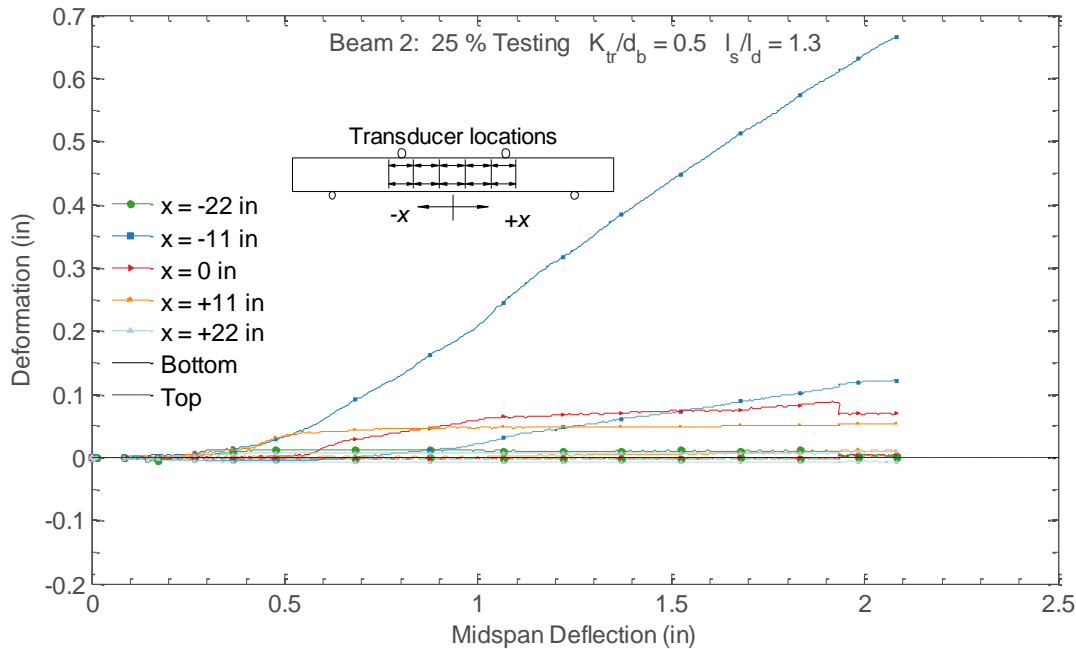
Figure 4.15. Measured longitudinal deformations for Beam 2

As anticipated, positive deformations (extension) were measured by transducers in the bottom row of instruments. Transducers in the top row of instruments initially measured negative deformations (compression), however these deformations were typically small (less than 0.01 in). This is attributed to the rod's location relative to the beam height. The rods were embedded approximately 2.0 in from the top surface of the beam, and the computed neutral axis depth at the nominal flexural strength of the beam section was about 2.6 in. After the splitting failure of concrete confinement of the splice, the longitudinal deformations measured by the top row of transducers became positive (extension) indicating the neutral axis had shifted above the location of the instruments.

Figure 4.16 shows the computed section rotation-midspan deflection relationships at the five measurement locations. Section rotations were computed by dividing the difference between the top and bottom deformation measurements by the average separation between the instruments using Equation 4.1,

55

$$\theta = \frac{2(d_{bot} - d_{top})}{h_1 + h_2},$$ (4.1)

where θ is the section rotation at the measurement location, d_{bot} is the deformation measured by the transducer in the bottom row of instruments, d_{top} is the deformation measured by the transducer in the top row of instruments, and h_1 and h_2 are the vertical spacing of the rods at either end of the transducers.
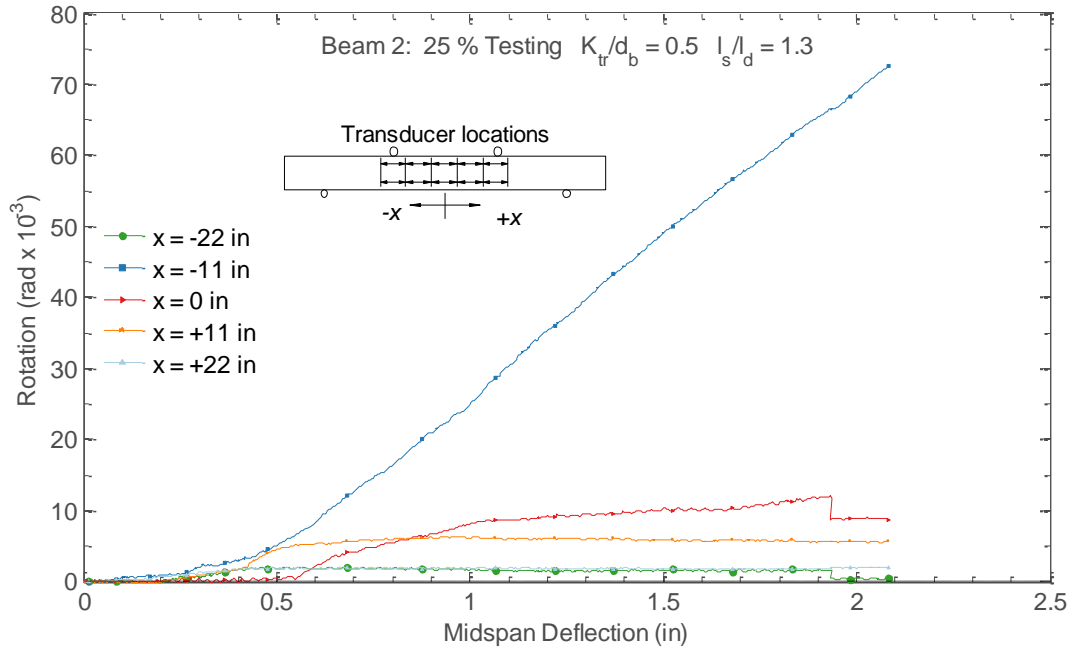

Figure 4.16. Computed section rotations for Beam 2

Figure 4.17 shows the distribution of rotations along the beam's length for a typical beam specimen. The rotation distribution is shown at the maximum moment capacity, M_{max}, and at several intermediate levels of applied moment corresponding to fractions of the nominal flexural strength of the beam section, M_n, determined in accordance with ACI 318-19.
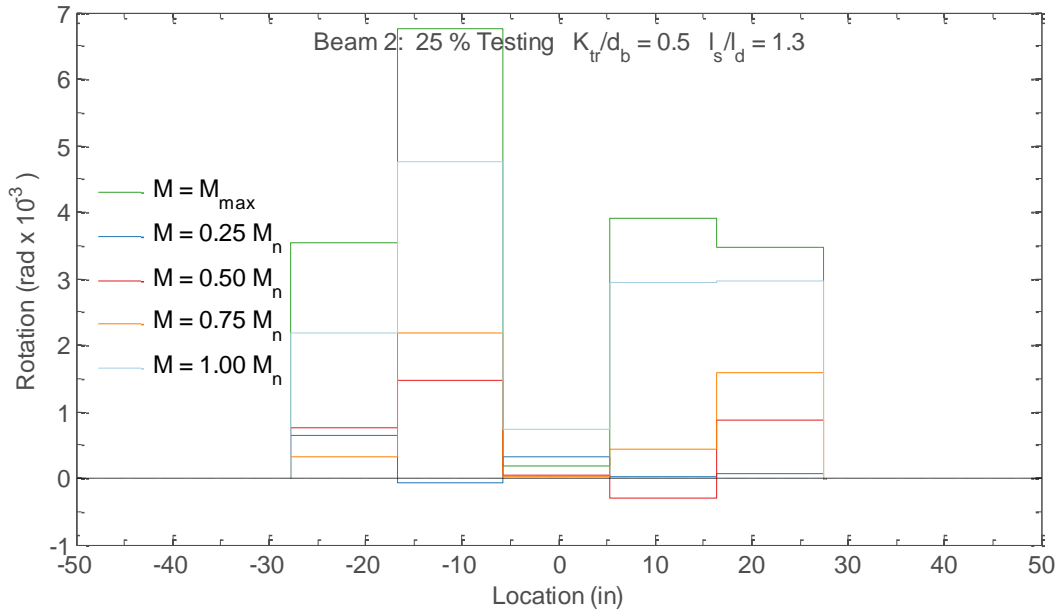
Figure 4.17. Measured section rotation profiles for Beam 2

The relative magnitude and distribution of rotations among the five measurement locations varied between tests. In general, rotations tended to be highest at either the second or fourth measurement locations (x=-11 in and x=+11 in in the figure), which spanned across the ends of the tensile reinforcement splice. For beams without spliced reinforcement, rotations tended to be concentrated at the third measurement location, at midspan (x=0 in).

Figure 4.18 shows the beam end rotation, with respect to a horizontal axis, measured over the supports at mid-height of the beam using inclinometers for a typical beam specimen. Rotations were roughly symmetric, especially at smaller vertical midspan deflections. Measured rotations were consistent with the deflections measured halfway between the supports and loading points. For example, the measured rotations at the east and west supports for Beam 2 at a load of 71±0.6 kip were 0.012±0.003 rad and 0.013±0.003 rad and the rotations calculated using the beam deflection measurements were 0.013±0.004 rad and 0.014±0.004 rad for the east and west supports, respectively.
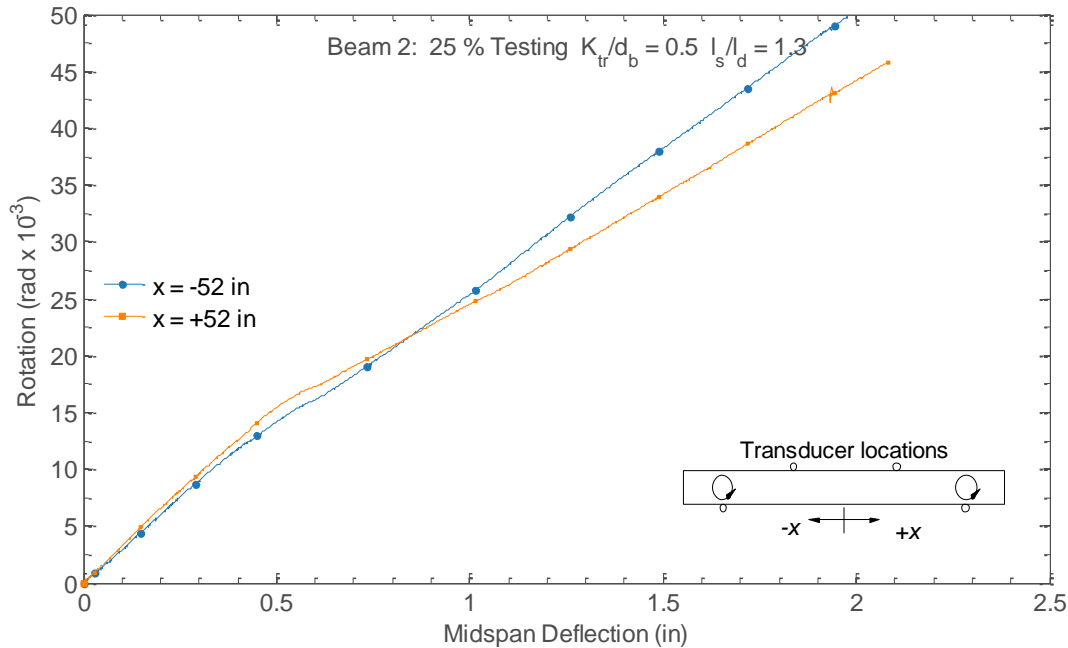
Figure 4.18. Measured end rotations for Beam 2

4.5.6   Moment-Rotation Behavior

Figure 4.19 and Figure 4.20 show the moment-rotation behavior for all 19 beam specimens. For each beam specimen, the rotation time history from the location of the maximum section rotation was used to produce the figures. As a result, the location of the plotted rotation along the beam's length varied between tests. For clarity, the data were truncated after the measured moment dropped below 80 % of the peak value or after the rotation exceeded 0.02 rad.

In Figure 4.19, each pane separates the beams specimens by the five target expansion levels. The splice length and confinement variables are designated in the figure by line color and marker type, respectively.

In Figure 4.20, each pane separates the beam specimens by the six normalized splice lengths. The target expansion level at testing and confinement are designated in the figure by line color and marker, respectively.
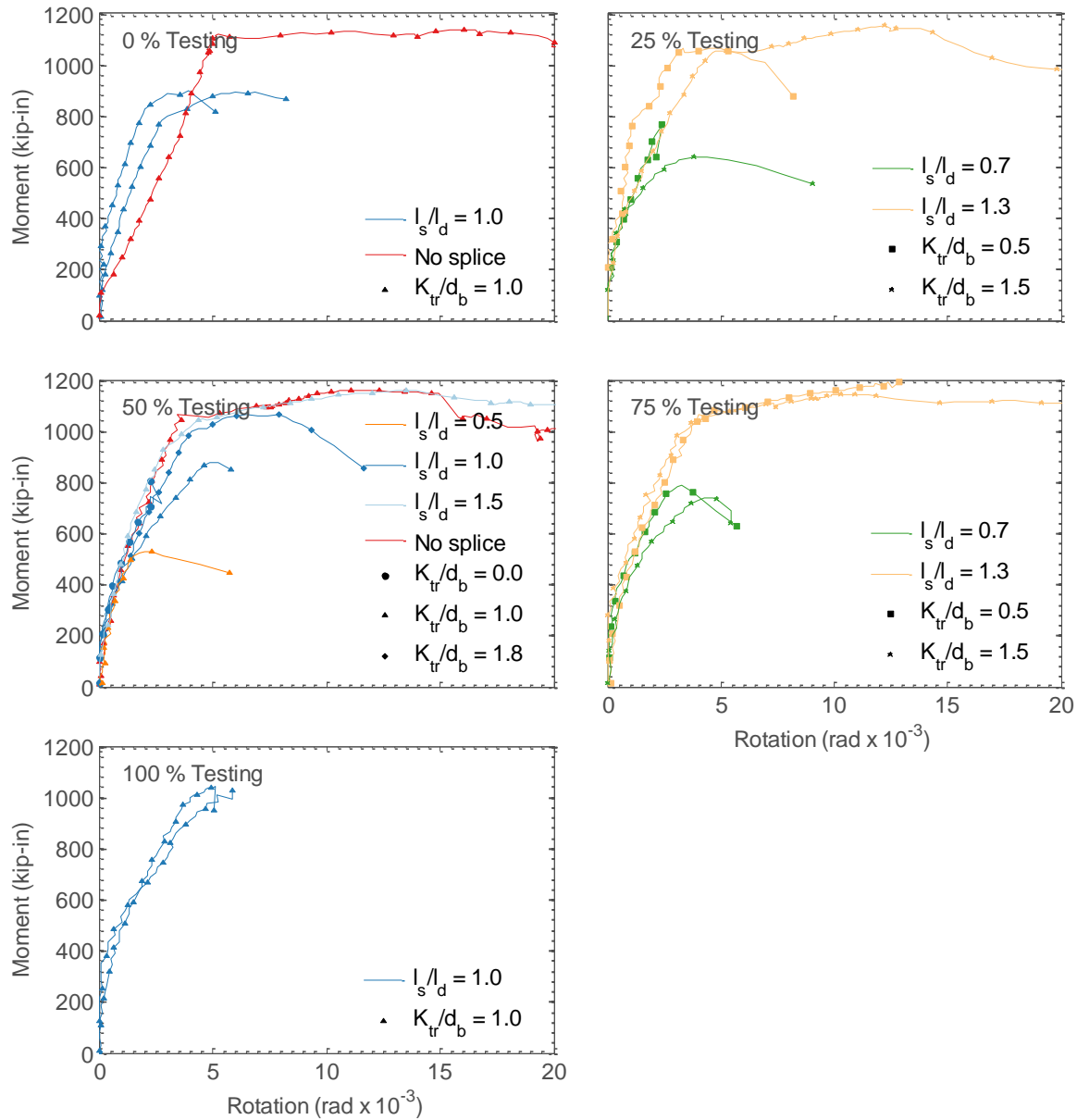
Figure 4.19. Moment-rotation behavior for 5 levels of target ASR expansion
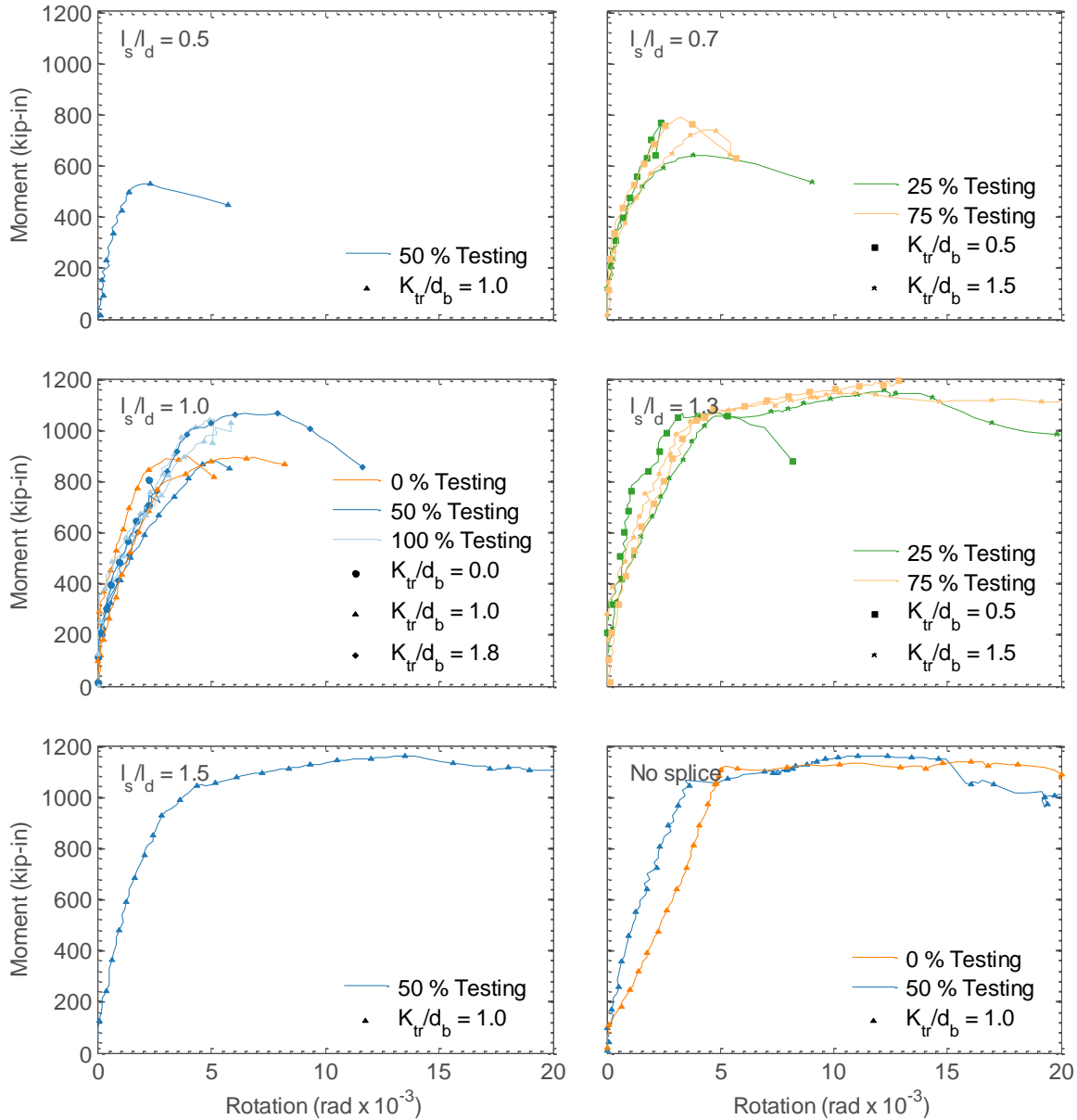
Figure 4.20. Moment-rotation behavior for all 19 beam specimens for 6 levels of normalized splice length

Overall, observations are similar to those made from the force-displacement plots in Section 4.5.4. Beams with normalized splice lengths, $\ell_s/\ell_d \geq 1.3$, (complying with ACI requirements) achieved the nominal flexural strength of the beam section and exhibited a plateau in their moment-rotation behavior at roughly 1100 kip-in, similar to the beams with continuous reinforcement. Beams with insufficient lap splices, conversely, were unable to achieve the nominal flexural strength of the beam section, M_n = 940 kip-in. The exception was for beams tested at 50 % and 100 % of the target expansion with normalized splice lengths of 1.0.

4.5.7 Strains in the Reinforcement

Figure 4.21 presents the calculated midspan moment as a function of the measured strain increment in the tensile reinforcement during testing for a typical beam specimen with spliced bottom bars. The strain increment is used here to differentiate the increase in strain during structural testing from the strains caused by ASR-induced expansion (i.e., the strain increment for all of the tested beams at the start of testing is zero). The strain increment during testing was measured at both the ends (red curves) and in the middle of splice region (blue curves), as described in Section 2.6 (see inset of Figure 4.21). For each of the gages, the strain increment was truncated at the location of the beam's maximum moment strength or when the gages failed during testing, whichever occurred first. In the figure, the marker designates the mean value of the strains for each gage location, while the error band at each marker corresponds to expanded uncertainty of the mean value.

Also plotted in the figure is the predicted increase in the midspan moment for a given strain increment based on an elastic section analysis using the nominal (28 day) material properties and both the transformed and cracked section properties. While the reduction in the elastic modulus measured during the test period (roughly 50 %) results in only a small change to the strain development assuming cracked properties (roughly 5 %), it results in a significant change to the strain development assuming transformed properties (decreases slope by 50 %) due to the change in the modular ratio (the ratio of the steel and concrete elastic moduli).
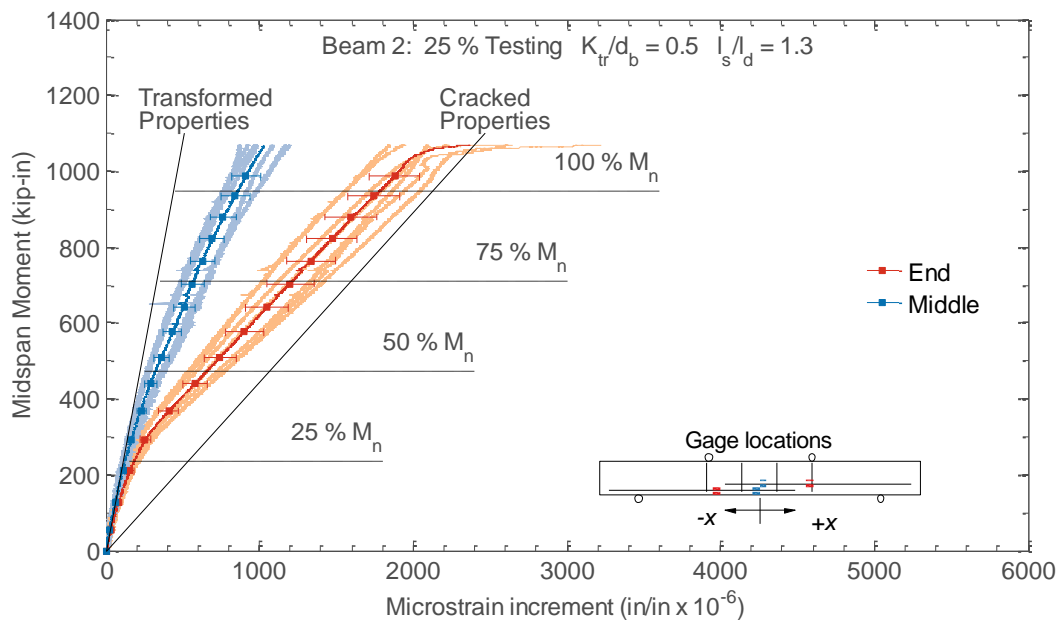

Figure 4.21. Calculated midspan moment vs. measured strain increment in the tensile reinforcement for Beam 2

The development of the strain increment with increasing midspan moment had several distinct phases. Up to a midspan moment of roughly 200 kip-in, the strain increments in the tensile reinforcement were similar at the two gage locations. This is consistent with elastic bending of the beam, prior to the formation

(or opening) of structural cracks. The development of the strain increment with increasing midspan moment was consistent with the assumption of the transformed beam properties, without a reduction of the concrete elastic modulus.

At a midspan moment of roughly 200 kip-in, the relationship between the strain increment and midspan moment deviated from the transformed section estimation, presumably due to flexural cracks forming (or opening) in the beam at the ends of the splice region. The estimated cracking moment, M_{cr}, assuming a nominal value for the concrete modulus of rupture, f_r=500 psi, was estimated to be 168 kip-in. This transition was sharper in beams tested at 0 % target ASR expansion as compared to beams tested at 25 % target ASR expansion, presumably due to opening of existing cracks present in the beams damaged by ASR. As expected, the strain increments in the reinforcement were highest at the ends of the splice, and strain increments at the middle of the splice were roughly half of the values at the end.

At a midspan moment of roughly 1100 kip-in, a sharp increase in the strain increment was observed at the end of the splice. This sharp increase is attributed to yielding of the reinforcement at the gage location. Based on the measured concrete mechanical properties at 28 days and the measured yield strength of the tensile reinforcement, the flexural strength of the section, M_{pr}, was estimated to be 1060 kip-in.

Figure 4.22 and Figure 4.23 show the calculated midspan moment as a function of the measured strain increment in the tensile reinforcement at the end of the splice for all 19 beam specimens. In the figures, the markers designate the mean value of the strains for each gage location, while the error band at each marker corresponds to expanded uncertainty of the mean value.

In Figure 4.22, each pane separates the beams specimens by the five target expansion levels. The splice length and confinement variables are designated in the figure by line color and marker type, respectively.

In Figure 4.23, each pane separates the beam specimens by the six normalized splice lengths, ℓ_s/ℓ_d. The target expansion levels and confinement parameter, K_{tr}/d_b, are designated in the figure by line color and marker, respectively.
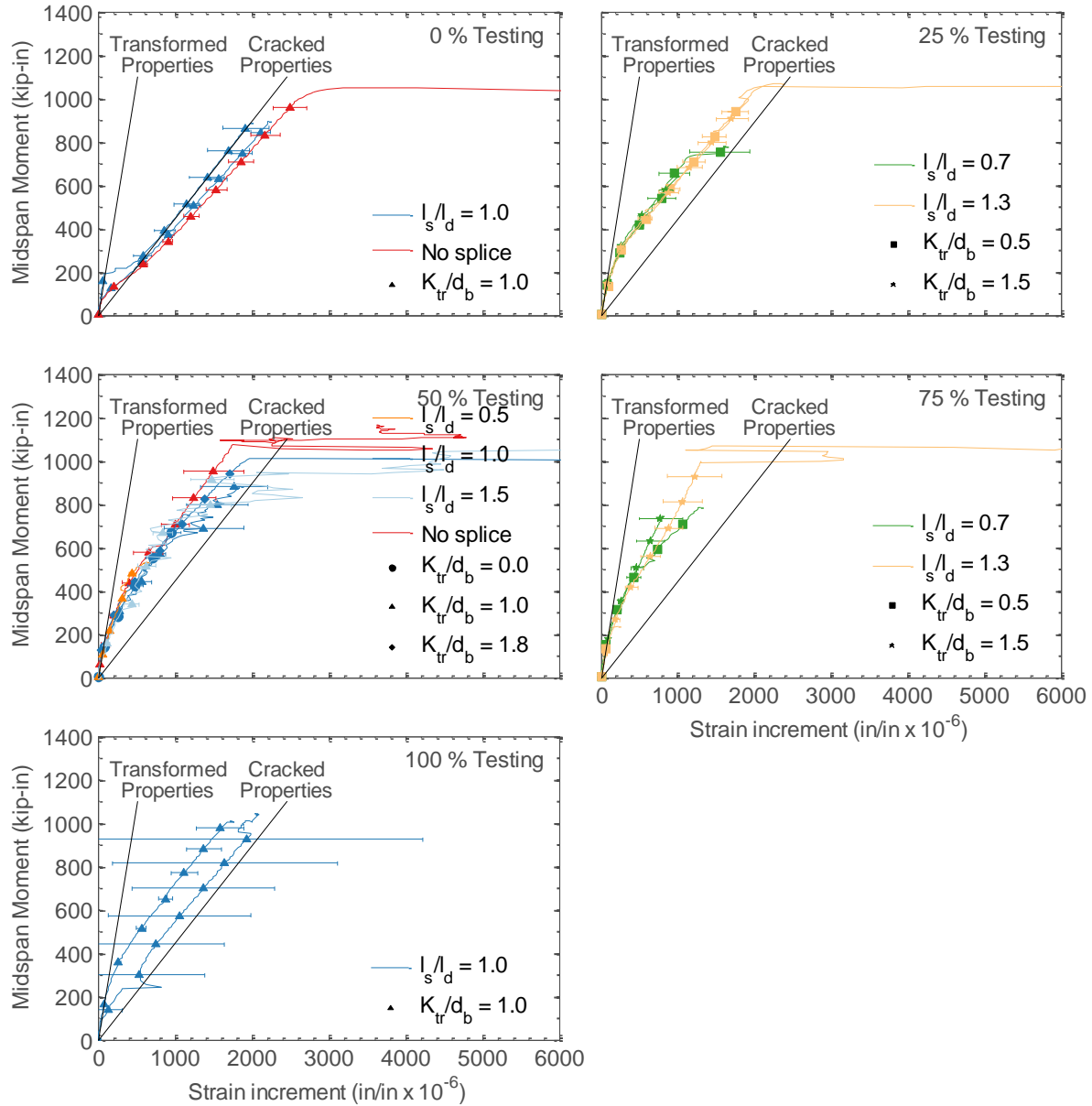
Figure 4.22. Calculated midspan moment vs. measured strain increment in the tensile reinforcement at the end of the splice for 5 levels of target ASR expansion
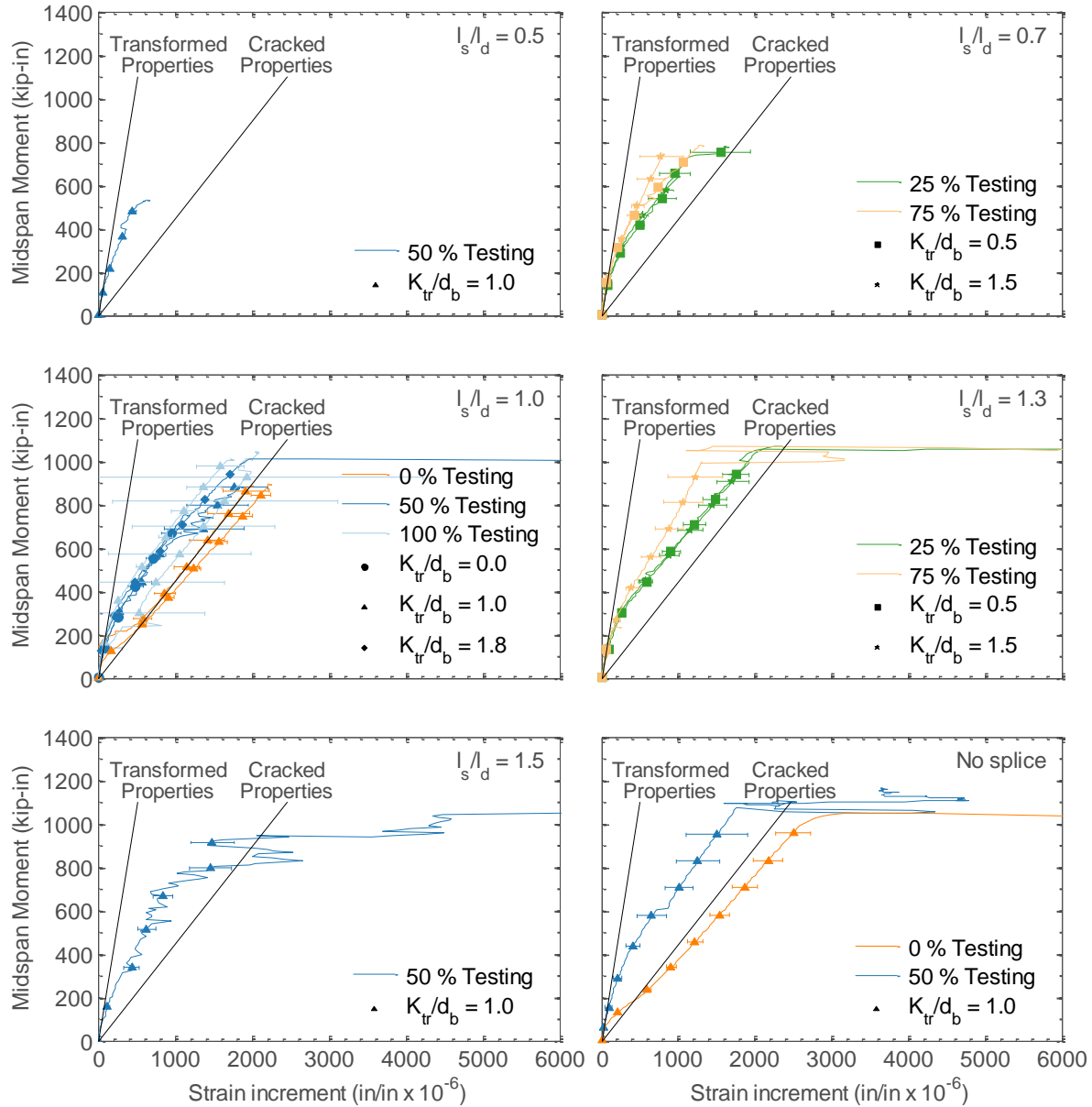
63

Figure 4.23. Calculated midspan moment vs. measured strain increment in the tensile reinforcement at the end of the splice for 6 levels of normalized splice length

In general, beams with normalized splice lengths, $\ell_s/\ell_d \geq 1.3$, showed signs of tensile reinforcement yielding, as is intended for under-reinforced sections. Conversely, beams with normalized splice lengths, $\ell_s/\ell_d \leq 0.7$, did not show signs of tensile reinforcement yielding. The development of the strain increment with increasing midspan moment did not appear to be significantly influenced by the normalized splice length or confinement parameter, K_{tr}/d_b. Beams tested at 0 % target expansion had larger strain increments for the same midspan moment when compared to beams tested with higher levels of ASR-induced expansion prior to testing, by as much as 1000 µε at a midspan moment of roughly 800 kip-in.

64

It was also observed that the development of the strain increment with increasing midspan moment was initially consistent with the transformed section estimation using the 28-day compressive modulus, regardless of the ASR induced expansion. The midspan moment where the relationship between the strain increment and midspan moment deviated from the transformed section estimation was smaller for the beams tested at 0 % target expansion than for beams tested at the higher target levels of expansion. This midspan moment value did not appear to change appreciably with an increase in ASR-induced expansion after the 25 % target expansion testing.

The development of strain increment with increasing midspan moment above a midspan moment of roughly 200 kip-in, was consistent with the slope of the cracked section estimation and this observation was independent of the normalized splice length, confinement parameter, and degree of ASR induced expansion.

Figure 4.24 presents the calculated midspan moment as a function of the measured strain increment in the stirrups during testing for a typical reactive beam specimen. The strain increment is used here to differentiate the increase in strain during structural testing from the strains induced by ASR expansion (i.e., the strain increment for all of the tested beams at the start of testing is zero). The strain increment during testing was measured on both the vertical legs (red curves) and the bottom (blue curves) of the stirrups in the splice region, as described in Section 2.6 (see inset of Figure 4.24). For each of the gages, the development of the strain increment with increasing midspan moment was truncated at the location of the beam's maximum moment strength or when the gages failed during testing, whichever occurred first. The measurement location on the stirrups is designated in the figure by color.
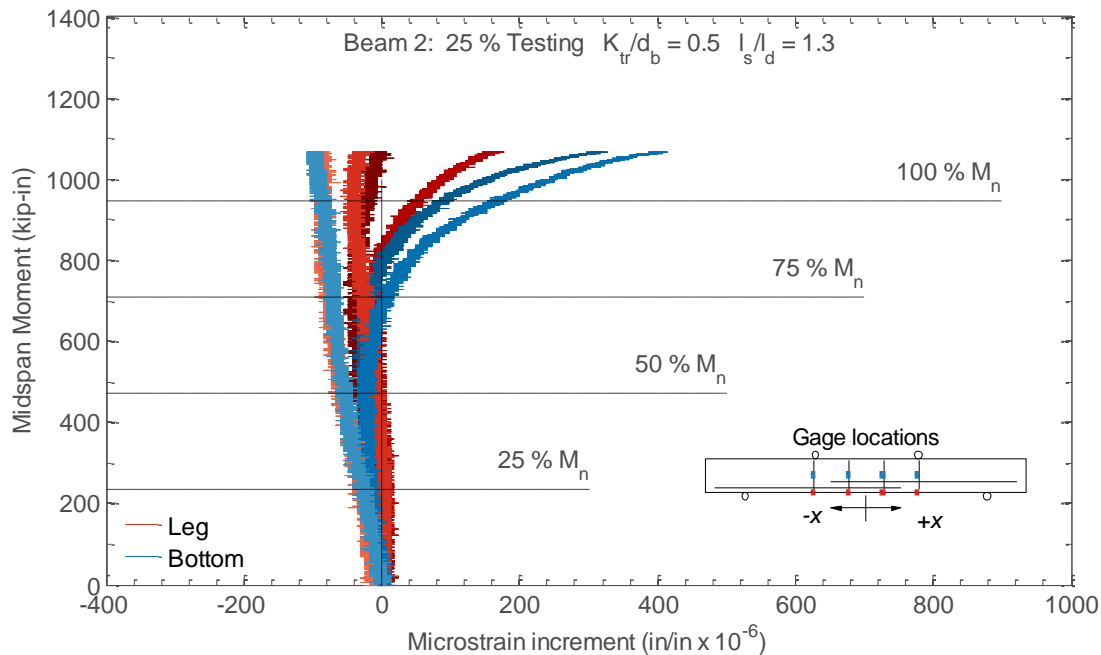
Figure 4.24. Calculated midspan moment vs. measured strain increment in the stirrups for Beam 2

In general, strain increments in the stirrups were small compared with strain increments in the tensile reinforcement and less than 50 % of the yield strain of the steel. In beams tested at 0 % target ASR expansion, the strain increments in the stirrups increased roughly linearly prior to the peak moment strength. In beams tested at higher levels of ASR expansion, strains in the stirrups were slightly negative (compressive) until near the peak moment. Strain increments generally showed significant increases near the peak moment of the beam.

4.5.8   Strain Distribution in the Splice Region

Figure 4.25 and Figure 4.26 show the distribution of normalized strain increments in the tensile reinforcement as a function of normalized length along the splice for two representative beam specimens. The distributions are shown at the maximum midspan moment during testing, M_{max}, and at several fractions of the nominal flexural strength of the beam section, M_n. Along the x-axis, 0.0 represents the free end of the splice and 1.0 represents one development length, ℓ_d, away from the free end. For example, the normalized splice length for the beam specimen in Figure 4.26 was $\ell_s/\ell_d = 1.3$ and strain data was collected at the middle and end of the splice, or at $\ell/\ell_d = 0.65$ and $\ell/\ell_d = 1.3$. The y-axis represents the measured strain increment divided by the yield strain of the reinforcing bar. The lightly colored circles in the figure indicate individual measurements and square marks and error bars indicate the mean value and the expanded uncertainty in the mean, respectively. Also plotted in the figure is a reference line from a normalized strain increment of 0.0 at the free end to a normalized strain increment of 1.0 at $\ell/\ell_d = 1.0$, corresponding to the code specified development length.
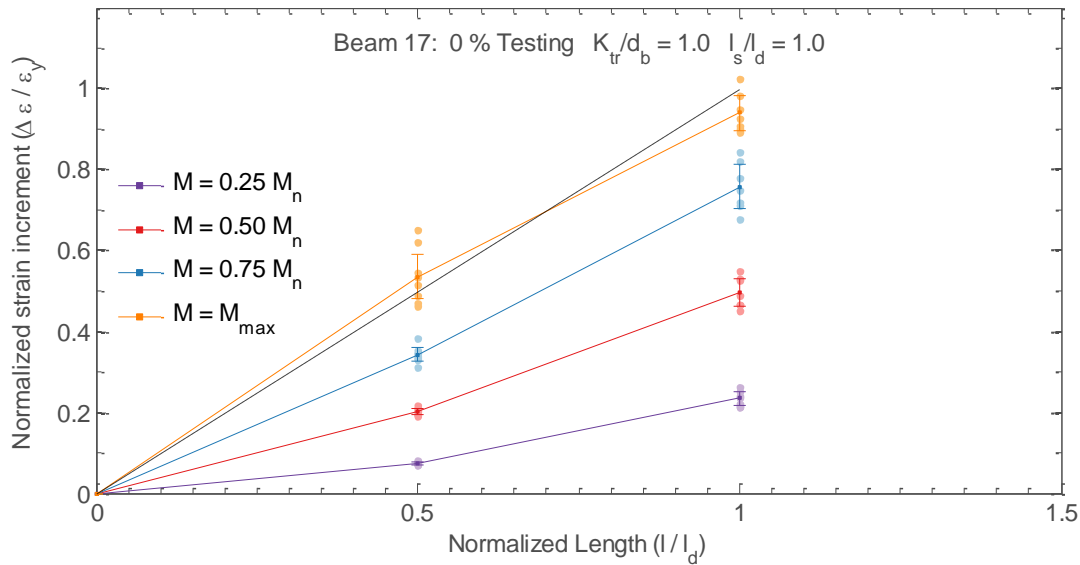
Figure 4.25. Distribution of normalized strain increments in the tensile reinforcement for Beam 17

Figure 4.25 shows the distribution of normalized strain increments in the tensile reinforcement as a function of normalized length for a typical beam tested at 0 % target ASR expansion. At the maximum

midspan moment, the change in the normalized strain increment across the splice varied roughly linearly, and the slope of the normalized strain increment with normalized length agreed with the 1:1 reference line.

Figure 4.26 shows the distribution of normalized strain increments in the tensile reinforcement as a function of normalized length for a typical beam tested at higher levels of ASR-induced expansion ($\varepsilon_{ASR} \geq$ 0.09 %). At the maximum midspan moment, the change in the normalized strain increment across the splice varied roughly linearly, however, the change in the normalized strain increment with normalized length was less than the reference line, by roughly 30 %. This is attributed to the initial strains in the reinforcement due to ASR-induced expansion, which would lead to larger stresses in the bar for the same strain increment when compared to a non-ASR beam. This can be observed in Figure 4.23, where the strain increments recorded in the ASR-affected beams were smaller, for the same nominal moment, than those recorded for beams tested at a target expansion of 0 %.
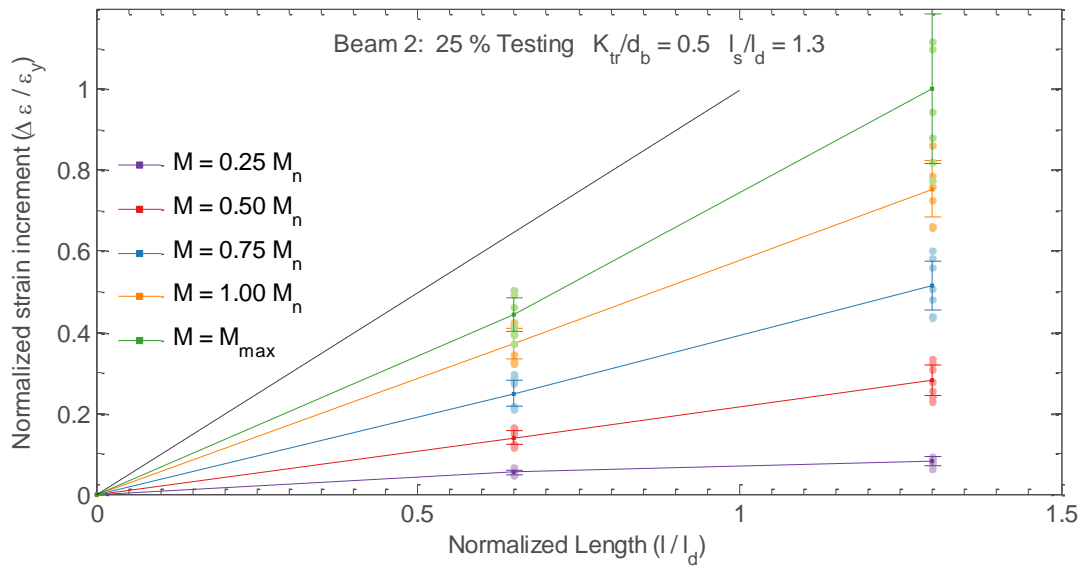
Figure 4.26. Distribution of normalized strain increments in the tensile reinforcement for Beam 2

4.5.9 Normalized Bond Strength

The maximum average bond strength, u, in the splice region was estimated based on the maximum recorded strain increments at the end of the splice during testing as:

$$u = d_b E_s \varepsilon_s / 4\ell_s, \qquad E_s \varepsilon_s \leq f_y, \tag{4.2}$$

where d_b is the bar diameter, E_s is the elastic modulus of the steel reinforcement, ε_s is the maximum average strain value in the reinforcement at the ends of the splice region, f_y is the yield stress of the tensile reinforcement (f_y= 68.6 ± 0.8 ksi, see Section 4.2), and ℓ_s is the length of the splice. In cases where

the maximum recorded strain exceeded the yield strain, the maximum stress in the bar was capped at the yield stress to limit the comparison to elastic bond stresses only.

In most cases, strain increments in the reinforcement were recorded until the beam reached its maximum moment strength. In three cases, however, the strain gages failed prior to this point. These three beam specimens achieved maximum moments similar to other beams where reinforcement yielded during testing, and strain increments estimated using a moment curvature analysis, similar to the approach used by ACI Committee 408, exceeded the yield strain at the achieved moment capacity in all three cases. Because of these factors, it was assumed that the bars yielded during testing, and the maximum average bond stresses were computed using the yield stress of the reinforcement (i.e., $E_s \varepsilon_s = f_y$ = 68.6 ksi in Equation 4-2).

Table 4.13 gives the normalized bond strength for all 19 of the beam tests. The maximum average bond strength, u, was normalized by the square root of the compressive strength of the concrete at the time of testing (the average compressive strengths reported in Table 4.1 and Table 4.2 for a given test date).

Table 4.13. Normalized maximum average bond stress for beam specimens

Specimen	Testing Target (% of $\varepsilon_{ASR\text{-}ult}$)	ε_{ASR} (%)	K_{tr}/d_b	ℓ_s/ℓ_d	$u/\sqrt{f_c'}$ ($\sqrt{psi}$)
1	25	0.09 ± 0.01	0.5	0.7	10.8
2	25	0.09 ± 0.01	0.5	1.3	11.2
3	25	0.09 ± 0.01	1.5	0.7	9.4
4	25	0.09 ± 0.01	1.5	1.3	16.2
5	75	0.17 ± 0.06	0.5	0.7	9.2
6	75	0.17 ± 0.06	0.5	1.3	11.2
7	75	0.17 ± 0.06	1.5	0.7	11.1
8	75	0.17 ± 0.06	1.5	1.3	16.3
9	50	0.14 ± 0.02	1.0	1.0	11.3
10	50	0.14 ± 0.02	1.0	N/A[‡]	N/A[‡]
11	0*	*	1.0	1.0	10.7
12	100	0.22**	1.0	1.0	14.6
13	50	0.14 ± 0.02	0.0[†]	1.0	4.3
14	50	0.14 ± 0.02	1.8	1.0	20.4
15	50	0.14 ± 0.02	1.0	0.5	7.1
16	50	0.14 ± 0.02	1.0	1.5	11.5
17	0*	*	1.0	1.0	11.2
18	0*	*	1.0	N/A[‡]	N/A[‡]
19	100	0.18**	1.0	1.0	11.3

** Only one gage remained functional at this date (these values should be treated only as estimates of the strain)

* Beam constructed with concrete treated with lithium nitrate solution to prevent expansion

[†] Beam had no stirrups in the constant moment region

[‡] Beam had continuous tensile reinforcement

The average of the normalized bond strength for reactive beam specimens that were reinforced with stirrups in the splice region and normalized splice lengths, $\ell_s/\ell_d \geq 1.0$, was computed to be 13.8 ± 2.5 $\sqrt{f_c'}$. In comparison, the average of the normalized average maximum bond stress for the non-reactive beams tested by Rezansoff *et al*. (1991) with similar cover, lap splice lengths, and confinement parameters was 12.8 ± 1.9 $\sqrt{f_c'}$. For the tested beam geometry and a confinement parameter, K_{tr}/d_b =1.0, the normalized average maximum bond stress estimated using ACI 318-19 (for normal, non ASR-affected concrete) was $10\sqrt{f_c'}$. Additional statistical analysis to examine the effects of ASR-induced expansion ε_{ASR}, the confinement parameter K_{tr}/d_b, and normalized lap splice length, ℓ_s/ℓ_d, on the normalized bond strength, $u/\sqrt{f_c'}$, as well as of beam structural capacity and failure mode is presented in Chapter 5.

This page intentionally left blank.

Chapter 5
STATISTICAL ANALYSIS OF MEASURED DATA

The statistical analysis focuses on three response variables: normalized moment capacity (M_{max}/M_n), normalized bond strength ($u/\sqrt{f_c'}$), and failure type (A/B) and four predictor variables: ASR-induced expansion (ε_{ASR}), normalized splice length (ℓ_s/ℓ_d), confinement parameter (K_{tr}/d_b), and failure type. Failure type had to act as both a predictor variable and a response variable because the relationship between M_{max}/M_n and ε_{ASR}, ℓ_s/ℓ_d, and K_{tr}/d_b changes with failure type. The same is observed for $u/\sqrt{f_c'}$. For each response two focus questions were answered:

1. Which predictor variables have the largest impact on the response variable?
2. How does the response variable change with the predictor variables that were identified to be most important?

The last three columns of Table 5.1 summarize the test results in terms of the moment capacity, average maximum bond stress, and the beam's failure type. For descriptions of Type A and Type B failures, refer to Section 4.5.2.

Table 5.1. Summary of beam test results

Beam	Testing Target (% of $\varepsilon_{ASR\text{-}ult}$)	ε_{ASR} (%)	ℓ_s/ℓ_d	K_{tr}/d_b	M_{max}/M_n	$u/\sqrt{f'_c}$ ($\sqrt{psi}$)	Failure Type
1	25	0.09	0.7	0.5	0.82	10.8	A
2	25	0.09	1.3	0.5	1.13	11.2	B
3	25	0.09	0.7	1.5	0.68	9.4	A
4	25	0.09	1.3	1.5	1.22	16.2	B
5	75	0.17	0.7	0.5	0.83	9.2	A
6	75	0.17	1.3	0.5	1.25	11.2	B
7	75	0.17	0.7	1.5	0.79	11.1	A
8	75	0.17	1.3	1.5	1.21	16.3	B
9	50	0.14	1.0	1.0	0.93	11.3	A
10	50	0.14	N/A‡	1.0	1.19	N/A‡	B
11	0*	0	1.0	1.0	0.94	10.7	A
12	100	0.18	1.0	1.0	1.10	14.6	B
13	50	0.14	1.0	0.0†	0.80	4.3	A
14	50	0.14	1.0	1.8	1.09	20.4	B
15	50	0.14	0.5	1.0	0.55	7.1	A
16	50	0.14	1.5	1.0	1.19	11.5	B
17	0*	0	1.0	1.0	0.91	11.2	A
18	0*	0	N/A‡	1.0	1.17	N/A‡	B
19	100	0.22	1.0	1.0	1.06	11.3	B

* Beam constructed with concrete treated with lithium nitrate solution to prevent expansion

† Beam had no stirrups in the constant moment region

‡ Beam had continuous tensile reinforcement

5.1   EXPERIMENT DESIGN

The experimental plan for this test series, summarized in Table 5.1, was constructed to be a rotatable central composite design (CCD, see Box *et al.*, 2005 and Myers, Montgomery, and Anderson-Cook 2016, Section 8.4.1) in ASR-induced expansion, ε_{ASR}; normalized splice length, ℓ_s/ℓ_d; and confinement parameter, K_{tr}/d_b. However, because of challenges in achieving the target expansion values (as outlined in Section 4.4), the measured values of ε_{ASR}, did not strictly follow the CCD prescription.

The lower triangle (i.e., the three plots in the lower left-hand corner) of Figure 5.1 depicts the values of ε_{ASR}, ℓ_s/ℓ_d, and K_{tr}/d_b used in the experiment. The six distinct levels of ε_{ASR} (instead of the targeted five) as well as the uneven spacing between the central value and the cube edges, differentiate the observed values of ε_{ASR}, ℓ_s/ℓ_d, and K_{tr}/d_b from those expected in a CCD. The correlations in the upper triangle of Figure 5.1 show that the design is nearly orthogonal; orthogonality is a desirable characteristic feature of good experimental designs. While the values of ε_{ASR}, ℓ_s/ℓ_d, and K_{tr}/d_b do not follow a CCD exactly, they permit similar analysis techniques, and so those techniques will be leveraged. Failure type (A or B, see Section 4.5.2) was not part of the experimental plan, but was added as a predictor variable

because M_{max}/M_n and $u/\sqrt{f_c'}$ can behave differently as a function of ASR, ℓ_s/ℓ_d, and K_{tr}/d_b for the two types.
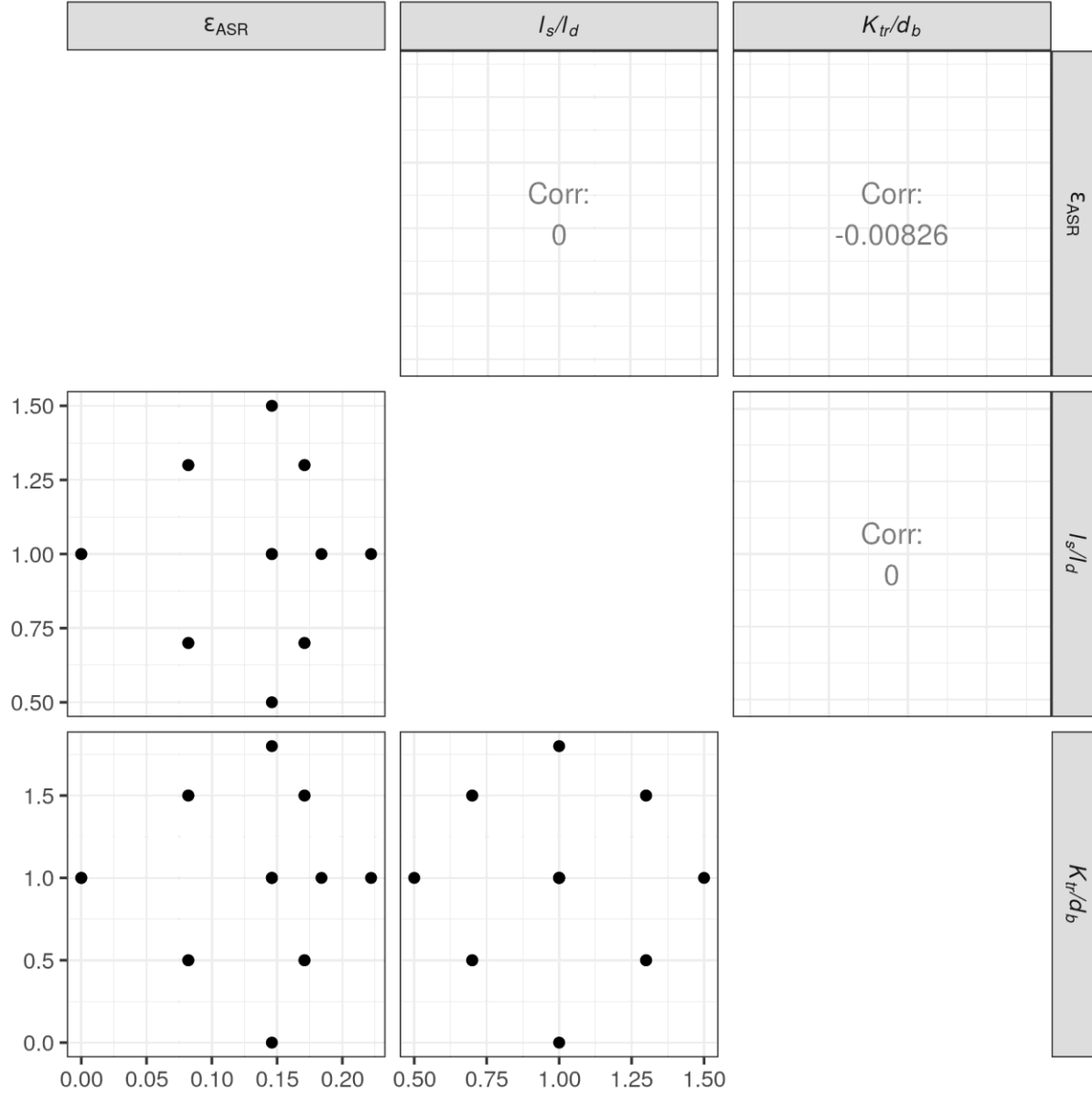
Figure 5.1. Observed values of ε_{ASR}, ℓ_s/ℓ_d, and K_{tr}/d_b as well as their pairwise correlations

5.2   NORMALIZED MOMENT CAPACITY M_{max}/M_n

To examine the influence of ε_{ASR} on the normalized moment capacity, M_{max}/M_n, the least absolute selection and shrinkage operator (LASSO) regularized linear regression method was utilized. The LASSO

method for generalized linear models was first introduced in Tibshirani (1996), and it acts as an automated operator to select the most important regression terms. The selection occurs because LASSO regularization can force the coefficient for a regression term to be exactly zero. Those input variables for which the regression coefficients are exactly zero are deemed less important for predicting the response than those with non-zero valued coefficients because the terms with zero-valued coefficients have no impact on the predictions. The *glmnet* package (Friedman *et al.*, 2010) for *R* (*R* Core Team 2020) was used to perform the computation. The parametric bootstrap described in Section 6.2 of Hastie *et al.* (2015) was used to assess uncertainty due to sampling variability.

The regression model that is fitted using the LASSO procedure is

$$
\begin{aligned}
M_{max}/M_n = \beta_0 + {} & \beta_1[\varepsilon_{ASR}] + \beta_2[\varepsilon_{ASR}^2] + \beta_3[\ell_s/\ell_d] + \beta_4[\varepsilon_{ASR} \cdot (\ell_s/\ell_d)] + \beta_5[(\ell_s/\ell_d)^2] \\
& + \beta_6[K_{tr}/d_b] + \beta_7[\varepsilon_{ASR} \cdot (K_{tr}/d_b)] + \beta_8[(\ell_s/\ell_d) \cdot (K_{tr}/d_b)] \\
& + \beta_9[(K_{tr}/d_b)^2] + \beta_{10}[T] + \beta_{11}[\varepsilon_{ASR} \cdot T] + \beta_{12}[(\varepsilon_{ASR})^2 \cdot T] \\
& + \beta_{13}[(\ell_s/\ell_d) \cdot T] + \beta_{14}[\varepsilon_{ASR} \cdot (\ell_s/\ell_d) \cdot T] + \beta_{15}[(\ell_s/\ell_d)^2 \cdot T] \\
& + \beta_{16}[(K_{tr}/d_b) \cdot T] + \beta_{17}[\varepsilon_{ASR} \cdot (K_{tr}/d_b) \cdot T] + \beta_{18}[(\ell_s/\ell_d) \cdot (K_{tr}/d_b) \cdot T] \\
& + \beta_{19}[(K_{tr}/d_b)^2 \cdot T] + \epsilon
\end{aligned}
\tag{5.1}
$$

The β_i's in Equation 5.1 are the regression coefficients to be estimated, and T identifies failure type as -1 for Type B failures and 1 for Type A failures. The term ϵ represents a random error. Equation 5.1 allows for a separate quadratic relationship between M_{max}/M_n and ε_{ASR}, ℓ_s/ℓ_d, and K_{tr}/d_b, for each failure type.

Figure 5.2 depicts the estimates and associated uncertainties of the β_i's using violin plots. Actually, the regression terms in Equation 5.1 are raw polynomial terms, but the coefficients depicted in Figure 5.2 are associated with orthogonal polynomial terms; thus, the estimated values of the β_i's depicted in Figure 5.2 are not directly interpretable, other than by their sign or in the special case that they equal zero. The form of the orthogonal polynomial is defined on pages 343 and 344 of Kennedy and Gentle (1980).
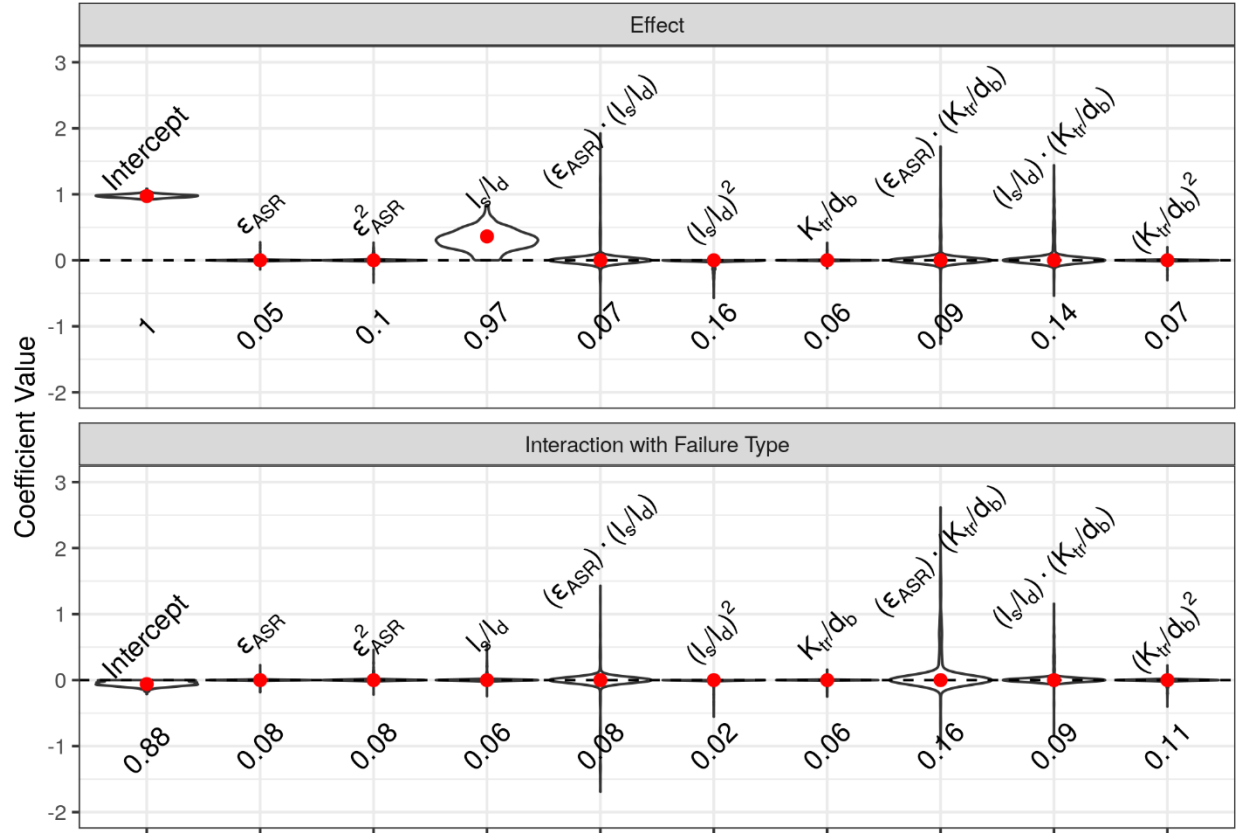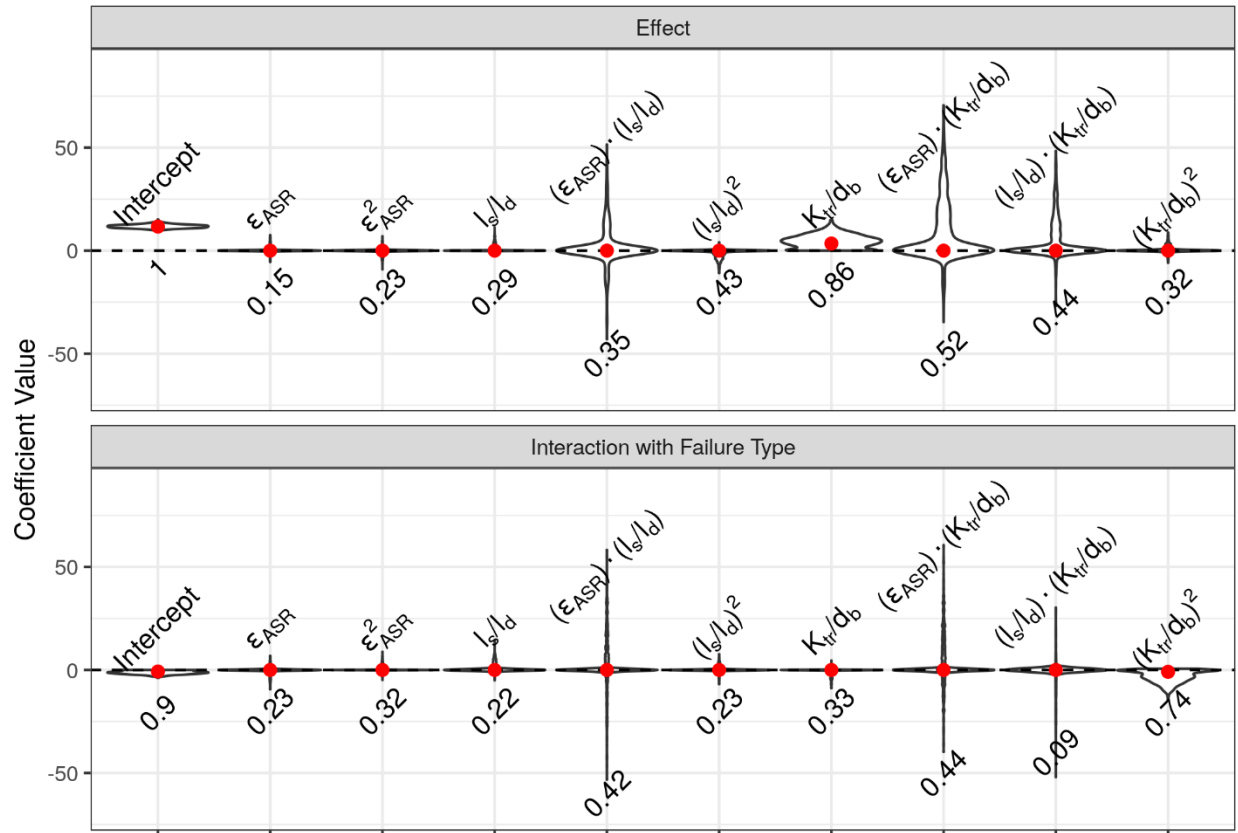
Figure 5.2. Estimates and associated uncertainties for the β_i's in Equation 5.1. The red points are the estimates, and the violin plots depict the bootstrap distributions, which quantify uncertainty. The numbers are the proportions of bootstrap samples for which the coefficient was non-zero.

The circular markers (red points) in Figure 5.2 are estimated values for the β_i's in Equation 5.1. The only non-zero estimates are for β_3 and β_{10} (the overall intercept, β_0, is always non-zero) which are the coefficient associated with the linear ℓ_s/ℓ_d term, and the interaction between failure type and the overall intercept, respectively. That observation provides an answer for both focus questions. Thus:

1) the primary variable affecting M_{max}/M_n is ℓ_s/ℓ_d, and

2) the relationship is positive, i.e. higher ℓ_s/ℓ_d implies a higher M_{max}/M_n on average.

The non-zero interaction between failure type and the overall intercept implies that an offset exists between failure types. Further, the negative value of the coefficient for that interaction implies that Type B failures lead to higher values of M_{max}/M_n than Type A failures, on average, with all other predictors fixed. The lack of an interaction between failure type and the linear ℓ_s/ℓ_d term implies that the same positive relationship between M_{max}/M_n and ℓ_s/ℓ_d governs for both failure types.

The parametric bootstrap algorithm described in Section 6.2 of Hastie *et al.* (2015) quantifies uncertainty due to sampling variability, i.e., would the same conclusion be reached if the experiment were run again, and a new set of measurements collected. While it is impracticable to run the experiment again, the

statistical bootstrap attempts to mimic what would happen if we could. Specifically, a bootstrap dataset is generated, and the same LASSO procedure that was used on the original dataset is applied to the bootstrap dataset. The violin plots in Figure 5.2 depict the results from 1000 bootstrap datasets and are referred to as the bootstrap distributions. The numbers are the proportions of the bootstrap datasets for which the β_i's were estimated to be non-zero. The linear ℓ_s/ℓ_d term was the most important since it was almost never estimated to be zero, and its bootstrap distribution was concentrated away from zero. The interaction between failure type and the overall intercept was also important because it was estimated to be non-zero for far more than 50 % of the bootstrap datasets. The violin plot for the interaction between failure type and the overall intercept was also concentrated away from zero, although less noticeably than for the linear ℓ_s/ℓ_d term. The remaining β_i's were estimated to be non-zero for less than 20 % of the bootstrap datasets, most for less than 10 %, and their violin plots were all concentrated around zero. This parametric bootstrap analysis shows that our previous answers to the focus questions for M_{max}/M_n are robust to sampling variability.

Figure 5.3 illustrates an estimate of Equation 5.1 (thick black curve), the measurements (black points), uncertainty due to sampling variability (grey curves), and an equation for comparison developed through section analysis of the tested beam sections, assuming the yield stress in the bar can be achieved for $\ell_s/\ell_d > 1$ (pink curve). Type A failure results are shown for $\ell_s/\ell_d < 1$ and Type B failure results are shown for $\ell_s/\ell_d > 1$. Figure 5.3 is divided into four combinations of ε_{ASR} and K_{tr}/d_b because some of the bootstrap replicates estimate non-zero coefficients for the interaction terms (e.g., $\varepsilon_{ASR} \cdot (K_{tr}/d_b)$). The thick black curve and the pink curve are identical between the four panes, but the grey curves may not be. Figure 5.3 implies that the equation developed through section analysis is generally consistent within sampling variability since the pink curve is enveloped by the grey curves over much of the design region. An exception is for large values of ℓ_s/ℓ_d.

For $1.3 \leq \ell_s/\ell_d \leq 1.5$, over 90 % of the bootstrap replicates (grey curves) are completely above the expression developed through section analysis (pink curve). For the individual panes, 927, 958, 986, and 982 out of 1000 of the grey curves are completely above the pink curve, moving in a clockwise manner starting in the upper left panel. This indicates that, for ASR-affected beams, constructed with similar geometries and reinforcement as tested in this study, the nominal flexural capacity determined in accordance with ACI section analysis is expected to be achieved ($M_{max}/M_n \geq 1.0$) when code compliant splice lengths ($\ell_s/\ell_d \geq 1.3$) are used, irrespective of the level of ε_{ASR} and K_{tr}/d_b.
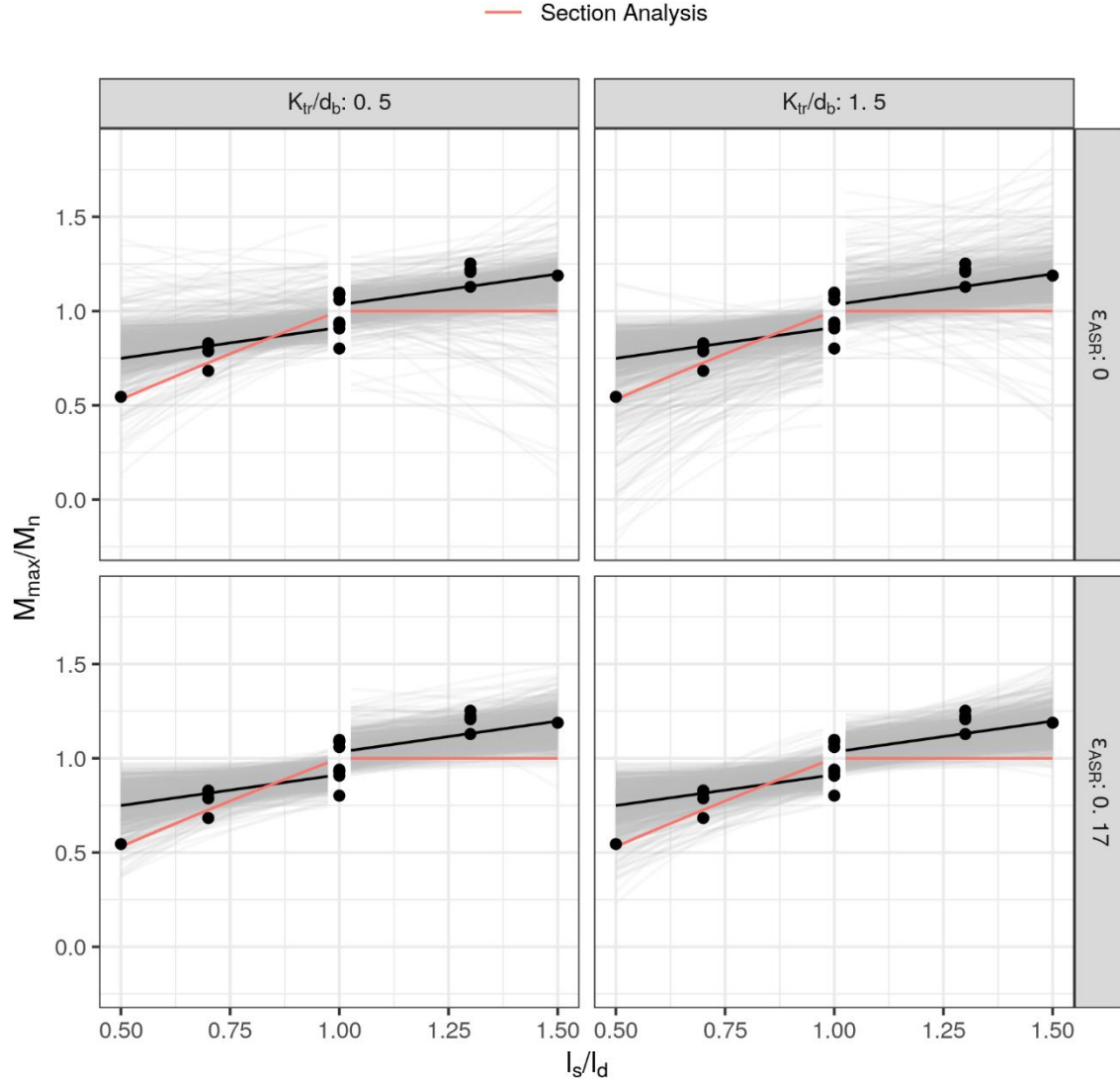
Figure 5.3. Comparison of our estimate of Equation 5.1 to an equation developed by section analysis. The thick black line is based on Equation 5.1, and the grey lines are 1000 bootstrap replicates conveying uncertainty due to sampling variability. The black points are the observed measurements. Type A failure results are shown for $\ell_s/\ell_d < 1$ and Type B for $\ell_s/\ell_d > 1$. The pink curve was developed by ACI section analysis.

5.3 AVERAGE BOND STRESS

The same statistical analysis implemented for M_{max}/M_n is also applied to $u/\sqrt{f_c'}$. For this purpose, Equation 5.1 becomes Equation 5.2:

$$u/\sqrt{f_c'} = \beta_0 + \beta_1[\varepsilon_{ASR}] + \beta_2[\varepsilon_{ASR}^2] + \beta_3[\ell_s/\ell_d] + \beta_4[\varepsilon_{ASR} \cdot (\ell_s/\ell_d)] + \beta_5[(\ell_s/\ell_d)^2]$$
$$+ \beta_6[K_{tr}/d_b] + \beta_7[\varepsilon_{ASR} \cdot (K_{tr}/d_b)] + \beta_8[(\ell_s/\ell_d) \cdot (K_{tr}/d_b)]$$
$$+ \beta_9[(K_{tr}/d_b)^2] + \beta_{10}[T] + \beta_{11}[\varepsilon_{ASR} \cdot T] + \beta_{12}[(\varepsilon_{ASR})^2 \cdot T]$$
$$+ \beta_{13}[(\ell_s/\ell_d) \cdot T] + \beta_{14}[\varepsilon_{ASR} \cdot (\ell_s/\ell_d) \cdot T] + \beta_{15}[(\ell_s/\ell_d)^2 \cdot T] \qquad (5.2)$$
$$+ \beta_{16}[(K_{tr}/d_b) \cdot T] + \beta_{17}[\varepsilon_{ASR} \cdot (K_{tr}/d_b) \cdot T] + \beta_{18}[(\ell_s/\ell_d) \cdot (K_{tr}/d_b) \cdot T]$$
$$+ \beta_{19}[(K_{tr}/d_b)^2 \cdot T] + \epsilon$$

Figure 5.4 is analogous to Figure 5.2 but corresponds to Equation 5.2. Because the vertical range is large in Figure 5.4, it is difficult to visually identify the non-zero valued coefficients. They are the coefficients associated with $(\ell_s/\ell_d)^2$, K_{tr}/d_b, $(\ell_s/\ell_d) \cdot (K_{tr}/d_b)$, the failure type interaction with the overall intercept, the failure type interaction with K_{tr}/d_b, and the failure type interaction with $(K_{tr}/d_b)^2$.
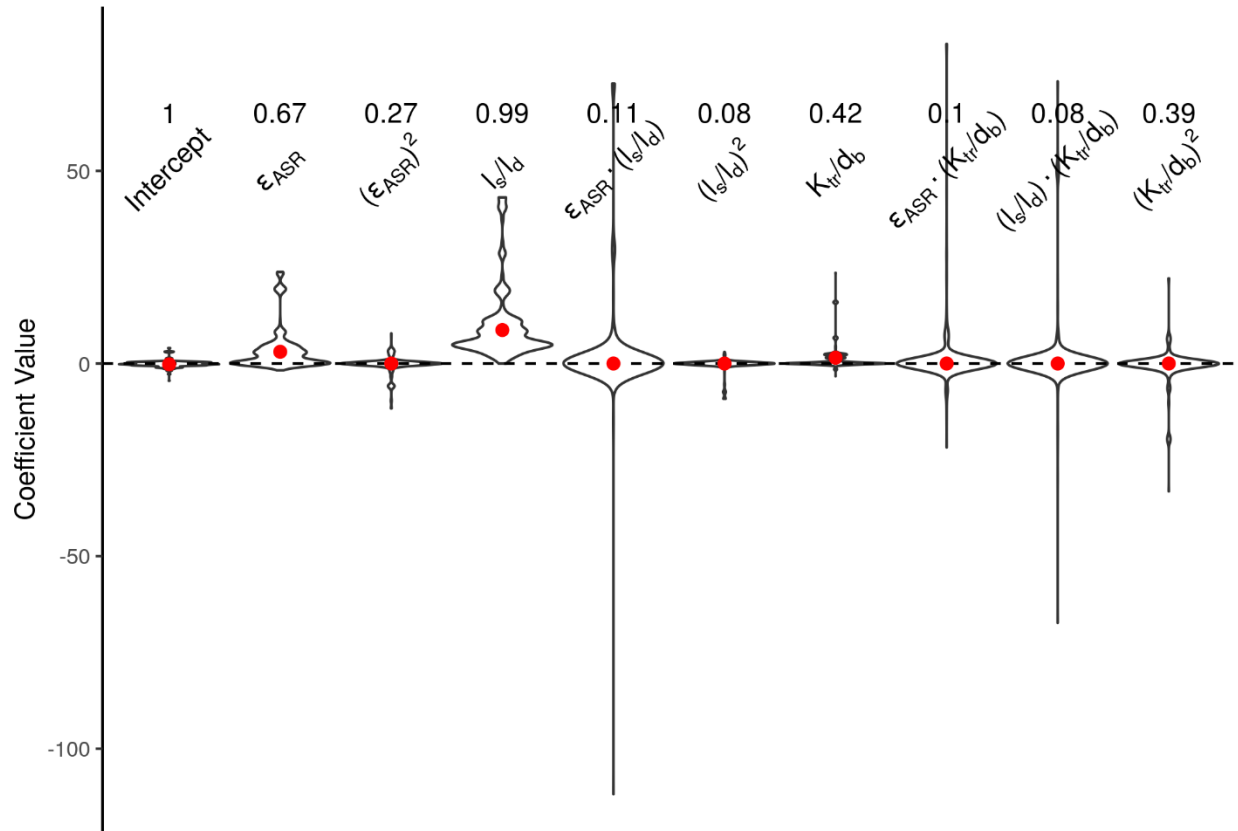

Figure 5.4. **Estimates and associated uncertainties for the β_i's in Equation 5.2. The red points are the estimates, and the violin plots depict the bootstrap distributions, which quantify uncertainty. The numbers are the proportions of bootstrap datasets for which the coefficient was non-zero.**

From this perspective, the most important variables for predicting $u/\sqrt{f_c'}$ are K_{tr}/d_b, ℓ_s/ℓ_d, and failure type. However, for $u/\sqrt{f_c'}$, the proportion of bootstrap replicates that identify each coefficient as non-zero gives a slightly contradictory answer. The regression terms with coefficients identified to be non-zero for more than 50 % of the bootstrap replicates are K_{tr}/d_b, $(\varepsilon_{ASR}) \cdot (K_{tr}/d_b)$, the interaction between failure type and the overall intercept, and the interaction between failure type and $(K_{tr}/d_b)^2$. This implies that the primary variables for predicting $u/\sqrt{f_c'}$ are ε_{ASR}, K_{tr}/d_b, and failure type. On the other hand, ε_{ASR} enters primarily through the $(\varepsilon_{ASR}) \cdot (K_{tr}/d_b)$ regression term, and the bootstrap distribution for the coefficient associated with that term is very wide, taking on both relatively large negative and positive values. Since the sign of the coefficient on the $(\varepsilon_{ASR}) \cdot (K_{tr}/d_b)$ term is in question, and no ε_{ASR} terms had non-zero coefficients for the measured data, we find sufficient evidence only to conclude that K_{tr}/d_b and failure type are the primary variables affecting $u/\sqrt{f_c'}$. Because the linear K_{tr}/d_b term and the interaction between failure type and $(K_{tr}/d_b)^2$ are both identified as important, the nature of the relationship between $u/\sqrt{f_c'}$ and K_{tr}/d_b is difficult to ascertain from only the estimated coefficients.

Figure 5.5 depicts an estimate of Equation 5.2 (thick black curves), the measurements (black points), uncertainty due to sampling variability for the estimate of Equation 5.2 (grey curves), and three other relationships found in codes and literature.
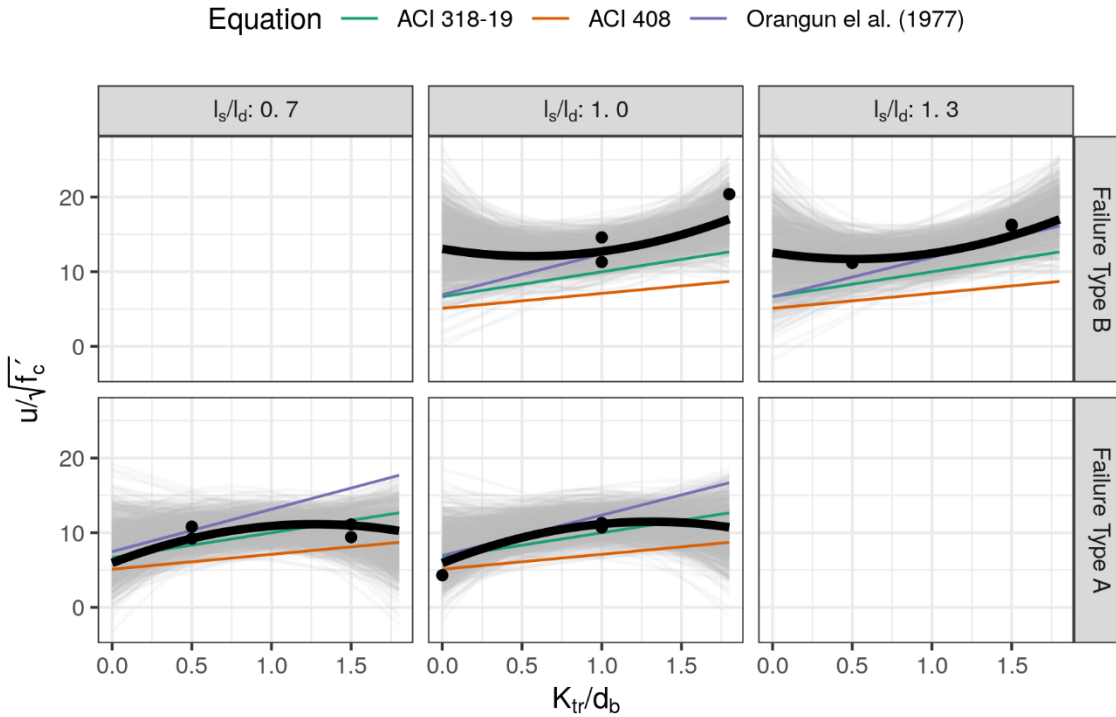
Figure 5.5. Comparison of our estimated relationship between $u/\sqrt{f_c'}$ and K_{tr}/d_b, and three other relationships from codes and literature. The thick black curve is our estimate of the relationship, and the grey lines are 1000 bootstrap replicates conveying uncertainty due to sampling variability. The black points are the observed measurements. The sources of the colored curves are identified in the legend.

The interaction between failure type and $(K_{tr}/d_b)^2$ is striking since the black curve for Type B failures has a convex shape, but for Type A failures its shape is concave. The panes separate values of ℓ_s/ℓ_d. There are no clear visual differences between panes within a row, supporting the assertion that the impact of ℓ_s/ℓ_d on $u/\sqrt{f_c'}$ is not dramatic over the range considered. From Figure 5.5, the relationship between $u/\sqrt{f_c'}$ and K_{tr}/d_b is flat or positive depending on the failure type and K_{tr}/d_b range. For insufficient lap splices, $\ell_s/\ell_d \leq 1.0$, increases in K_{tr}/d_b are effective until a limiting value, consistent with the recommendations of ACI 318-19 that limit the combination of $(K_{tr} + c_b)/d_b \leq 2.5$. Conversely, for sufficient lap splices, $\ell_s/\ell_d \geq 1.0$, increases in the confinement parameter, K_{tr}/d_b, are effective at increasing $u/\sqrt{f_c'}$ in the range that was investigated, consistent with the observations of Rezansoff *et al.* (1991) who investigated beams with $\ell_s/\ell_d = 1.0$ (The beams in their study would generally be classified as Type B failures).

Figure 5.5 compares the measurements and estimate of Equation 5.2 to three relationships developed for non-reactive reinforced concrete beams described in Section 1.1.1: Orangun *et al.* (1977), ACI 408 Committee, and ACI 318-19. The design expressions developed by ACI Committee 408 (orange curve, $5.1 + 2(K_{tr}/d_b)$) and ACI318-19 (green curve, $6.66 + 3.33(K_{tr}/d_b)$) are identical between the panels, since they do not depend on ℓ_s/ℓ_d. The expression developed by Orangun *et al.* (1977) (purple curves, $5.7 + 1.23(\ell_s/\ell_d)^{-1} + 0.615(K_{tr}/d_b)(\ell_s/\ell_d)^{-1} + 4.8(K_{tr}/d_b))$ change slightly between the panes because the relationship for $u/\sqrt{f_c'}$ includes terms with $(\ell_s/\ell_d)^{-1}$. The relationships are generally consistent within the estimated uncertainty due to sampling variability, depending on the K_{tr}/d_b range.

For the estimate of Equation 5.2, assuming Type B failure (top panes of Figure 5.5) and a range of the confinement parameter, $0.5 \leq K_{tr}/d_b \leq 1.8$, 998 out of the 1000 bootstrap replicates were completely above the relationship developed by the ACI 408 Committee for $\ell_s/\ell_d = 1.0$, and 995 out of 1000 for $\ell_s/\ell_d = 1.3$. The corresponding numbers for the ACI 318-19 expression were 908 and 877, respectively. This indicates that for beams constructed with similar geometries and reinforcement, reinforced with stirrups, and with, $\ell_s/\ell_d \geq 1.0$, $u/\sqrt{f_c'}$ predicted by both code equations would be reasonable lower bounds for the mean value of $u/\sqrt{f_c'}$, despite the presence of ASR-induced expansion.

5.4 FAILURE TYPE

The statistical analysis was concluded by answering the focus questions considering failure category as a binary response, and ε_{ASR}, (ℓ_s/ℓ_d), and K_{tr}/d_b as predictors. The same statistical methods were employed, except linear regression was replaced by logistic regression. Let the probability of a Type B failure (achieving the nominal flexural strength of the beam) be denoted by $P(B)$, and then Equations 5.1 and 5.2 become

$$
\begin{aligned}
\log\left[\frac{P(B)}{1 - P(B)}\right] = {} & \beta_0 + \beta_1[\varepsilon_{ASR}] + \beta_2[\varepsilon_{ASR}^2] + \beta_3[\ell_s/\ell_d] + \beta_4[\varepsilon_{ASR} \cdot (\ell_s/\ell_d)] + \beta_5[(\ell_s/\ell_d)^2] \\
& + \beta_6[K_{tr}/d_b] + \beta_7[\varepsilon_{ASR} \cdot (K_{tr}/d_b)] + \beta_8[(\ell_s/\ell_d) \cdot (K_{tr}/d_b)] \\
& + \beta_9[(K_{tr}/d_b)^2]
\end{aligned}
\tag{5.3}
$$

Note the lack of a random error term in Equation 5.3. The random error is replaced by an assumption that the occurrence of a Type B failure follows a binomial distribution, and then the log odds ratio is a function of the three predictor variables. Tibshirani (1996) also introduced the LASSO regularization method for logistic regression. As for M_{max}/M_n and $u/\sqrt{f'_c}$, the regression terms are orthogonal polynomials.

Figure 5.6 is analogous to Figures 5.2 and 5.4 and depicts the estimates and associated uncertainties for the β_i's in Equation 5.3. The red points are the estimated values. The only non-zero estimates are β_1, β_3, and β_6, the coefficients associated with the three linear terms. The violin plots depict uncertainty due to sampling variability estimated by a parametric bootstrap algorithm. The numbers are the proportion of bootstrap datasets for which the coefficients are non-zero. From Figure 5.6, only β_1 and β_3 are estimated to be non-zero for more than 50 % of the bootstrap replicates. Thus, we conclude that ε_{ASR} and ℓ_s/ℓ_d affect failure type most strongly, and that the relationships are positive, i.e., higher values of ε_{ASR} and ℓ_s/ℓ_d imply a higher probability of a Type B failure.

Figure 5.6. Estimates and associated uncertainties for the β_i's in Equation 5.3. The red points are the estimates, and the violin plots depict the bootstrap distributions, which quantify uncertainty. The numbers are the proportions of bootstrap samples for which the coefficient was non-zero.

Figure 5.7 shows an estimate of the probability of a Type B failure using Equation 5.3 (black curves) and the estimated uncertainty due to sampling variability (grey curves). The uncertainty due to sampling variability is quite large, covering almost all probabilities [0, 1] for any combination of ε_{ASR}, ℓ_s/ℓ_d, and K_{tr}/d_b. This is common in logistic regression with such a small sample size relative to the number of regression terms (17 observations and 10 regression coefficients). In the parametric bootstrap algorithm, a switch of a single specimen from a Type A failure to a Type B failure or vice versa, just by random chance, had a large impact on the resulting estimate of the probability of a Type B failure. Some of the grey curves in Figure 5.7 are horizontal, indicating no association between the probability of a Type B failure and ℓ_s/ℓ_d, and some show a decreasing probability of a Type B failure with increasing ℓ_s/ℓ_d. While those observations contradict the conclusions reached from Figure 5.6, they do not dominate the plot. The dominant trends in Figure 5.7 are that as ℓ_s/ℓ_d or ε_{ASR} (ASR-induced expansion) increases, the probability of achieving the nominal flexural strength increases as well.
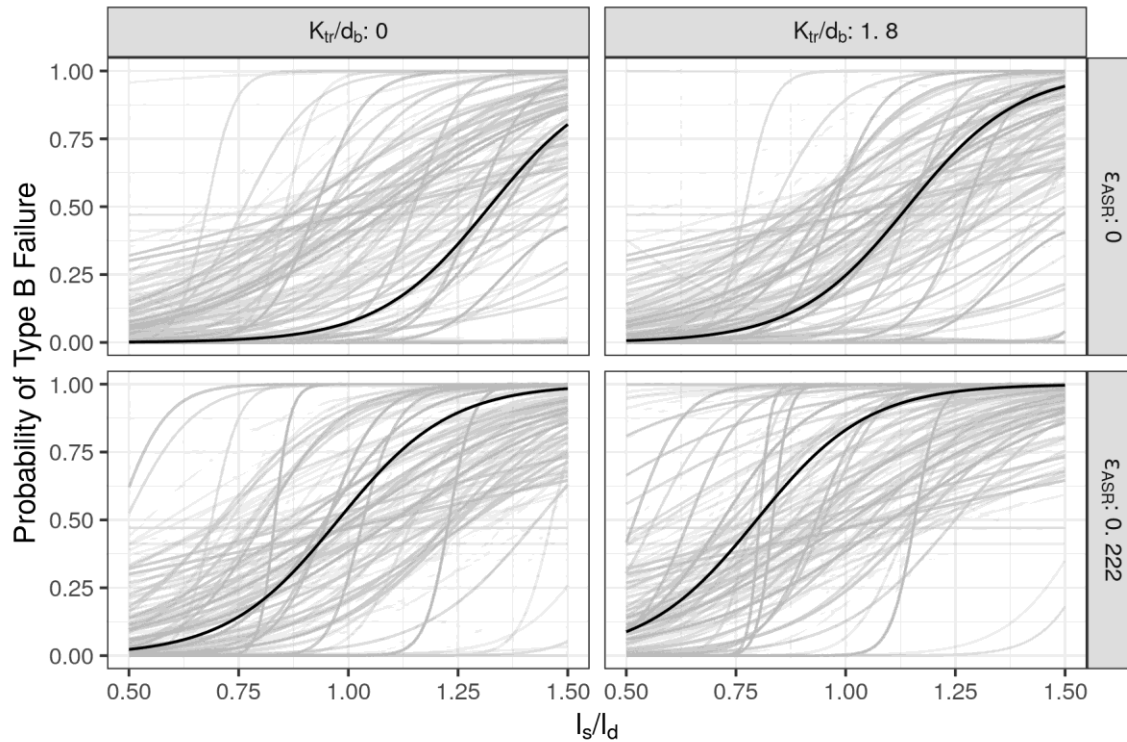
Figure 5.7. The thick black curves are our estimate of the probability of a Type B failure, and the grey curves are 1000 bootstrap replicates conveying uncertainty due to sampling variability.

Chapter 6
COMPUTATIONAL MODELING AND ANALYSIS OF BEAMS

6.1 INTRODUCTION

Computational analyses of the beam tests were carried out using high-fidelity finite element models with a large number of elements: solid elements for concrete and beam elements for both longitudinal and transverse reinforcement. The objectives of the analyses were to: (1) develop and validate high-fidelity finite element models of the beams that can reproduce the behavior of the beams during curing (i.e., with increasing ASR expansion) and during load testing; (2) gain insight into the behavior and failure modes of the beams, including the strain development in the concrete and reinforcing bars due to ASR expansion; and (3) contrast the behavior of the beams with and without splices in the tensile reinforcement under the four-point bending tests. Of particular interest was the effect of ASR-induced prestressing on the response of the beams and the loss of bond in the spliced beams. In general, close agreement was observed between the experimental and computational results. The beam models were capable of capturing the primary response characteristics during both the curing phase and the load testing.

The finite element analyses presented in this chapter were performed using explicit time integration in LS-DYNA (Hallquist, 2012), a general-purpose, commercially available, finite element software package. The analyses considered both geometrical and material nonlinearities. In addition, the beam models accounted for two unique features that required making additions to the LS-DYNA software: (1) an algorithm to calculate the bond-slip forces between the reinforcing bars and surrounding concrete (see section 6.3), and (2) modifications to the concrete material model in LS-DYNA (MAT_159) to allow for ASR expansion and associated material degradation (see Section 6.4).

Section 6.2 describes the seven beams that were selected for the computational modeling in this chapter. Section 6.3 presents a description of the models. Section 6.4 provides an overview of the material models used in the analyses, including those pertaining to the reinforcing bars, the concrete, and bond-slip. Section 6.5 provides the details of the ASR modeling. Sections 6.6 and 6.7, respectively, present the analysis results for the non-reactive and reactive beams used in the computational study. Section 6.8 provides a summary of the analysis results.

6.2 SELECTION OF BEAMS FOR COMPUTATIONAL STUDY

Of the 19 beams used in the experimental study, seven were selected for the computational modeling. The selected beams are shown in Table 6.1. All selected beams had a reinforcement confinement ratio, K_{tr}/d_b, of 1.0. The selected beams are categorized into two groups:

- Non-reactive beams: Highlighted in green in the Table 6.1, these beams included Beam 18 with continuous tensile reinforcing bars and Beams 11 and 17 with spliced tensile reinforcing bars ($\ell_s = 22$ in). Beam 18 allowed examination of the accuracy of the models by capturing the basic response characteristics without the complications of the splice behavior and the ASR reaction.

Non-reactive, spliced Beams 11 and 17 allowed for validation and calibration of the bond-slip model for cases with no ASR expansion.

- Reactive beams: This group is highlighted in orange in the table and included Beam 10 with continuous tensile reinforcing bars and Beams 9, 12, and 19 with spliced tensile reinforcing bars ($\ell_s = 22$ in). Beam 10 allowed examining the accuracy of the ASR material models in capturing the primary response characteristics without the complications of the splice behavior. Beam 9 (spliced, and with ASR expansion of 0.15 %) and Beams 12 and 19 (spliced, and with ASR expansion of 0.22 %) allowed for validation and calibration of the bond-slip model that accounts for varying degrees of ASR expansion.

Table 6.1. Beams selected for the computational study

Beam	Testing Target (% of $\varepsilon_{ASR\text{-}ult}$)	ε_{ASR} (%)	K_{tr}/d_b	ℓ_s/ℓ_d	ℓ_s (in)
1	25	0.09 ± 0.01	0.5	0.7	18.0
2	25	0.09 ± 0.01	0.5	1.3	32.0
3	25	0.09 ± 0.01	1.5	0.7	12.0
4	25	0.09 ± 0.01	1.5	1.3	22.0
5	75	0.17 ± 0.06	0.5	0.7	18.0
6	75	0.17 ± 0.06	0.5	1.3	32.0
7	75	0.17 ± 0.06	1.5	0.7	12.0
8	75	0.17 ± 0.06	1.5	1.3	22.0
9	50	0.14 ± 0.02	1.0	1.0	22.0
10	50	0.14 ± 0.02	1.0	N/A‡	N/A‡
11	0*	*	1.0	1.0	22.0
12	100	0.22**	1.0	1.0	22.0
13	50	0.14 ± 0.02	0.0†	1.0	32.0
14	50	0.14 ± 0.02	1.8	1.0	18.0
15	50	0.14 ± 0.02	1.0	0.5	10.0
16	50	0.14 ± 0.02	1.0	1.5	32.0
17	0*	*	1.0	1.0	22.0
18	0*	*	1.0	N/A‡	N/A‡
19	100	0.18**	1.0	1.0	22.0

** Only one gage remained functional at this date (these values should be treated only as estimates of the strain)

* Beam constructed with concrete treated with lithium nitrate solution to prevent expansion

† Beam had no stirrups in the constant moment region

‡ Beam had continuous tensile reinforcement

6.3   MODEL DESCRIPTION

Finite element models of the beams outlined in Section 6.2 were developed to study their response characteristics during ASR expansion and under four-point bending (load testing). The model had more than 23,000 solid and beam elements. An overview of the model used in the analysis is shown in Figure 6.1. Solid elements in the right-hand portion of the model were hidden to show the embedded reinforcing bars. The model consisted of solid elements representing the concrete and beam elements representing longitudinal and transverse reinforcing bars. The length of the solid elements was 1 in and the length of the beam elements was about 1 in for the longitudinal reinforcing bars and stirrups.
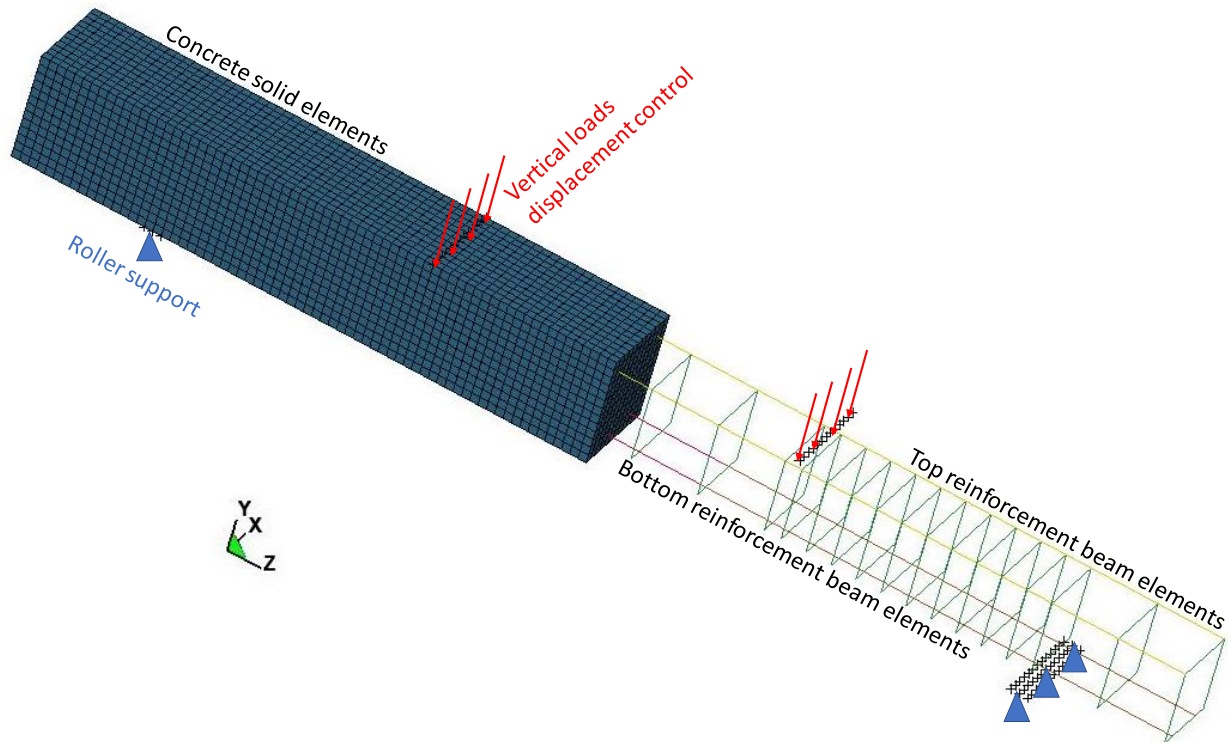
Figure 6.1. Overview of the high-fidelity finite element model of the beams, with solid elements hidden on the right-hand-side of the beam to display the embedded reinforcing bars

Bond-slip was modeled between the beam's bottom (tensile) longitudinal reinforcing bars and surrounding concrete (see Section 6.4.3). As a result, two sets of nodes were defined, with the concrete nodes specified as master nodes and the reinforcement nodes specified as slave nodes. Bond-slip was not considered for the top (compression) and transverse reinforcement, but different node numbering was still specified for the concrete and reinforcing bars to allow for flexibility in model development. All beam elements representing the reinforcing bars in the model were constrained within the solid elements using the CONSTRAINED_BEAM_IN_SOLID card which allowed for either (1) a user-defined function or user provided subroutine that calculated the axial shear force based on the slip between reinforcing bar elements and concrete solid elements, or (2) a complete merging between reinforcing bar nodes and surrounding concrete solid elements. For beams that had a bottom reinforcing bar splice, each spliced

85

reinforcing bar was modeled explicitly with nodes sharing the same coordinates, but with different node numbering to allow for realistic development of axial forces in the reinforcing bars during the analysis.

Very fine meshing of solid elements would be required to directly capture the progress of concrete cracking under ASR expansion or under loading, which could cause a nonobjective (divergent) response due to localization. Since simulation of cracking was not a focus of this study, the level of refinement of the solid element mesh described above (with solid elements of approximately 1 in length) was considered reasonable. Even while cracks were not modeled explicitly, evidence of concrete cracking is reflected by contours of the damage index computed by the concrete material model, see Section 6.4.2.

As shown in Figure 6.1, the cross section of the beam was defined in the X-Y plane, where Y represented the gravity direction. The Z-axis was defined along the length of the beam. During the ASR expansion phase of the response, the following boundary conditions were applied:

- Symmetric boundary conditions were applied along the centerlines in the Z and Y directions
- Y-displacements were restrained at the locations of the supports at the bottom of the beam.

During the load testing, the previous boundary conditions remained in effect, and the following additional boundary and loading conditions were imposed:

- X-displacements were restrained at the beam top where the load was applied.
- The load was applied at the beam top under displacement control at a slow rate to avoid dynamic amplification.

6.4   MATERIAL MODELING

6.4.1   Reinforcement

The material model used for the reinforcing bars was a piecewise linear plasticity model (MAT_PIECEWISE_LINEAR_PLASTICITY in LS-DYNA). In this model, effective stress versus plastic strain curves were defined, along with a plastic strain to failure. Since fracture of reinforcing bars was not observed during the experiments, failure and erosion of beam elements representing reinforcing bars was not considered. For the two sizes of reinforcing bars used in the test specimens (No. 4 and No. 8 bars), the material model parameters were developed based on the engineering stress-strain curves obtained from standard tensile tests of the reinforcing bars used in the test specimens. Figure 4.6 shows the engineering stress-strain curves for the two bar sizes considered in the study (see Chapter 4).

For each reinforcing bar size, the engineering stress-strain curves shown in Figure 4.6 were averaged and then converted into the true stress versus effective plastic strain curve. The resulting true stress versus effective plastic strain relationships used in the analysis are presented in Figure 6.2.
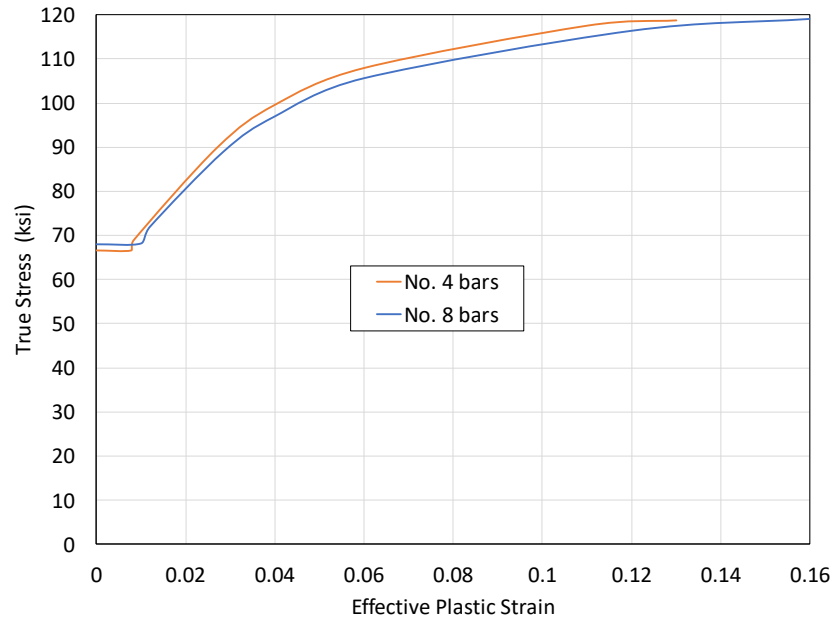
Figure 6.2. True stress versus effective plastic strain curves for No. 4 and No. 8 reinforcing bars

6.4.2 Concrete

For the solid elements used in the models, a continuous surface cap model (MAT_CSCM_CONCRETE or MAT_159 in LS-DYNA) was used as the material model for concrete. In this model, a smooth and continuous intersection is formulated between the failure surface and the hardening cap. The main features of the model are isotropic constitutive equations, a yield surface formulated in terms of three stress invariants with translation for pre-peak hardening, a hardening cap that expands and contracts, and damage-based softening with erosion and modulus reduction. This model can capture confinement effects and softening (post-peak) behavior both in tension and compression. By using a regulation technique, the model can achieve convergent softening behavior with reasonable mesh refinement. Shear behavior of the concrete material is modeled explicitly by the model. More details about this model can be found in Murray (2007) and Murray *et al*. (2007).

To demonstrate the capability of the concrete model to account for confinement effects, a single element example is shown in Figure 6.3. As shown, loading and boundary conditions were imposed to simulate a lateral confinement to the concrete solid element. The element was pushed downward by applying a controlled displacement to the top four nodes. Stress-strain curves were developed for the cases with zero and with 150 psi confinement pressure. Figure 6.3 shows the effect of confinement on the compressive strength of concrete.
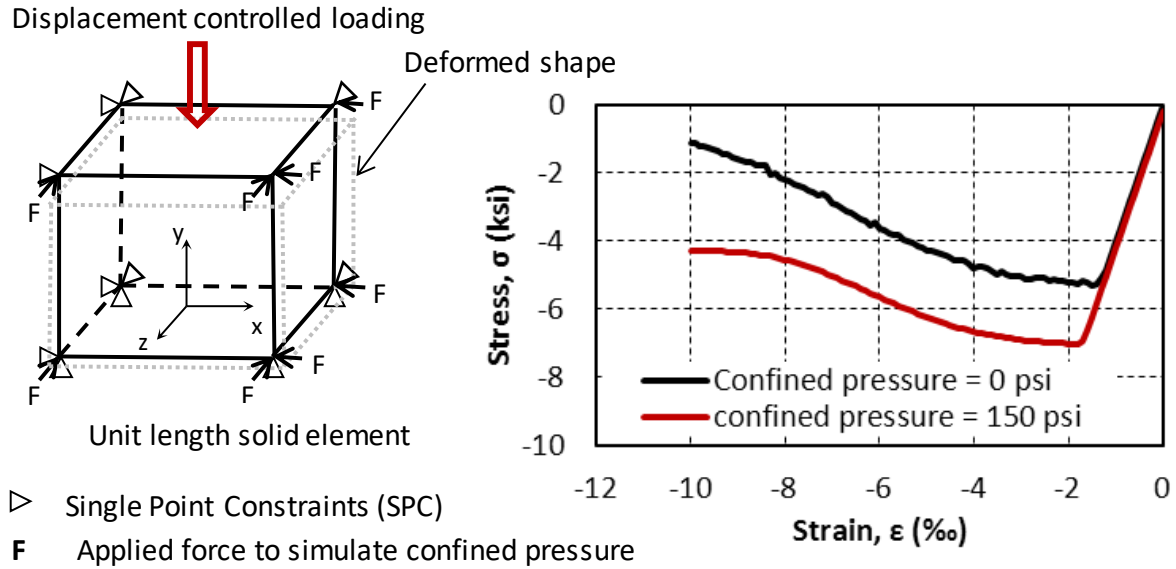
Figure 6.3. Compressive stress-strain curves of concrete with and without confinement

An output of the analysis using this model is a damage index that ranges from zero to one, which indicates the level of concrete damage calculated by the model. A damage index of zero indicates no damage, implying that concrete strength and stiffness are those originally specified. On the other hand, a damage index of one signifies maximum damage, in which the concrete strength and stiffness are reduced to zero. Elements may be eroded when the damage index exceeds 0.99, but element erosion was not considered in the analyses reported herein as this might result in numerical difficulties.

6.4.3 Bond-Slip Effects

The bond-slip effect is an important feature that needs to be considered in developing the computational model, especially for beams with spliced tension reinforcement. If bond-slip is neglected, the model cannot capture the bond failure mode observed in the experiments. For the detailed models used herein, bond-slip behavior between the solid elements representing concrete and the beam elements representing reinforcing bars was defined using the CONSTRAINED_BEAM_IN_SOLID card wherein a user-provided subroutine was developed to calculate the axial shear force based on the slip between reinforcing bar nodes and concrete solid elements. The bond-slip relationship used in this study was based on the local bond stress–slip model for ribbed bars presented in Section 6.1.1 in the *fib* Model Code (2010). The *fib* Model Code was used instead of the ACI 318-19 provisions since the *fib* Model Code provided a local bond-slip model which was not available in the ACI code provisions.

For development of the bond stress-slip relationship, column 6 of Table 6.1-1 of *fib* (2010) for the splitting case, rather than pull-out case was considered. Bond failure may occur in either splitting or pull-out failure modes, with the splitting failure mode being weaker and less ductile. In addition, the local bond-slip model developed herein considers "all other bond conditions" since the beams did not qualify for the "good bond condition" as defined in Section 6.1.3.2 of *fib* Model Code (2010). For this case, the bond-slip model used in this study is shown in Figure 6.4.
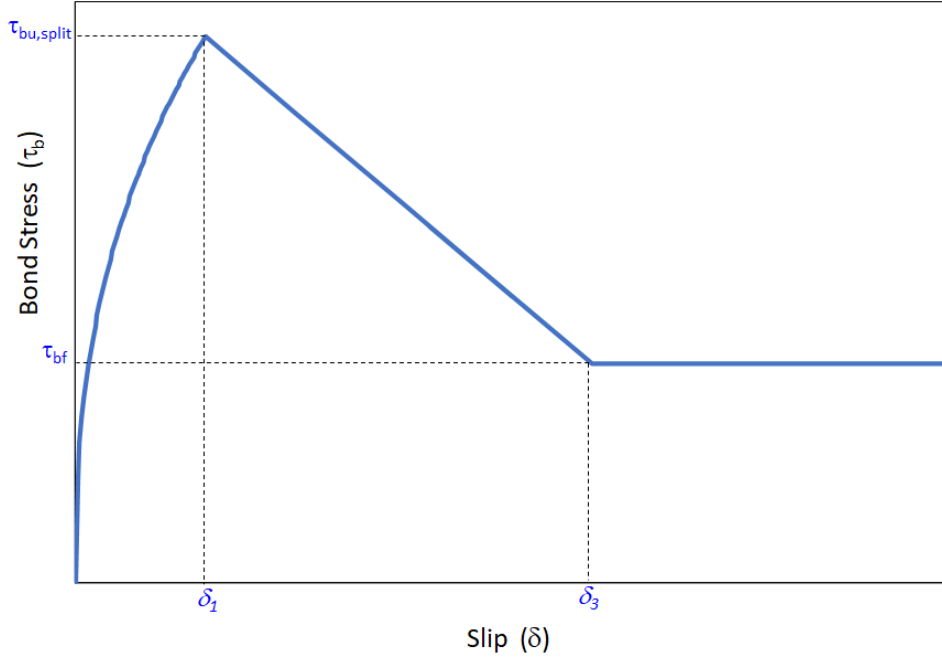
Figure 6.4. Local bond-slip model based on *fib* Model Code (2010)

For the initial, ascending portion of the bond-slip model, the bond stress, τ_b, up to the peak splitting bond resistance, $\tau_{bu,split}$, is calculated as a function of the slip, δ, as:

$$\tau_b = \tau_{bmax} \left(\frac{\delta}{\delta_1}\right)^{0.4} \tag{6.1}$$

Where the maximum value of bond stress, τ_{bmax}, (in N/mm^2) is calculated as a function of the mean cylinder concrete compressive strength in N/mm^2, f_{cm}, as:

$$\tau_{bmax} = 1.25 \sqrt{f_{cm}} \tag{6.2}$$

Note that Equations 6.2 and 6.3 are presented in metric units (N and mm) to be consistent with the *fib* Model Code (2010). The peak local bond resistance in the presence of confining stirrups, $\tau_{bu,split}$, is calculated as:

$$\tau_{bu,split} = 0.7 \times 6.5 \left(\frac{f_{cm}}{25}\right)^{0.25} \left(\frac{25}{d_b}\right)^{0.2} \left[\left(\frac{c_{min}}{d_b}\right)^{0.33} \left(\frac{c_{max}}{c_{min}}\right)^{0.1} + k_m K_{tr}\right] \tag{6.3}$$

where d_b is the bar diameter in mm, $c_{min} = min\left\{\frac{c_s}{2}, c_x, c_y\right\}$, $c_{max} = max\left\{\frac{c_s}{2}, c_x\right\}$, and k_m is an empirical factor that ranges between 0 and 12, and represents the efficiency of confinement from transverse reinforcement. For the bottom reinforcing bars inside the beams in this study, k_m was set equal to 6 (see *fib* Model Code 2010 for details). Dimensions c_s, c_x, c_y are shown in Figure 6.5. K_{tr} is the ratio of the density of transverse reinforcement to the anchored or lapped bars, and is equal to:

$$K_{tr} = \frac{n_t A_{st}}{n\, d_b\, s} \leq 0.05 \tag{6.4}$$

where n_t is the number of legs of confining reinforcement (stirrups) crossing a potential splitting failure surface at a section, A_{st} is the cross-sectional area of one leg of a confining bar, s is the longitudinal spacing of confining reinforcement, and n is the number of anchored bars or pairs of lapped bars in the potential splitting surface. Note the difference between the transverse reinforcement index, K_{tr}, shown in Section 1.1.1 based on the ACI 318 provisions and the ratio of the density of transverse reinforcement to the anchored or lapped bars, K_{tr}, shown in Equation (6.4) based on the *fib* Model Code. Note also that while the development of the maximum allowable bond stress, u, shown in Section 1.1.1 based on ACI 318-19 is different from the peak local bond resistance, $\tau_{bu,split}$, shown in Equation (6.3) based on the *fib* Model Code, they both yield close estimates of the bond strength.

$$c_{min} = min\ (c_s/2,\ c_x,\ c_y)$$
$$c_{max} = max\ (c_s/2,\ c_x)$$
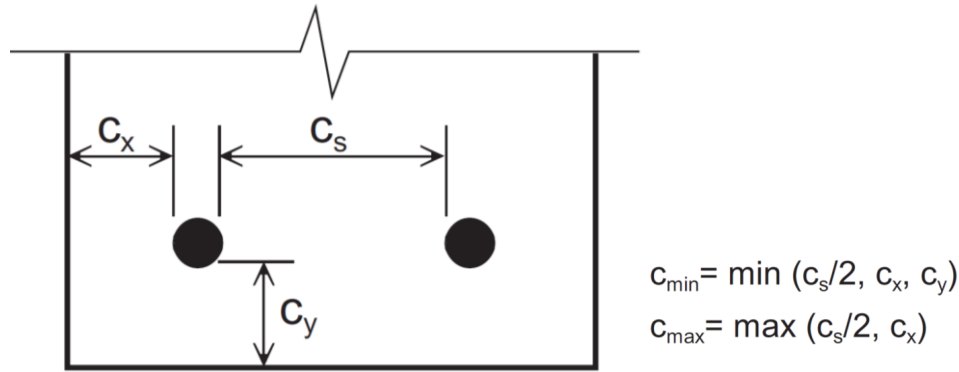
Figure 6.5. Definition of bar spacing and cover based on *fib* Model Code (2010)

Slip δ_1 is calculated based on Equation (6.1) as 1.8 mm multiplied by $\left(\frac{\tau_{bu,split}}{\tau_{bmax}}\right)^{(1/0.4)}$. In Figure 6.4, $\tau_{bf} = 0.4\ \tau_{bu,split}$ and slip δ_3 is set equal to one half of the clear distance between the ribs of the reinforcing bars.

For the beams considered in this computational study, the bond stresses shown above are to be multiplied by a modification factor to account for the possibility of reinforcing bar yielding (*fib* Model Code 2010). This yielding modification factor, Ω_y, is calculated by:

$$\Omega_y = 1.0 \qquad\qquad\qquad\qquad\qquad \text{for } \varepsilon_s < \varepsilon_{sy}$$

$$\Omega_y = 1.0 - 0.85(1 - e^{-5c}) \qquad\qquad \text{for } \varepsilon_{sy} < \varepsilon_s < \varepsilon_{su}$$

where ε_s is the axial strain in the reinforcing bar and ε_{sy} and ε_{su} signify, respectively, the yield and ultimate tensile strains of the reinforcing bar steel. In the above equations, $c = a^b$, where $a = (\varepsilon_s - \varepsilon_{sy})/(\varepsilon_{su} - \varepsilon_{sy})$, and $b = \left[2 - (f_{tm}/f_{ym)}\right]^2$. f_{tm} and f_{ym} are the mean values of the tensile and yield strength of the reinforcing bars, respectively.

An algorithm with the above bond-slip model was developed in the FORTRAN programming language and implemented into the LS-DYNA file *dyn21.F*. The file was then compiled and linked to the software to generate an executable file that was used for the beam analyses.

6.5   MODELING OF ASR EFFECTS

This section describes the development of a numerical model to characterize the behavior of ASR-affected concrete structures. A new module was added to the LS-DYNA software package to account for ASR-induced expansion and degradation. For that purpose, the source code of the continuous surface cap model (MAT_CSCM_CONCRETE or MAT_159 in LS-DYNA) was obtained from the Livermore Software Technology Corporation (LSTC), the developer of LS-DYNA. Description of the MAT_159 material model can be found in Murray (2007) and Murray *et al*. (2007). The source code for the concrete material model was modified by adding the features outlined in the next subsections. The additions were based on the work of Saouma and Perotti (2006) and Saouma (2014). A flowchart of the additions to the source code is shown in Figure 6.6. The ASR-induced strain is treated as the initial strain which is uncoupled from the material constitutive model itself. As the flowchart shows, the ASR kinetics in rate form, which described ASR expansion as function of time, was used as an input. Then, the program followed the following steps: (1) calculate the volumetric strain increment at the given time step, (2) call the added subroutines to determine the principal stresses and directions and calculate expansion weights in each direction, (3) distribute ASR strain increment consistent with each principal direction and their calculated weights, (4) transform the principal ASR strain increment back to the original coordinate system and update the total ASR strain and current time, and (5) apply material degradation models. The primary steps in the program are as follows:

```
┌─────────────────────────────────────┐
│  Read ASR Kinetics (or the 'S' curve) from │
│            input file                │
└─────────────────────────────────────┘
                  │
                  ▼
┌─────────────────────────────────────┐
│  Initialization: material constants; ASR │
│  beginning/terminating time; target  │
│  expansion, material degradation, etc. │
└─────────────────────────────────────┘
                  │
                  ▼
┌─────────────────────────────────────┐
│  Calculate ASR volumetric strain incremental │
│            ε̇ᵥᴬˢᴿ(t,T)                │
└─────────────────────────────────────┘
                  │
                  ▼
┌─────────────────────────────────────┐
│  Calculate principal stresses and directions │
└─────────────────────────────────────┘
                  │
                  ▼
┌─────────────────────────────────────┐
│  Calculate weights on principal directions │
└─────────────────────────────────────┘
                  │
                  ▼
┌─────────────────────────────────────┐
│  Calculate ASR strain incremental    │
│            ε̇ᵢⱼᴬˢᴿ(t,T)               │
└─────────────────────────────────────┘
                  │
                  ▼
┌─────────────────────────────────────┐
│  Calculate ASR-induced degradation in │
│       stiffness and strength         │
└─────────────────────────────────────┘
                  │
                  ▼
┌─────────────────────────────────────┐
│  Update total ASR strain and current material │
│            properties                │
└─────────────────────────────────────┘
```

The flowchart boxes are:

- Read ASR Kinetics (or the 'S' curve) from input file
- Initialization: material constants; ASR beginning/terminating time; target expansion, material degradation, etc.
- Calculate ASR volumetric strain incremental $\dot{\varepsilon}_V^{ASR}(t,T)$
- Calculate principal stresses and directions
- Calculate weights on principal directions
- Calculate ASR strain incremental $\dot{\varepsilon}_{ij}^{ASR}(t,T)$
- Calculate ASR-induced degradation in stiffness and strength
- Update total ASR strain and current material properties

Figure 6.6. Flowchart of ASR-induced strain and degradation calculations

6.5.1 ASR Expansion Kinetics

The expression used to describe the evolution of the unconfined ASR expansion with time in the Saouma-Perotti model was based on Larive (1998), where an S-curve similar to that shown in Figure 6.7 was proposed. The figure shows the normalized ASR-induced volumetric expansion (solid line) along with the rate of that expansion (dashed line). While the actual ASR expansion takes years or decades to develop (and months for accelerated testing similar to what was done in this and other studies), scaled time was used in the analyses until a target expansion was reached. As is shown in Section 6.7, the scaled (analysis) time to reach the target expansion was 2 s. It should be noted that no attempt was made in this study to calibrate the S-curve shown in Figure 6.7 against expansion data from the beam specimens because changing the shape of the S-curve (as long as the same target expansion value is reached) should not impact the response of the structure at the end of the ASR expansion.
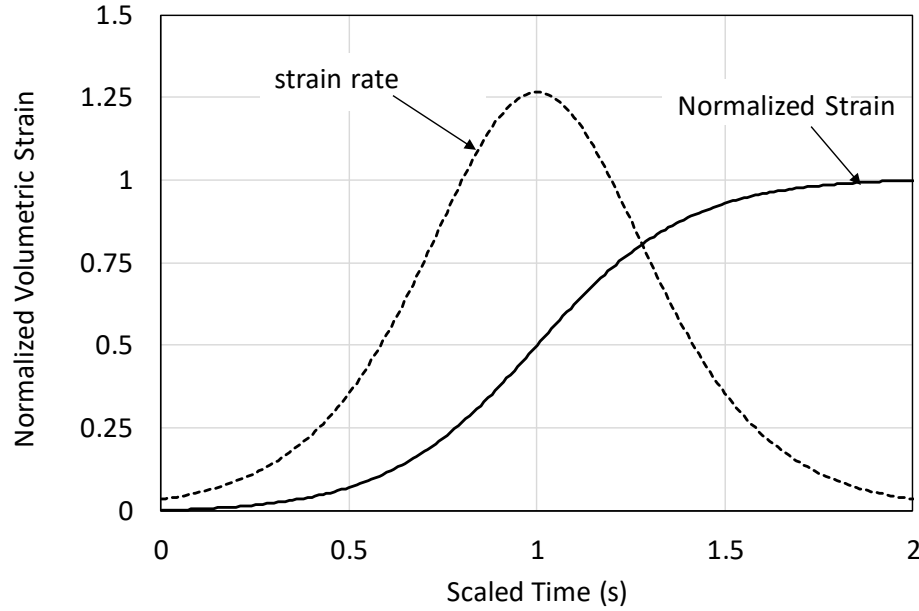
Figure 6.7. ASR expansion kinetics

6.5.2   Principal Stresses and Directions and Weights for Distribution of Expansion

Saouma and Perotti (2006) and Saouma (2014) developed a model that accounted for the anisotropy of the ASR expansion through the different weights assigned to each of the three principal directions. They showed, based on the work of Larive (1998) and Multon (2003), that when the ASR expansion is constrained by compression, the expansion is redirected in other less-constrained principal directions. In their model, this was accomplished by assigning weights to each of the three principal directions; relatively high compressive stresses inhibit ASR expansion due to the formation of microcracks or macrocracks that absorb the expanding gel; high compressive hydrostatic stresses slow down the reaction; triaxial compressive state of stress reduces but does not eliminate expansion.

The determination of the weights for concrete confined uniaxially, biaxially, and triaxially was presented in Saouma and Perotti (2006) and was implemented in the material model for MAT_159. Once developed in LS-DYNA, a benchmark test was carried out to verify the accuracy of the developed model in calculating strain weights. The benchmark problem used a single element similar to that shown in Figure 6.3. The element was subjected to the ASR expansion shown in Figure 6.7 with an ultimate volumetric free expansion of 0.005 and several analyses were performed. In the analyses, σ_1, σ_2, and σ_3 were the principal stresses (for convenience, assuming the current stresses were in the principal directions, i.e., the transformation matrix was an identity matrix). Different combinations of the three principal stresses were used and the expansions in the three orthogonal directions were calculated. Figure 6.8 presents two of these combinations. The figure shows the effect of the state of stress on apportioning the strains in the three orthogonal directions. The results in Figure 6.8 were consistent with those reported in Saouma (2014).
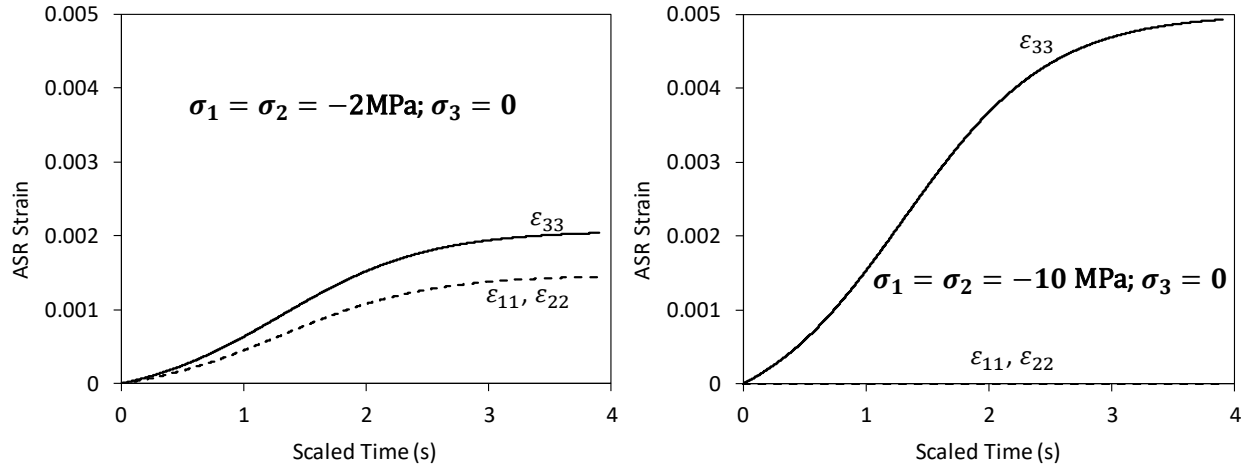
Figure 6.8. Benchmark testing of strain distribution in three orthogonal directions

6.5.3 ASR-Induced Stiffness and Strength Degradation

Degradation of the modulus of elasticity and tensile strength due to ASR were included in the model. The model, though, did not consider changes in the compressive strength of concrete due to ASR. As shown in Section 6.7.1, changes in the compressive strength did not have significant impact on the response of ASR-affected beams used in this study.

Degradation of the modulus of elasticity was considered by making the modulus ASR expansion-dependent. At first, linear degradation of the elastic modulus with ASR expansion, similar to that proposed by Saouma (2014), was used. A single element similar to that shown in Figure 6.3 was used where ASR expansion was applied, employing a 1/3 reduction in the modulus at the end of the ASR expansion. This was followed by applying uniaxial compression in the element under displacement control until loss of capacity was observed. Figure 6.9 shows the compressive stress-strain response of the element: (1) assuming no reduction in the elastic modulus and (2) assuming the loss of 1/3 of the modulus. These results show that the model accurately captured the ASR-induced reduction in the elastic modulus. For the analyses reported in Section 6.7, the degradation model was based on the measured modulus of elasticity for concrete used in the experimental study, see Figure 4.2. The model, shown in Figure 6.10, assumed a linear degradation of the modulus between unconfined ASR linear expansion of zero to 0.075 % where the modulus lost 50 % of its value. For expansions larger than 0.075 %, the degraded modulus of elasticity remained constant.
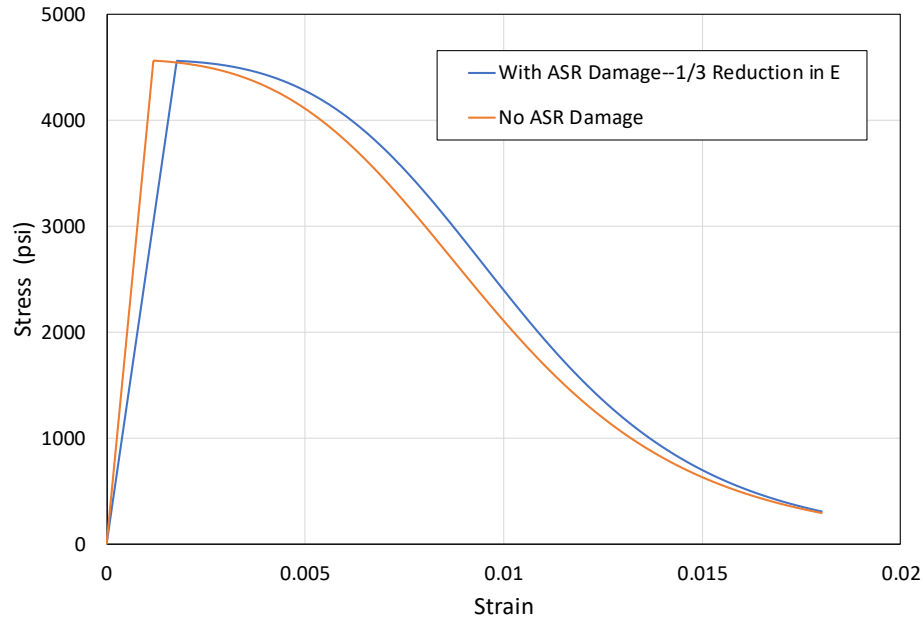
Figure 6.9. Compressive stress-strain relationship with and without degradation of the modulus of elasticity
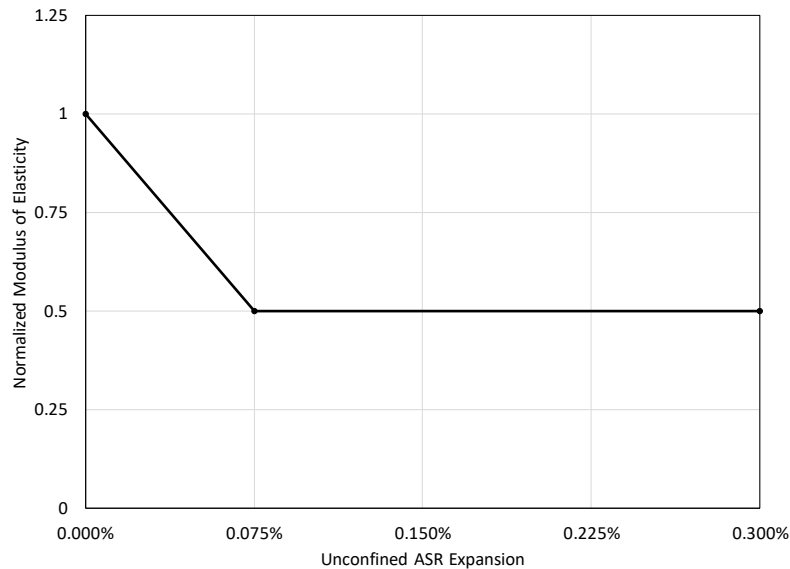
Figure 6.10. Degradation model for the modulus of elasticity

Degradation of the tensile strength was considered by applying a reduction in the tensile strength as pre-damage to concrete, a utility of the original MAT_159 model (Murray, 2007). It was found, however, that this reduction did not significantly impact the results of the beam analyses in Section 6.7. On the contrary, inclusion of the tensile strength reduction resulted in a measurable impact on the analysis runtime, and as a result, it was ignored Additionally, it was found in this test program that splitting tensile strength was least reduced compared with compressive and elastic modulus of ASR-affected concrete.

6.6   ANALYSIS OF NON-REACTIVE BEAMS

The analyses reported in this section simulated the four-point bending test without ASR effects. In these analyses, the nodes at top of the beam, where load was applied, were pushed down under displacement control until failure occurred. Displacements were increased at a slow rate to ensure a static response (no dynamic amplification), similar to the test conditions.

6.6.1   Beam 18

Figure 6.11 shows an elevation view of non-reactive Beam 18. The beam had continuous bottom reinforcement and an 8 in stirrup spacing in the constant moment region, resulting in a K_{tr}/d_b ratio of 1.0. During the four-point bending test, the beam exhibited ductile behavior before failure, which was characterized by yielding of the tensile reinforcement, followed by compressive failure of the concrete in the compression zone.
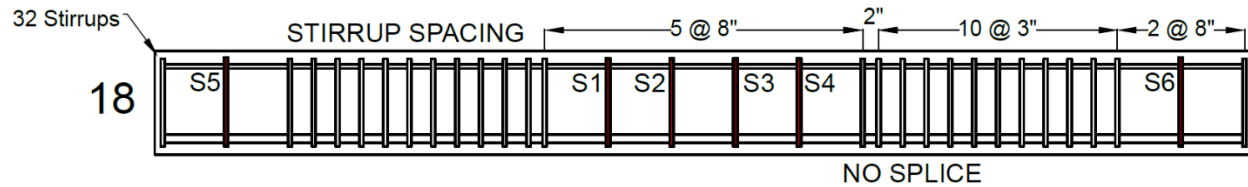
Figure 6.11. Elevation of Beam 18

Two analyses were performed using the finite element model of Beam 18. In the first, the reinforcing bar nodes were merged with those of the surrounding concrete solid elements. The other used the bond-slip model described in Section 6.4.3. The total applied load versus midspan deflection is plotted in Figure 6.12 for the two analyses, along with the load-deflection curve measured during the experiment. The figure shows only minor differences between the analysis using the bond-slip model and that using the merged-nodes assumption (less than a 5 % difference in load for a given displacement value). This result was expected since for beams with continuous tensile bars, bond failure was not a significant consideration. The analysis results showed a higher beam stiffness throughout the initial phase of the response than did the experimental results, and both analyses overestimated the peak load by about 5 %. For the range of displacements considered in the analyses, the models did not capture the reduction in applied load due to concrete crushing at a midspan deflection of about 1.1 in. Figure 6.13 shows the forces in the tensile reinforcement based on the strain measurements on the bottom bars during the experiment (grey lines). For the rest of this chapter, the reinforcing bar force in the experiment was calculated as the measured strain increment during the tests multiplied by the slope of the average measured stress-strain curve from the standard bar tests (see Section 4.2) and area of the bar; values of the tensile force larger than the yield force should, therefore, be disregarded. Also shown in Figure 6.13 is the predicted force in the tensile reinforcement based on the analysis using the bond-slip model (red line). Figure 6.13 shows that, when compared with the experimental results, the model was capable of accurately capturing the axial force development in the reinforcement.
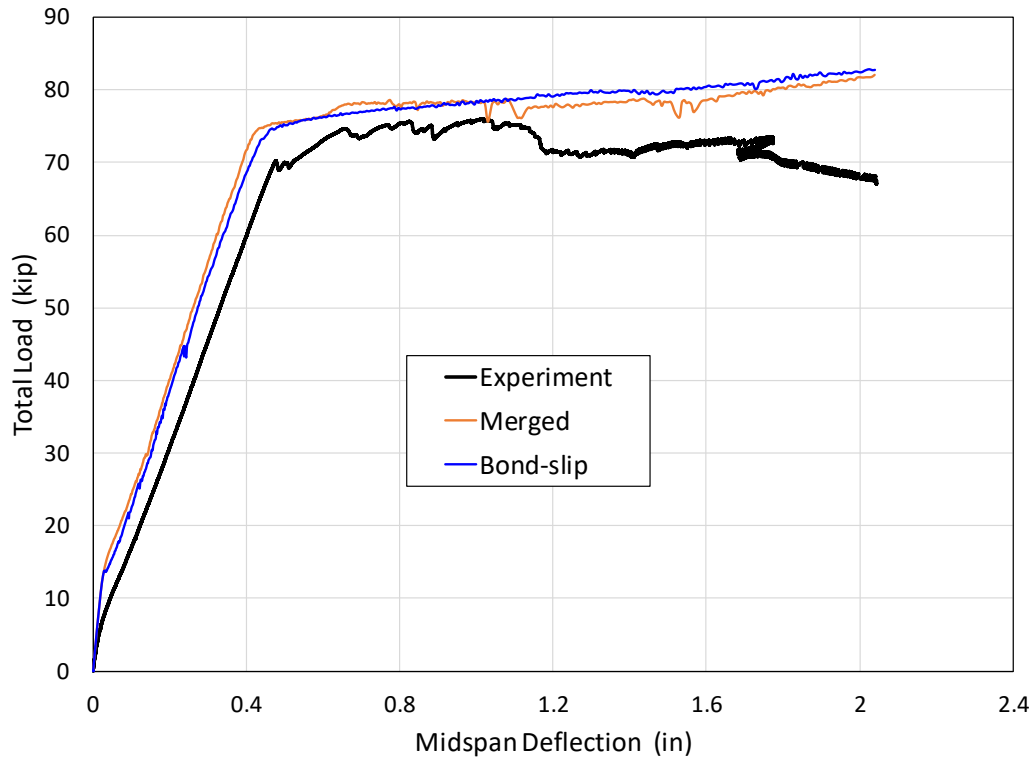
Figure 6.12. Total applied load versus midspan deflection of Beam 18
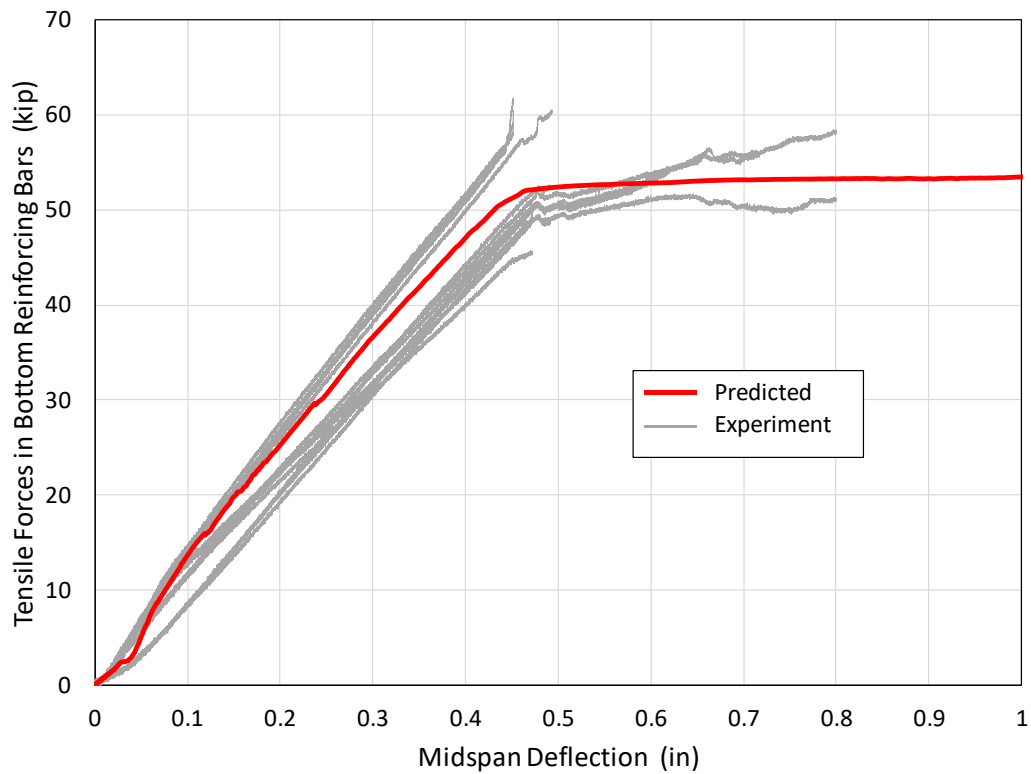
Figure 6.13. Predicted and measured axial forces in tensile reinforcement versus midspan deflection of Beam 18

Figure 6.14(a) shows the deflected shape of the beam and predicted concrete damage at different levels of midspan defection. As indicated in Section 6.4.2, damage indices of zero and one signify no damage and maximum damage, respectively. The plots show an increasing level of damage with increased deflections. Figure 6.14(b) shows the observed damage of the beam at the end of the experiment. The comparison between Figure 6.14(a) and Figure 6.14(b) indicates that the model captured the flexural cracking of concrete in the tension zone but did not capture the crushing failure of concrete in the compression zone at beam top.

(a)

(b)
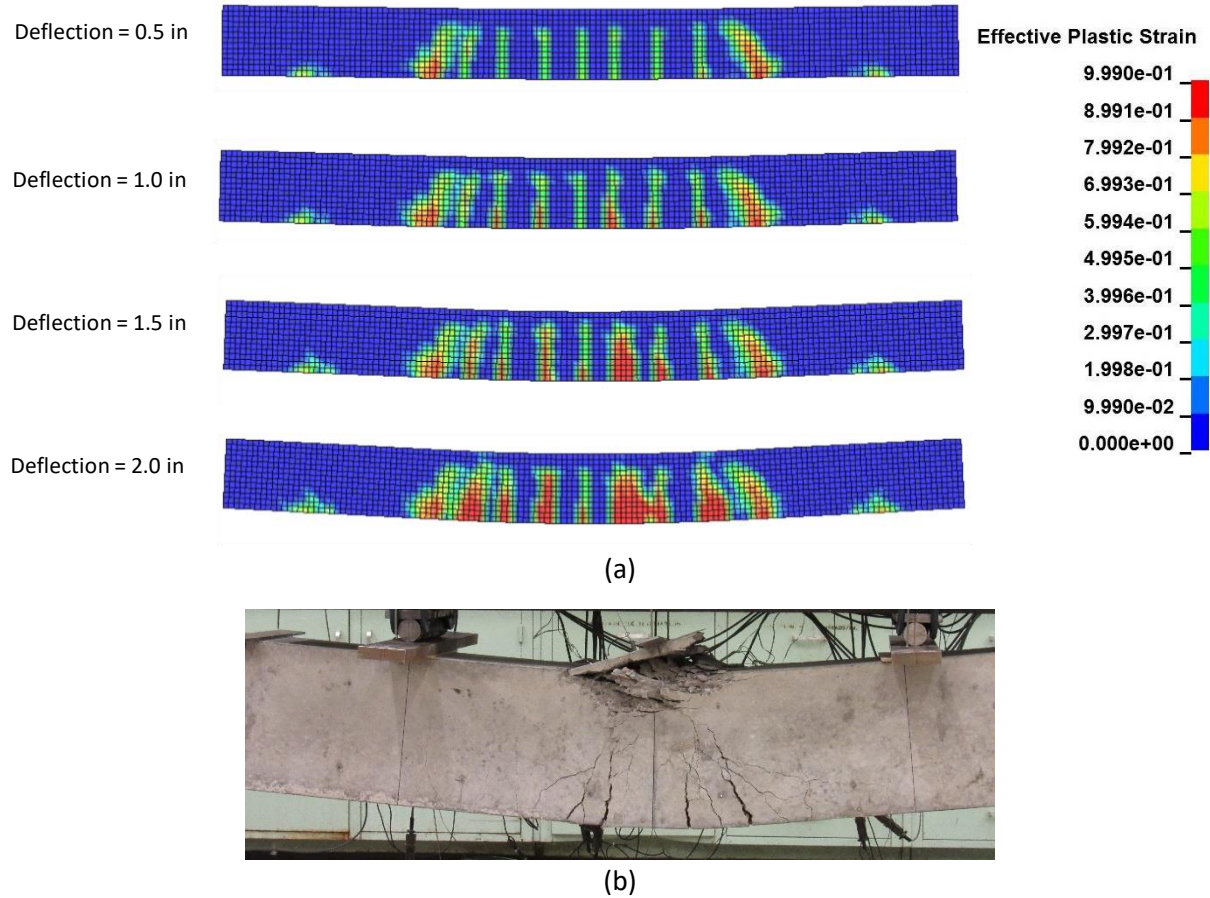
Figure 6.14. (a) Predicted concrete damage at various levels of deformation and (b) observed damage at end of experiment of Beam 18

Figure 6.15 depicts the development of axial forces in the top (compressive) and bottom (tensile) reinforcement as a function of the midspan deflection as predicted by the computational model. Figure 6.16 shows the predicted axial forces in the top and bottom reinforcement along with concrete stresses at a midspan deflection of 0.5 in, corresponding to a midspan moment of 1074 kip-in and yielding of the tensile reinforcement. This figure shows that, while the concrete stresses were larger than the compressive strength of concrete (4500 psi), concrete crushing was not captured by the model. This could be attributed to confinement effects provided by the stirrups in the numerical model. The moment

predicted by the model at a midspan deflection of 0.5 in, was within 2 % of the value of 1054 kip-in computed using section analysis in accordance ACI 318-19 and the measured concrete and steel material properties. The equilibrium sketch to the left of Figure 6.16 was based on the computational model results and is consistent with the section analysis of the beam in accordance ACI 318-19.
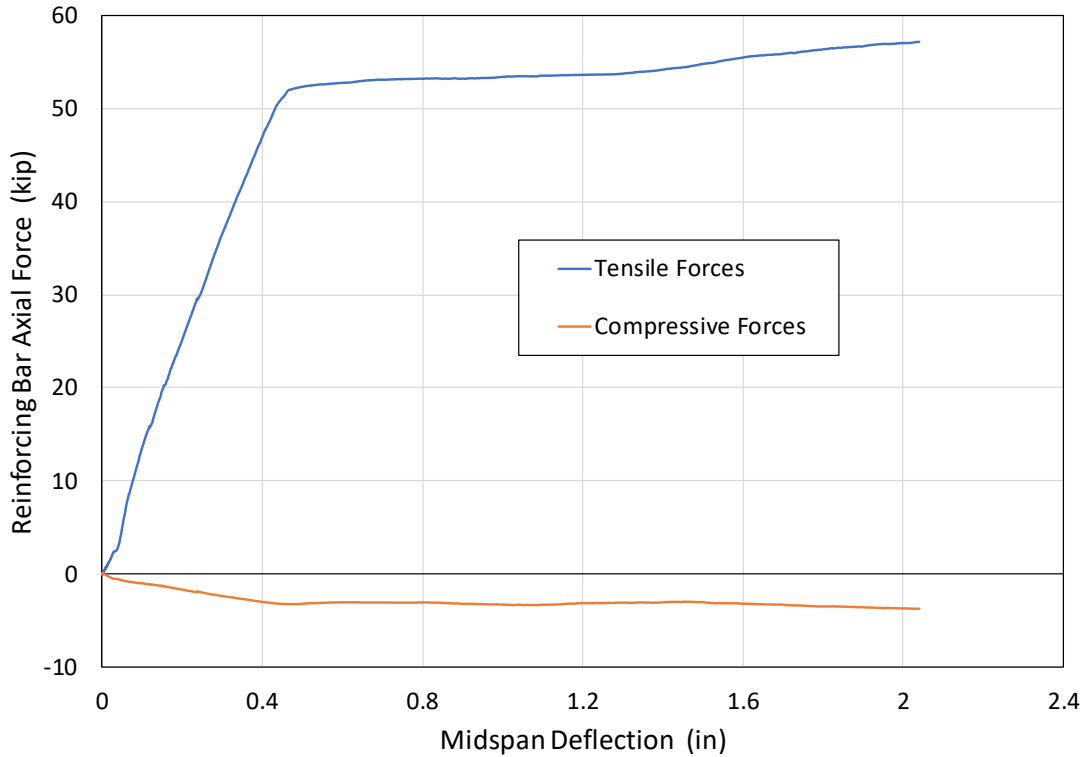
Figure 6.15. Predicted axial forces in top and bottom reinforcement versus midspan deflection of Beam 18
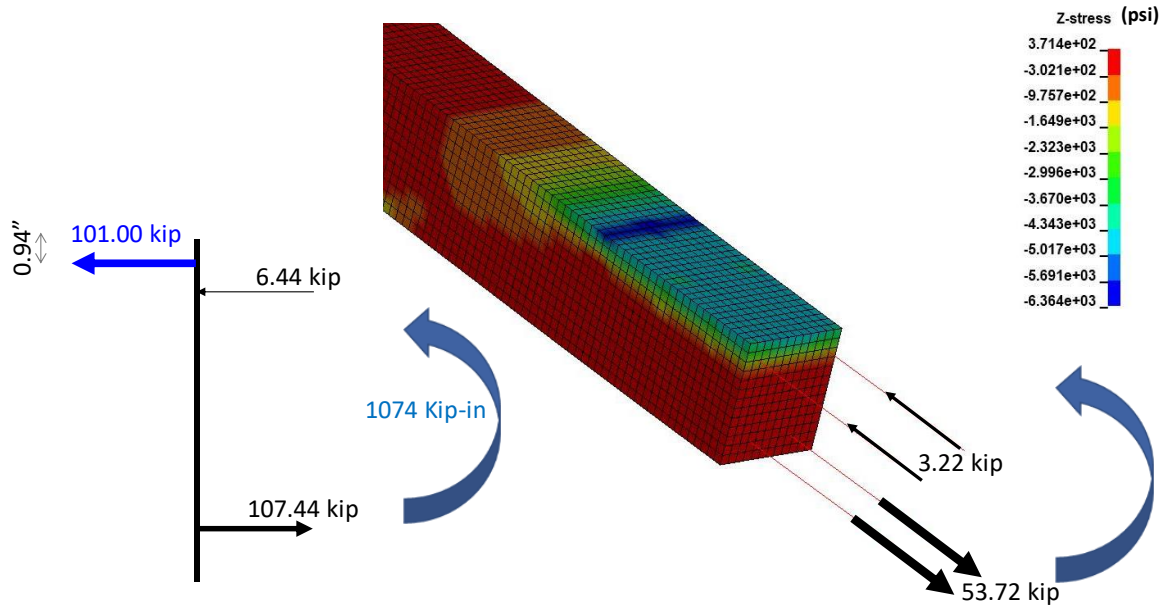
Figure 6.16. Predicted axial forces in top and bottom reinforcement and concrete stresses at midspan deflection of 0.5 in for Beam 18

6.6.2 Beams 11 and 17

Figure 6.17 shows an elevation view of non-reactive Beams 11 and 17. The beams had spliced bottom reinforcement with a splice length of 22 in and an 8 in stirrup spacing in the constant moment region, resulting in both ℓ_s/ℓ_d and K_{tr}/d_b ratios being equal to 1.0. During the four-point bending test, the predominant mode of failure was loss of bond at the bottom, spliced tensile reinforcement.
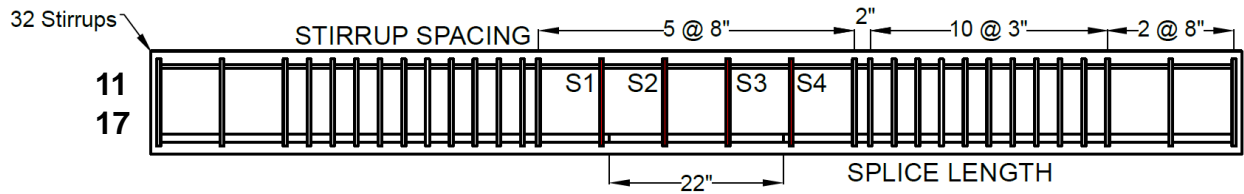
Figure 6.17. Elevation of Beams 11 and 17

Figure 6.18 presents the total applied load versus midspan deflection based on experimental measurements for Beams 11 (black curve) and 18 (blue curve). Additionally, the figure shows load-deflection curves for three different analyses as follows:

The first analysis, designated as Method 0 (green curve in Figure 6.18), used the bond-slip model as described in Section 6.4.3 to characterize the axial bond forces developed along the tensile bars including the spliced region. While the analysis captured well the initial phase of the response, it overestimated the peak load by about 32 % and the corresponding deflection by about 200 %. This indicates that the bond-slip model overestimated the bond strength, especially in the spliced region. This is attributed to the

100

model being based on a bond-slip relationship for a single reinforcing bar embedded in concrete with a certain concrete cover and distance between bars. For spliced tensile bars, however, due to the proximity of the two spliced bars (Figure 6.19), the full bond forces are not expected to be developed between the tensile bars and surrounding concrete. As a result, two methods were proposed and used in the spliced region to reduce the bond strength in the bond-slip relationship described in Section 6.4.3.
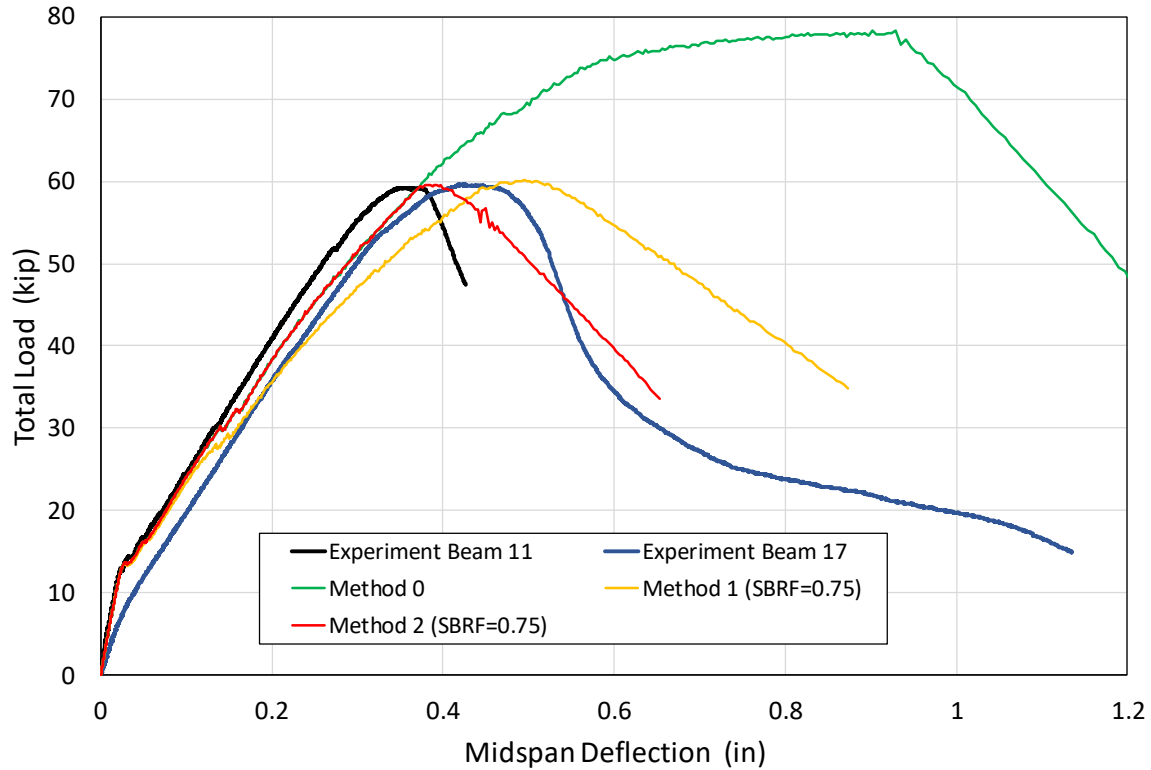
Figure 6.18. Total applied load versus midspan deflection for Beams 11 and 17 using different methods for modeling bond-slip
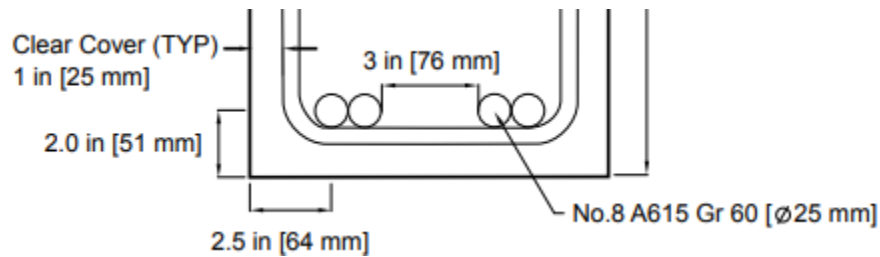
Figure 6.19. Spliced bottom reinforcement in the beam

The first method, Method 1, is shown in Figure 6.20(a). This method modified the bond-slip relationship by multiplying the bond stresses for all slip values by a constant factor (less than unity) labeled splice bond-slip reduction factor (SBRF). This resulted in a reduction in both initial stiffness and bond strength in the splice region as shown in Figure 6.20(a). The second, Method 2, is shown in Figure 6.20(b). The

method reduced only the bond strength by an SBRF and as a result, the initial stiffness was not affected as shown in Figure 6.20(b). In both methods, the reduction was applied only to the beam elements in the spliced region; the rest used the original bond-slip model in Section 6.4.3. A parametric study was carried out to determine the SBRF value that provided the best match with the measured peak load. It was found that for both methods, SBRF of 0.75 provided the best results. The total applied load versus midspan deflection using Method 1 (yellow curve) and Method 2 (red curve) is plotted in Figure 6.18, along with the load-deflection curve measured during the experiment and predicted based on the analysis using Method 0. As Figure 6.18 indicates, Method 1 provided a more flexible response than both experiments (Beams 11 and 17). Method 2, on the other hand, provided better agreement with the measured response. Figure 6.21 provides a cleaner comparison showing the experimental results along with the analysis using Method 2. The predicted peak load based on Method 2 was within 1 % of the measured peak load from the two experiments and the corresponding midspan deflection was in the middle between the two experimental results. In addition, the predicted failure mode of the beam was a loss of bond at the spliced tensile reinforcement, matching the experimental observation. For the rest of this chapter, only Method 2 was used.
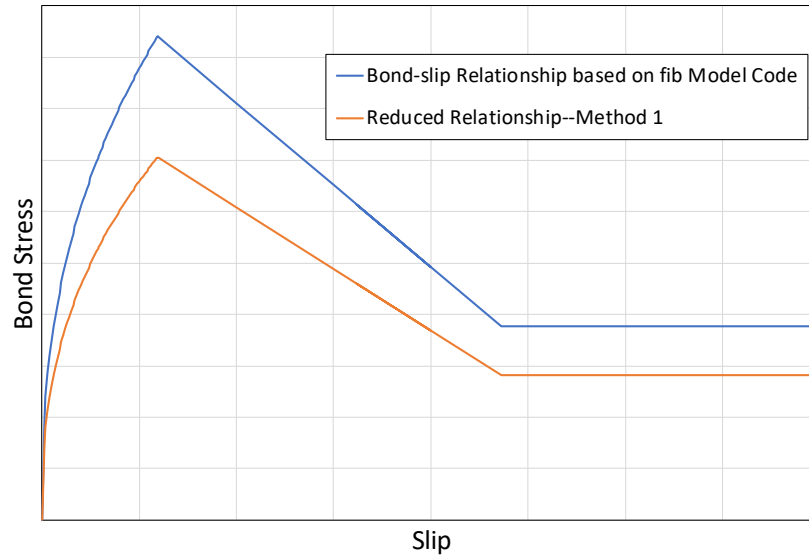
(a)
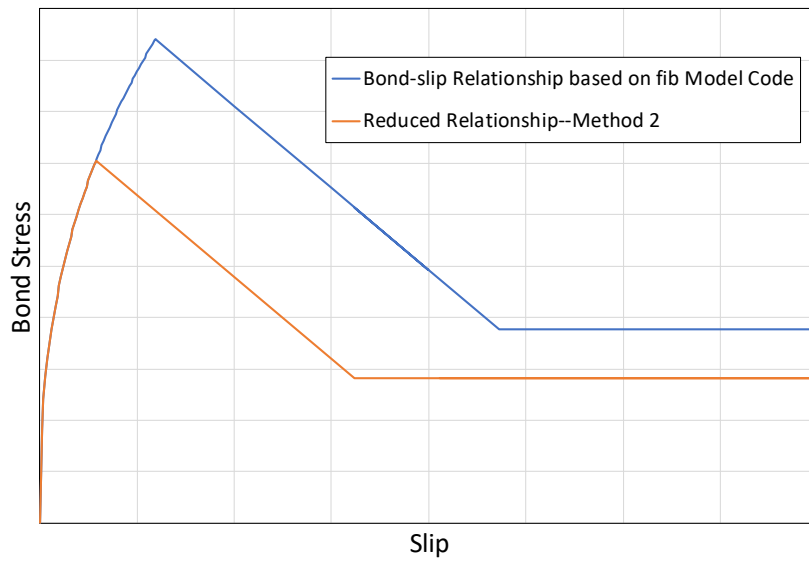
(b)

Figure 6.20. Reduced bond-slip relationships for reinforcing bar splices: (a) Method 1 (reduced bond stress and slip) and (b) Method 2 (reduced slip only)
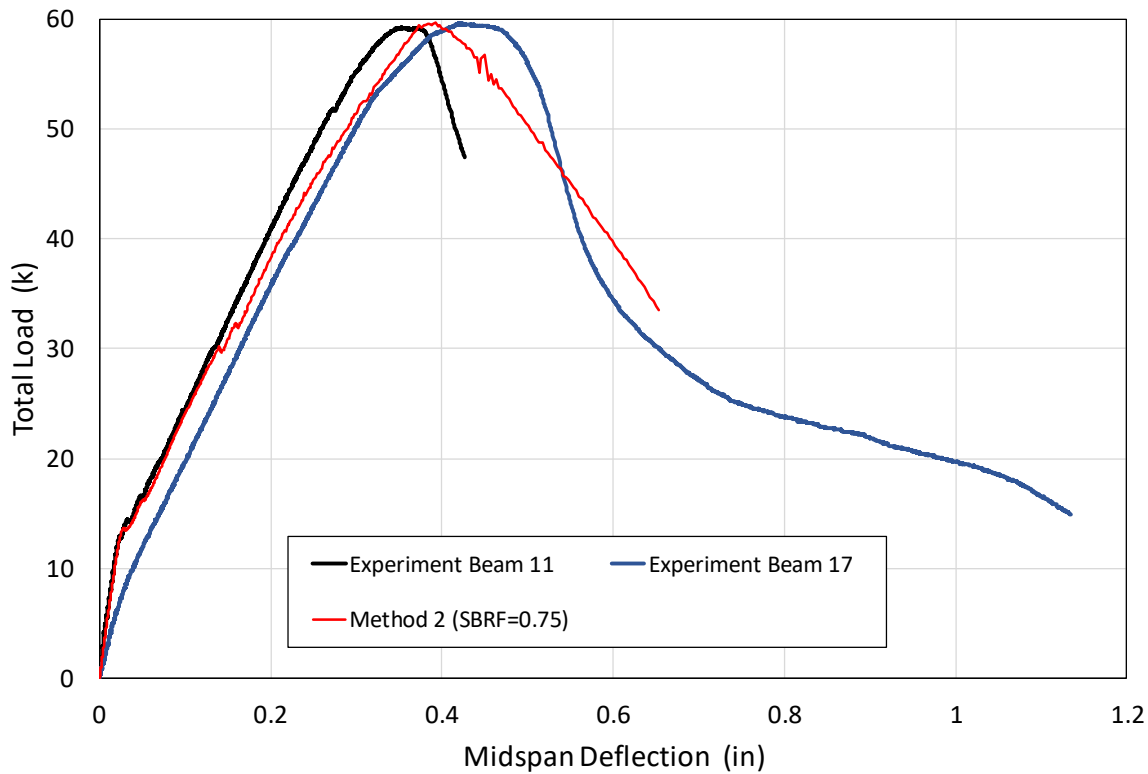
Figure 6.21. Total applied load versus midspan deflection of Beams 11 and 17 using Method 2 for modeling bond-slip in the splice region

Figure 6.22 shows the forces in the tensile reinforcement on the bottom reinforcing bars during the experiment (light blue lines for splice end and light grey lines for mid-splice) for Beam 11 (plot (a)) and Beam 17 (plot (b)). The reinforcing bar forces in the experiment were calculated as shown in Section 6.6.1 based on strain measurements at splice end and at mid-splice. Also shown in Figure 6.22 are the predicted forces in the tensile reinforcement based on the analysis (blue line for splice end and black line for mid-splice). Figure 6.22 shows that, when compared with the experimental results, the model was capable of capturing the axial force development in the reinforcement. Both experimental and computational results show that the strains and forces at splice end were roughly twice those at mid-splice.
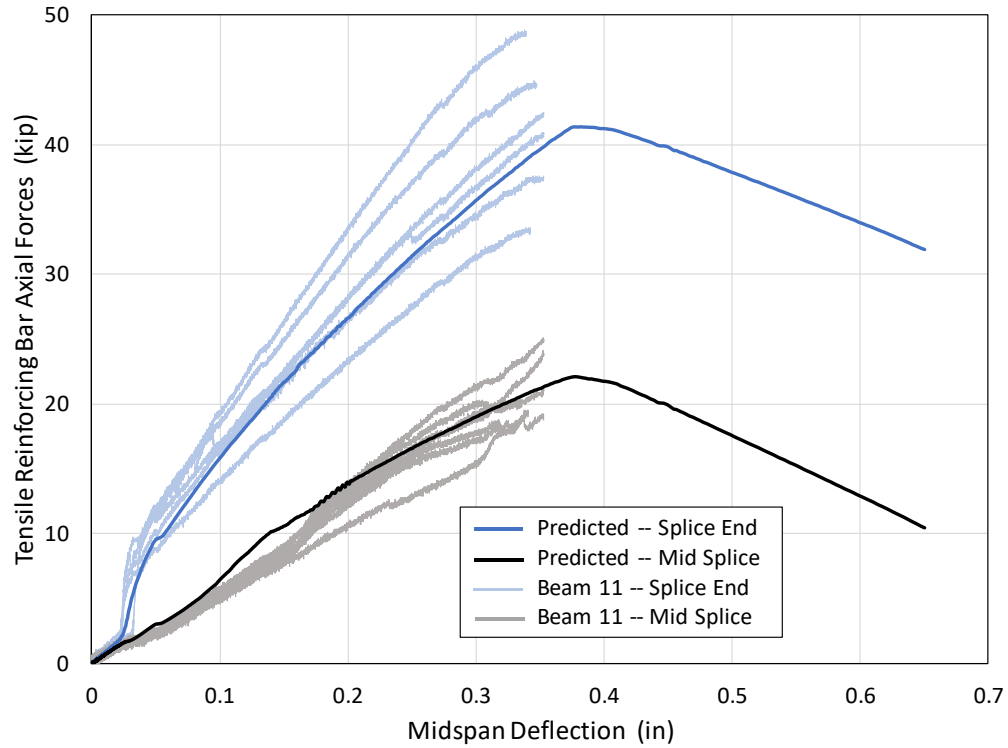
(a)
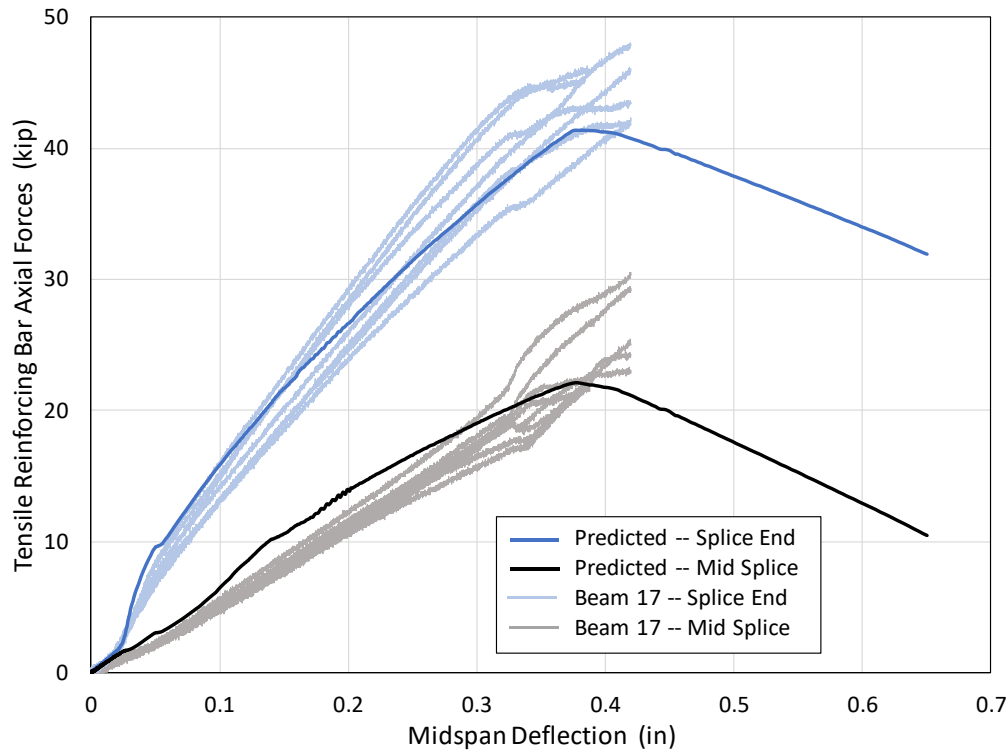
(b)

Figure 6.22. Predicted and measured axial forces in tensile reinforcement versus midspan deflection of (a) Beam 11 and (b) Beam 17

Figure 6.23(a) shows the deflected shape of the beam and predicted concrete cracking at different levels of midspan defection. While the plots show an increasing level of cracking with increased deflections, the cracking was much less extensive than that predicted for Beam 18 with continuous tensile bars. The reason is that Beam 18 experienced increased larger deflections and reinforcing bar yielding that resulted in more concrete damage, while Beams 11 and 17 failed at a smaller load due to loss of bond. Figure 6.23(b) shows the observed damage of Beams 11 and 17 at the end of the experiment. The visual comparison between Figure 6.23(a) and Figure 6.23(b) indicates a reasonable agreement between the experiment and modeling results.

(a)

(b)
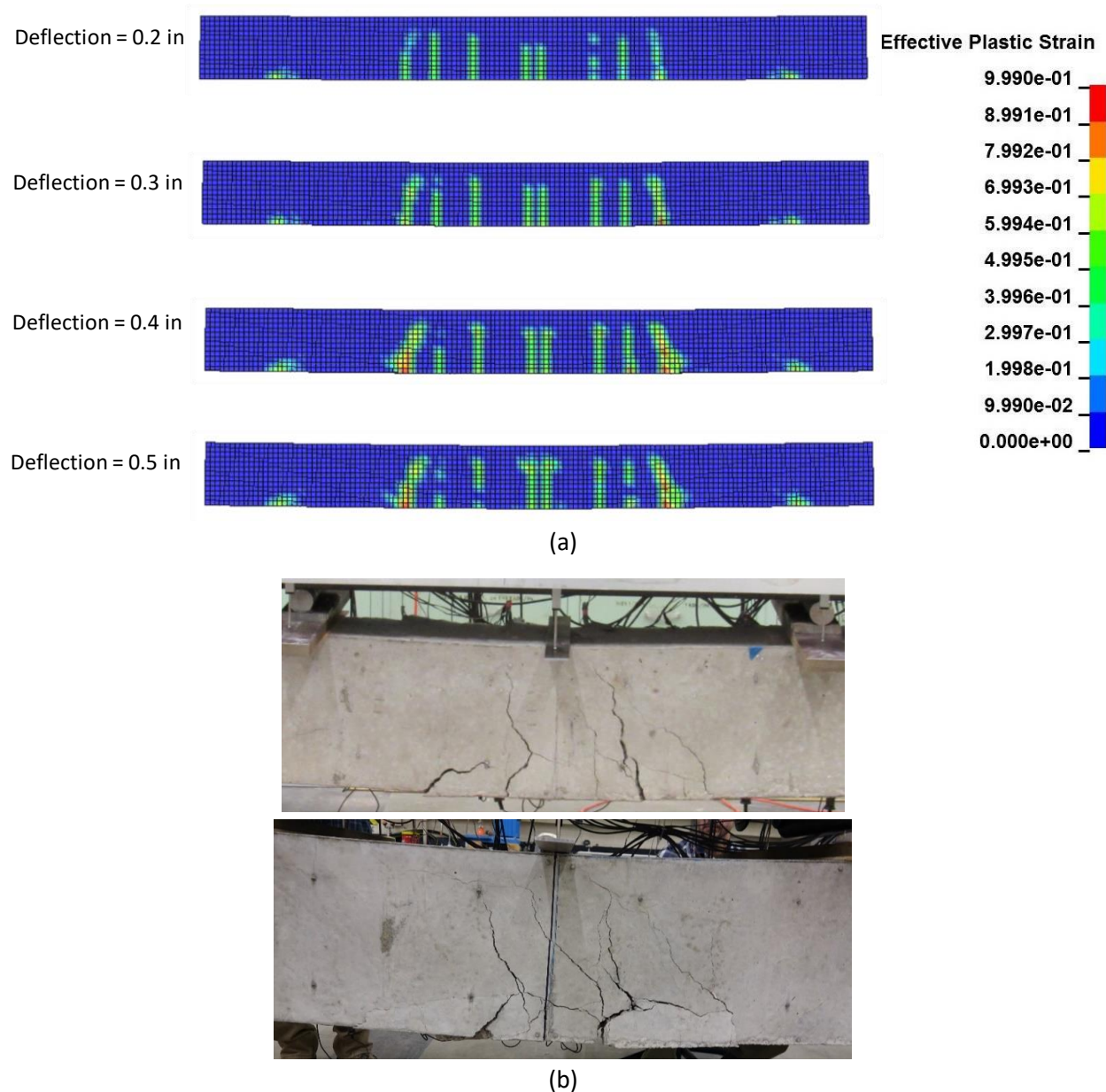
Figure 6.23. (a) Predicted concrete damage at various levels of deformation and (b) observed damage at end of experiment of Beams 11 and 17

Figures 6.24 and 6.25 provide insights into the behavior of the beam prior to bond failure and loss of load carrying capacity. Figure 6.24 shows the predicted axial forces in the top and bottom reinforcement along with concrete stresses at a midspan deflection of 0.39 in, corresponding to the peak load with a midspan moment of 847 kip-in. The equilibrium sketch to the left of Figure 6.25 is based on the computational model results. Figure 6.25 depicts the distribution of axial tensile forces in the bottom, spliced reinforcement along the length of the tensile bars (location zero signifies mid-splice) corresponding to the peak applied load as predicted by the computational model.
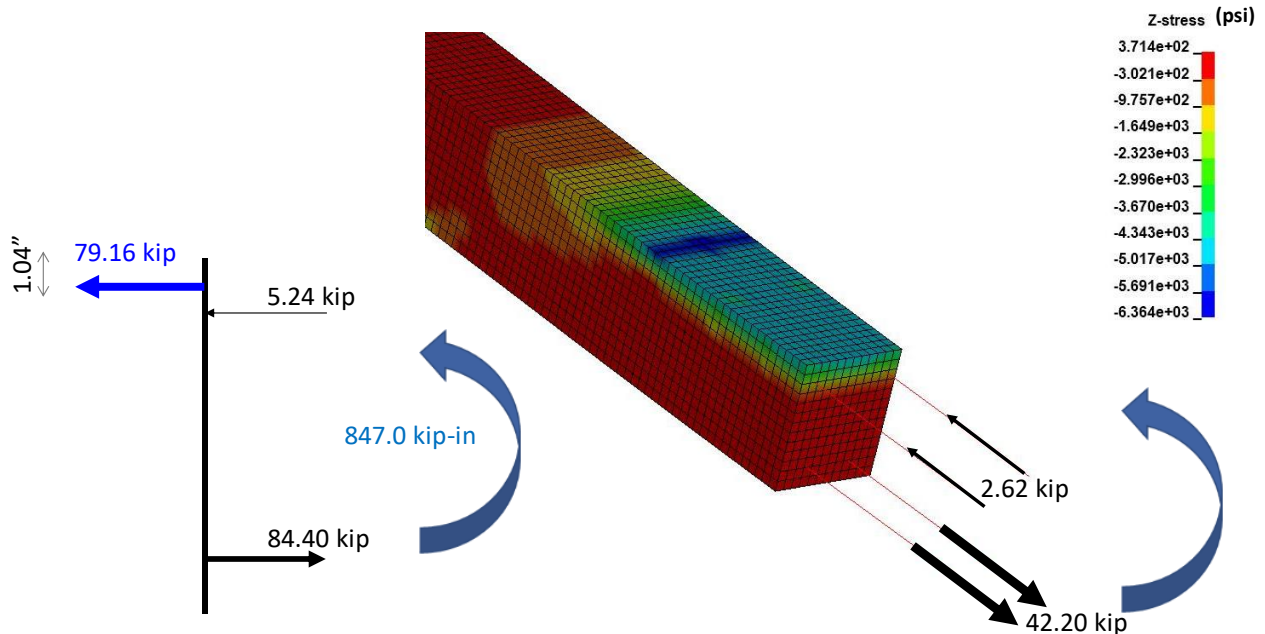
Figure 6.24. Predicted axial forces in top and bottom reinforcement and concrete stresses at peak load (midspan deflection of 0.39 in) for Beams 11 and 17
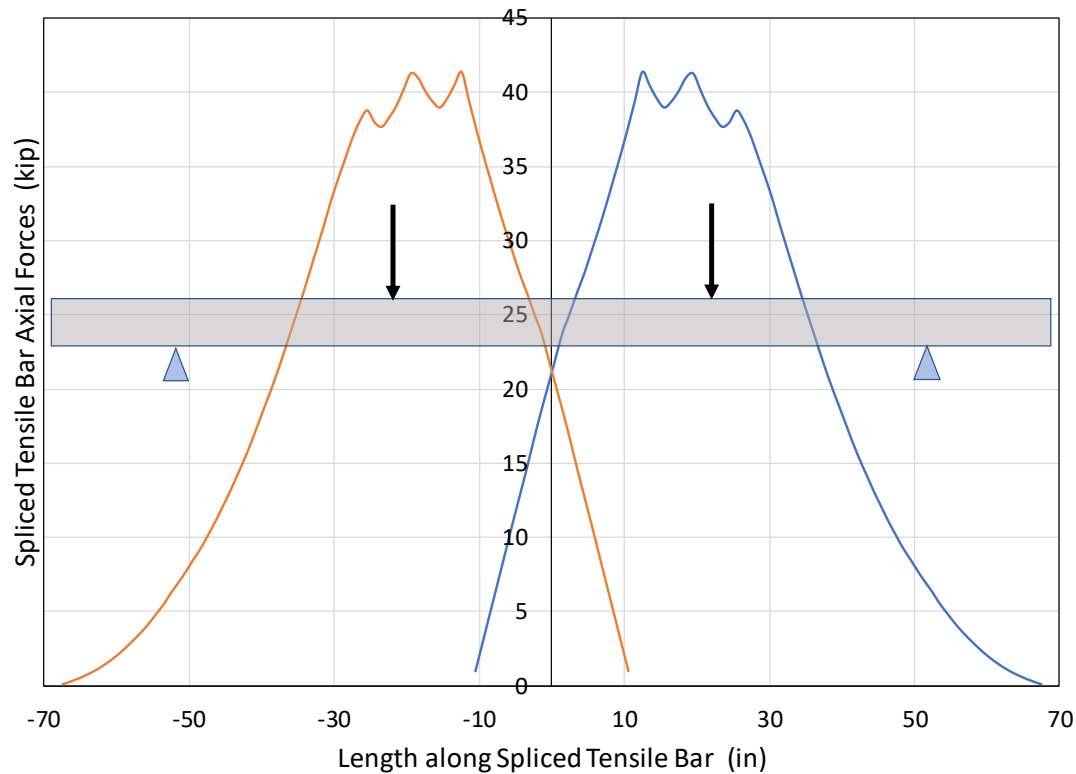
Figure 6.25. Predicted axial forces in bottom reinforcement along the length of the reinforcing bars corresponding to peak load for Beams 11 and 17. Different colors are used to represent each of the spliced bottom bars.

6.7 ANALYSIS OF REACTIVE BEAMS

Analysis of ASR-affected beams included two steps:

- Step 1: *ASR expansion*: In this step, internal volumetric strains representative of ASR expansion (equivalent to three times the target linear expansion) were applied under strain control to all concrete solid elements, see Section 6.5. A smooth S-curve up to the target expansion level (target linear strains of 0.15 % for Beams 10 and 9 and 0.22 % for Beams 12 and 19) was used to ensure no dynamic amplifications. The expansion was applied over two seconds.
- Step 2: *Four-point bending test*: After the completion of step 1 (end of ASR expansion), the beam was vertically loaded at two locations, where the nodes corresponding to the loading locations at top of the beam were pushed downward under displacement control until failure occurred similar to the procedure used in Section 6.6.

6.7.1   Beam 10

Beam 10 was identical to Beam 18 (Figure 6.11), with continuous bottom reinforcement and an 8 in stirrup spacing in the constant moment region. The beam was tested after being cured for about six months in the NIST environmental chamber, reaching a linear expansion level in the stirrups of about 0.15 %. During the four-point bending test, the beam exhibited a ductile behavior before failure similar to that observed in Beam 18: yielding of tensile reinforcement, followed by compressive failure of concrete in the compression zone.

Step 1: ASR expansion

Figure 6.26 shows the deflected shape of the beam (with deflections amplified by a factor of 50) at the end of the ASR expansion based on the finite element analysis. Similar to experimental observations (Chapter 3), the figure shows the predicted upward deflection of the beam due to the difference between the top (two No. 4 bars) and bottom (two No. 8 bars) reinforcement. The predicted upward deflection was 0.132 in, while the measured deflection was (0.16±0.06) in, see Table 3.2. This indicates that the predicted deflection was lower than the best estimate of the measurement by approximately 15 %, but was within the bounds of the expanded uncertainty. Figure 6.26 also presents the predicted average strains along the edges of the beam in three-directions. The average strains were calculated as $(l_{ASR} - l_0) / l_0$, where l_{ASR} is the edge length at the end of ASR expansion and l_0 is the original length of the edge. As the figure indicates, the top of the beam experienced larger strains (0.155 %) compared with the bottom of the beam (0.097 %) in the longitudinal (z-) direction. This is again due to the non-symmetric reinforcement of the beam with respect to the neutral axis (different amounts of reinforcement between the tension and compression zones). This observation indicates that average surface strains due to ASR expansion are highly dependent on the structural response of elements, state of stress inside the element, and the amount and distribution of reinforcement. This highlights one of the shortcomings of using surface strains to measure the ASR-induced expansion of structural elements (see Sadek *et al.*, 2021).
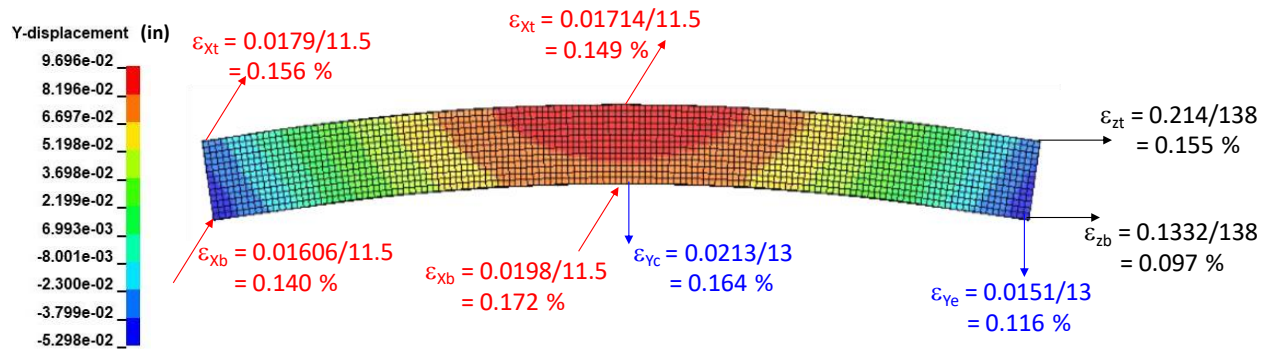
Figure 6.26. Predicted deflected shape and beam edge average strains at end of ASR expansion for Beam 10 (deflections amplified by a factor of 50)

Table 6.2 presents a comparison between the predicted axial strain in the bottom reinforcing bars and the stirrups and the corresponding average strain measurements at the end of ASR expansion (average over all beam measurements at time of beam testing). The averages are provided in Table 4.9. Table 6.2

shows good agreement between the model prediction and the average measurement. Compared with the average values, the model overestimated the strains in the bottom reinforcing bars by about 24 % and underestimated the strains in the stirrups by 9 % to 11 %. In all cases, the predictions were within the uncertainty bounds of the measurement.

Table 6.2. Measured and predicted strains in reinforcement of Beam 10 at the end of ASR expansion

	Measurement (%)	Prediction (%)
Bottom bars	0.07 ± 0.02	0.087
Stirrups	0.14 ± 0.02	0.124 (legs) 0.128 (bottom)

Figure 6.27 presents the predicted distribution of axial forces in the top and bottom reinforcement along the length of the bars (location zero signifies centerline of beam) at the end of ASR expansion. The figure shows that both top and bottom reinforcement were in tension. The ratio of the average forces in the top bars to that in the bottom bars was about 0.39. Given that the area of the top bars (No. 4) was 1/4 that of the bottom bars (No. 8), the strain in the top bar would be about 1.55 times the strain in the bottom bar. This is consistent with the average longitudinal strains in Figure 6.26. Figure 6.27 shows smaller forces in both top and bottom bars in the central region of the beam with larger stirrup spacing (8 in versus 3 in spacing in the neighboring region). This is attributed to the fact that the less transverse confinement in the central region of the beam allows for more expansion in the transverse direction compared with the longitudinal direction (Saouma, 2014), hence the smaller longitudinal forces compared with the region with larger transverse confinement.
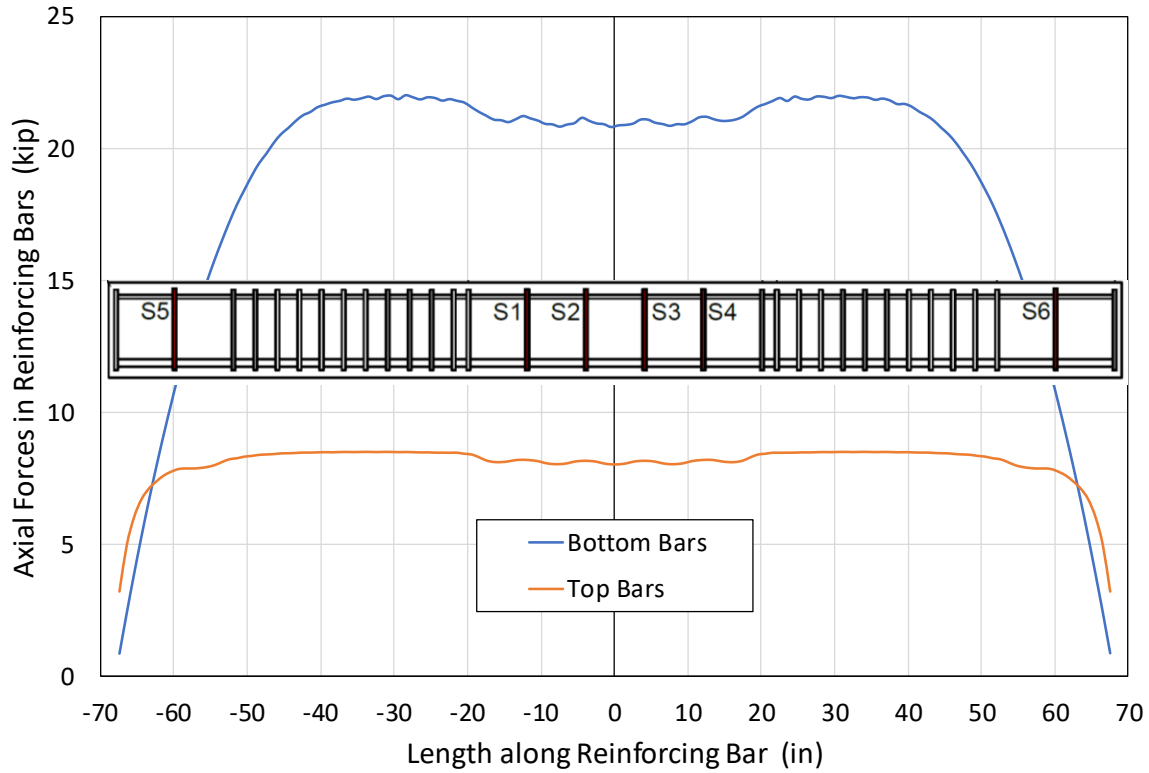
Figure 6.27. Predicted axial forces in bottom and top reinforcement along the reinforcing bar length at end of ASR expansion for Beam 10

Figure 6.28 shows the predicted axial forces in the top and bottom reinforcement along with concrete stresses at the end of the ASR expansion. The equilibrium sketch to the left of Figure 6.28 shows that compressive concrete stresses were in equilibrium with the tensile forces in the top and bottom reinforcement. In the absence of external forces or moments, the concrete cross section was totally in compression with a distribution that can be approximated as triangular (highest stress at bottom).
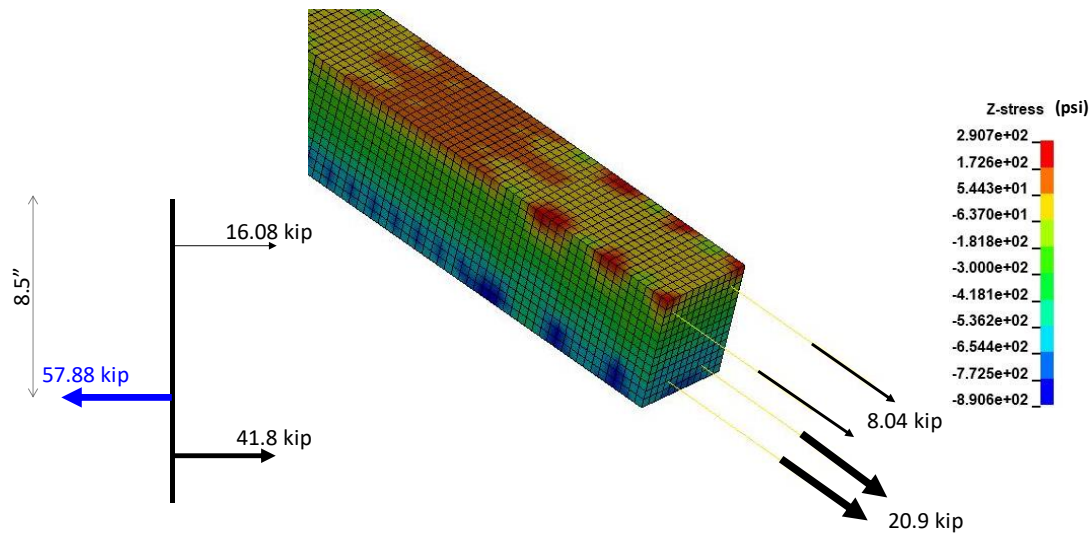
Figure 6.28. Predicted axial forces in top and bottom reinforcement and concrete stresses at end of ASR expansion for Beam 10

Step 2: four-point bending test

The analysis of Beam 10 considered two values for the concrete compressive strength: the 28-day strength (4500 psi) and the strength at the time of testing (3735 psi). The total applied load versus midspan deflection is plotted in Figure 6.29 for the two analyses, along with the load-deflection curve measured during the experiment. Note that for the modeling results, zero mid-span deflection in the figure was considered from the end of ASR expansion analysis (step 1) to be consistent with the measured load-deflection curve. The figure shows only minor differences between the analysis using the two compressive strength values (less than a 3 % difference in load for a given displacement value). The analysis results had a slightly less stiff response throughout the initial phase of the response than did the experimental results. Both analyses were in full agreement with the experiment during the transition from the linear to the nonlinear range, indicating that the bottom reinforcing bars yielded at the same deflection. For the range of displacements considered in the analyses, the models did not capture the reduction in applied load due to concrete crushing at a midspan deflection of about 1.2 in. Figure 6.30 shows the forces in the tensile reinforcement based on the strain measurements on the bottom bars during the experiment (grey lines). The reinforcing bar force in the experiment were calculated as shown in Section 6.6.1 based on strain measurements on the bottom reinforcing bars. Also shown in Figure 6.30 is the predicted force in the tensile reinforcement based on the computational model (red line). The predicted force shown in the figure did not account for the ASR-induced forces (Figure 6.27) to allow the comparison with the experimental results. Figure 6.30 shows that, when compared with the experimental results, the model was capable of capturing the axial force development in the reinforcement.

112
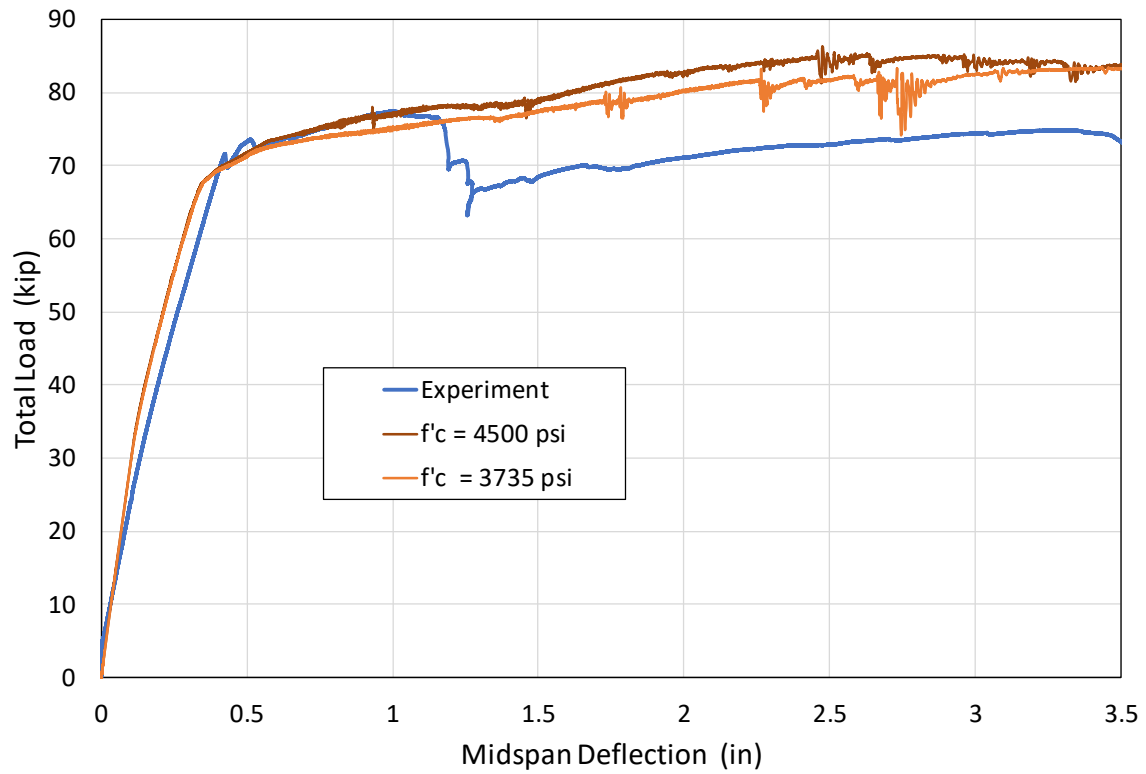
Figure 6.29. Total applied load versus midspan deflection of Beam 10
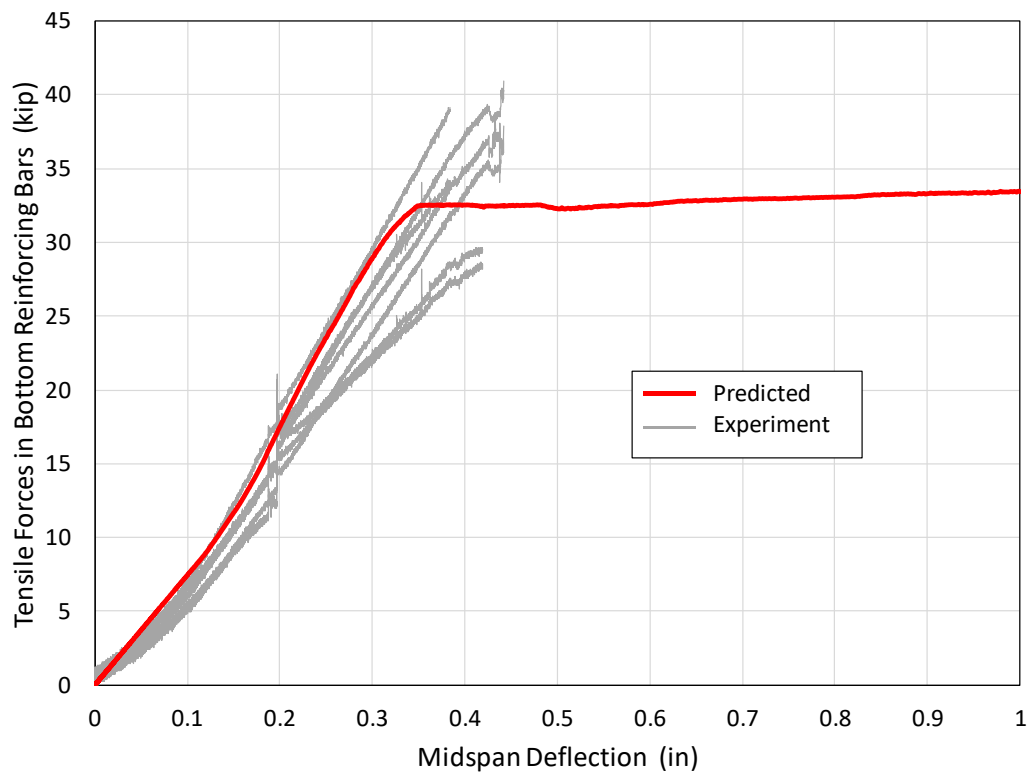
Figure 6.30. Predicted and measured axial forces in tensile reinforcement versus midspan deflection of Beam 10

113

Figure 6.31(a) shows the deflected shape of the beam and predicted concrete damage at different levels of midspan defection. The plots show an increasing level of damage with increased deflections. Figure 6.31(b) shows the observed damage of the beam at the end of the experiment. The comparison between Figure 6.31(a) and Figure 6.31(b) indicates that the model captured the concrete cracking in the tensile zone, but did not capture the concrete crushing at beam top.

(a)

(b)
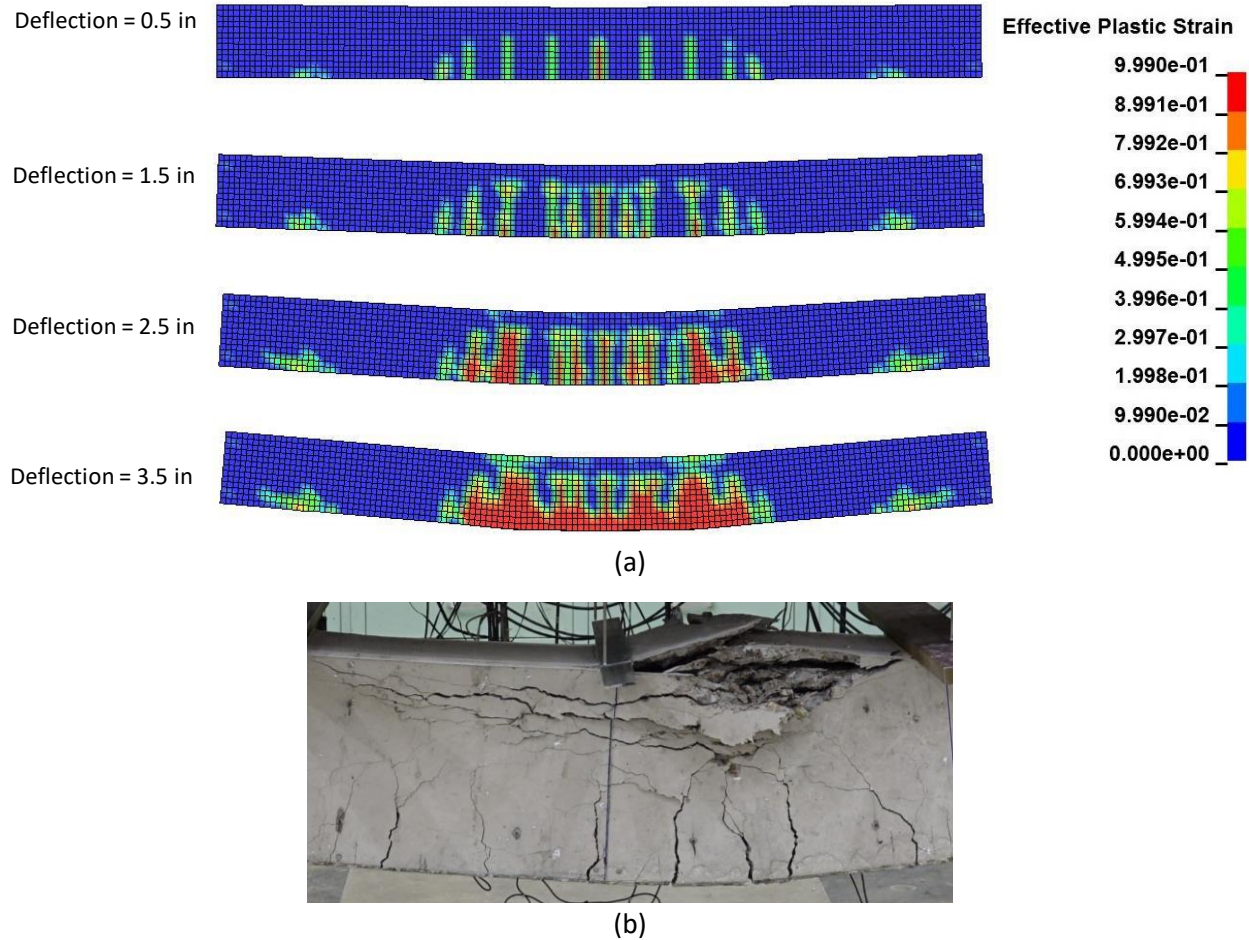
Figure 6.31. (a) Predicted concrete damage at various levels of deformation and (b) observed damage at end of experiment of Beam 10

Figure 6.32 depicts the development of axial forces in the top and bottom reinforcement as a function of the midspan deflection as predicted by the computational model. Note that in this figure, zero mid-span deflection was considered from the start of the ASR expansion (step 1) and the ASR-induced upward deflection is shown with negative values. As before, the figure indicates that at the end of ASR expansion, both top and bottom reinforcement were in tension. During the four-point bending test (step 2), the bottom bars experienced increased tensile forces until yielding occurred. The top bars experienced reduction in the tensile forces, and the forces switched to compression after yielding of the bottom bars. Figure 6.33 shows the predicted axial forces in the top and bottom reinforcement along with concrete stresses, corresponding to the yielding of the bottom reinforcement. The equilibrium sketch to the left of Figure 6.33 is based on the computational model results.

114
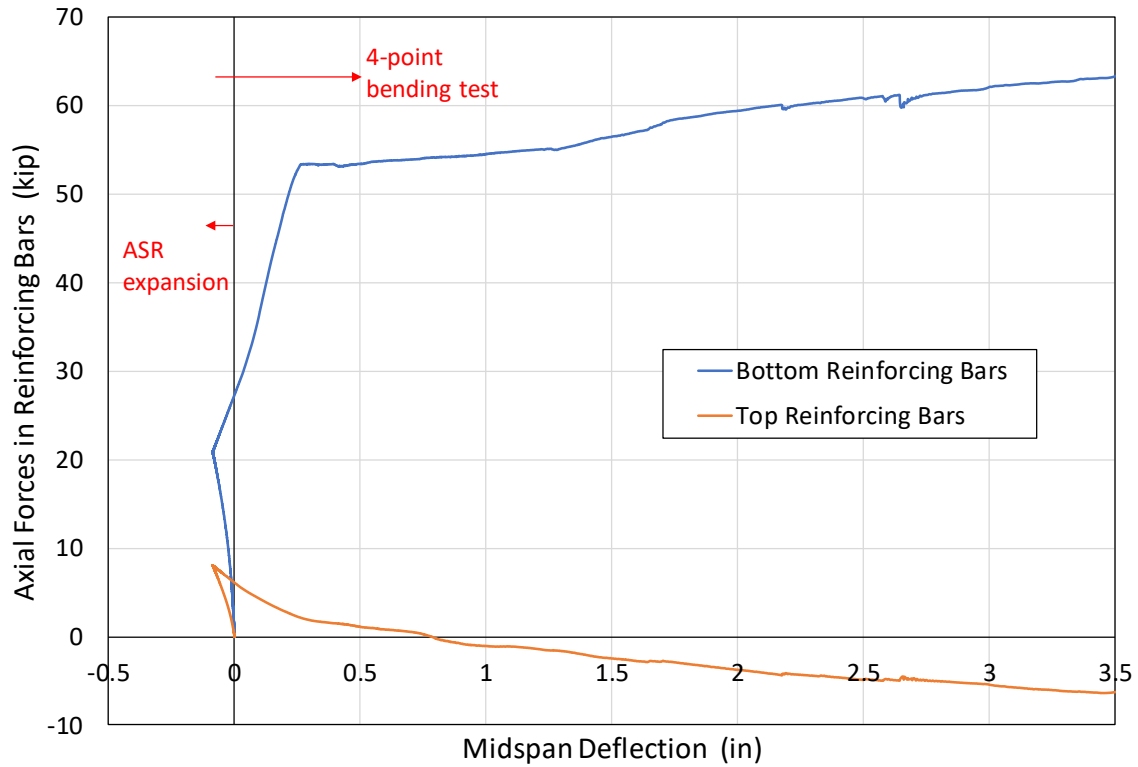
Figure 6.32. Predicted axial forces in top and bottom reinforcement versus midspan deflection of Beam 10
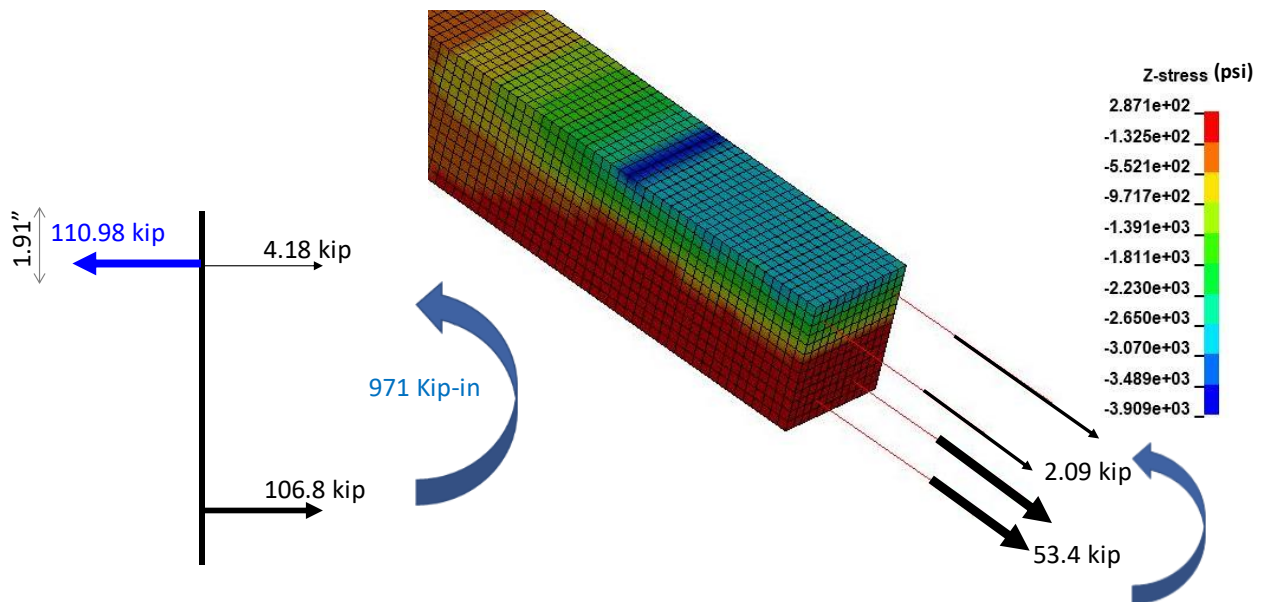
Figure 6.33. Predicted axial forces in top and bottom reinforcement and concrete stresses corresponding to bottom bar yielding for Beam 10

115

6.7.2   Beam 9

Reactive Beam 9 construction was identical to Beams 11 and 17 (Figure 6.17) with spliced bottom reinforcement with a splice length of 22 in and an 8 in stirrup spacing in the constant moment region. The beam was tested after being cured for about six months, reaching a linear expansion level in the stirrups of about 0.15 %. During the four-point bending test, the predominant mode of failure of the beam was loss of bond at the bottom, spliced reinforcement.

Step 1: ASR expansion

Figure 6.34 shows the deflected shape of the beam (deflections amplified by a factor of 50) at the end of the ASR expansion based on the finite element analysis. A comparison between Figures 6.34 and 6.26 shows no appreciable difference in the response of Beam 10 with continuous bottom reinforcement and Beam 9 with spliced bottom reinforcement. Similar to experimental observations (Chapter 3), the figure shows the upward deflection of the beam due to the difference between the top and bottom reinforcement and the ASR-induced prestressing. The predicted upward deflection was 0.136 in, while the measured deflection was (0.15 ± 0.06) in, see Table 3.2. This indicates that the predicted deflection was lower than the best estimate of the measurement by approximately 11 % but was within the bounds of the expanded uncertainty. Figure 6.34 also presents the predicted average strains along the edges of the beam in three-directions, and the same findings developed for Beam 10 apply for Beam 9.
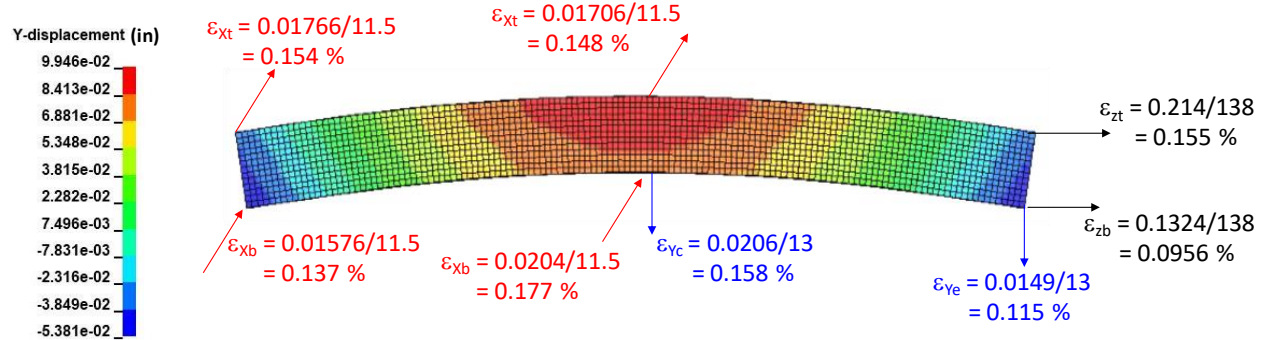
Figure 6.34. Predicted deflected shape and beam edge average strains at end of ASR expansion for Beam 9 (deflections amplified by a factor of 50)

Table 6.3 presents a comparison between the predicted axial strain in the bottom reinforcing bars and the stirrups and the corresponding average strain measurements at the end of ASR expansion. The measured averages are provided in Table 4.9. Table 6.3 shows that when compared with the measured average ASR-induced strains, the predictions were within the uncertainty bounds of the measurements.

Table 6.3. Measured and predicted strains in reinforcement of Beam 9 at the end of ASR expansion

	Measurement (%)	Prediction (%)
Bottom bars	0.07 ± 0.02	0.090 (splice end) 0.052 (splice end)
Stirrups	0.14 ± 0.02	0.126 (legs) 0.141 (bottom)

Figure 6.35 presents the predicted distribution of axial forces in the top and bottom reinforcement along the length of the bars at the end of ASR expansion. The figure shows that both top and bottom reinforcement were in tension. Similar to for Beam 10, the ratio of the average forces in the top bars to that in the bottom bars was about 0.39, resulting in top bar strains of about 1.55 times the strains the bottom bar, which is consistent with the average longitudinal strains in Figure 6.34.
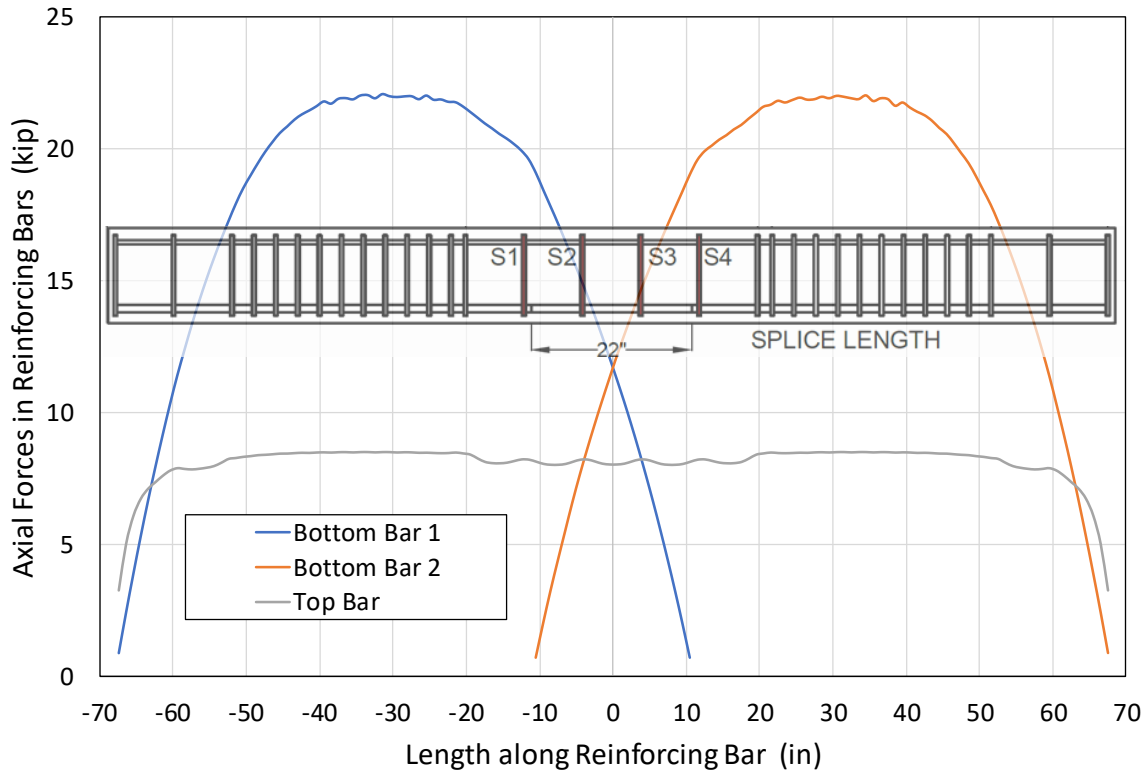
Figure 6.35. Predicted axial forces in bottom and top reinforcement along the reinforcing bar length at end of ASR expansion for Beam 9. Different colors are used to represent each of the spliced bottom bars.

Figure 6.36 shows the predicted axial forces in the top and bottom reinforcement along with concrete stresses at the end of the ASR expansion. The equilibrium sketch to the left of Figure 6.36 shows that compressive concrete stresses were in equilibrium with the tensile forces in the top and bottom reinforcement. Similar to Beam 10, the concrete cross section was totally in compression with a distribution that can be approximated as triangular (highest stress at bottom).

117
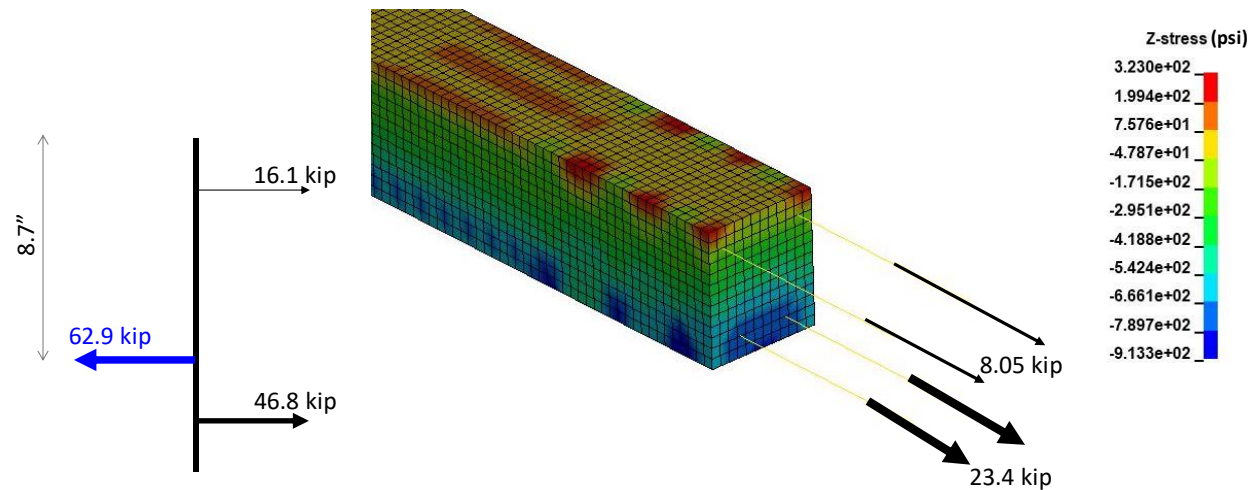
Figure 6.36. Predicted axial forces in top and bottom reinforcement and concrete stresses at end of ASR expansion for beam 9

Step 2: four-point bending test

The analysis of Beam 9 was conducted using Method 2, outlined in Section 6.6.2, to reduce the bond strength in the spliced bottom bars. At first, the analysis was conducted with SBRF of 0.75 similar to that used in Section 6.6.2 for non-reactive Beams 11 and 17. Figure 6.37 presents the total applied load versus midspan deflection based on this analysis, along with the load-deflection curve measured during the experiment. Note that for the modeling results, zero mid-span deflection in the figure was considered from the end of ASR expansion analysis (step 1) to be consistent with the measured load-deflection curve. The figure shows that the analysis with SBRF=0.75 underestimated the measured peak load and the corresponding deflection by about 5 % and 8 %, respectively. Another analysis was conducted with SBRF=0.78 which resulted in a better match with the experimental results as shown in the figure. The predicted failure mode of the beam was a loss of bond at the spliced bottom reinforcement, matching the experimental observation. Figure 6.38 shows the forces in the tensile reinforcement based on the strain measurements on the bottom bars during the experiment (light grey and blue lines for mid-splice and splice end, respectively). The reinforcing bar force in the experiment was calculated based on the measured strain increment during the tests as before. Also shown in Figure 6.38 is the predicted force in the tensile reinforcement based on the computational model with SBRF of 0.78. Figure 6.38 shows that, when compared with the experimental results, the model underestimated the axial force development in the reinforcement, especially at the splice end.
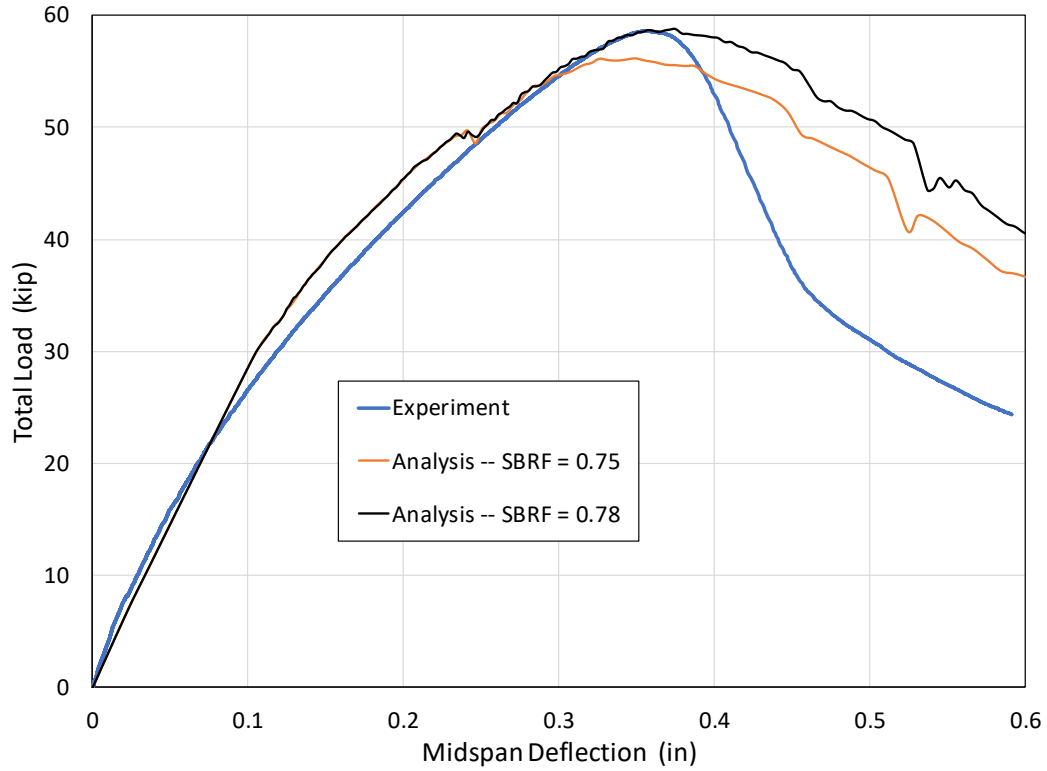
Figure 6.37. Total applied load versus midspan deflection of Beam 9
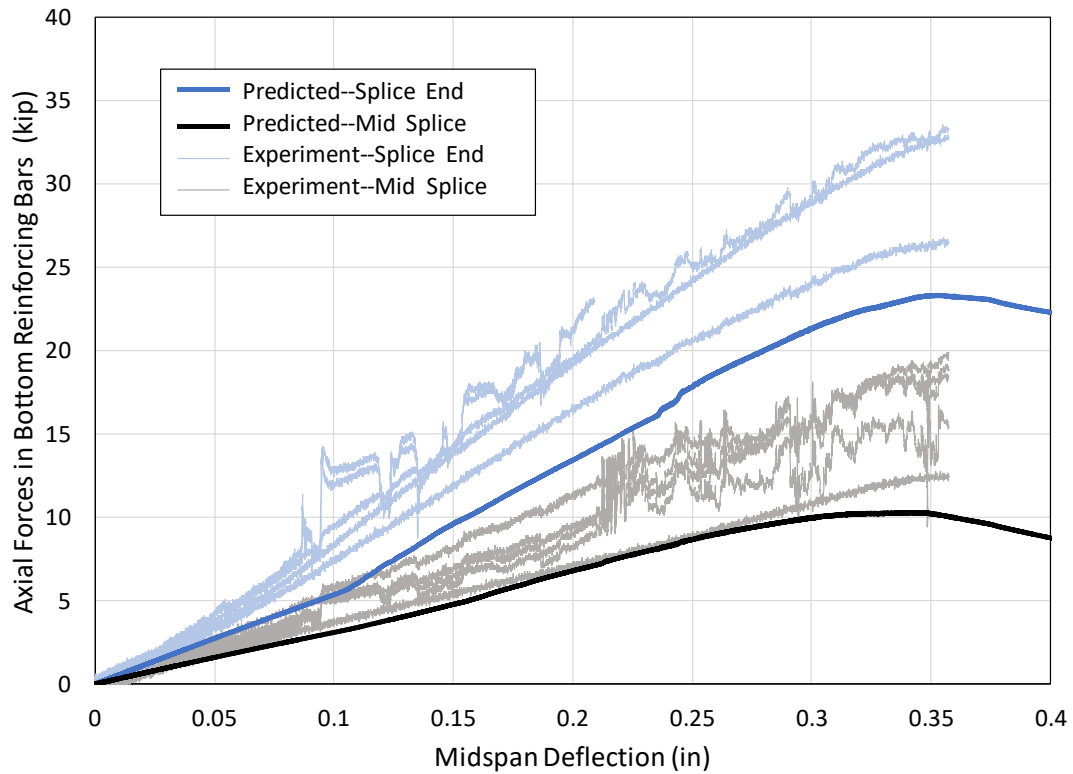
Figure 6.38. Predicted and measured axial forces in bottom reinforcement versus midspan deflection of Beam 9

Figure 6.39(a) shows the deflected shape of the beam and predicted concrete cracking at different levels of midspan defection. The plots show an increasing level of cracking with increased deflections, but the cracking was much less intensive than that predicted for Beam 10. Figure 6.39(b) shows the observed damage of the beam at the end of the experiment. The comparison between Figure 6.39(a) and Figure 6.39(b) indicates that the model captured the concrete cracking in the tensile zone after loss of bond in the bottom reinforcing bars.

(a)

(b)
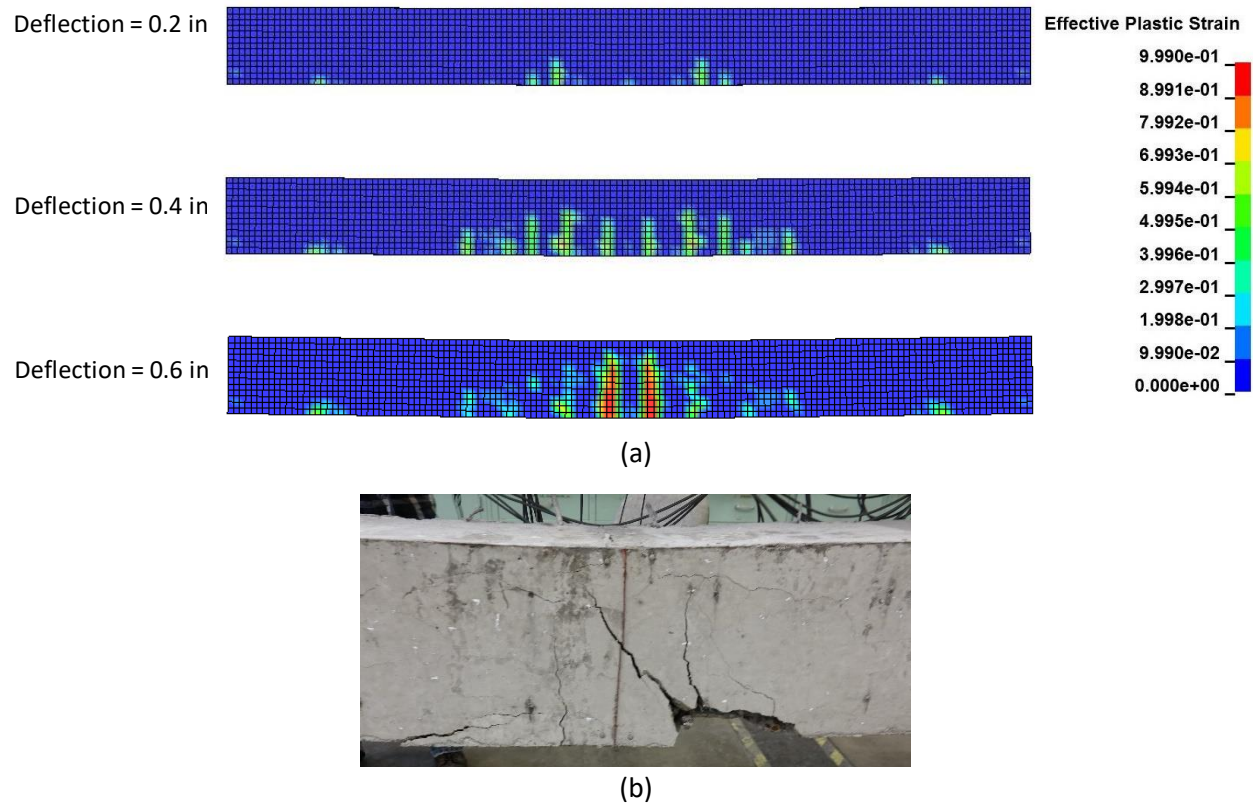
Figure 6.39. (a) Predicted concrete damage at various levels of deformation and (b) observed damage at end of experiment of Beam 9

Figure 6.40 depicts the development of axial forces in the top and bottom reinforcement as a function of the midspan deflection as predicted by the computational model. As before, the figure indicates that at the end of ASR expansion, both top and bottom reinforcement were in tension. As external loads were applied, the bottom bars experienced increased tensile forces while the top bars experienced reduction in the tensile forces but remained in tension throughout the test. Figure 6.41 shows the predicted axial forces in the top and bottom reinforcement along with concrete stresses, corresponding to the peak load sustained by the beam. The equilibrium sketch to the left of Figure 6.41 was based on the computational model results.
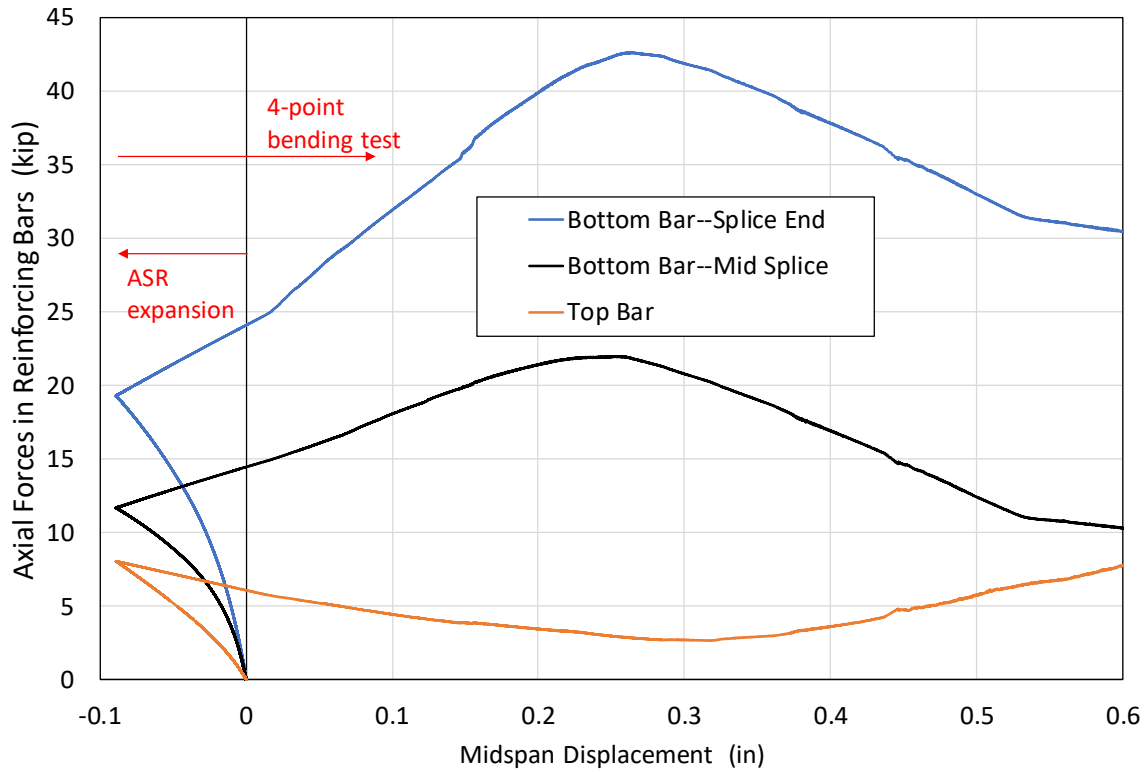
Figure 6.40. Predicted axial forces in top and bottom reinforcement versus midspan deflection of Beam 9
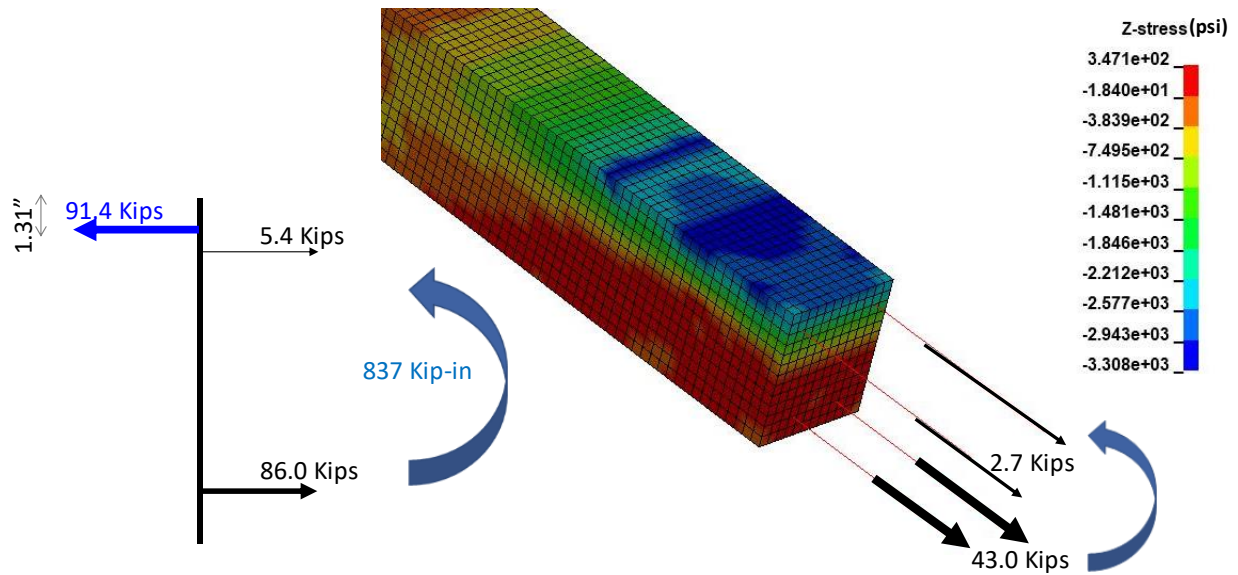
Figure 6.41. Predicted axial forces in top and bottom reinforcement and concrete stresses corresponding to bottom bar yielding for Beam 9

121

6.7.3 Beams 12 and 19

The construction of reactive Beams 12 and 19 was identical to Beams 9, 11, and 17 (Figure 6.17). Beams 19 and 12 were tested after being cured for about 12 months and 20 months, respectively, reaching a linear expansion level in the stirrups of about 0.22 % and 0.18 %. For step 1 of the analysis, only a linear expansion of 0.22 % was considered. During the four-point bending test, the predominant mode of failure of the beams was loss of bond at the bottom, spliced reinforcement.

Step 1: ASR expansion

Figure 6.42 shows the deflected shape of the beam (deflections amplified by a factor of 50) at the end of the ASR expansion based on the finite element analysis. As expected, the ASR-induced strains in the beam were larger than those calculated for Beams 10 and 9. Similar to experimental observations (Chapter 3), the figure shows the upward deflection of the beam caused by the ASR expansion. The predicted upward deflection was 0.23 in, while the measured deflections were (0.38 ± 0.06) in and (0.31 ± 0.06) in for Beams 12 and 19, respectively; see Table 3.2. This indicates that the predicted deflection was lower than the best estimate of the measurement by approximately 39 % and 26 % for Beams 12 and 19, respectively. These large differences may be attributed to creep effects, which were not included in the computational model as the specimens remained in the environmental chamber for a longer period of time than the rest of the beam specimens. Figure 6.34 also presents the predicted average strains along the edges of the beam in three-directions, and the same findings as shown for Beams 10 and 9 apply for Beams 12 and 19.
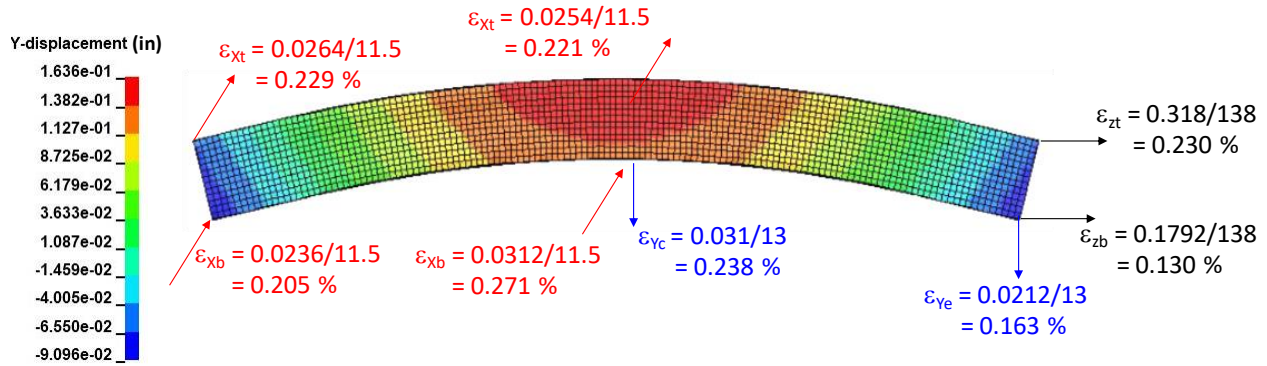
Figure 6.42. Predicted deflected shape and beam edge average strains at end of ASR expansion for Beams 12 and 19 (deflections amplified by a factor of 50)

Table 6.4 presents a comparison between the predicted axial strain in the bottom reinforcing bars and the stirrups and the corresponding strain measurements at the end of ASR expansion. The measured strains are provided in Table 4.9 based on a single measurement only. Table 6.4 shows a reasonable agreement between the model prediction and the measurement, albeit from a single measurement. Compared with the measured values, the model underestimated the strains in the stirrups by 21 % (legs) and 9 % (bottom). For the bottom bars, the measured strain was between the predicted strains at splice end and at mid-splice.

Table 6.4. Measured and predicted strains in reinforcement of Beam 12 and Beam 19 at the end of ASR expansion

	Measurement (%)	Prediction (%)
Bottom bars	0.09[**]	0.107 (splice end)
		0.065 (mid-splice)
Stirrups	0.22[**]	0.174 (legs)
		0.201 (bottom)

[**] Only one gage remained functional, see Table 4.9

Figure 6.43 presents the distribution of axial forces in the top and bottom reinforcement along the length of the bars (location zero signifies centerline of beam) at the end of ASR expansion as predicted by the computational model. The figure shows that both top and bottom reinforcement were in tension. The peak tensile force in the top reinforcing bars was 11.7 kip; about 11 % less than the yield force of the top bars of 13.2 kip.
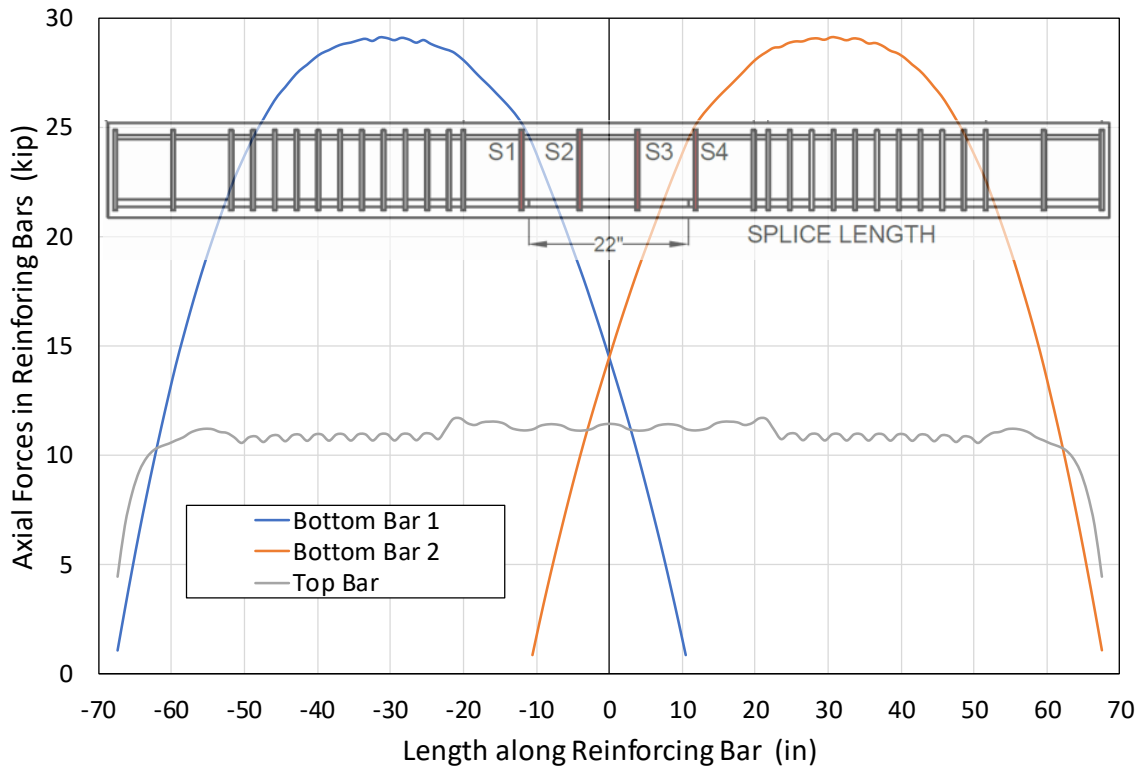
Figure 6.43. Predicted axial forces in bottom and top reinforcement along the reinforcing bar length at end of ASR expansion for Beams 12 and 19. Different colors are used to represent each of the spliced bottom bars.

Figure 6.44 shows the predicted axial forces in the top and bottom reinforcement along with concrete stresses at the end of the ASR expansion. The equilibrium sketch to the left of Figure 6.44 shows that compressive concrete stresses were in equilibrium with the tensile forces in the top and bottom reinforcement. Similar to other ASR-affected beams, the concrete cross section was totally in compression with a distribution that can be approximated as triangular (highest stress at bottom).
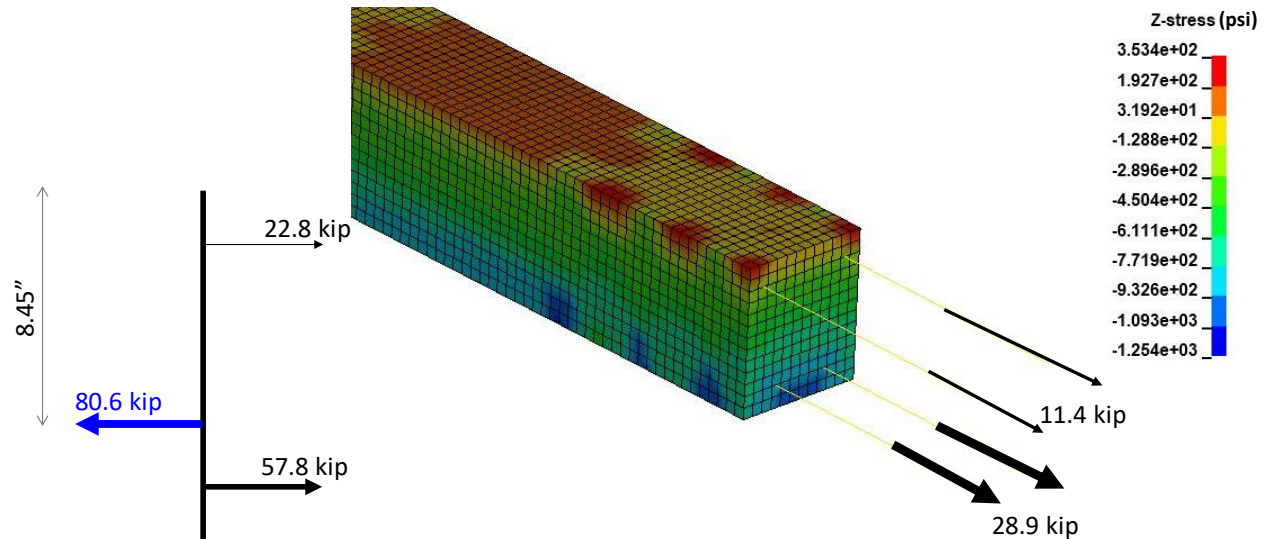
Figure 6.44. Predicted axial forces in top and bottom reinforcement and concrete stresses at end of ASR expansion for Beams 12 and 19

Step 2: four-point bending test

The analysis of Beams 12 and 19 was conducted using Method 2, outlined in Section 6.6.2, to reduce the bond strength in the spliced bottom bars. It was found that values of SBRF of 0.90 and 0.95 provided the best match with the experimental results. Figure 6.45 presents the total applied load versus midspan deflection for the two analyses, along with the load-deflection curve measured during the experiment. SBRF values in the range of 0.90 to 0.95 for reactive Beams 12 and 19 compared with SBRF value of 0.75 for non-reactive Beams 11 and 17 indicated that the ASR expansion resulted in larger bond strength by about 20 % to 25 %, likely due to ASR-induced prestressing effect. The figure shows that the models captured well the initial stiffness and the deflections corresponding to the peak loads for both beams. The predicted failure mode of the beam was a loss of bond at the spliced bottom reinforcement, matching the experimental observation. Figure 6.46 shows the forces in the tensile reinforcement based on the strain measurements on the bottom bars during the experiment (light grey and blue lines for mid-splice and splice end, respectively) for Beam 19 (Beam 12 did not provide meaningful strain data during the test). Also shown in Figure 6.46 is the predicted force in the tensile reinforcement based on the computational model with SBRF of 0.95. Figure 6.46 shows that, when compared with the experimental results, the model underestimated the axial force development in the reinforcement, especially at the splice end, similar to Beam 9. The reason for this discrepancy may be attributed to the complexity of the behaviors

124

being modeled. The beams exhibited the combined effects of ASR-induced expansion and degradation, creep effects (which were not modeled), and bond-slip. These combined, complex behaviors were beyond the capabilities of the current model and may require additional research.
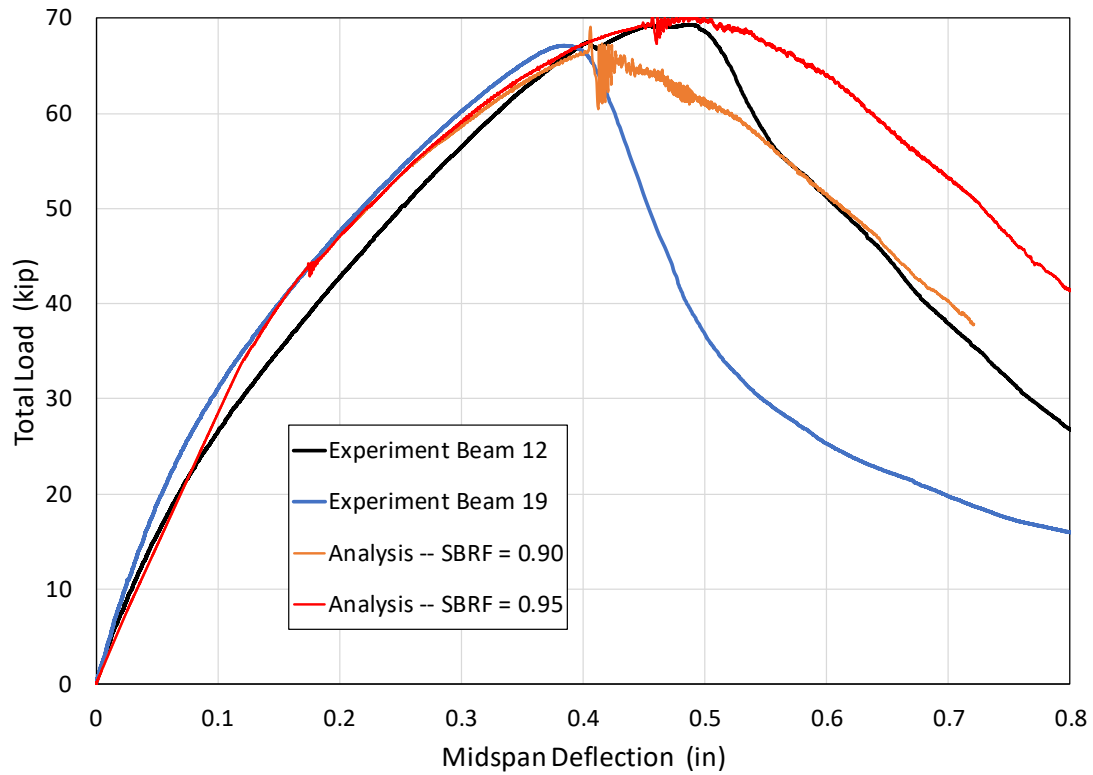
Figure 6.45. Total applied load versus midspan deflection of Beams 12 and 19
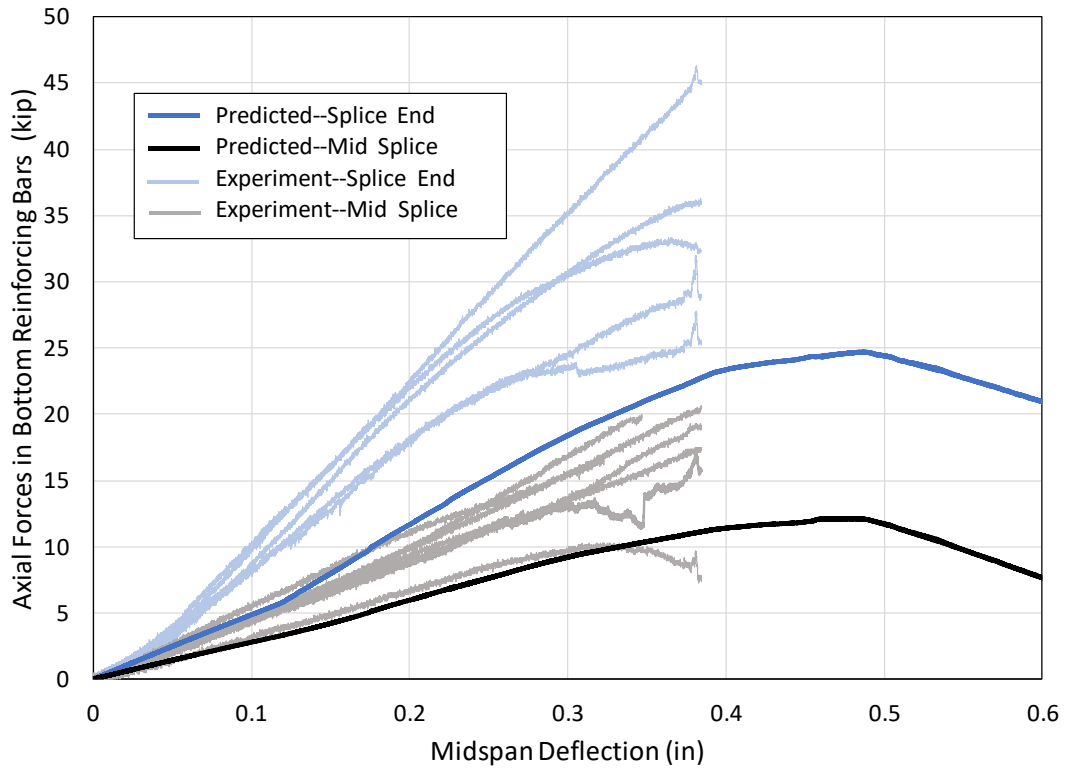
Figure 6.46. Predicted and measured axial forces in bottom reinforcement versus midspan deflection of Beam 19

Figure 6.47(a) shows the deflected shape of the beam and predicted concrete cracking at different levels of midspan deflection. Figure 6.47(b) shows the observed damage of the two beams at the end of the experiment. The comparison between Figure 6.47(a) and Figure 6.47(b) indicates that the model captured the concrete cracking in the tensile zone after loss of bond in the bottom reinforcing bars.

(a)

(b)
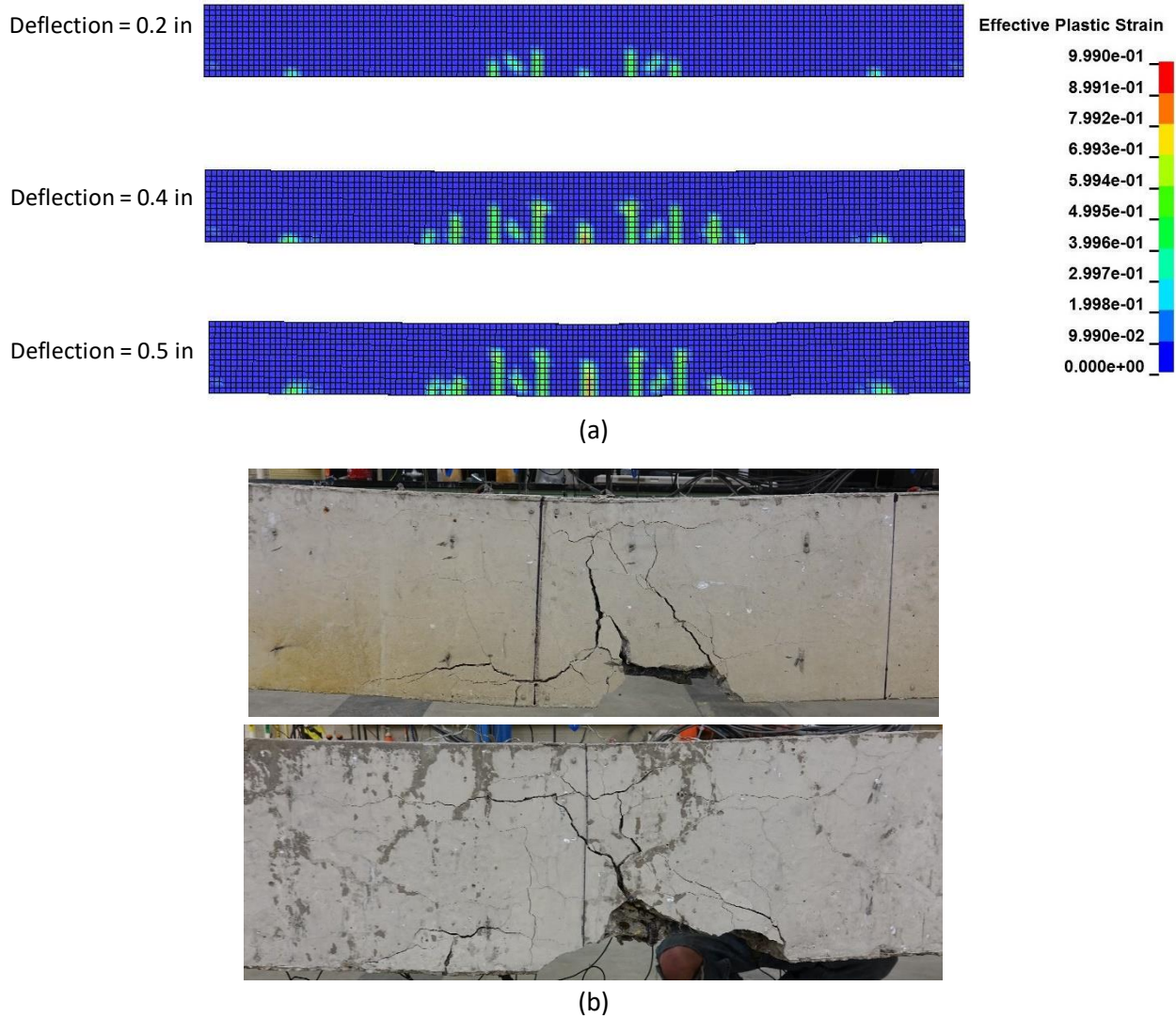
Figure 6.47. (a) Predicted concrete damage at various levels of deformation and (b) observed damage at end of experiment of Beams 12 and 19

Figure 6.48 depicts the development of axial forces in the top and bottom reinforcement as a function of the midspan deflection as predicted by the computational model. As before, both top and bottom reinforcement were in tension at the end of ASR expansion. As external loads were applied, the bottom bars experienced increased tensile forces while the top bars experienced reduction in the tensile forces, but remained in tension throughout the test. The figure also shows that the bottom reinforcements remained in the elastic range and did not yield, with the maximum tensile stress in the tension reinforcement about 8 % below the steel yield limit. Figure 6.49 shows the predicted axial forces in the top and bottom reinforcement along with concrete stresses, corresponding to the peak load sustained by the beam. The equilibrium sketch to the left of Figure 6.49 is based on the computational model results.
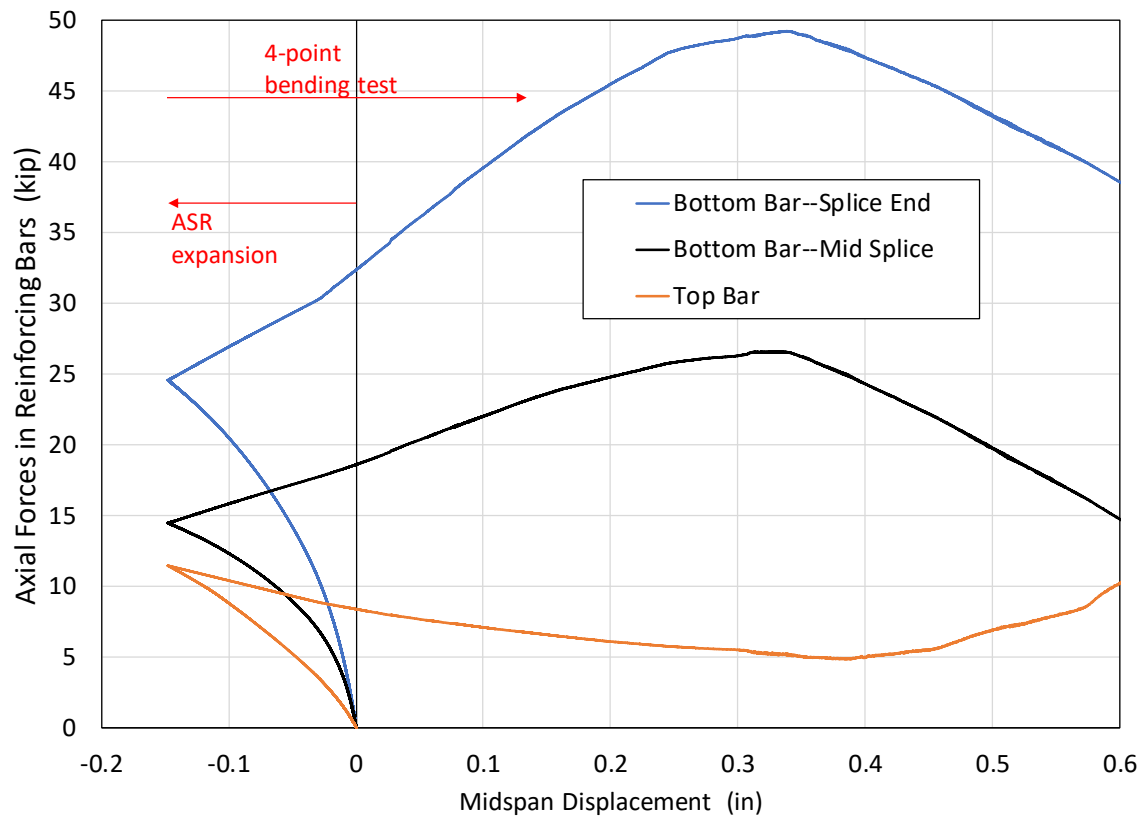
Figure 6.48. Predicted axial forces in top and bottom reinforcement versus midspan deflection of Beams 12 and 19
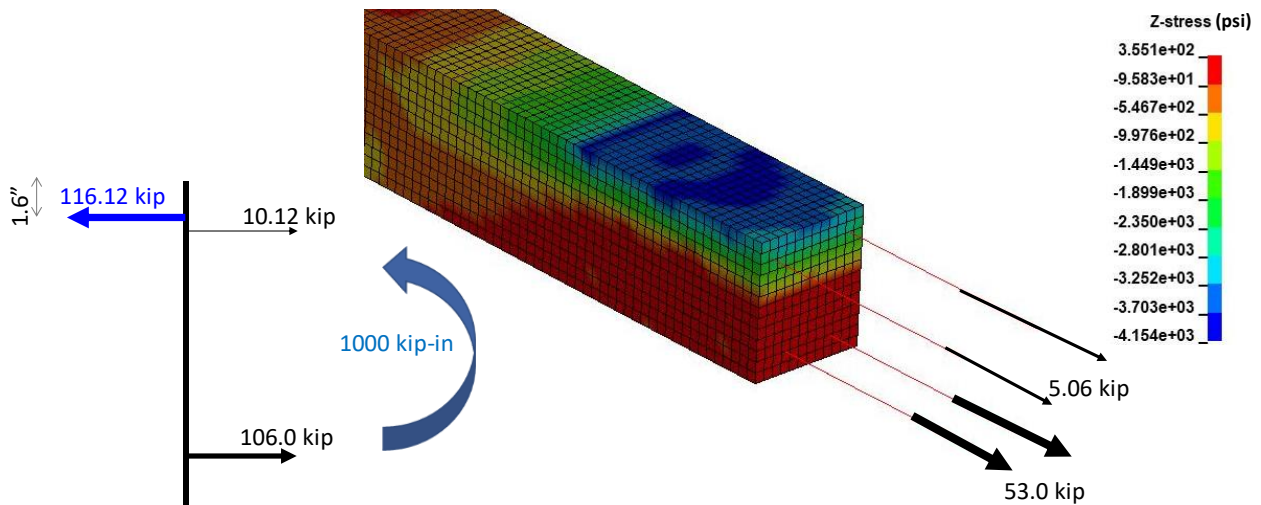
Figure 6.49. Predicted axial forces in top and bottom reinforcement and concrete stresses corresponding to bottom bar yielding for Beams 12 and 19

6.8   SUMMARY

- High-fidelity finite element models of the ASR-affected beams were developed. These models accounted for ASR expansion, degradation in material properties such as modulus of elasticity and tensile strength, and bond-slip at the bottom reinforcing bar splices.
- Modeling ASR-affected beams necessitated substantial changes to LS-DYNA's concrete model (MAT_159) and bond-slip model; implementing these changes required programming and re-compilation of the LS-DYNA program.
- The models provided useful insights into behavior of the beams during the ASR expansion process and during the four-point bending test, including distribution of forces in the reinforcing bars and stresses in concrete, preceding the failure of the beam.
- For the non-reactive beams, the models were validated and the bond-slip model was calibrated against experimental measurements. The predicted loads and deflections matched those based on the experiment, where the predicted peak loads sustained by the beams were within 5 % of the measured values. The predicted forces in the reinforcing bars closely matched the forces calculated based on strain measurements.
- For the reactive beams, the success of the models in capturing the measured response parameters varied:
  - o For the ASR expansion: The predicted upward deflection and strains on reinforcing bars were within the expanded uncertainty of the measurement for beams at the 0.15 % expansion level. For beams at the 0.22 % expansion level, the model underestimated the upward deflection by about 26 % to 39 % and the strains on reinforcing bars by about 9 % to 21 % (albeit for one measurement only), likely due to creep effects which were not included in the models.
  - o For the four-point bending test: The predicted load deflections matched those based on the experiment, where the predicted peak loads sustained by the beams and the corresponding displacements were within 5 % of the measured values. The predicted forces in the reinforcing bars closely matched the forces based on strain measurements for the beam with continuous reinforcing bars. For beams with spliced bottom bars, the models underestimated the predicted forces when compared with the forces based on strain measurements.
- For the beams modeled in this chapter, the models captured the failure modes observed in the experiments, except for those beams with continuous reinforcing bars where, after yielding of the tensile reinforcement, a small drop in the applied load due to compressive failure of the compression zone was not captured.
- Consistent with the findings of Task 1, the analysis of the ASR-induced expansion indicated that average surface strains in a structural element due to ASR are highly dependent on the structural response of the element, state of stress inside the element, and the amount and distribution of reinforcement. This highlights one of the shortcomings of using surface strains to measure the expansion of structural elements due to ASR.
- The models showed that, for the beams considered in the computational study, the bond strength in the region of the splice was larger with increased ASR expansion (by about 20 % to 25 % for an ASR expansion of 0.22 %).

This page intentionally left blank.

Chapter 7
SUMMARY, FINDINGS, AND CONCLUSIONS

7.1 SUMMARY

A series of 19 beam specimens, comprising 16 beams constructed with reactive aggregates and three reference beams constructed using the same reactive aggregates treated with a lithium nitrate solution to mitigate ASR, were tested under four-point loading. The beams were all under-reinforced and expected to fail in flexure in the constant moment region. The beams were stored in an environmental chamber prior to testing to accelerate ASR-induced expansion. The test program was designed as a rotatable central composite design (CCD) to facilitate examination of the effects of ASR-induced expansion, confinement provided by stirrups, and lap splice length on the flexural performance of beams with lap-spliced tensile reinforcement and on bond strength. In addition, the applicability of existing ACI code equations for the estimation of the bond strength and flexural capacity of reinforced concrete beams affected by ASR was assessed.

Specifically, the effects of the following three primary variables were investigated:

- ASR-induced expansion, $0 \leq \varepsilon_{ASR} \leq 0.22\,\%$, measured as averaged strain in the vertical and horizontal legs of the stirrups;

- normalized splice length, $0.5 \leq \ell_s/\ell_d \leq 1.5$, where ℓ_s is the provided splice length and ℓ_d is the development length of the tensile reinforcement, determined in accordance with ACI 318-19; and

- confinement parameter, $0 \leq K_{tr}/d_b \leq 1.8$, where d_b is the nominal diameter of the spliced reinforcement and K_{tr} is the transverse reinforcement index, determined in accordance with ACI 318-19.

The influence of the above variables on the following response parameters was investigated:

- the normalized moment capacity, M_{max}/M_n, of the beams, where M_{max} is the maximum measured moment strength during testing and M_n is the nominal moment capacity of the beam section, computed in accordance with ACI 318-19;

- the normalized bond strength, $u/\sqrt{f_c'}$, where u is the maximum average bond stress measured during testing and f_c' is the compressive strength of the companion concrete cylinders tested at the same time as the beam specimens; and

- the beam failure category, which indicated whether the specimen achieved the nominal flexural strength of the beam section (designated as Type B) or failed in bond splitting failure prior to achieving the nominal flexural strength of the beam section (designated as Type A).

The geometry and longitudinal reinforcement of the beams were selected to match beams previously tested by Rezansoff *et al*. (1991). Each beam had a cross section of 11.0 in × 13.0 in; a length between supports of 104.0 in; and a constant moment region, between loading points, of 44.0 in. The tensile reinforcement consisted of two No. 8 (1.0 in diameter) bars. Compression reinforcement, consisting of two No. 4 (0.5 in diameter) bars, was provided continuously along the beam's length to facilitate construction of the reinforcement cage. Closed No. 4 stirrups, with 135° hooks, were provided along the length of the beams. In the shear spans, the stirrup spacing was constant at 3 in. This dense arrangement of stirrups was selected to prevent spurious failure of the beam in shear. In the constant moment region, the stirrup spacing was varied between specimens, conforming to the levels of the confinement parameter, K_{tr}/d_b, specified in the experimental design. The clear concrete cover, between the outside of the stirrup and the beam face, was 1.0 in on all sides. This led to distances from the center of the outermost tensile bar to the side and bottom faces of the beams of 2.5 in and 2.0 in, respectively.

The beams were stored in an environmental chamber to accelerate the ASR reaction. For the first five months, the environmental chamber was kept at a temperature of roughly 80 °F and relative humidity above 95 %. After this initial period, the temperature in the chamber was increased to roughly 100 °F until approximately one year after casting, when all but one reactive beam had been tested. During this time, strains in the reinforcement were monitored for five of the beam specimens. The development of strain over time in the five beams was, for the most part, similar, despite varying stirrup spacings and lap splice lengths. Typically, strains in the longitudinal tensile reinforcement due to ASR-induced expansion were roughly half of the strains recorded in the stirrups at time of testing.

Although the target ASR expansion, measured as averaged strains in the vertical and horizontal legs of the beam stirrups, for the test program was 0.3 %, strains in the stirrups never achieved this level. Strains reached a value of 0.15 % expansion (half of the target expansion) after roughly 6 months, after which the increase slowed. The first two sets of specimens were tested at their target expansion values; however, beam specimens after this point were tested at roughly 3-month intervals. The maximum recorded strain in the stirrups was approximately 0.22 %.

A rigorous statistical analysis of the measured data was conducted to quantify the influence of ASR-induced expansion, ε_{ASR}; normalized splice length, ℓ_s/ℓ_d; and the reinforcement confinement, K_{tr}/d_b, on the normalized maximum midspan moment, M_{max}/M_n, and the normalized bond strength, $u/\sqrt{f_c'}$. This analysis also assessed the applicability of existing ACI code equations for estimating the bond strength and flexural capacity of reinforced concrete beams affected by ASR and permitted quantification of the uncertainty due to sampling variability using a parametric bootstrap algorithm.

High-fidelity finite element models of seven of the tested beams were developed and validated against the test data. Four of the modeled beams were constructed with reactive concrete and were tested at two levels of ASR expansion. The variables examined in the modeling study were the degree of ASR expansion and the presence of continuous or spliced tensile reinforcement. These models utilized the measured concrete and steel properties and accounted for ASR expansion, degradation in material properties, and bond-slip in the reinforcement splice region.

7.2 FINDINGS

This section summarizes the findings from the experimental and computational program.

- Concrete cylinders cast at the same time as the reactive beams showed a decrease in mechanical properties over time (with increasing ASR-induced expansion). The maximum reductions, compared to the 28-day values, were roughly 15 %, 60 %, and 13 % for the compressive strength, modulus of elasticity, and splitting tensile strength, respectively. Unreinforced prism specimens, made with the same ASR 3 concrete and kept in the same environment as the beams and cylinders, had linear expansions over the same period of roughly 0.3 %. These reductions in the mechanical properties were consistent with the findings of the Task 1 study (Sadek *et al.*, 2021).

- The relationship between the concrete modulus of elasticity and the compressive strength of normalweight concrete recommended by ACI 318-19 overpredicted the compressive modulus of the reactive concrete cylinders by up to 50 %. This was particularly evident at higher expansion values and is consistent with the findings of the Task 1 study (Sadek *et al.*, 2021).

- The relationship between the splitting tensile strength and the compressive strength of normalweight concrete suggested by ACI 318-14 was found to be in good agreement with the measurements for the reactive concrete mixture used in the study, within 20 %, throughout the testing period.

- Significant surface cracking was observed on all of the reactive beam specimens prior to testing, and exudation of presumed ASR gel was also observed on the surface of the beams at the crack locations. The observed cracking pattern was randomly oriented; none of the observed cracks appeared to be preferentially aligned with the embedded reinforcement, and no discoloration was observed that would suggest corrosion of the reinforcement cages. The maximum crack width observed before testing was roughly (0.020 ± 0.004) in.

- For beams with ASR-induced expansions, $\varepsilon_{ASR} \geq 0.14$ %, visible cambering (upward deflection) of the beams was observed. The maximum camber observed before testing was (0.38 ± 0.06) in.

- Beams constructed with continuous tensile reinforcement failed through compressive failure of the concrete in the compression zone following flexural cracking and yielding of the tensile reinforcement. This behavior was expected as the beam sections were under-reinforced.

- For beams constructed with spliced tensile reinforcement, damage typically progressed from the formation of flexural cracks at the ends of the reinforcement splice, progressive widening of these cracks as midspan displacements increased, and finally bond splitting failure on the underside of the beam and a precipitous drop in capacity with increasing displacement. Two beams with code compliant lap splice lengths had damage progressions similar to the beams with continuous reinforcement.

- Beam deflections were generally symmetric about midspan; section rotations were generally largest at the ends of the splice region; strain increments in the tensile reinforcement due to loading were largest at the ends of the splice; and strain increments at mid-splice due to loading were roughly half the value at the ends of the splice.

- Within the range of ASR expansion examined in this test program ($\varepsilon_{ASR} \leq 0.22$ %) the stiffness of the beams did not appear to decrease due to ASR-induced expansion (or reduction of compressive

133

concrete modulus), and the development of strain in the longitudinal reinforcement did not appear to be significantly influenced by the normalized splice length or confinement provided by the stirrups.

- Through a statistical analysis of the test results, ASR-induced expansion was not found to decrease either the normalized moment strength or the normalized bond strength in the range of the parameters experimentally studied.

- For normalized lap splice lengths, $\ell_s/\ell_d \geq 1.3$ (complying with the code specified minimum lap splice length) and in the range of the confinement parameter, $0.5 \leq K_{tr}/d_b \leq 1.5$, the normalized bond strength relationship implied by the ACI 318-19 code equation for development length (Equation 1.7 in this report) and the recommended equation proposed by ACI Committee 408 for development length (Equation 1.9) were found to be conservative estimates (i.e., underpredict the bond strength) of the regression model fitted to the measured bond stress.

- The finite-element models were successful at estimating the upward cambering and strains in the reinforcement due to ASR-induced expansion as well as the load-deflection behavior of the beams during structural loading. The models also provided useful insights into the behavior of the beams, including the distribution of forces in the reinforcing bars and stresses in the concrete, preceding the failure of the beams.

7.3   CONCLUSIONS

This study investigated the behavior of ASR-affected beams with under-reinforced sections, asymmetric top and bottom reinforcement, spliced tensile reinforcement, and closed stirrups in the splice region. The beams were designed to fail in flexure in the constant moment region. Spurious failure in shear was prevented through providing closely spaced stirrups in the shear spans. The conclusions presented below should be interpreted within the scope of the experimental program conducted and the ranges of experimental variables examined.

7.3.1   Statistical Analysis of Measured Data

From the analysis of the measured test results, the following conclusions were reached:

- There is no evidence that the mean normalized moment capacity, M_{max}/M_n, or the stiffness of the beams was reduced by the effects of ASR in the range of expansions studied, despite a reduction in the concrete compressive strength of up to 15 % and compressive elastic modulus up to 60 %.

- The normalized moment capacity, M_{max}/M_n, increased with increasing normalized splice length, ℓ_s/ℓ_d, within the range of the normalized splice length, $0.5 \leq \ell_s/\ell_d \leq 1.5$, used in this study.

- Beams constructed with normalized splice lengths, $\ell_s/\ell_d \geq 1.3$ (i.e., complying with the ACI 318-19 specified splice length), achieved or exceeded the nominal flexural strength of the section ($M_{max}/M_n > 1$) regardless of the degree of ASR-induced expansion when compared to the 90 % lower confidence bounds for the range of ASR-induced expansions considered ($\varepsilon_{ASR} \leq 0.22$ %).

- The measured increase in the normalized moment capacity, M_{max}/M_n, as a function of the normalized splice length, ℓ_s/ℓ_d, was generally consistent with the relationship predicted using section analysis based on the nominal strengths of the concrete and reinforcement (i.e., assuming no degradation in material properties due to ASR).

- For beams with normalized splice lengths $\ell_s/\ell_d \geq 1.3$ (i.e., complying with the ACI 318-19 specified splice length), the nominal beam moment strength M_n, computed using ACI 318 section analysis and nominal strengths of the concrete and reinforcement (i.e., assuming no degradation in material properties due to ASR) was a reasonable lower bound estimate for beam moment capacity (i.e., $M_{max}/M_n \geq 1.0$), regardless of degree of ASR expansion (up to 0.22 %).

- The mean normalized bond strength, $u/\sqrt{f_c'}$, was not found to be reduced by ASR-induced expansion, in the range of expansions studied ($\varepsilon_{ASR} \leq 0.22\,\%$). It should be noted that the measured compressive strength at the time of testing was used for this normalization.

- For beams with confinement parameters, $0 \leq K_{tr}/d_b \leq 1.8$, and a normalized splice length, $\ell_s/\ell_d = 1.3$ (i.e., the ACI 318-19 specified splice length), the normalized bond strength relationship implied by the ACI 318-19 code equation for development length (Equation 1.7 of this report) and the recommended equation proposed by ACI Committee 408 for development length (Equation 1.10 of this report) were reasonable lower bound estimates for the normalized bond strength, $u/\sqrt{f_c'}$, measured for ASR-affected concrete beams in this study; 99.8 % of the bootstrap replicate curves were completely above the bond strength implied by the ACI Committee 408 equation and 87.0 % of the curves were completely above the bond strength implied by the ACI 318-19 equation.

7.3.2 Computational Modeling and Analysis of Beams

The computational models investigated the influence of two primary variables:

- ASR-induced expansion, $\varepsilon_{ASR} = 0\,\%, 0.15\,\%, 0.22\,\%$, considered as the unconfined linear expansion of the concrete and

- The splice condition of the tensile reinforcement, which was either continuous or spliced.

The confinement parameter was held constant in each of the models, $K_{tr}/d_b = 1.0$. The normalized splice length in the models containing splices was also constant, $\ell_s/\ell_d = 1.0$.

From the results of the numerical models, the following conclusions were developed:

- The model developed by Saouma and Perotti (2006) and Saouma (2014) for predicting the progression of ASR-induced expansion was able to predict the upward deflection and strains on reinforcing bars within the expanded uncertainty of the measurement for beams at the 0.15 % expansion level.

- For beams at the 0.22 % expansion level, the model underestimated the upward deflection by up to 39 % and the strains on reinforcing bars by up to 21 %. It should be noted that the material formulation used in the beam models did not include the effects of creep.

- For beams with continuous reinforcement, models that incorporated the bond-slip relationship proposed by the *fib* Model Code (2010) predicted the peak strength of the beams and the corresponding deflections within 5 %. The predicted forces in the reinforcing bars closely matched the forces based on strain measurements during testing.

- In order to capture the force-deflection behavior of the tested beam specimens with lapped spliced reinforcement, reduction in the bond strength in the relationship proposed by the *fib* Model Code (2010) was required in the region of the splice. For beams with ASR-induced expansions of 0 %, 0.15 %, and 0.22 %, this reduction was 25 %, 22 %, and 5 %-10 %, respectively. This supports an increase in the bond strength with increasing ASR-induced expansion for the modeled specimens. Models of the tested beams with the reduced peak bond strengths predicted the peak strength of the beams and the corresponding deflections within 5 %, however the forces in the reinforcement based on measured strains in spliced bars were underestimated.

REFERENCES

ACI 318-14. Building Code Requirements for Structural Concrete, American Concrete Institute, Farmington Hills, MI, 2014.

ACI 318-19. Building Code Requirements for Structural Concrete, American Concrete Institute, Farmington Hills, MI, 2019.

ACI Committee 408 (2003). *408R-03: Bond and Development of Straight Reinforcing Bars in Tension*. Farmington Hills: American Concrete Institute, 2008.

ASTM C39/C39M-17a. Standard Test Method for Compressive Strength of Cylindrical Concrete Specimens, ASTM International, West Conshohocken, PA, 2017.

ASTM C469/C469M-14. Standard Test Method for Static Modulus of Elasticity and Poisson's Ratio of Concrete in Compression, ASTM International, West Conshohocken, PA, 2014.

ASTM C496/C496M-11. Standard Test Method for Splitting Tensile Strength of Cylindrical Concrete Specimens, ASTM International, West Conshohocken, PA, 2004.

ASTM A615 / A615M-20, Standard Specification for Deformed and Plain Carbon-Steel Bars for Concrete Reinforcement, ASTM International, West Conshohocken, PA, 2020

ASTM A370-19e1, Standard Test Methods and Definitions for Mechanical Testing of Steel Products, ASTM International, West Conshohocken, PA, 2019

ASTM C1293-20, Standard Test Method for Determination of Length Change of Concrete Due to Alkali-Silica Reaction, ASTM International, West Conshohocken, PA, 2020

ASTM E83-16, Standard Practice for Verification and Classification of Extensometer Systems, ASTM International, West Conshohocken, PA, 2016

ASTM C33 / C33M-18, Standard Specification for Concrete Aggregates, ASTM International, West Conshohocken, PA, 2018

Ahmed, T.; Burley, E. and Rigden, S. (1998) "The Static and Fatigue Strength of Reinforced Concrete Beams Affected by Akali-Silica Reaction." *ACI Materials Journal* 95(4) pp. 376-388.

Bach, F., Thorsen, T.S., and Nielsen, M.P. (1993) "Load-carrying capacity of structural members subjected to alkali-silica reactions." Construction and Building Materials, 7(2), pp. 109-115.

Bangert, F., Kuhl, D., and Meschke, G. (2004), Chemo-hygro-mechanical modeling and numerical simulation of concrete deterioration caused by alkali-silica reaction, *International Journal for Numerical and Analytical Methods in Geomechanics*, Vol. 28, pp. 689-714.

Bažant, Z. and Steffens, A. (2000), Mathematical model for kinetics of alkali–silica reaction in concrete, *Cement and Concrete Research*, vol. 30, pp. 419-428.

Bektas, F., Turanli, L., and Ostertag, C.P. (2006), New approach in mitigating damage caused by alkali-silica reaction, *Journal of Materials Science*, vol. 51, pp. 5760-5763.

Bérubé, M.-A., Chouinard, D., Pigeon, M., Frenette, J., Boisvert, L., and Rivest, M. (2002a), "Effectiveness of sealers in counteracting alkali-silica reaction in plan or air-entrained laboratory concretes exposed to wetting and drying, freezing and thawing, and salt water," *Canadian Journal of Civil Engineering*, Vol. 29, 289-300.

Bérubé, M.-A., Chouinard, D., Pigeon, M., Frenette, J., Boisvert, L., and Rivest, M. (2002b), "Effectiveness of sealers in counteracting alkali-silica reaction in highway median barriers exposed to wetting and drying, freezing and thawing, and deicing salt," *Canadian Journal of Civil Engineering*, Vol. 29, 329-337.

Box, G.E.P., Hunter, W.G., and Hunter, J.S. (2005). *Statistics for Experimenters: An Introduction to Design, Data Analysis, and Model Building*. 2nd edition. John Wiley & Sons, New York.

Bracci, J. M., Gardoni, P., Eck, M. K., and Trejo, D., (2012), "Performance of Lap Splices in Large-Scale Column Specimens Affected by ASR and/or DEF, Report 0-5722-1, Texas Transportation Institute, Texas A&M University, College Station, Texas.

Carles-Gibergues, A., Cyr, M., Moisson, M. and Ringot, E. (2008), A simple way to mitigate alkali-silica reaction, Materials and Structures, vol. 41, pp. 73-83.

Chana, P.S. (1989), Bond strength reinforcement in concrete affected by alkali-silica reaction, Contract Report 141, Transport and Road Research Laboratory, Department of Transport, UK.

Chana, P.S. and Koroboski, G.A. (1992), Structural performance of reinforced concrete affected by alkali-silica reaction: Phase II, Contract Report 311, Transport and Road Research Laboratory, Department of Transport, UK.

Charlwood, R., Scrivener, K., and Sims, I. (2012), Recent developments in the management of chemical expansion of concrete in dams and hydro projects – Part 1: Existing structures, Hydro 2012, Bilboa Spain, October 29-30

Clark, L.A. (1989), Critical review of structural implications of alkali-silica reaction in concrete, Transport and Road Research Laboratory, Department of Transport, UK, Contract CON/9951/65.

Deschenes, D.J., Bayrak, O., and Folliard, K.J. (2009), ASR/DEF-Damaged Bent Caps: Shear Tests and Field Implications, Technical Report No. 12-8XXIA006, University of Texas, Austin, TX,

Drimalas, T., Folliard, K.J., Thomas, M.D.A., Fournier, B., and Bentivegna, A. (2012), "Study of the Effectiveness of Lithium and Silane Treatments on Field Structures Affected by ASR," Proceedings of the 14th International Conference on AAR (ICAAR), Austin, TX.

Fan, S. and Hanson, J.M. "Effect of Alkali-Silica Reaction Expansion and Cracking on Structural Behavior of Reinforced Concrete Beams." *ACI Structural Journal* Vol. 95 No. 5 (1998): 498-505.

fib (2013) *Model Code for Concrete Structures 2010*. Wilhelm Ernst & Sohn: International Federation for Structural Concrete (*fib*).

Folliard, K.J., Barborak, R., Drimalas, T., Du, L., Garber, S., Ideker, J., Ley, T., Williams, S., Juenger, M., Fournier, B., Thomas, M.D.A. (2006), Preventing ASR/DEF in New Concrete: Final Report, FHWA/TX-06/0-4085-5, Texas Department of Transportation, Austin TX, 234 pp.

Fournier, B., Bérubé, M.-A., Thomas, M.D.A., Smaoui, N., Folliard, K.J. (2004), Evaluation and Management of Concrete Structures Affected by Alkali-Silica Reaction – A Review, Report MTL 2004-11, CANMET Materials Technology Laboratory, 59 pp.

Fournier, B., Bérubé, M.-A., Folliard, K.J., and Thomas, M.D.A. (2010), Report on the Diagnosis, Prognosis, and Mitigation of Alkali-Silica Reaction (ASR) in Transportation Structures, FHWA-HIF-09-004, Federal Highway Administration, McLean, VA.

Friedman, Jerome, Trevor Hastie, and Rob Tibshirani. 2010. "Regularization Paths for Generalized Linear Models via Coordinate Descent." *Journal of Statistical Software* 33 (1): 1.

Habibi, F., Sheikh, S.A., Vecchio, F., and Panesar, D.K. (2018) "Effects of Alkali-Silica Reaction on Concrete Squat Shear Walls" *ACI Structural Journal*, V. 115(5): 1329-1339

Hallquist, J. (2012), LS-DYNA Keyword User's Manual, Livermore Software Technology Corporation, Livermore, CA, Version 971

Hansen, W.C., (1944), "Studies relating to the mechanism by which the alkali-aggregate reaction produces expansion in concrete", *Journal of the American Concrete Institute*, Vol. 15, p. 213-227.

Hastie, Trevor, Robert Tibshirani, and Martin Wainwright. *Statistical learning with sparsity: the lasso and generalizations*. CRC press, 2015.

Jensen, A.D., Chatterji, S., Christensen, P., and Thaulow, N. (1984), Studies of alkali–silica reaction. Part II – Effect of air-entraining on expansion, Cement and Concrete Research, Vol. 14, pp. 311–314.

Kennedy, W. J. Jr and Gentle, J. E. (1980) Statistical Computing Marcel Dekker.

Kobayashi, K., Inoue, S., Yamazaki, T., and Nakano, K. (1987) "Structural behaviour of prestressed concrete beams affected by alkali-aggregate reaction. *Transcriptions of the Japan Concrete Institute*, vol 9, 1987, pp 211-218.

Lane, D.S. and Ozyildirim, H.C. (1995), Use of Fly Ash, Slag, or Silica Fume to Inhibit Alkali-Silica Reactivity, Report No. 95-R21, Virginia Transportation Research Council

Lane, D.S. and Ozyildirim, C. (1999), Preventive measures for alkali-silica reactions (binary and ternary systems), Cement and Concrete Research, Vol. 29, pp. 1281-1288.

Larive, C., 1998, "Apports Combin'es de l'Experimentation et de la Modélisation à la Comprehension del'Alcali-Réaction et de ses Effets Mécaniques," PhD thesis, Thése de Doctorat, Laboratoire Central des Ponts et Chaussées, Paris.

Mander, J.B., Karthik, M.M., and Hurlebaus, S. (2015), "Structural Assessment of "D" Regions Affected by Premature Concrete Deterioration: Technical Report." Report 0-5722-2, Texas Transportation Institute, Texas A&M University, College Station, Texas.

Mather, B. (1999), "How to make concrete that will not suffer deleterious alkali-silica reaction," Cement and Concrete Research, Vol. 29, pp. 1277-1280.

McCoy, W.J., and Caldwell, A.G. (1951), New approach in inhibiting alkali–aggregate expansion. ACI Journal, Vol. 22, No. 9, pp. 693–706.

McLeish, A. (1990), Structural implications of the alkali-silica reaction in concrete, Contract Report 177, Transport and Road Research Laboratory, Department of Transport, UK.

Monette, L.J., Gardner, N.J., and Grattan-Bellew, P.E. (2002). "Residual Strength of Reinforced Concrete Beams Damaged by Alkali-Silica Reaction—Examination of Damage Rating Index Method." ACI Materials Journal, 99, 42–50.

Morenon, P., Multon, S., Sellier, A., Grimal, E., Hamon, F. Kolmayer, P. (2019) "Flexural performance of reinforced concrete beams damaged by Alkali-Silica Reaction" *Cement and Concrete Composites*. 104 (2019) 103412.

Multon, S., 2003, "Evaluation Expérimentale et Théorique des Effets Mécaniques de l'Alcali Réaction sur des Structures Modéles," PhD thesis, Université de Marne la Vallée, France.

Multon, S., Seignol, J.F., and Toutlemonde, F. (2005). "Structural Behavior of Concrete Beams

Affected by Alkali-Silica Reaction. *ACI Materials Journal*, 102, 67–76.

Murray, Y.D. (2007), "Users Manual for LS-DYNA Concrete Material Model 159," FHWA-HRT-05-062, Federal Highway Administration, McLean, VA.

Murray, Y.D., Abu-Odeh, A., and Bligh, R. (2007), "Evaluation of LS-DYNA Concrete Material Model 159," FHWA-HRT-05-063, Federal Highway Administration, McLean, VA.

Myers, Raymond H, Douglas C Montgomery, and Christine M Anderson-Cook. 2016. *Response Surface Methodology: Process and Product Optimization Using Designed Experiments*. John Wiley & Sons.

Orangun, C.O., Jirsa, J.O., and Breen, J.E., (1977), A re-evaluation of test data on development length and splices, *Journal of American Concrete Institute,* Vol 74, pp. 114-122.

Pesavento, F., Gawin, D., Wyrzykowski, M., Schrefler, B.A., and Simoni, L. (2012), Modeling alkali-silica reaction in non-isothermal, partially saturated cement-based materials, Computer Methods in Applied Mechanics and Engineering, Vol. 225-228, pp. 95-115.

Phan, L.T., Sadek, F, Thonstad, T.E., Lew, H.S., Marcu, S., Philip, J., (2019), "Effects of Alkali-Silica Reaction on Mechanical Properties and Structural Capacities of Reinforced Concrete Structures" Structural Mechanics in Reactor Technology (SMiRT) 25, Charlotte, NC, United States, August 2019.

Pleau, R., Bérubé, M.A., Pigeon, M., Fournier, B., and Raphael, S. (1989), Mechanical behavior of concrete affected by ASR. In Proceedings of the Eight International Conference on Alkali–Aggregate Reaction in Concrete, Kyoto, Japan, August 1989. Edited by K. Okada, S. Nishibayashi and M. Kawamura. pp. 721–726.

R Core Team. (2020). *R: A Language and Environment for Statistical Computing*. Vienna, Austria: R Foundation for Statistical Computing. https://www.R-project.org/.

Rezansoff, T.; Konkankar, U.S.; and Fu, Y.C. (1992) "Confinement Limits for Tension Lap Splices under Static Loading." *Canadian Journal of Civil Engineering*, 19, pp. 447-453

Sadek, F., Thonstad, T., Marcu, S., Weigand, J.M., Barrett, T.J., Lew, H.S., Phan, L.T., and Pintar, A.L. (2021) "Structural Performance of Nuclear Power Plant Concrete Structures Affected by Alkali-Silica Reaction (ASR) Task 1: Assessing In-Situ Mechanical Properties of ASR-Affected Concrete" NIST TN 2121, National Institute of Standards and Technology, Gaithersburg, Maryland.

Saouma, V. and Perotti, L. (2006), "Constitutive model for alkali-aggregate reactions, ACI Material Journal, 103(194-202).

Saouma, V. (2014), Numerical Modeling of AAR, CRC Press, Taylor & Francis Group, Boca Raton, FL.

Smaoui, N., Bissonnette, B., Bérubé, M.A., Fournier, B., and Durand, B. (2006), Mechanical properties of ASR-affected concrete containing fine or coarse reactive aggregates, Journal of ASTM International, Vol. 3, No. 3, pp. 1-16.

Snyder, K., and Lew, H.S., (2013), "Alkali-Silica Reaction Degradation of Nuclear Power Plant Concrete Structures: A Scoping Study" NISTIR 7937, National Institute of Standards and Technology, Gaithersburg, Maryland.

Stanton, T.E. (1940), "Expansion of Concrete Through Reaction Between Cement and Aggregate," Proceedings, *American Society of Civil Engineers*, Vol. 66, p. 1781-1811.

Swamy, R.N., and Al-Asali, M.M. (1989). "Effect of Alkali-Silica Reaction on the Structural Behavior of Reinforced Concrete Beams." *ACI Materials Journal*, 86, 451–459.

Swamy, R.N. and Al-Asali, M.M. (1990) "Control of Alkali-Silica Reaction in Reinforced Concrete Beams." *ACI Materials Journal,* 87(1), pp. 38-46.

Taylor, H.F.W. (1990), Cement Chemistry, Academic Press, New York.

Tibshirani, R. (1996). "Regression Shrinkage and Selection via the Lasso." *Journal of the Royal Statistical Society: Series B (Methodological)* 58 (1): 267–88.

Thomas, M.D.A, Fournier, B., and Folliard, K.J. (2008), Report on Determining the Reactivity of Concrete Aggregates and Selecting Appropriate Measures for Preventing Deleterious Expansion in NewConcrete Construction, FHWA-HIF-09-001, Federal Highway Administration, McLean, VA.

Thomas, M.D.A, Folliard, K.J., Fournier, B., and Ahlstrom, G. (2012a), "A Prescriptive Specification for the Selection of Measures for Preventing Alkali-Silica Reaction," Proceedings of the 14th International Conference on AAR (ICAAR), Austin, TX.

Thomas, M.D.A, Fournier, B., and Folliard, K.J. (2012b), Selecting Measures to Prevent Deleterious Alkali-Silica Reaction in Concrete: Rationale for the AASHTO PP65 Prescriptive Approach, FHWAHIF-13-002, Federal Highway Administration, McLean, VA,

Ulm, F.-J., Coussy, O., Kefei, L., Larive, C. (2000), Thermo-Chemo-Mechanics of ASR expansion in concrete structures, Journal of Engineering Mechanics, Vol. 126, pp. 233-242.

APPENDIX A
MEASUREMENT UNCERTAINTIES

This appendix presents measurement uncertainties for the instruments/devices used to measure structural responses in this report.

Table A-1. Measurement Uncertainty

Measurement/Component	Type	Component Standard Uncertainty	Combined Standard Uncertainty	Total Expanded Uncertainty (k=2)
Actuator position				
Uncertainty in secondary standard	B	0.2 mm (0.006 in)	0.2 mm (0.007 in)	0.4 mm (0.015 in)
Uncertainty in calibration procedure (N=32)	A	0.2 mm (0.004 in)		
Actuator load				
Uncertainty in secondary standard	B	1.3 kN (0.3 kip)	1.3 kN (0.3 kip)	2.6 kN (0.6 kip)
Uncertainty in calibration procedure (N=32)	A	0.4 kN (0.1 kip)		
Compressive Stress, 4 in × 8 in Concrete Cylinder				
Uncertainty in secondary standard	B	165 kPa (23.9 psi)	174 kPa (25.2 psi)	347 kPa (50.4 psi)
Uncertainty in calibration procedure (N=32)	A	54.9 kPa (7.96 psi)		
Compressive Stress, 6 in × 12 in Concrete Cylinder				
Uncertainty in secondary standard	B	73.2 kPa (10.6 psi)	77.1 kPa (11.2 psi)	154 kPa (22.4 psi)
Uncertainty in calibration procedure (N=32)	A	24.4 kPa (3.54 psi)		
Compressive Stress, 3 in × 6 in Concrete Core				
Uncertainty in secondary standard	B	341 kPa (49.4 psi)	359 kPa (52.1 psi)	718 kPa (104 psi)
Uncertainty in calibration procedure (N=32)	A	114 kPa (16.5 psi)		

Table A-1 (Continued): Measurement Uncertainty

Measurement/Component	Type	Component Standard Uncertainty	Combined Standard Uncertainty	Total Expanded Uncertainty (k=2)
Axial Extensometer, 4 in gage length				
Uncertainty in secondary standard	A/B	1.52 μm (0.00006 in)	16.9 μm (0.00066 in)	33.7 μm (0.00132 in)
Uncertainty in calibration procedure (N=20)	A	16.8 μm (0.00066 in)		
Axial Extensometer, 2 in gage length				
Uncertainty in secondary standard	A/B	1.52 μm (0.00006 in)	20.2 μm (0.00079 in)	40.3 μm (0.00158 in)
Uncertainty in calibration procedure (N=20)	A	20.1 μm (0.00079 in)		
Axial Compressive Strain, 4 in × 8 in Concrete Cylinder (calculated using 4 in gage length axial extensometer)				
Uncertainty in secondary standard	A/B	15.0 με	166 με	331 με
Uncertainty in calibration procedure (N=20)	A	165 με		
Axial Compressive Strain, 3 in × 6 in Concrete Core (calculated using 2 in gage length axial extensometer)				
Uncertainty in secondary standard	A/B	30.0 με	396 με	792 με
Uncertainty in calibration procedure (N=20)	A	395 με		
Displacement Transducer				
Uncertainty in secondary standard (N=8)	A/B	2 μm (0.00006 in)	0.3 mm (0.01 in)	0.6 mm (0.02 in)
Uncertainty in calibration procedure (N=20)	A	0.3 mm (0.01 in)		

APPENDIX B
DRAWINGS

This appendix contains drawings that describe the reinforcement and instrumentation configuration for all 19 beam specimens.

Bearing Pad (TYP)
4 in x 11 in x 1 in
[102 mm x 279 mm x 25 mm]

STIRRUPS — Varies — 11 @ 3 in [76 mm] — Varies — 11 @ 3 in [76 mm] — Varies

End Cover
1 in [25 mm]

A

A

LOADING — 30 in [762 mm] — 44 in [1118 mm] — 30 in [762 mm]

138"

ELEVATION

11 in [279 mm]

No.4 A615 Gr 60
[Ø13 mm]

No.4 A615 Gr 60
[Ø13 mm]

13 in [330 mm]

3 in [76 mm]

Clear Cover (TYP)
1 in [25 mm]

2.0 in [51 mm]

2.5 in [64 mm]

No.8 A615 Gr 60 [Ø25 mm]

SECTION A-A

NUM	BEAM DESCRIPTION	
	STIRRUP SPACING	SPLICE LENGTH
1,5	18 in [457 mm]	18 in [457 mm]
2,6	16 in [406 mm]	32 in [813 mm]
3,7	5.5 in [140 mm]	12 in [305 mm]
4,8	5.5 in [140 mm]	22 in [559 mm]
9,11,12,17,19	8 in [203 mm]	22 in [559 mm]
13	None	32 in [813 mm]
14	4.5 in [114 mm]	18 in [457 mm]
15	8 in [203 mm]	10 in [254 mm]
16	8 in [203 mm]	32 in [813 mm]
10,18	8 in [203 mm]	None

Notes:

1. Design compressive strength of 5 ksi [34.5 MPa]
2. Beams 17 and 18 are reference specimens
3. Stirrup spacing and splice in constant moment region are symmetric about midspan

National Institute of Standards and Technology

Assembly: Task 2 Beam Specimens	Drawn By: TT
Title: Beam Geometry	Designed By: TJB / TT
File Name:	Checked By: TJB
Contacts:	Drawing: 1 of 4
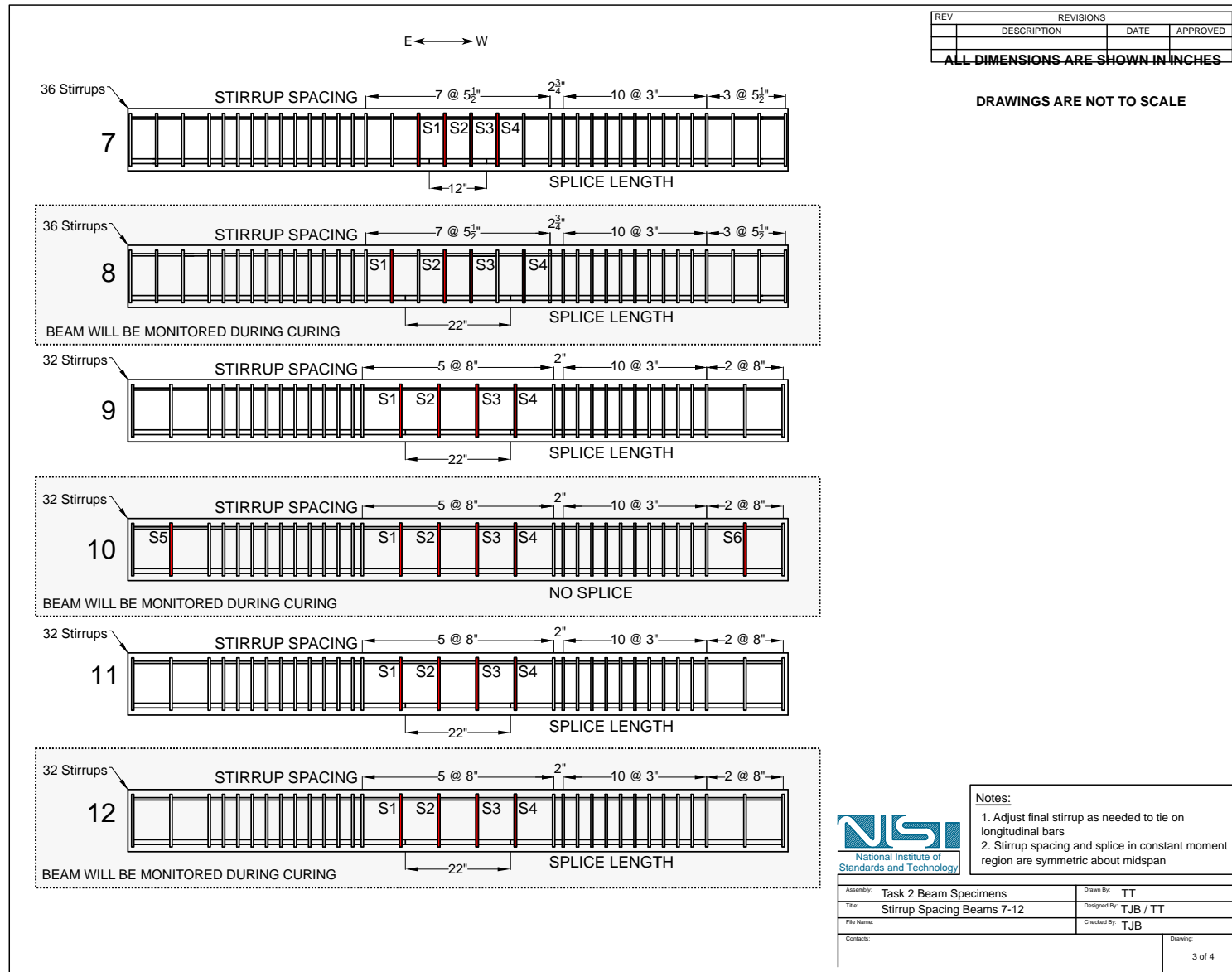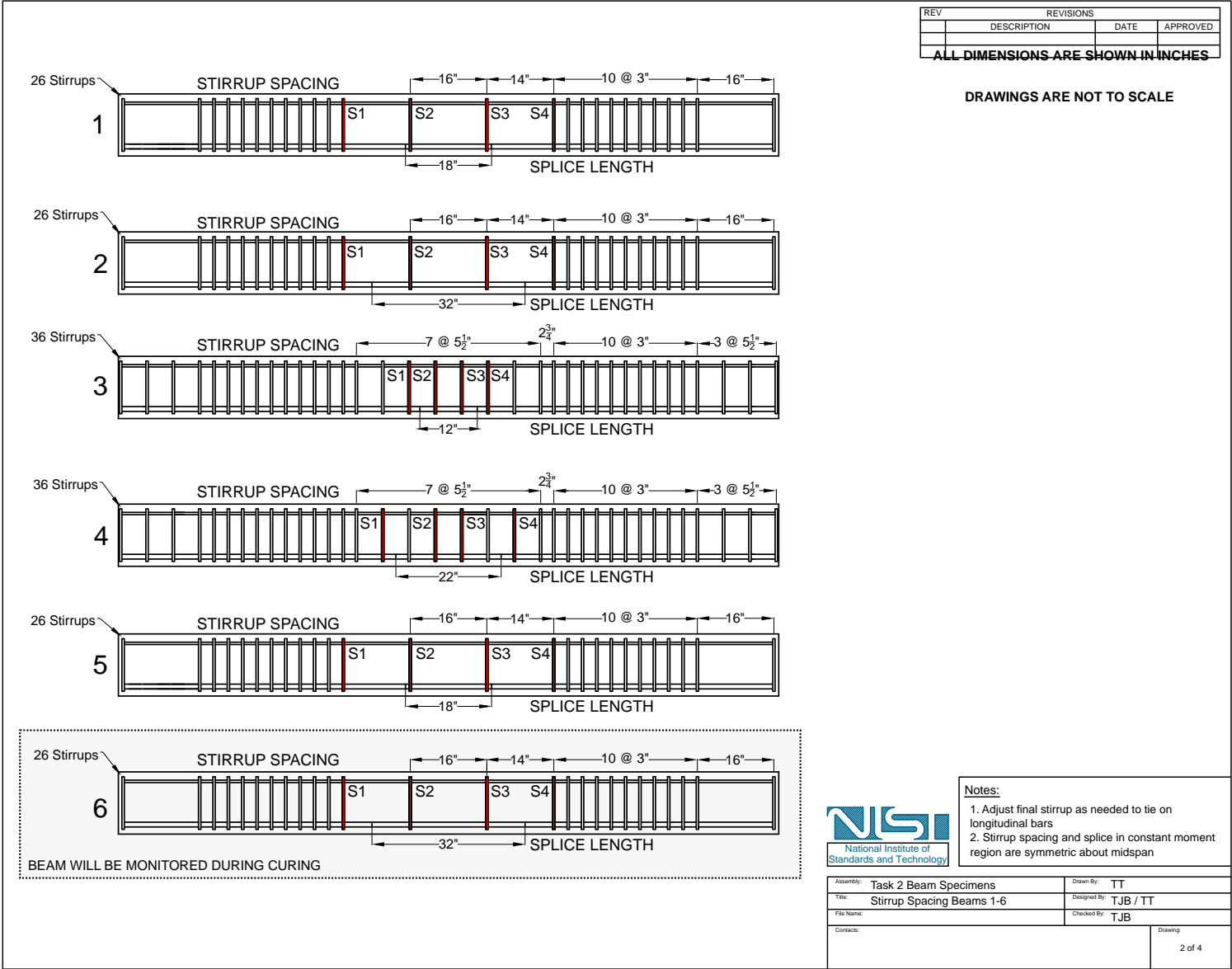
146

NOTE: South side of beam looking north

ELEVATION

SECTION A-A

NOTE: Curvatures will be measured on south side of beam during testing

REV	REVISIONS		
	DESCRIPTION	DATE	APPROVED

ALL DIMENSIONS ARE SHOWN IN INCHES

DRAWINGS ARE NOT TO SCALE

INSTRUMENTATION		
	NAME	INSTRUMENT
MOD1-ai0	DN1	Novotechnik TR-100
MOD1-ai1	DN2	Novotechnik TR-100
MOD1-ai2	DN3	Novotechnik TR-100
MOD1-ai3	DN4	Novotechnik TR-100
MOD1-ai4	DN5	Novotechnik TR-100
MOD1-ai5	DS1	Novotechnik TR-100
MOD1-ai6	DS2	Novotechnik TR-100
MOD1-ai7	DS3	Novotechnik TR-100
MOD2-ai0	DS4	Novotechnik TR-100
MOD2-ai1	DS5	Novotechnik TR-100
MOD2-ai2	C1T	Alliance LRE-19-050-R-50-A-10
MOD2-ai3	C1B	Alliance LRE-19-050-R-50-A-10
MOD2-ai4	C2T	Alliance LRE-19-050-R-50-A-10
MOD2-ai5	C2B	Alliance LRE-19-050-R-50-A-10
MOD2-ai6	C3T	Alliance LRE-19-050-R-50-A-10
MOD2-ai7	C3B	Alliance LRE-19-050-R-50-A-10
MOD3-ai0	C4T	Alliance LRE-19-050-R-50-A-10
MOD3-ai1	C4B	Alliance LRE-19-050-R-50-A-10
MOD3-ai2	C5T	Alliance LRE-19-050-R-50-A-10
MOD3-ai3	C5B	Alliance LRE-19-050-R-50-A-10
MOD3-ai4	DN0	Celesco PT-101-20A-7374
MOD3-ai5	DS0	Celesco PT-101-20A-7374
MOD3-ai6	R1	Accustar Clinometer 02111102-000
PCI6363-ai18	R2	Accustar Clinometer 02111102-000
PCI6363-ai19		

Notes:

National Institute of Standards and Technology

Assembly:	Task 2 Beam Specimens	Drawn By:	TT
Title:	Instrumentation Layout	Designed By:	TJB / TT
File Name:		Checked By:	
Contacts:			Drawing: 1 of 1

APPENDIX C
MEASURED DATA

This Appendix presents the measured data for all 19 beam specimens. The measurements follow the same order as in Chapter 4.

Displacement

The figures below show the measured deflections during testing on the North and South sides of the beams (the beam specimens were placed on supports spanning East to West) for the beam specimens. Deflections were measured at midspan, the two loading points, and halfway between each of the loading points and the adjacent support. The measurements in the figure are labeled based on their locations along the beam span, with midspan serving as the origin (x=0). The actuator displacement is shown in grey for reference.
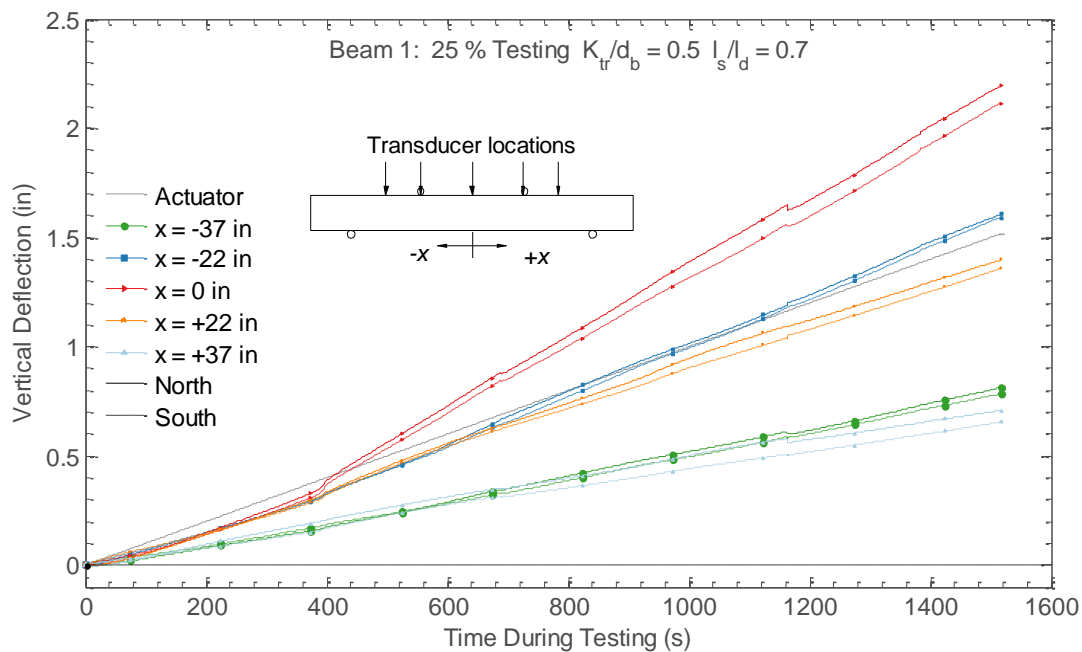
Figure C.1. Measured deflections for Beam 1
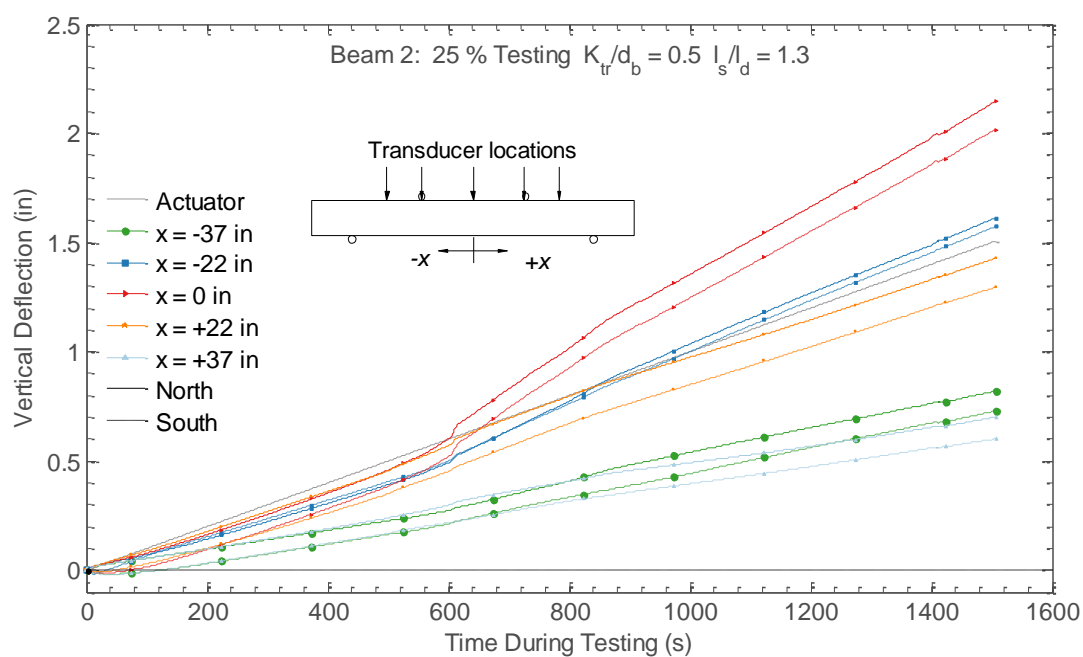
Figure C.2. Measured deflections for Beam 2
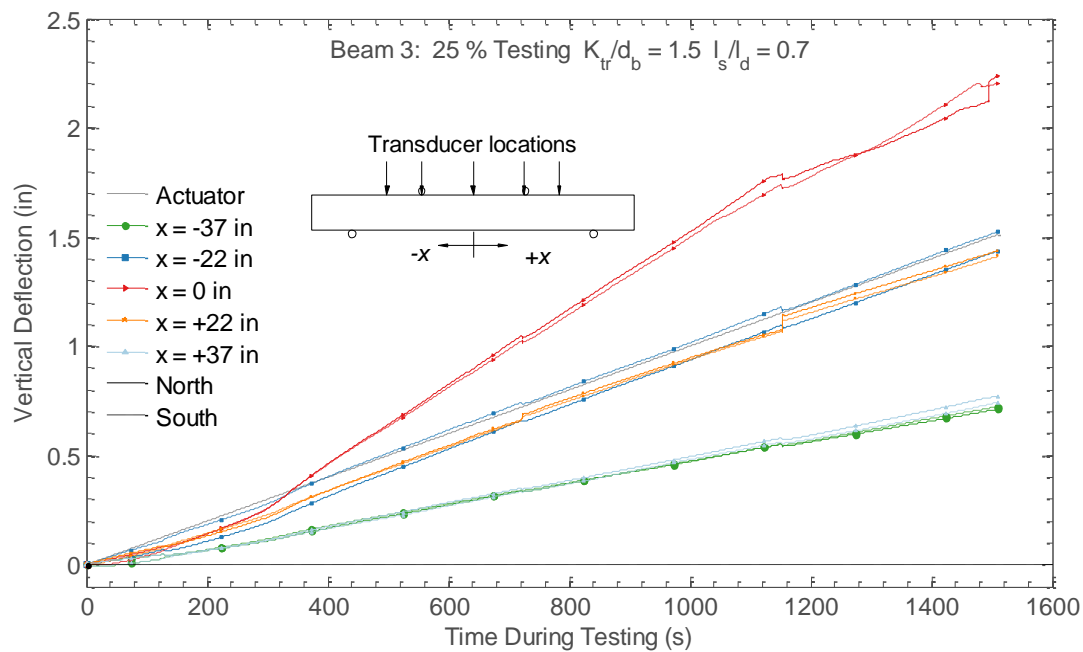
Figure C.3. Measured deflections for Beam 3

153
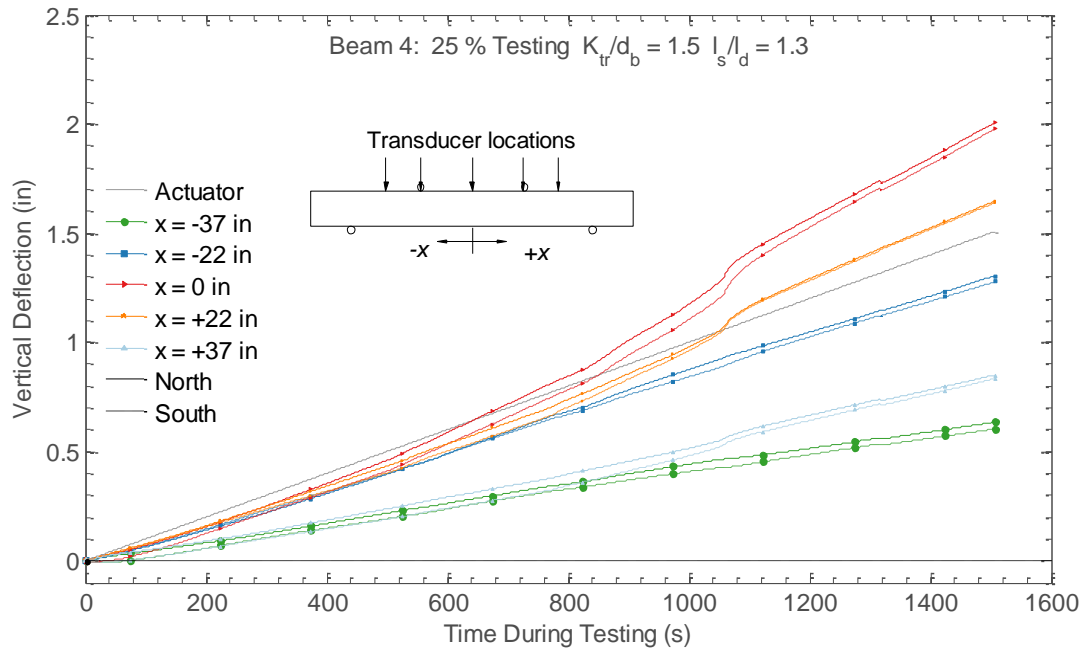
Figure C.4. Measured deflections for Beam 4
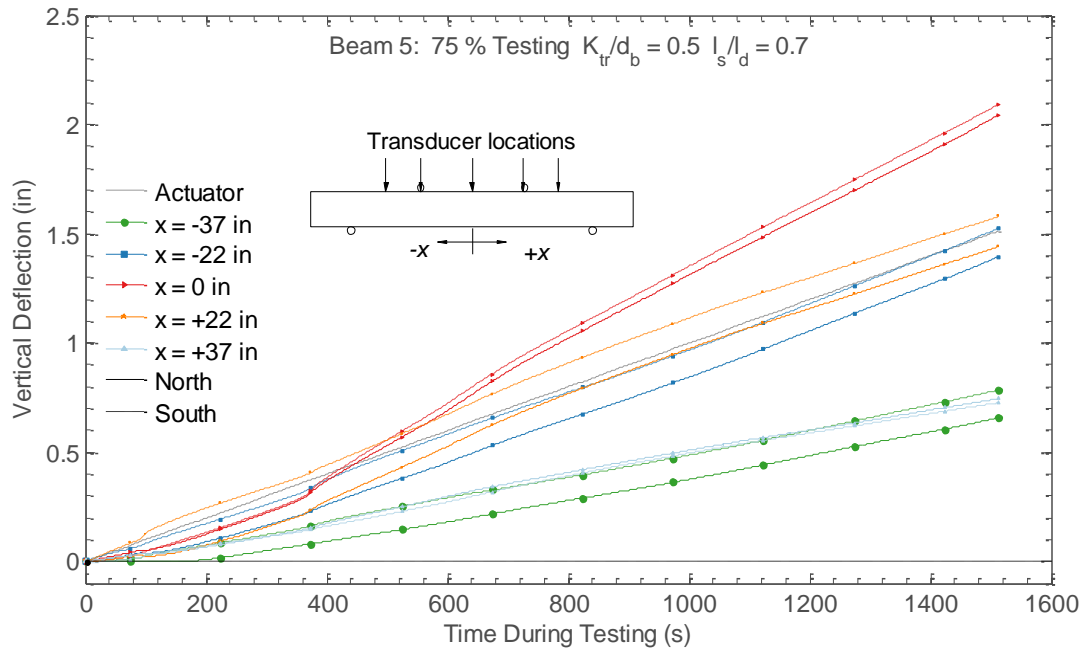
Figure C.5. Measured deflections for Beam 5

154
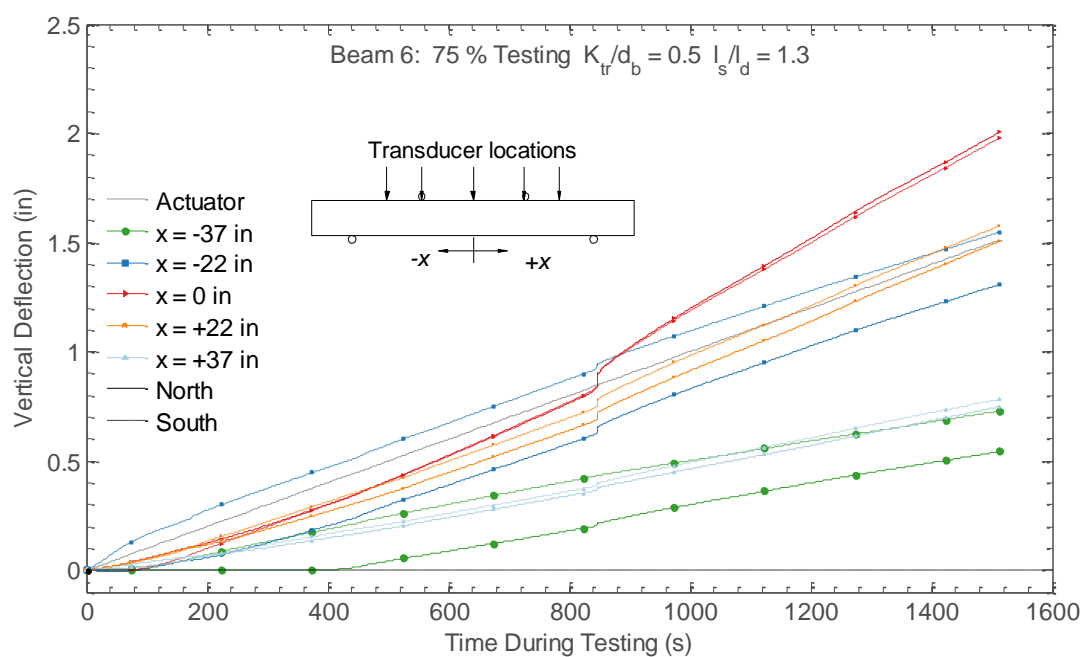
Figure C.6. Measured deflections for Beam 6
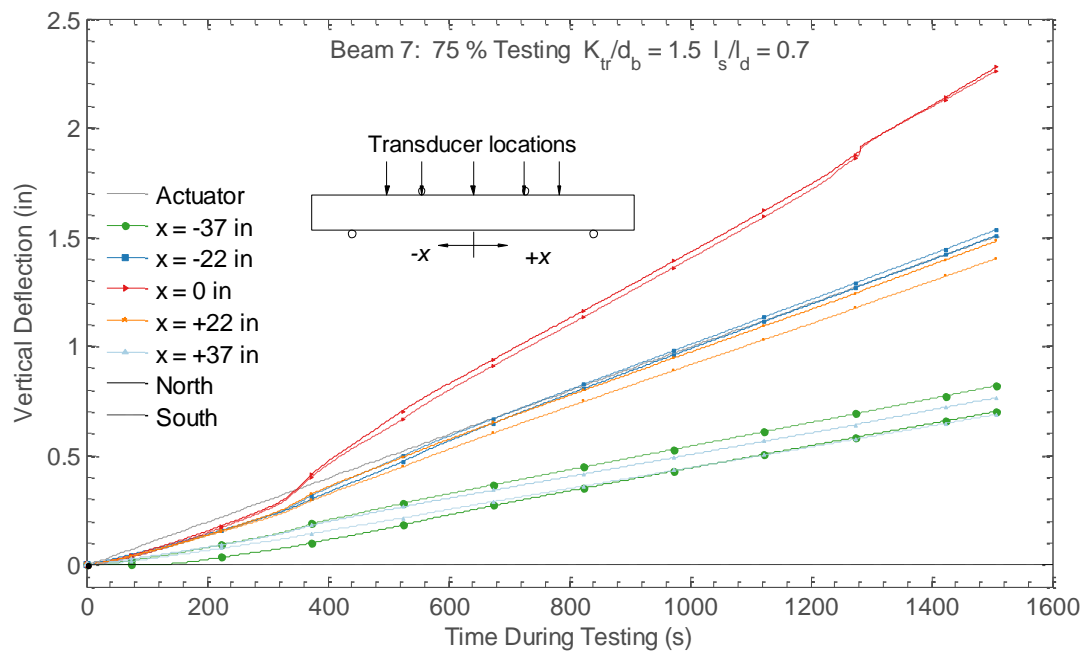
Figure C.7. Measured deflections for Beam 7

155
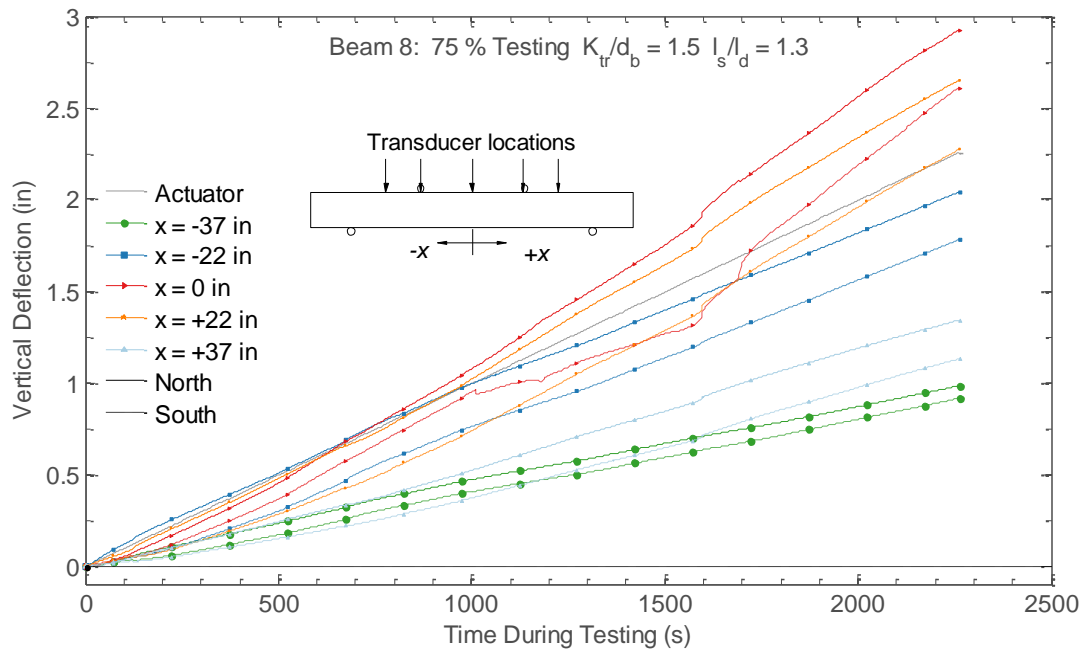
Figure C.8. Measured deflections for Beam 8
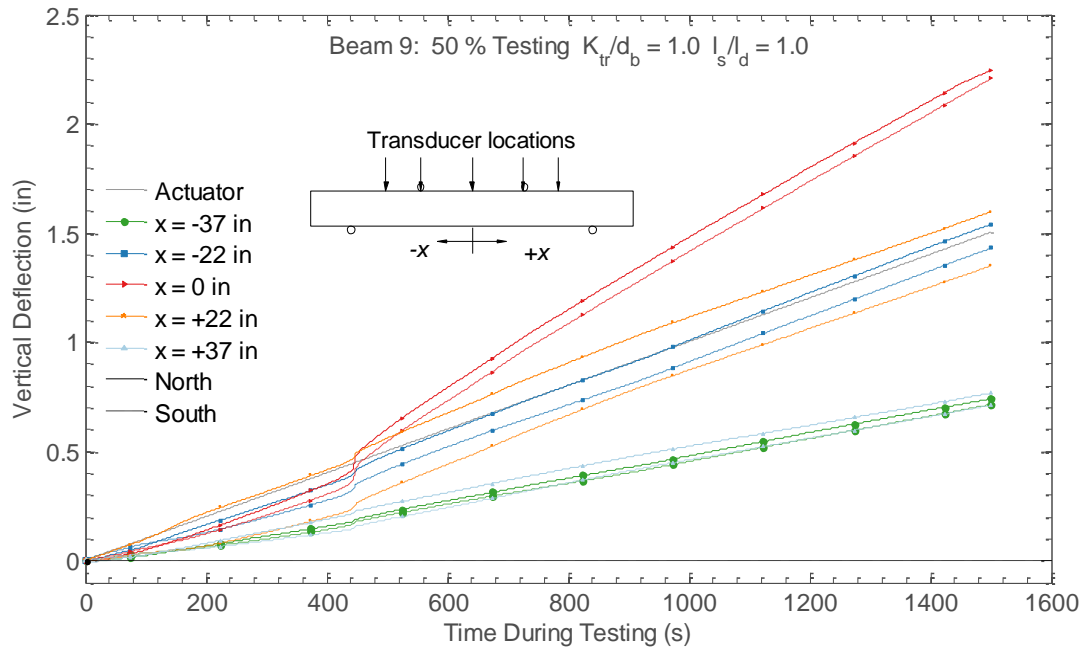
Figure C.9. Measured deflections for Beam 9

156
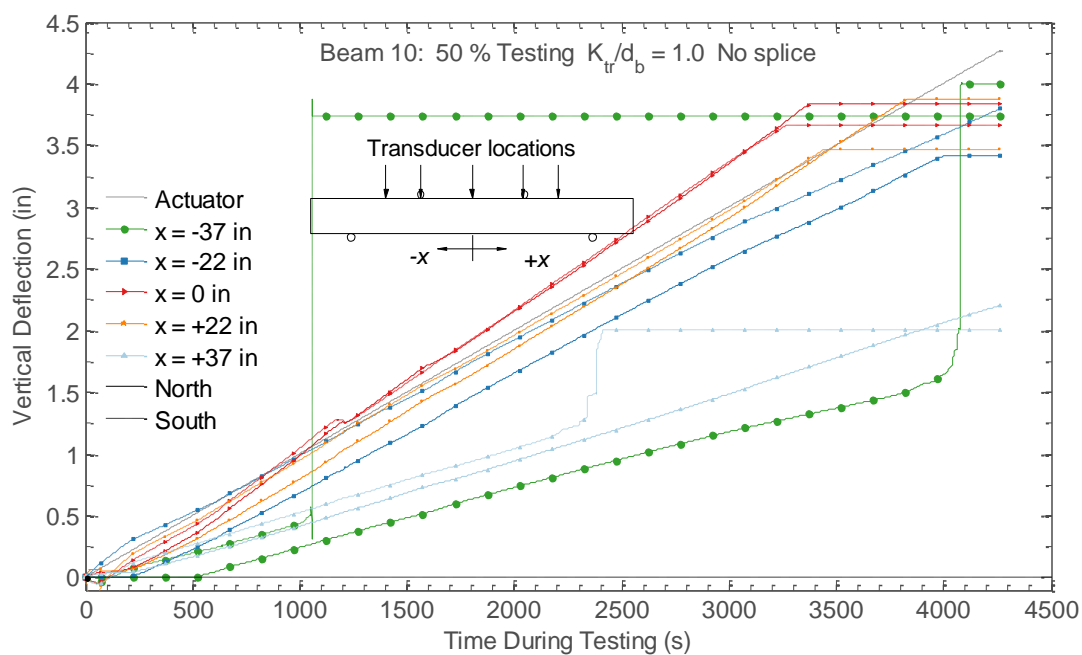
Figure C.10. Measured deflections for Beam 10
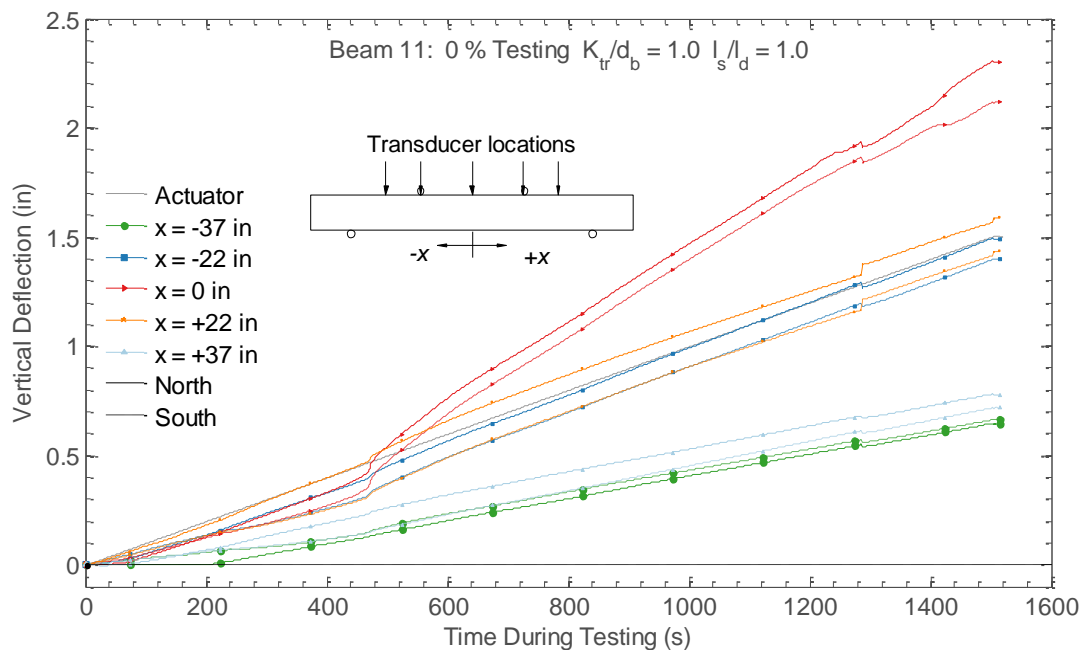
Figure C.11. Measured deflections for Beam 11

157
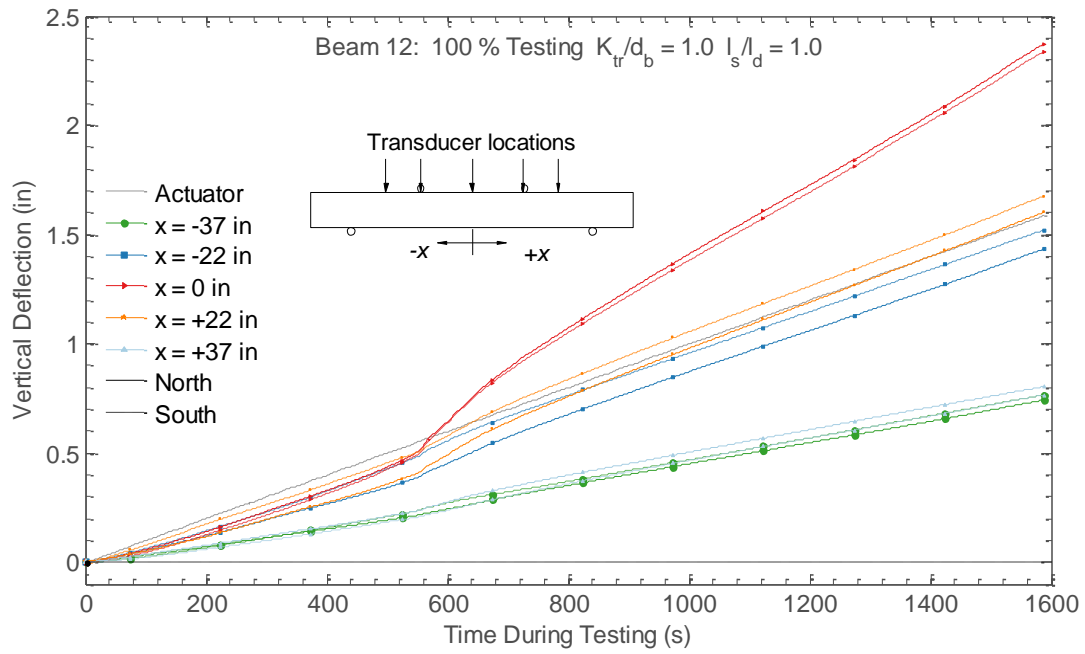
Figure C.12. Measured deflections for Beam 12
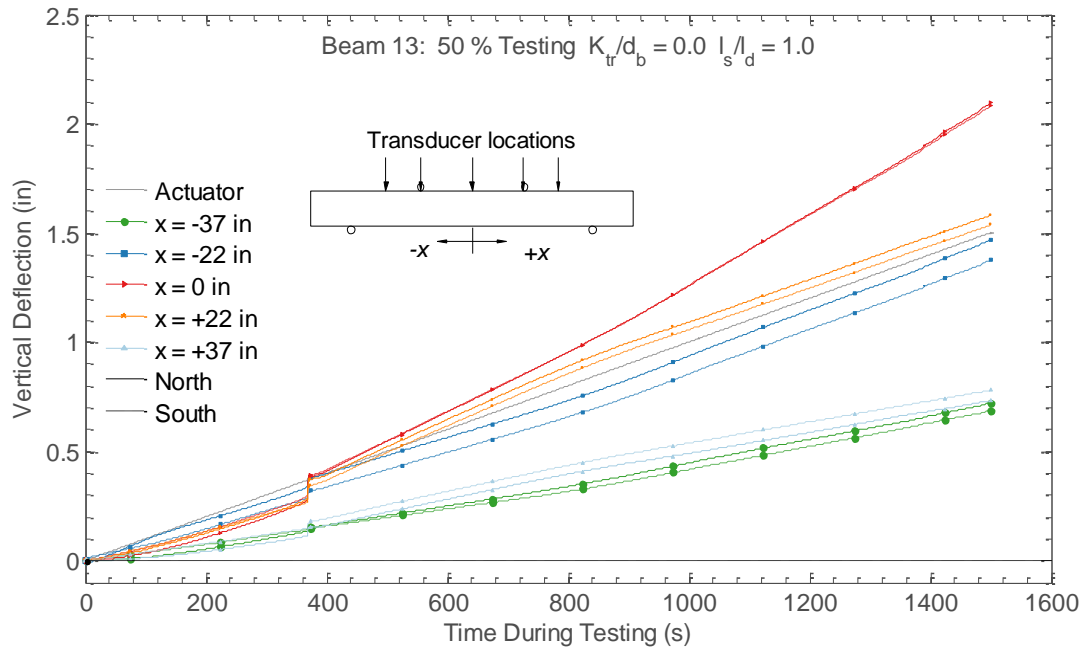
Figure C.13. Measured deflections for Beam 13

158
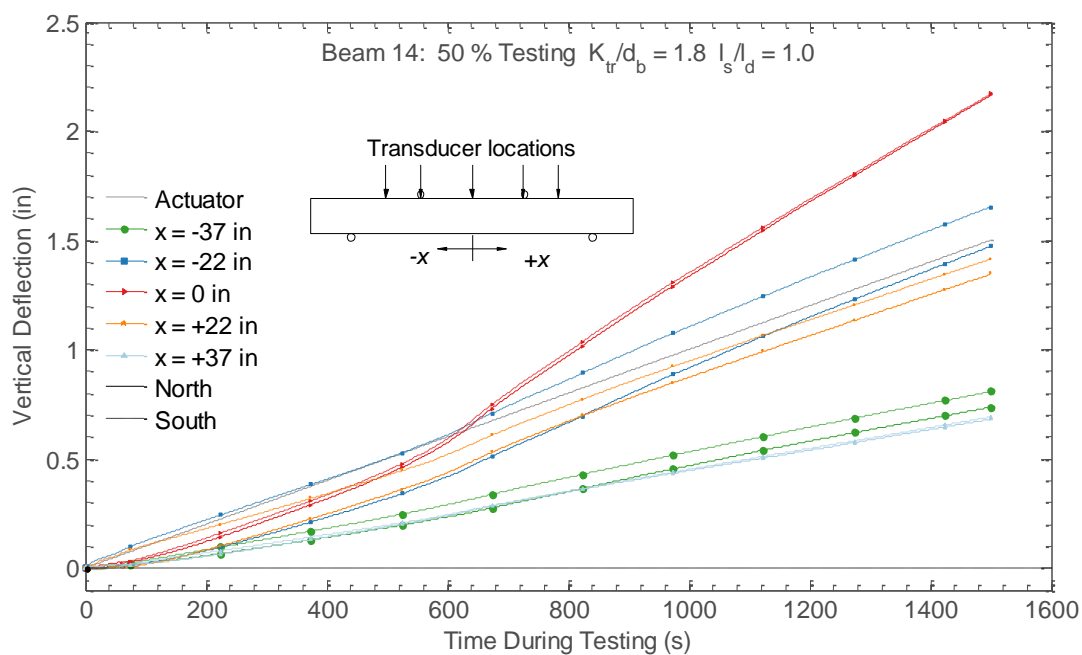
Figure C.14. Measured deflections for Beam 14
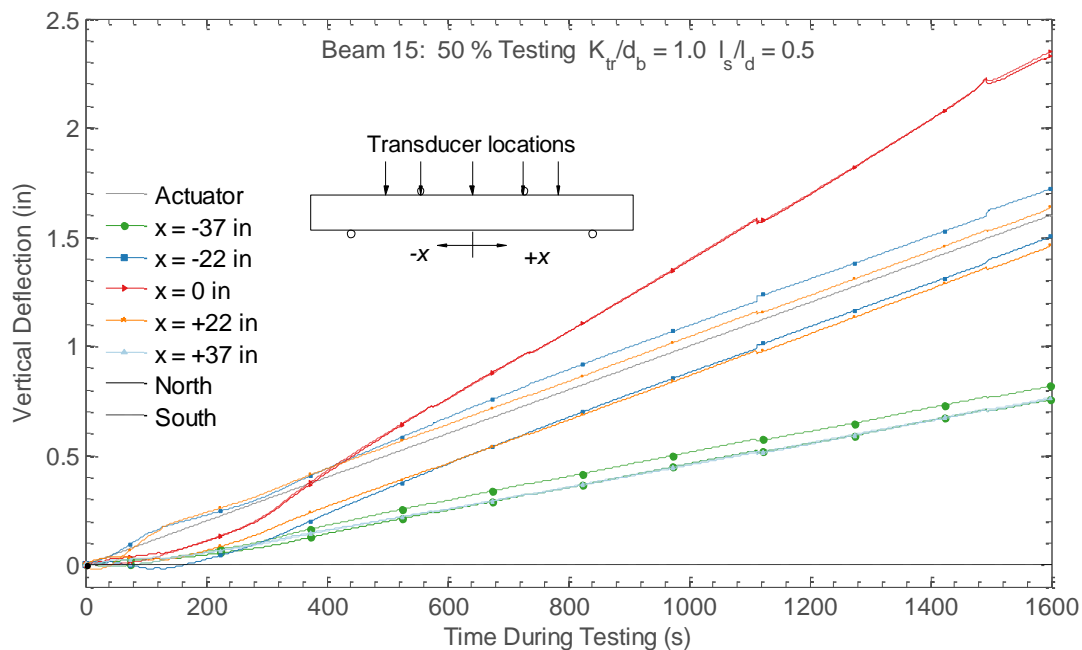
Figure C.15. Measured deflections for Beam 15

159
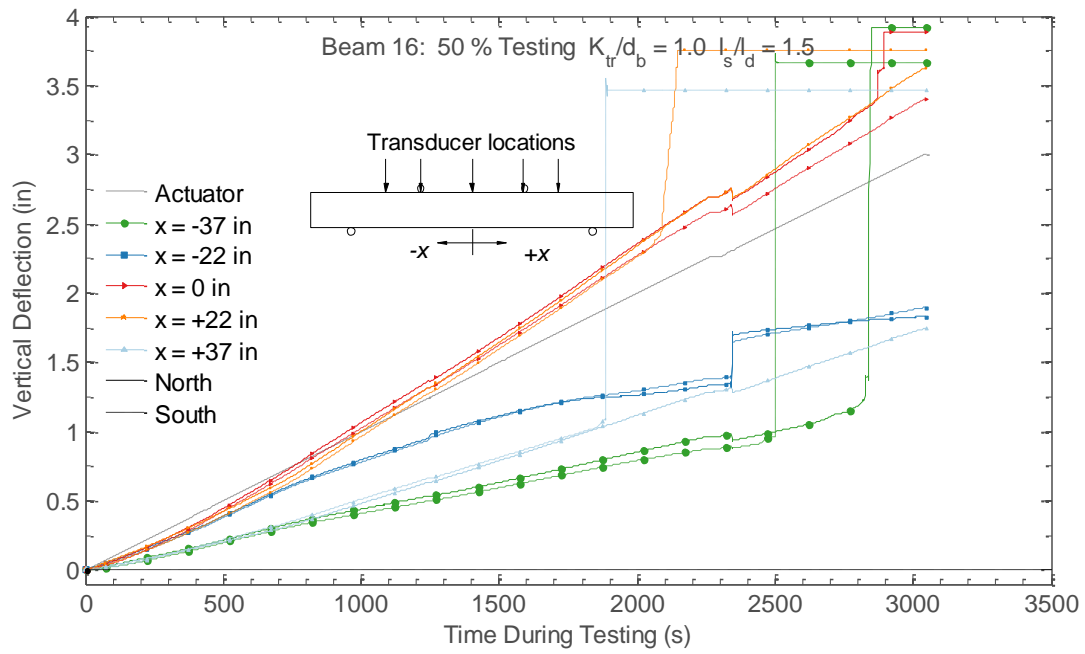
Figure C.16. Measured deflections for Beam 16
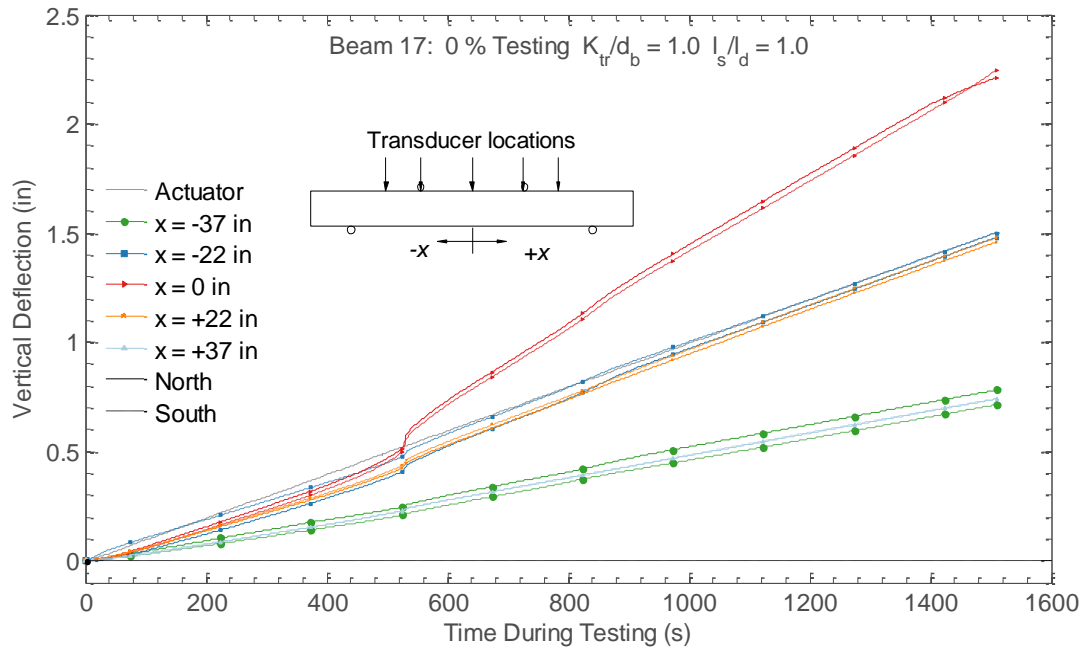
Figure C.17. Measured deflections for Beam 17

160
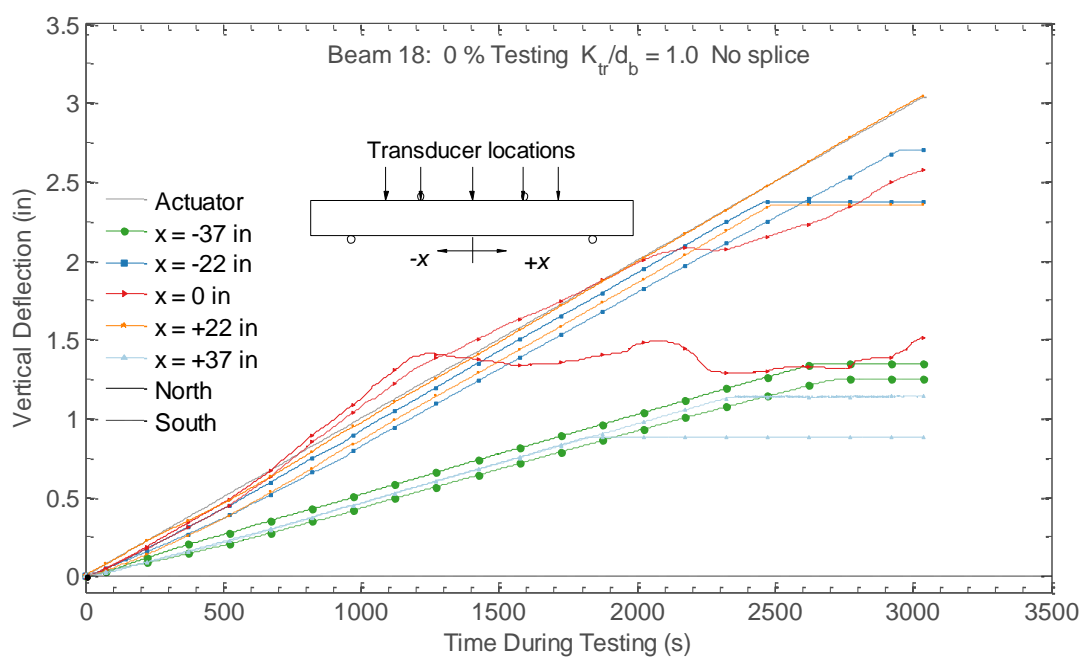
Figure C.18. Measured deflections for Beam 18
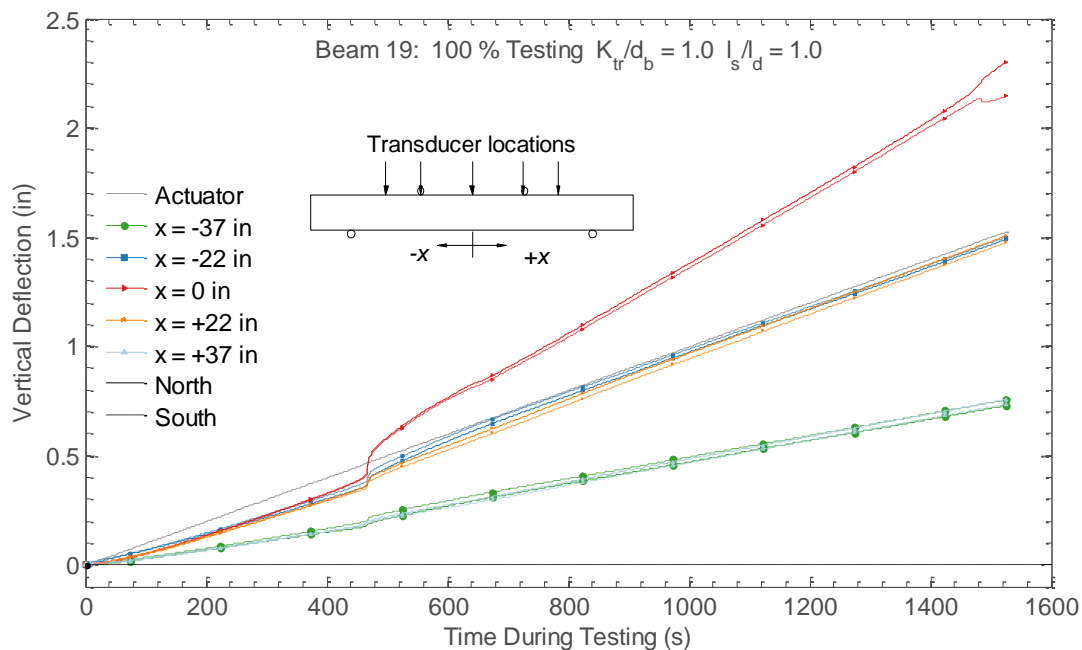
Figure C.19. Measured deflections for Beam 19

161

Deflection Profile

The figures below show the deflection profiles for the beam specimens at the maximum moment strength and at several intermediate levels of applied moment corresponding to fractions of the ACI nominal moment strength for the beams. The vertical deflections at the supports were assumed to be negligible.
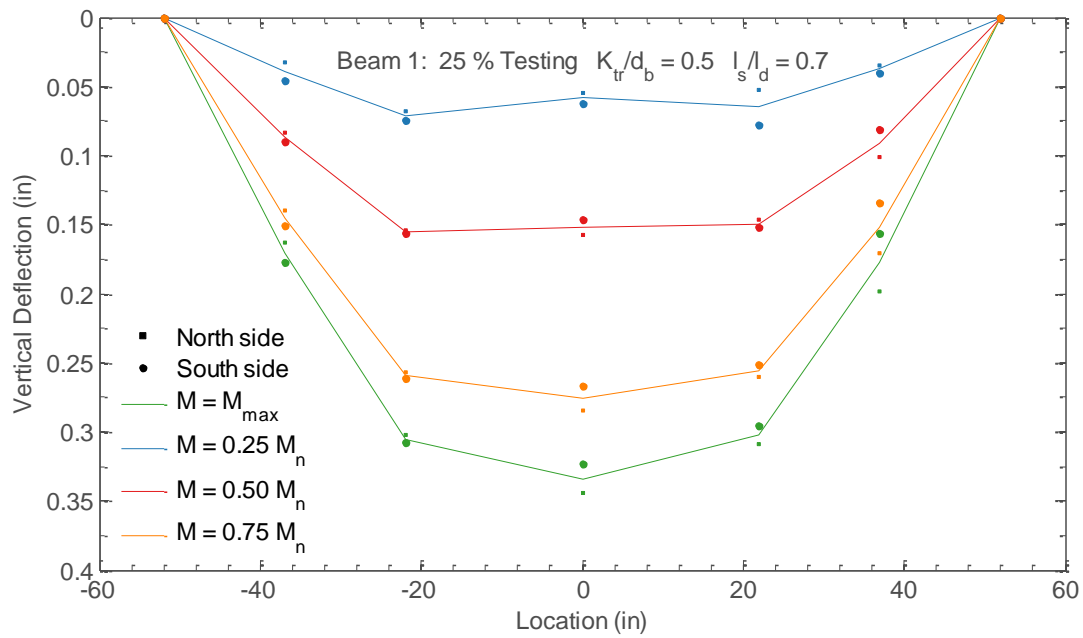
Figure C.20. Measured deflection profiles for Beam 1
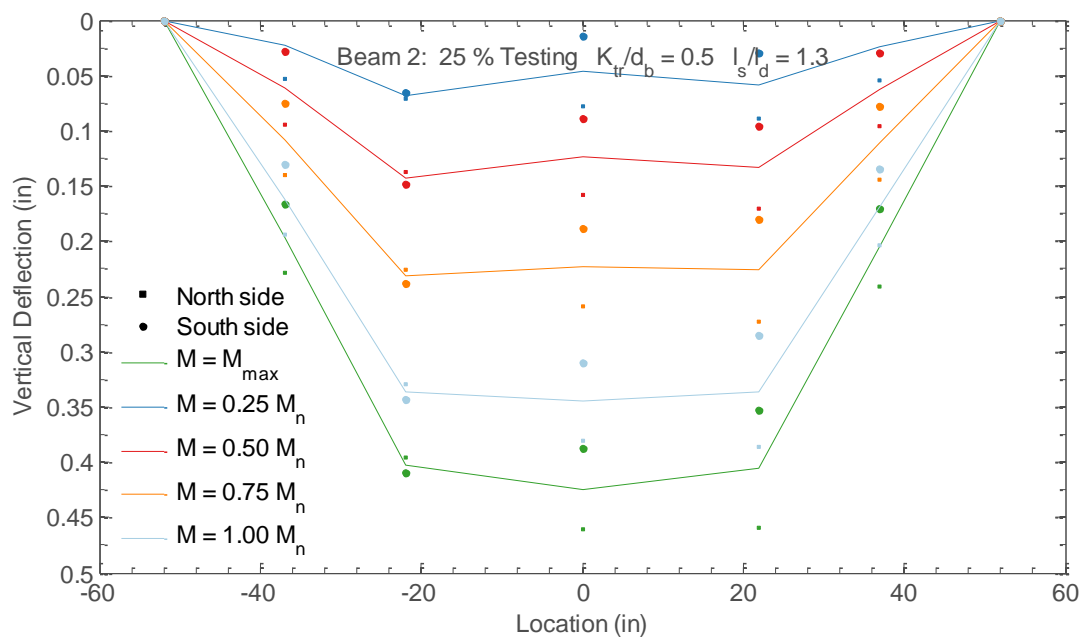
Figure C.21. Measured deflection profiles for Beam 2
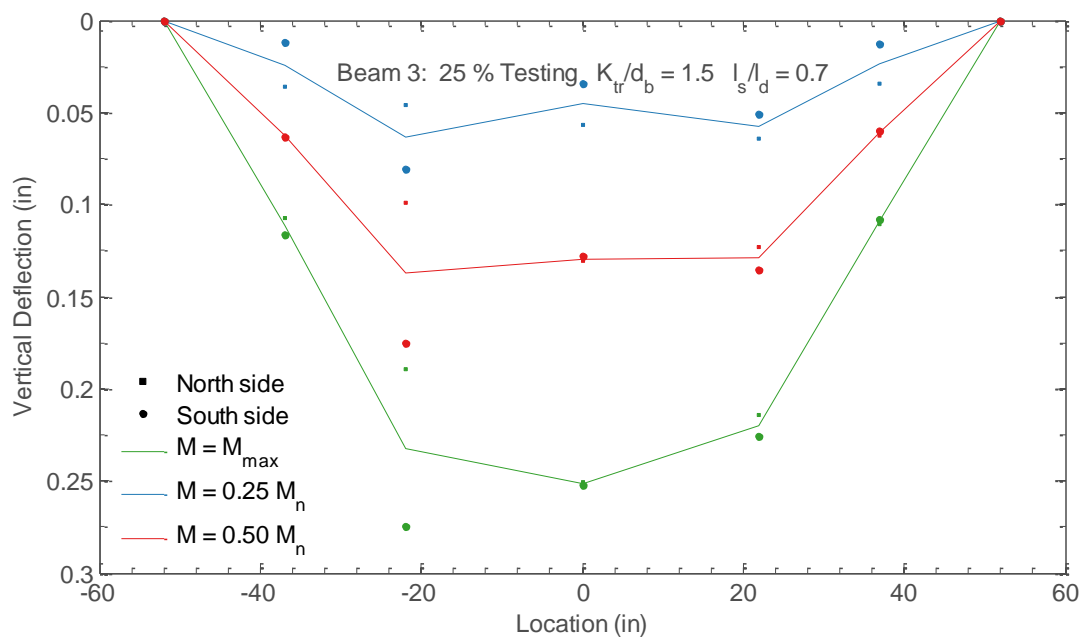
Figure C.22. Measured deflection profiles for Beam 3

163
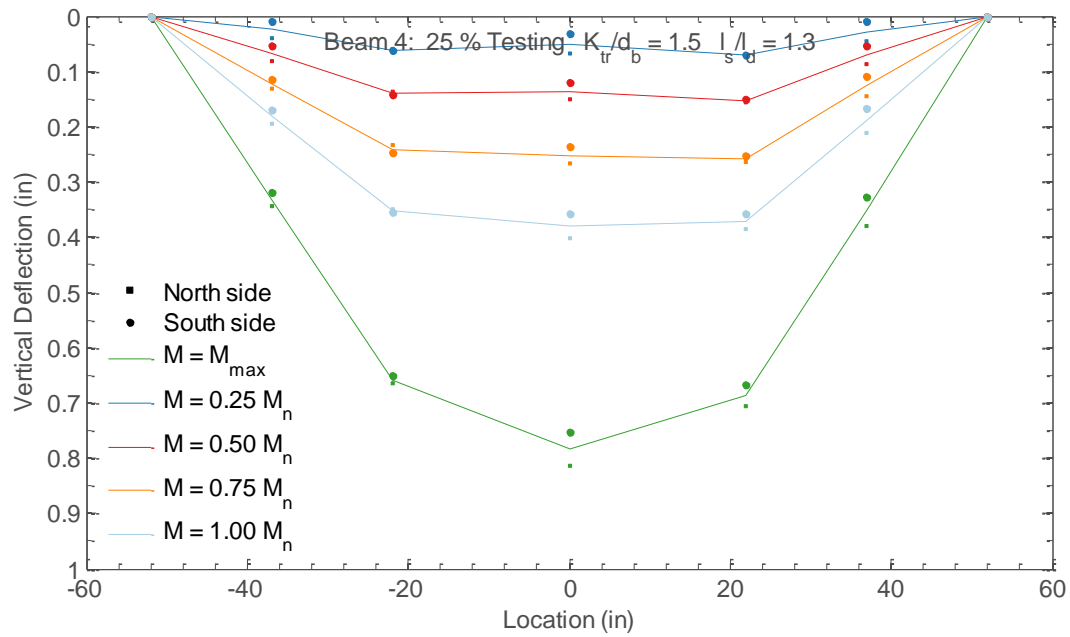
Figure C.23. Measured deflection profiles for Beam 4
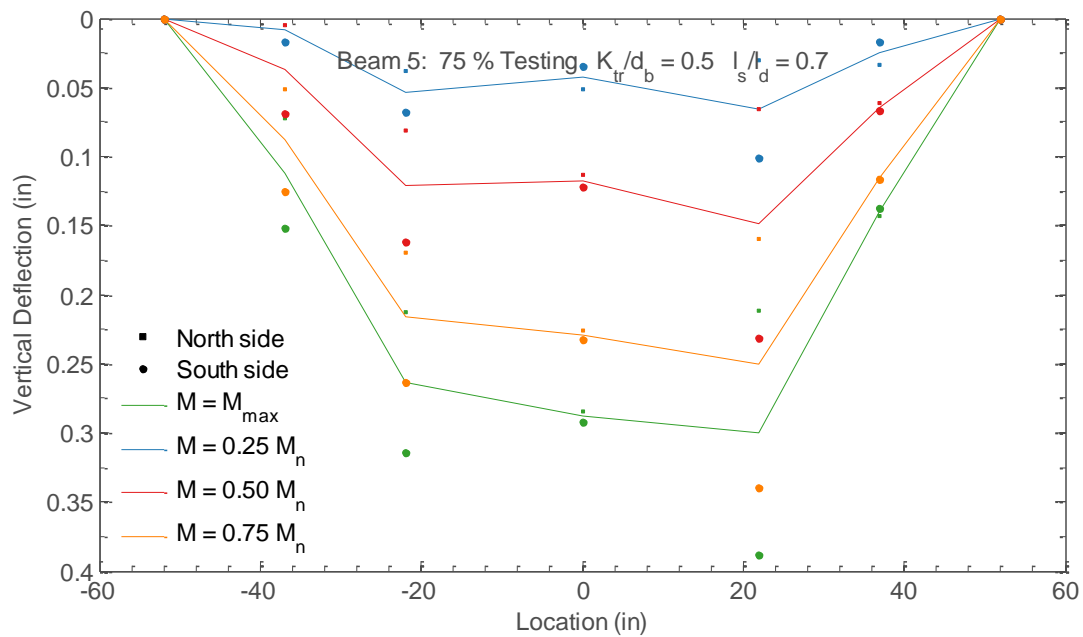
Figure C.24. Measured deflection profiles for Beam 5
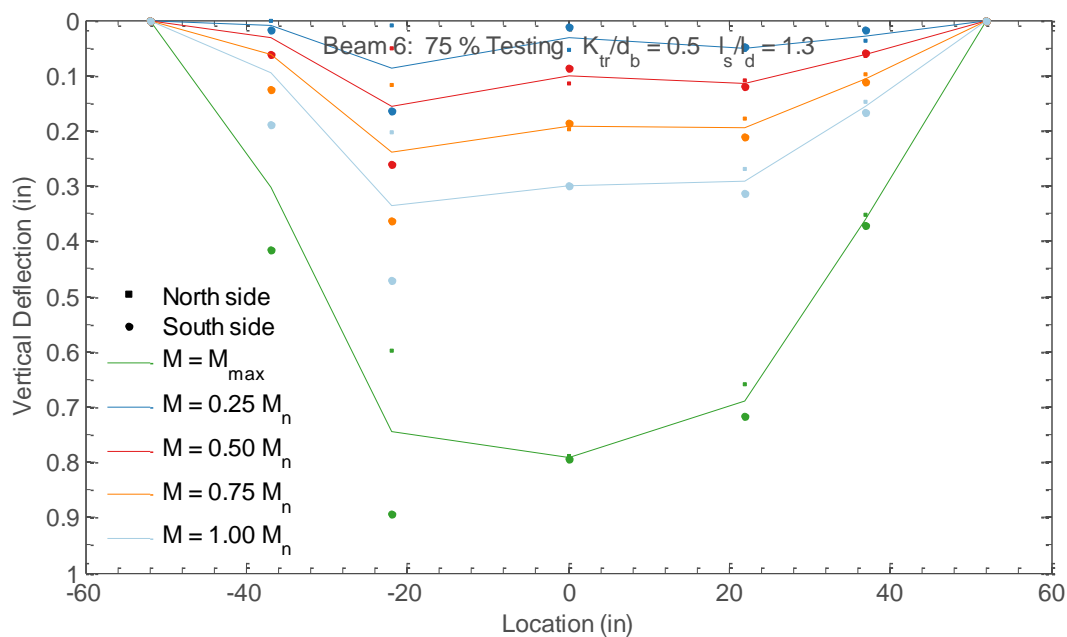
Figure C.25. Measured deflection profiles for Beam 6
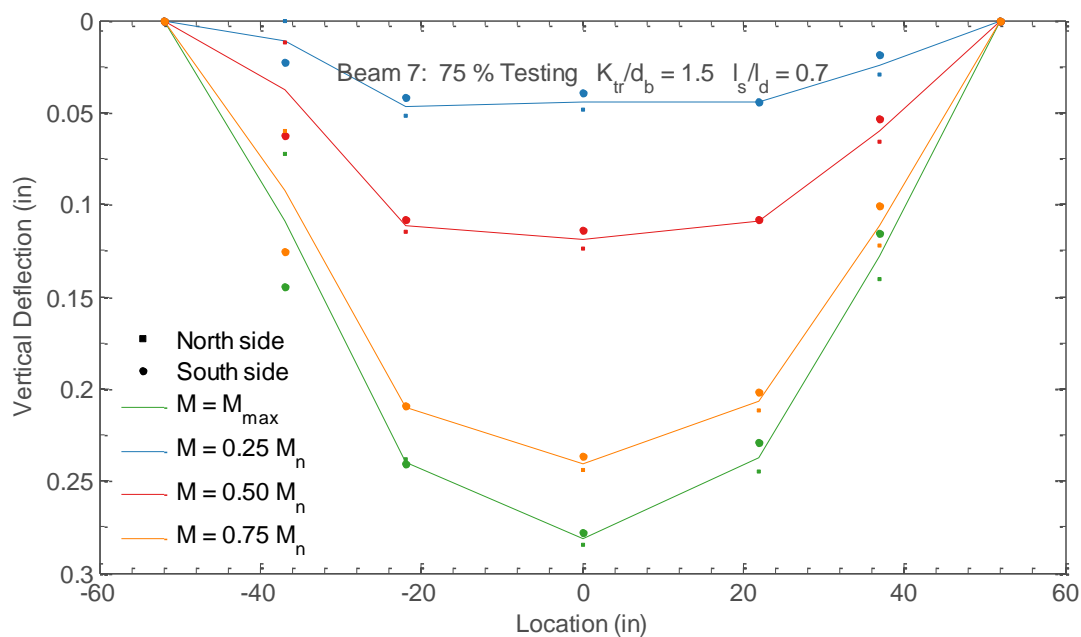
Figure C.26. Measured deflection profiles for Beam 7

165
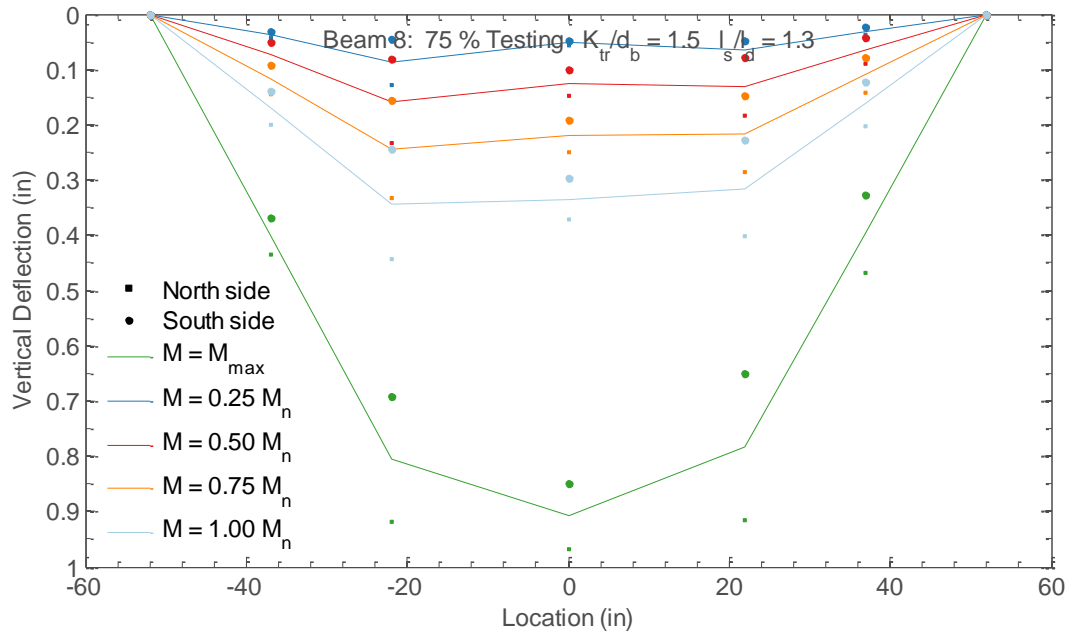
Figure C.27. Measured deflection profiles for Beam 8
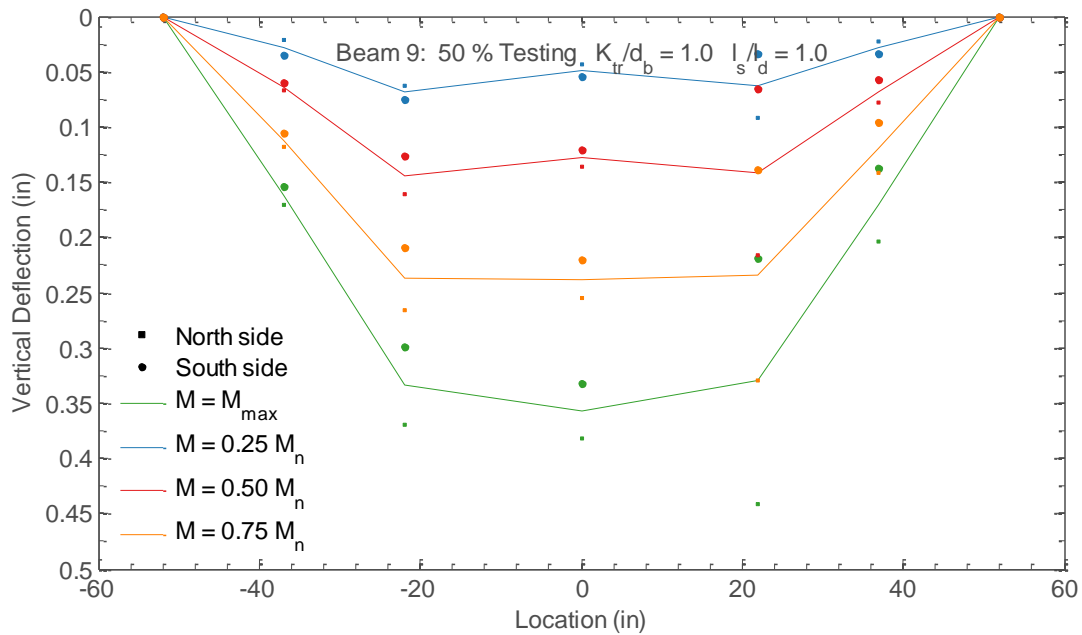
Figure C.28. Measured deflection profiles for Beam 9
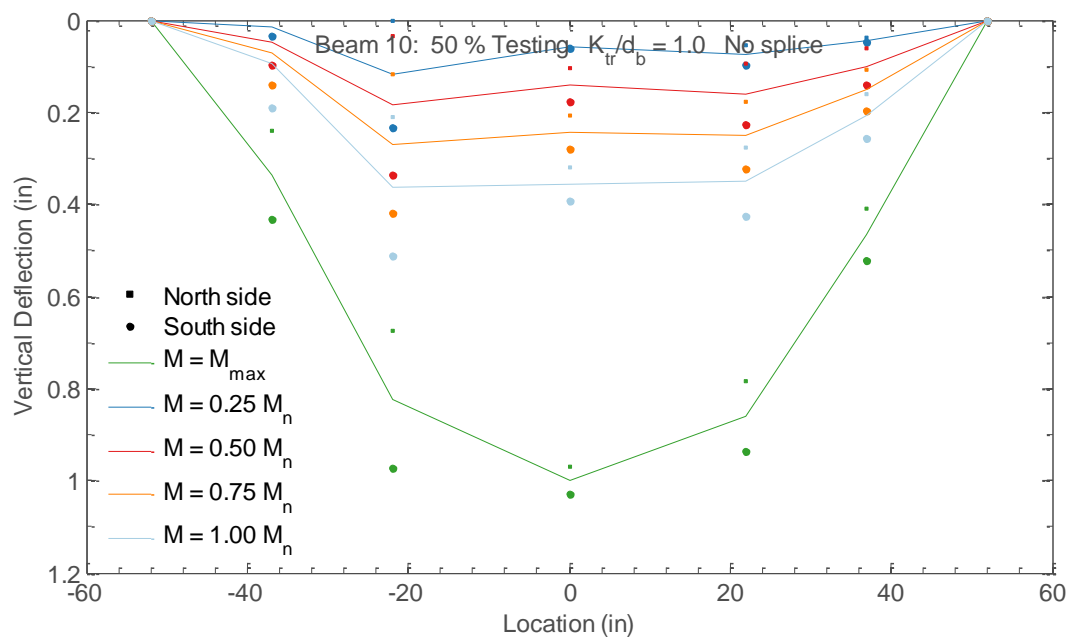
Figure C.29. Measured deflection profiles for Beam 10
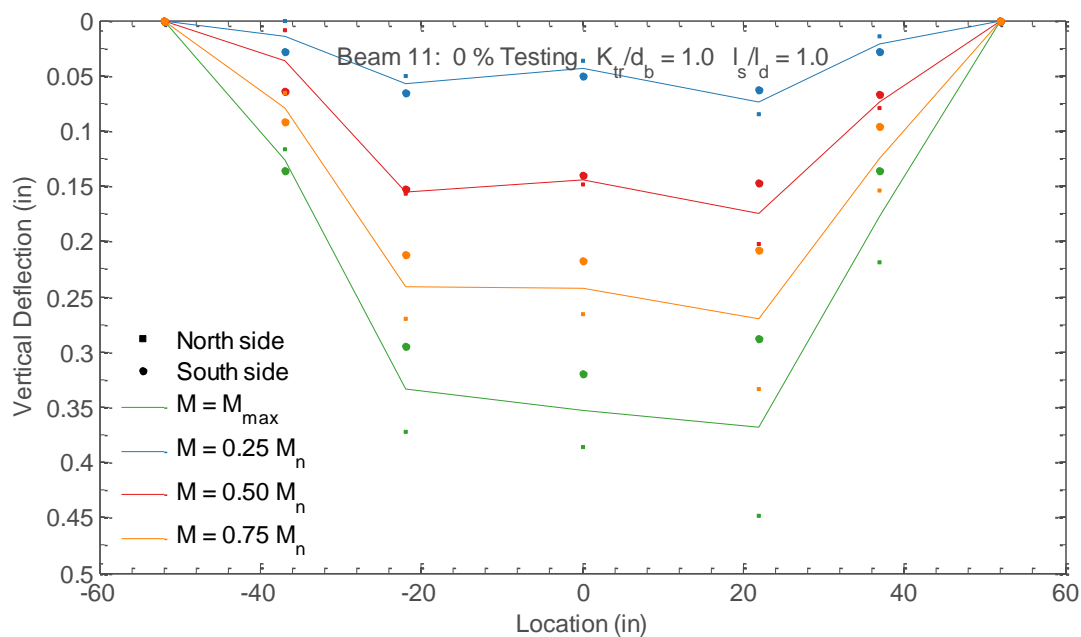
Figure C.30. Measured deflection profiles for Beam 11
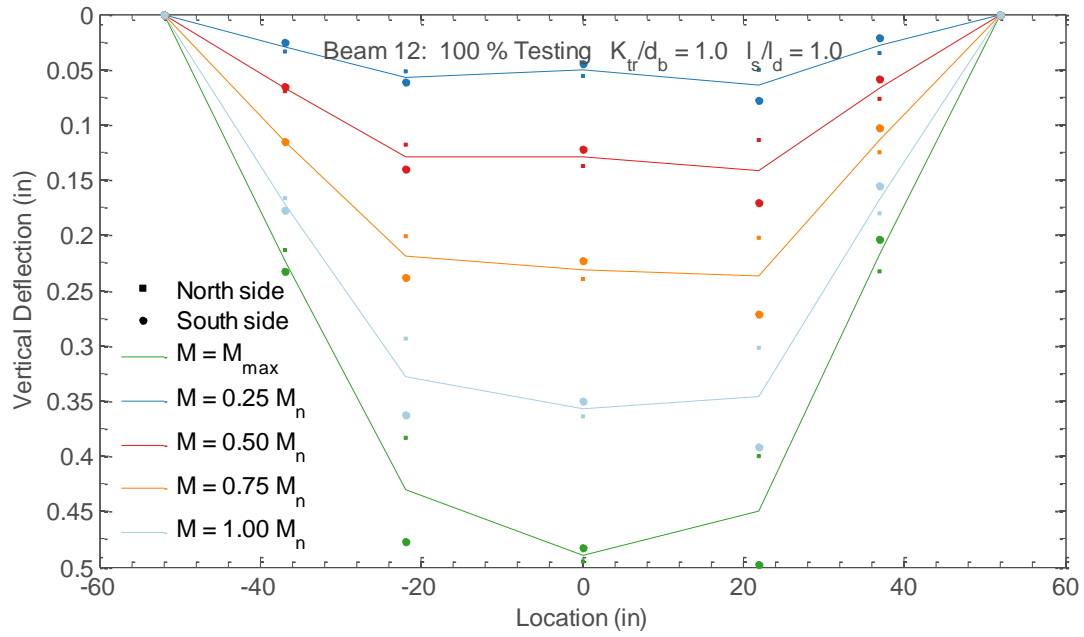
Figure C.31. Measured deflection profiles for Beam 12
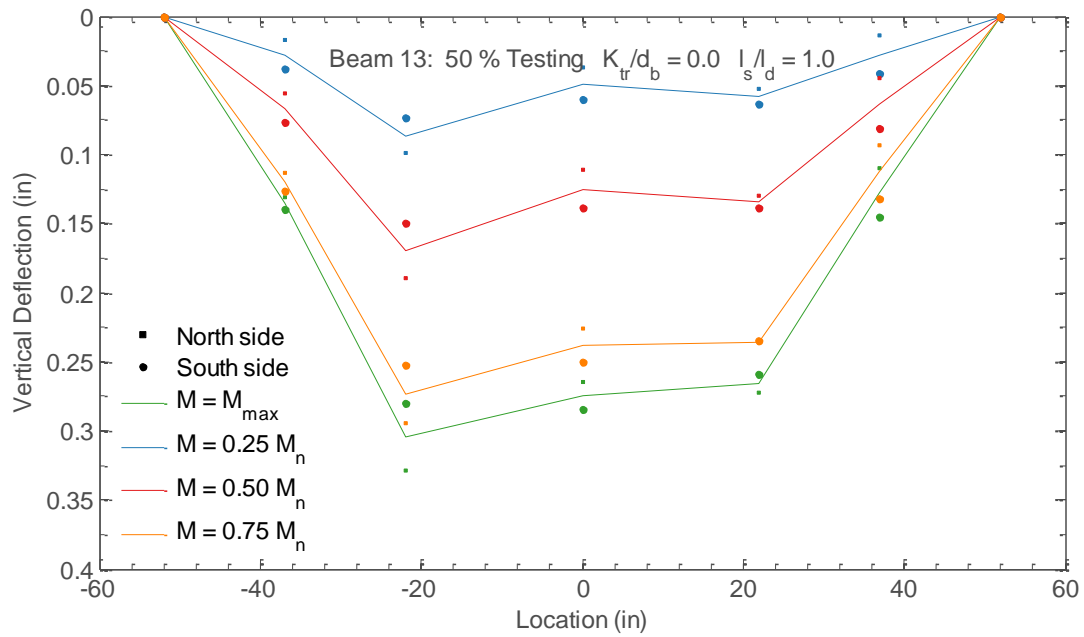
Figure C.32. Measured deflection profiles for Beam 13
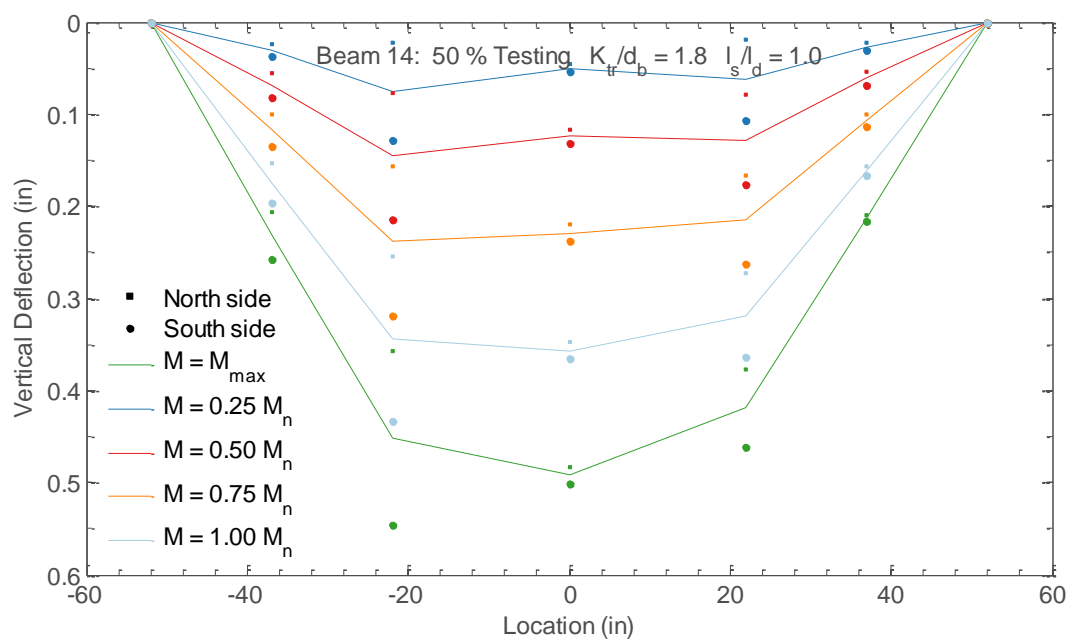
Figure C.33. Measured deflection profiles for Beam 14
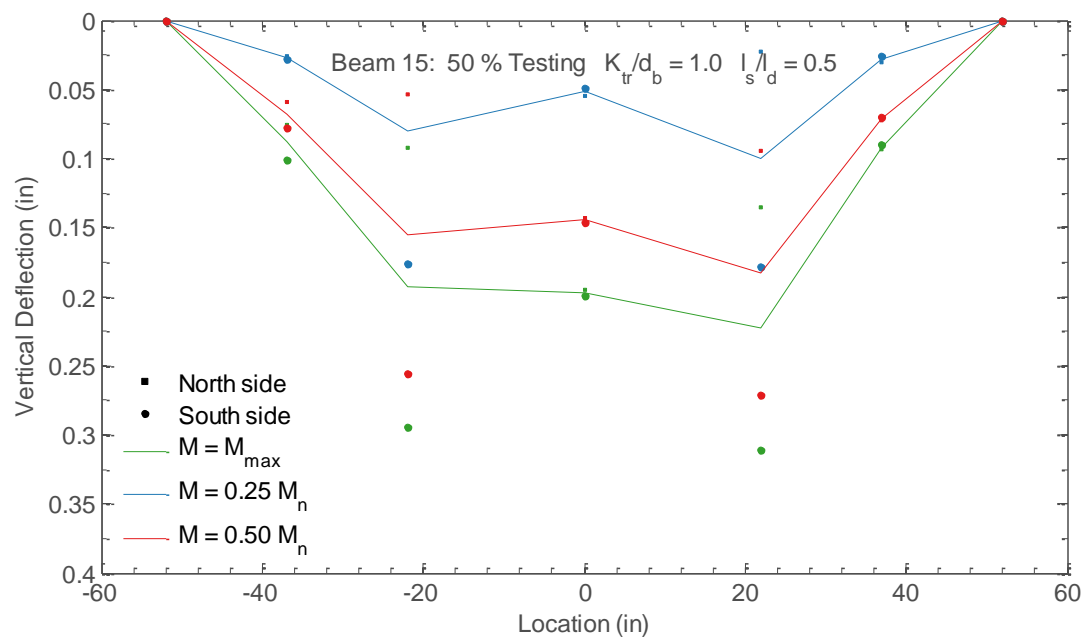
Figure C.34. Measured deflection profiles for Beam 15
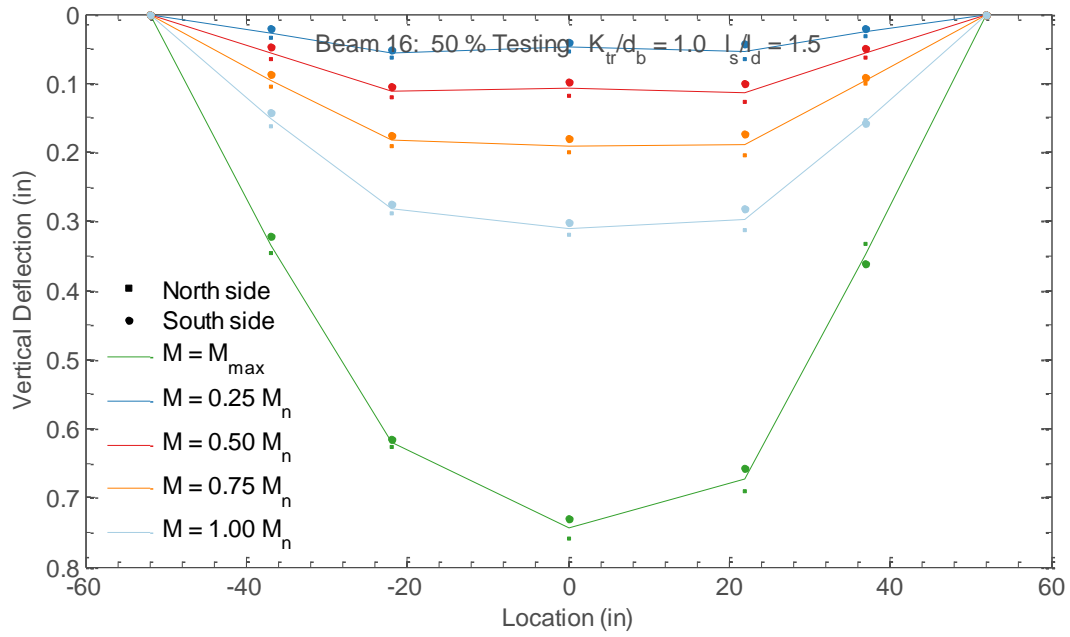
Figure C.35. Measured deflection profiles for Beam 16
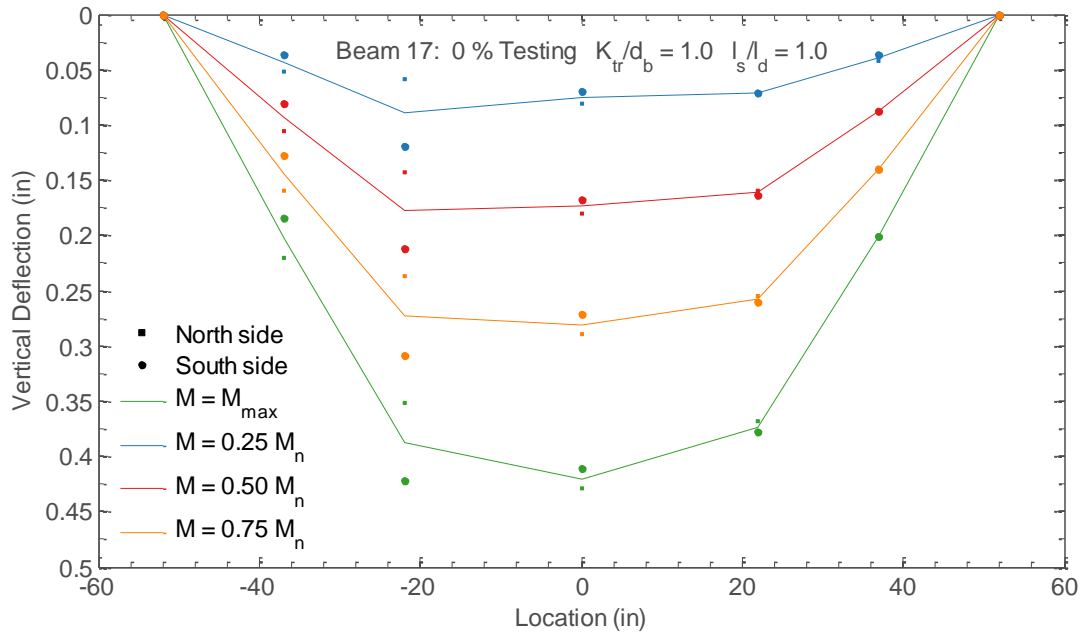
Figure C.36. Measured deflection profiles for Beam 17
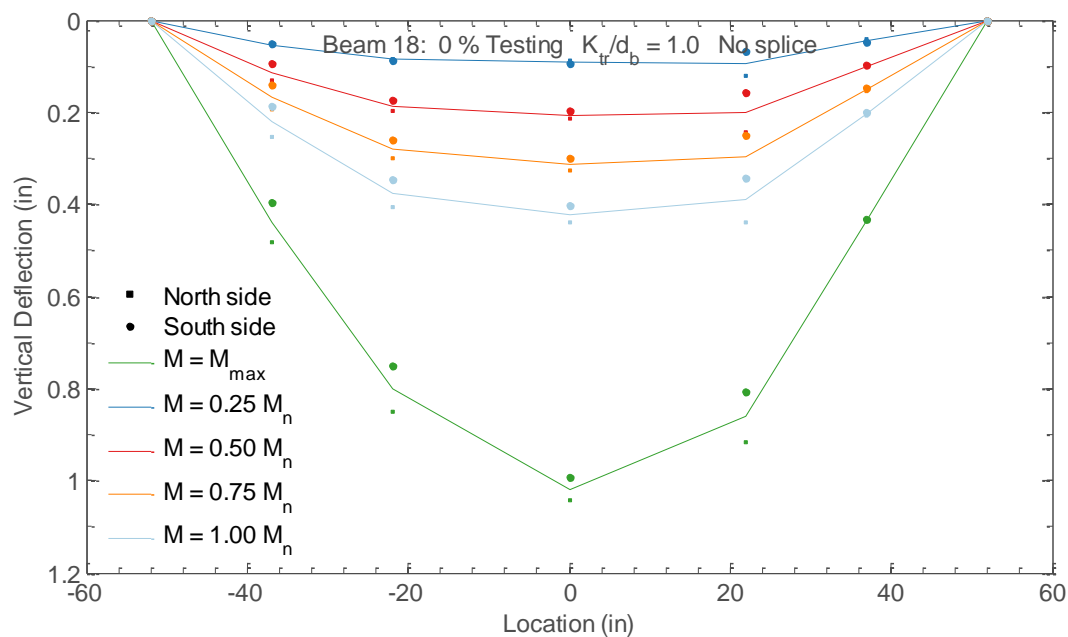
Figure C.37. Measured deflection profiles for Beam 18
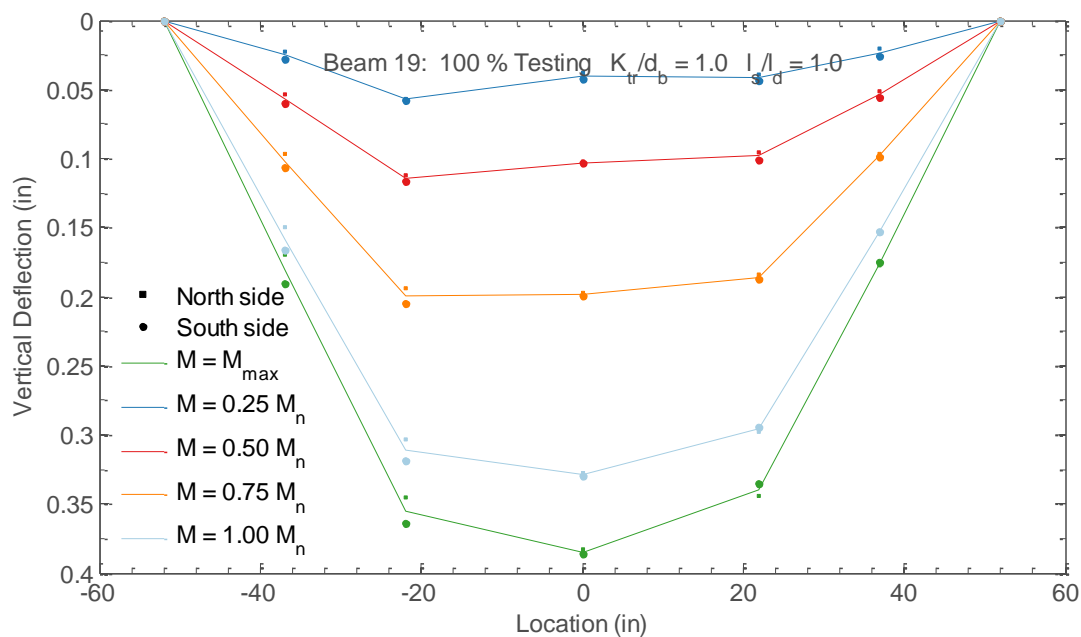
Figure C.38. Measured deflection profiles for Beam 19

Section Deformations

The figures below show the longitudinal deformations of the beam specimen measured by transducers affixed to a series of embedded horizontal rods for the beam specimens. Transducers were placed in two rows, one near the top of the beam and one near the bottom. In the figures, transducers located in the bottom row are shown with solid lines and those located in the top row with dashed lines. The instruments are identified based on the nominal location of the measurement along the beam's length with the beam's midspan serving at the origin. Since the transducers spanned between two successive rods, a position halfway between the rods was used to locate the measurements.
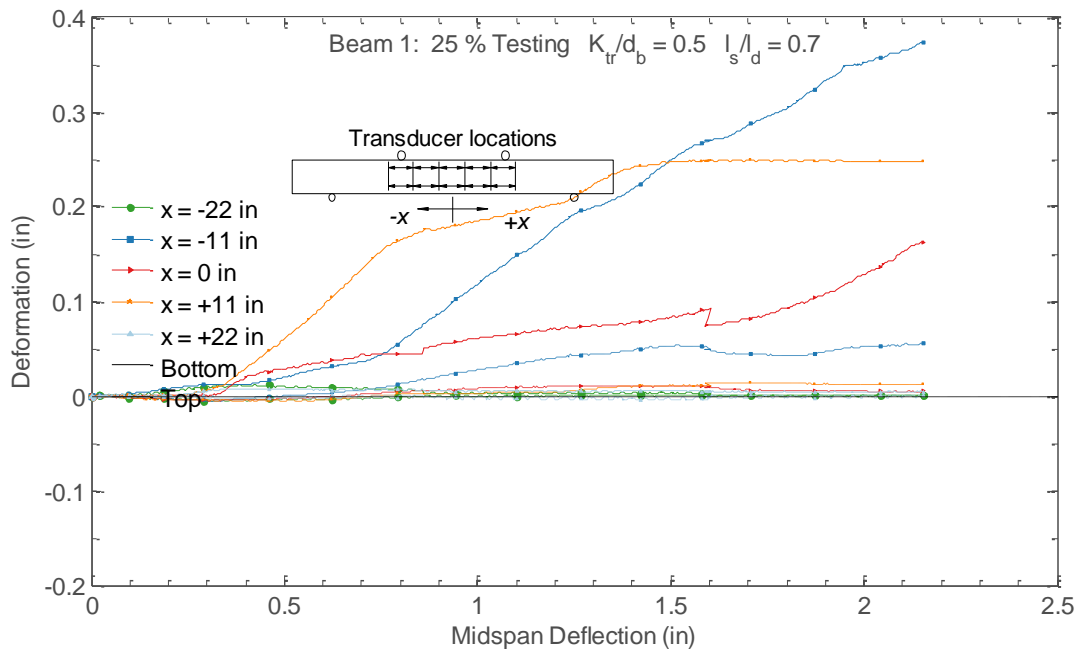
Figure C.39. Measured section deformations for Beam 1
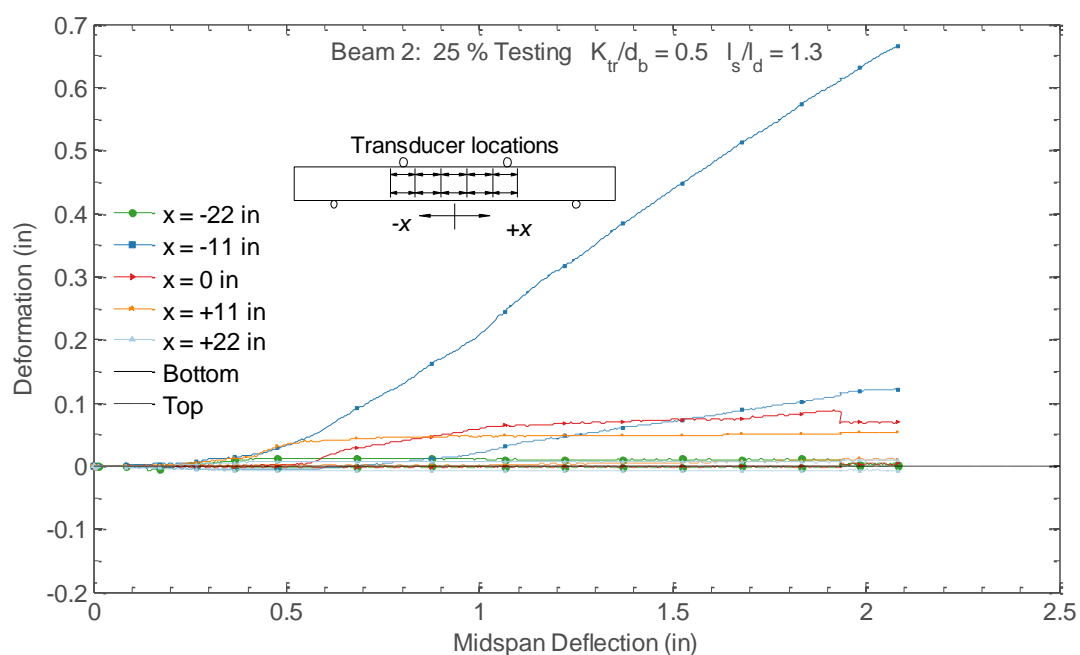
Figure C.40. Measured section deformations for Beam 2
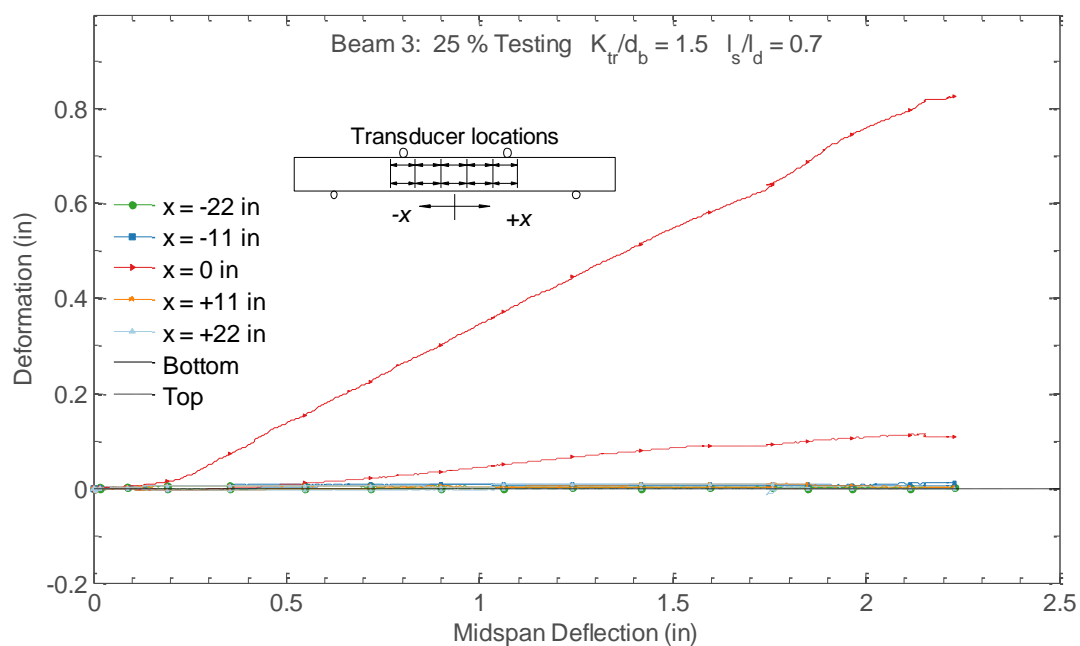
Figure C.41. Measured section deformations for Beam 3

173
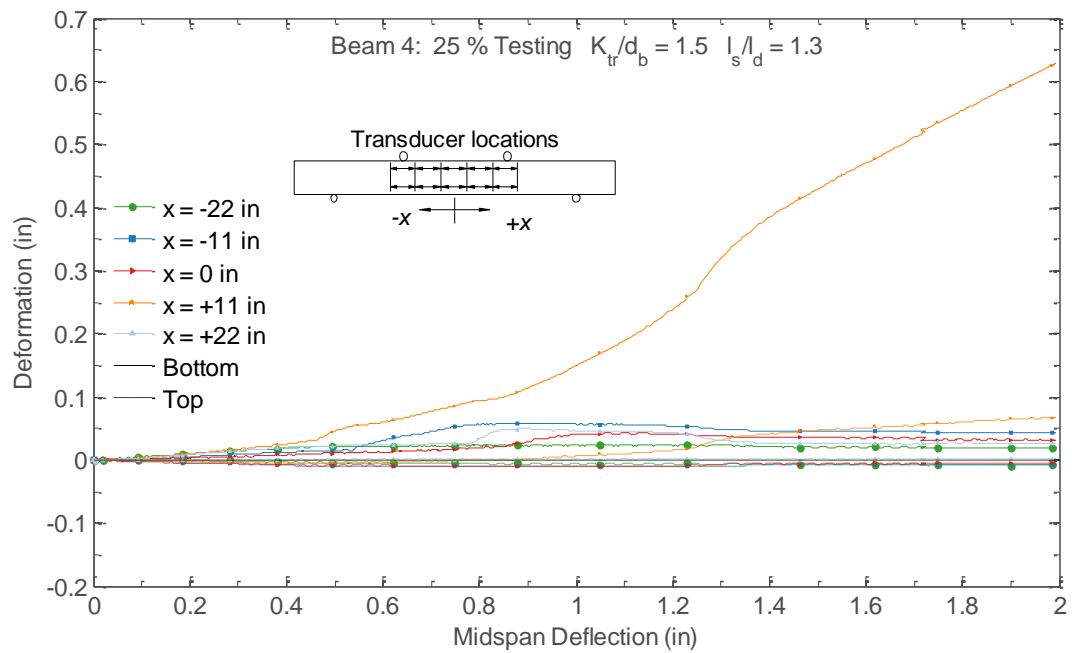
Figure C.42. Measured section deformations for Beam 4
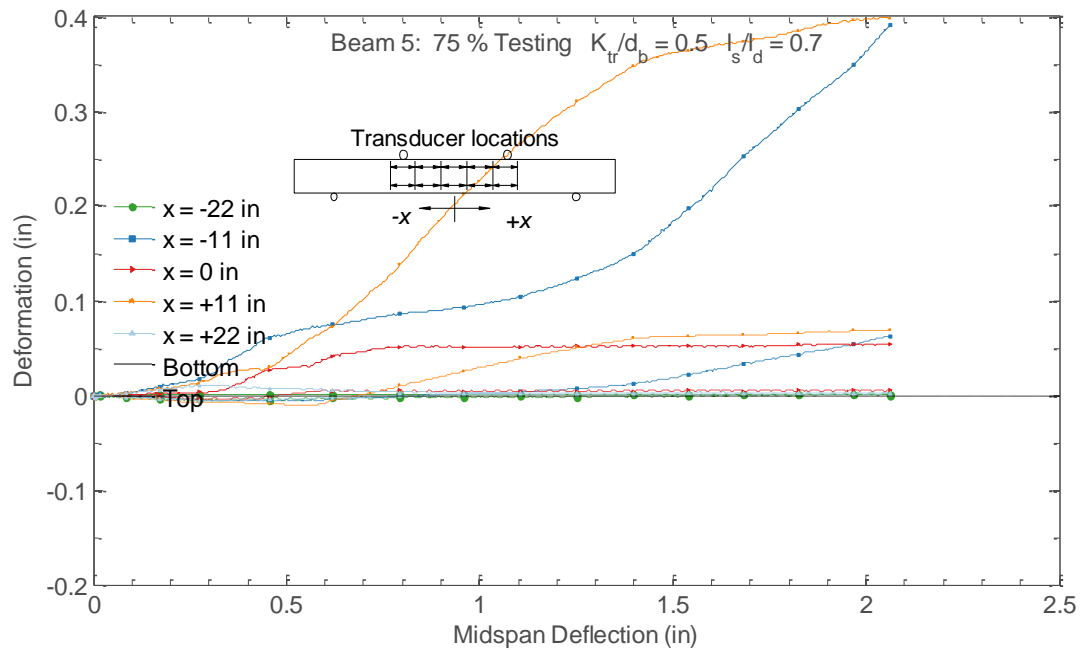
Figure C.43. Measured section deformations for Beam 5

174
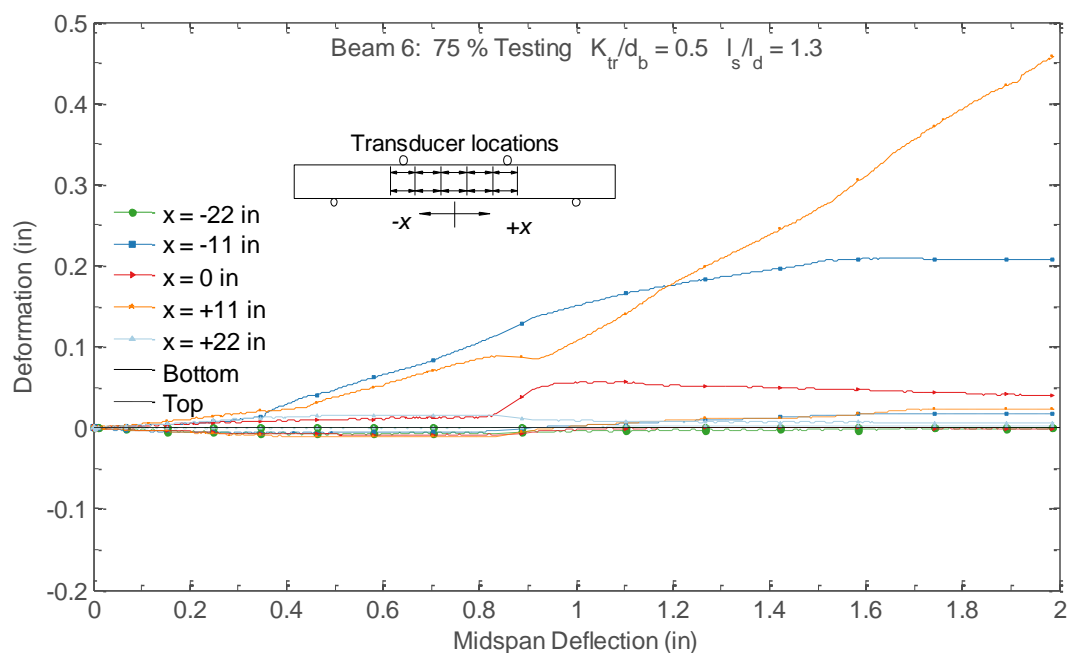
Figure C.44. Measured section deformations for Beam 6
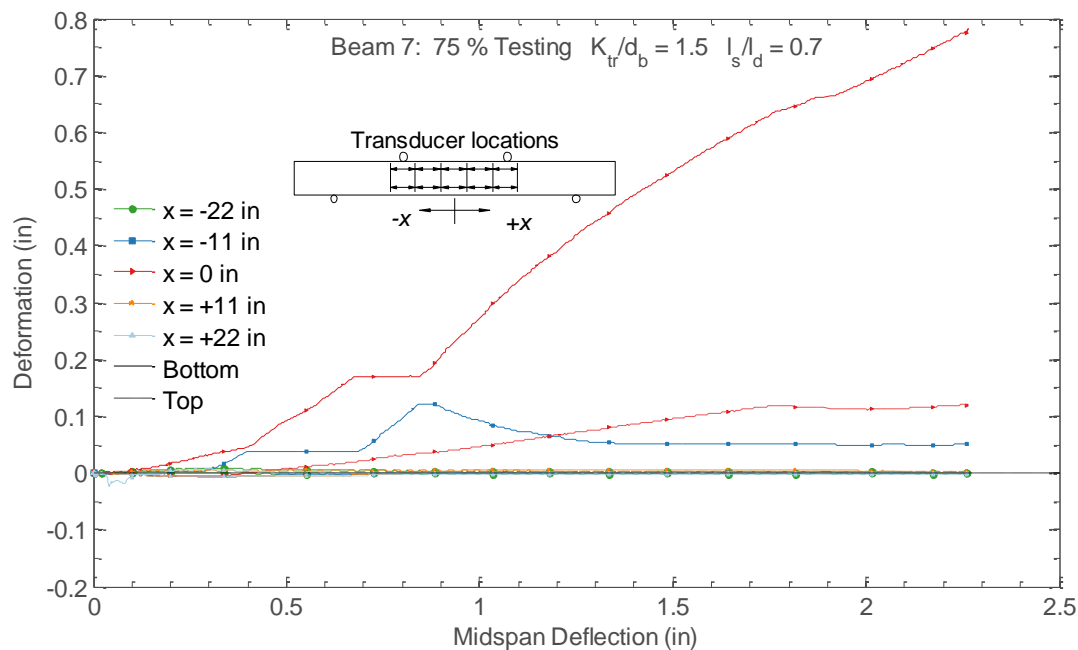
Figure C.45. Measured section deformations for Beam 7

175
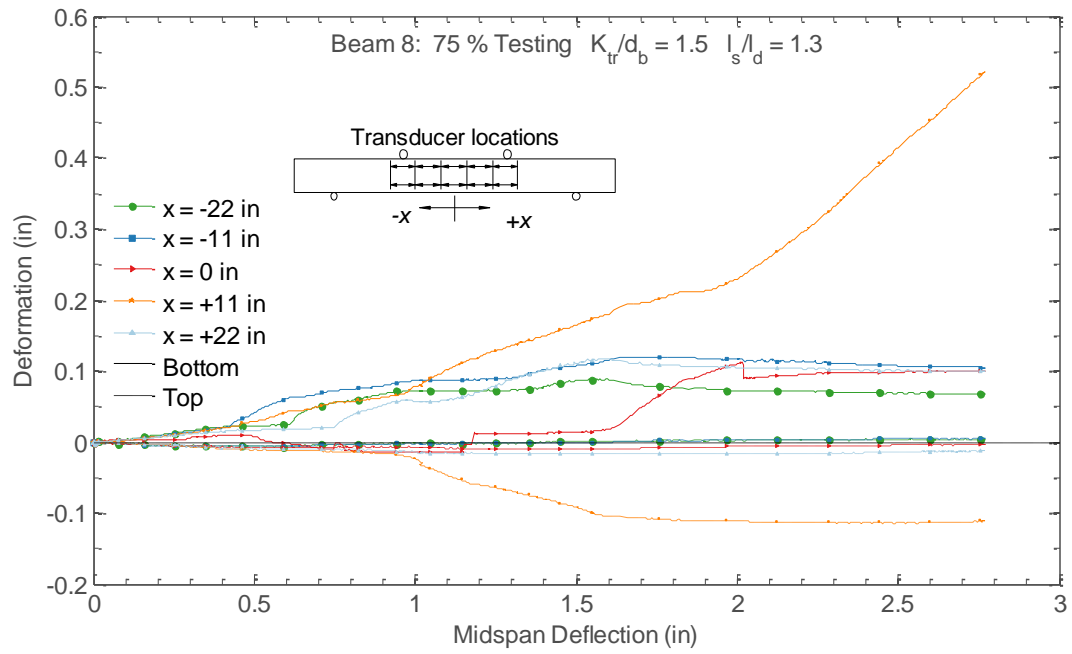
Figure C.46. Measured section deformations for Beam 8
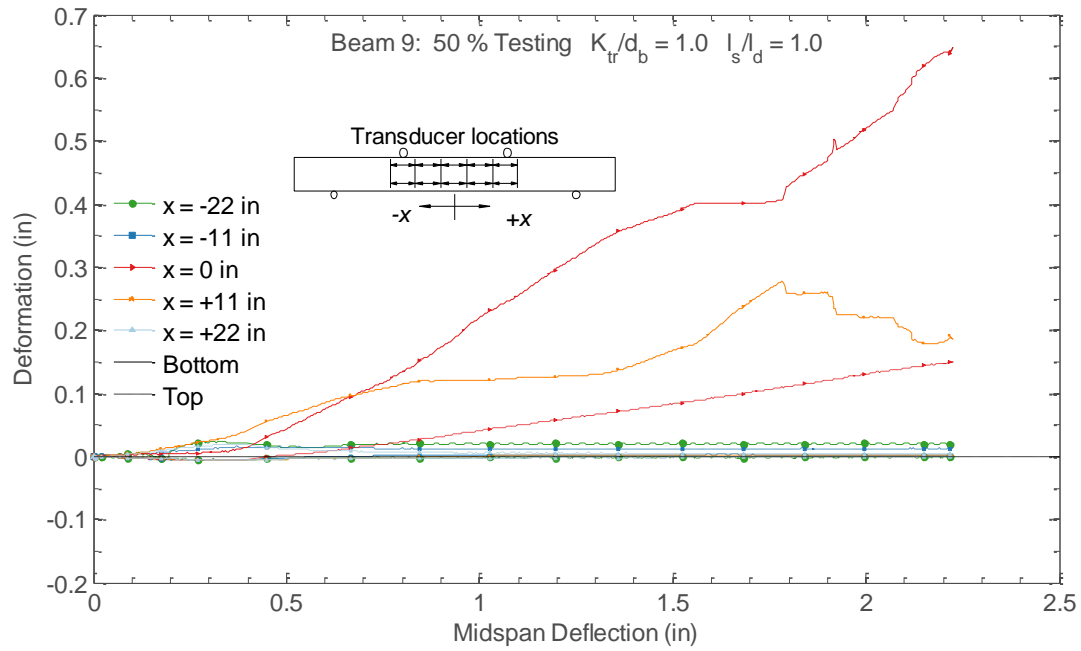
Figure C.47. Measured section deformations for Beam 9

176
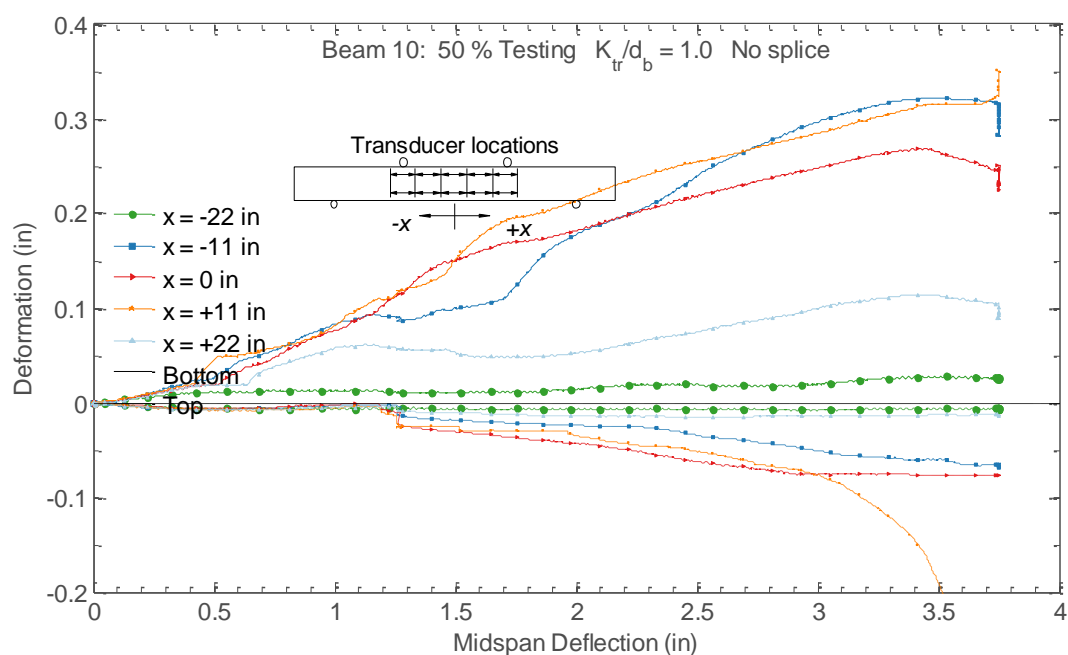
Figure C.48. Measured section deformations for Beam 10
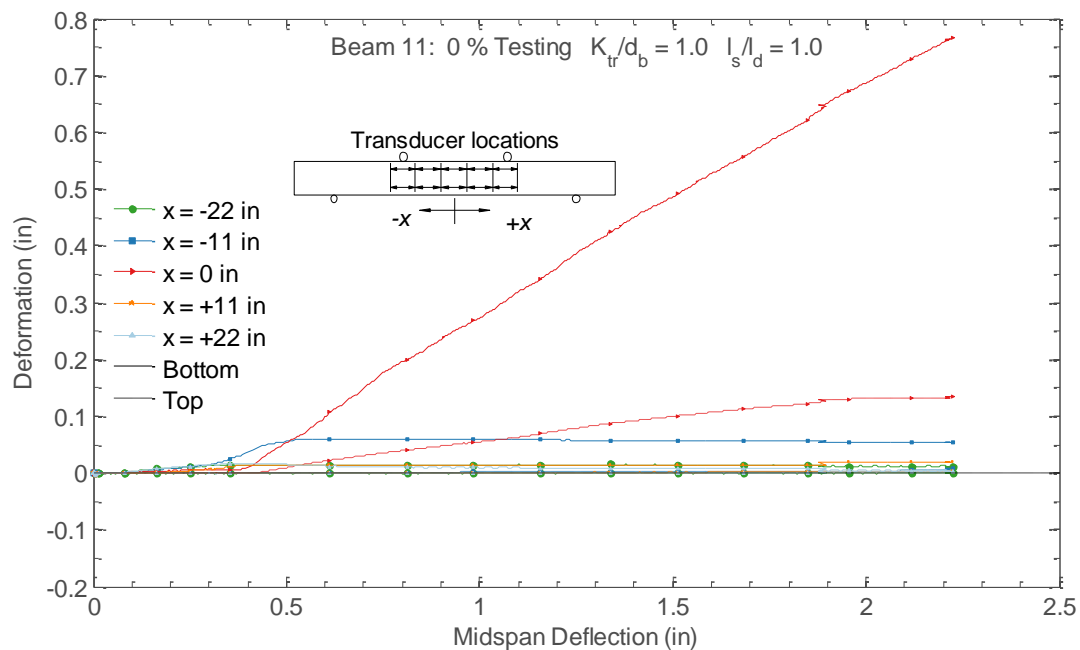
Figure C.49. Measured section deformations for Beam 11

177
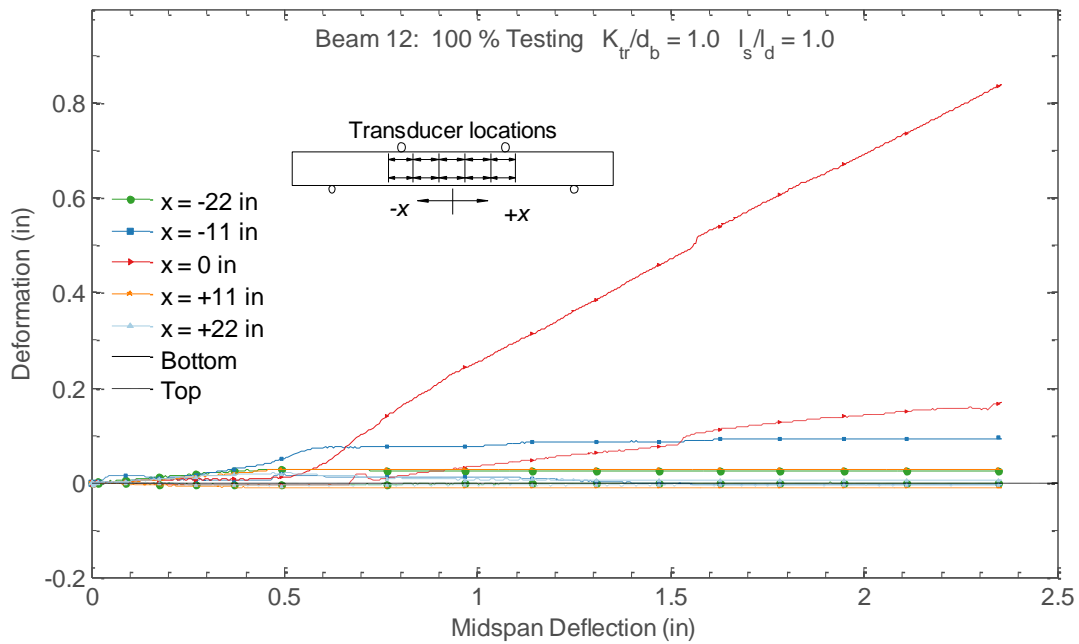
Figure C.50. Measured section deformations for Beam 12
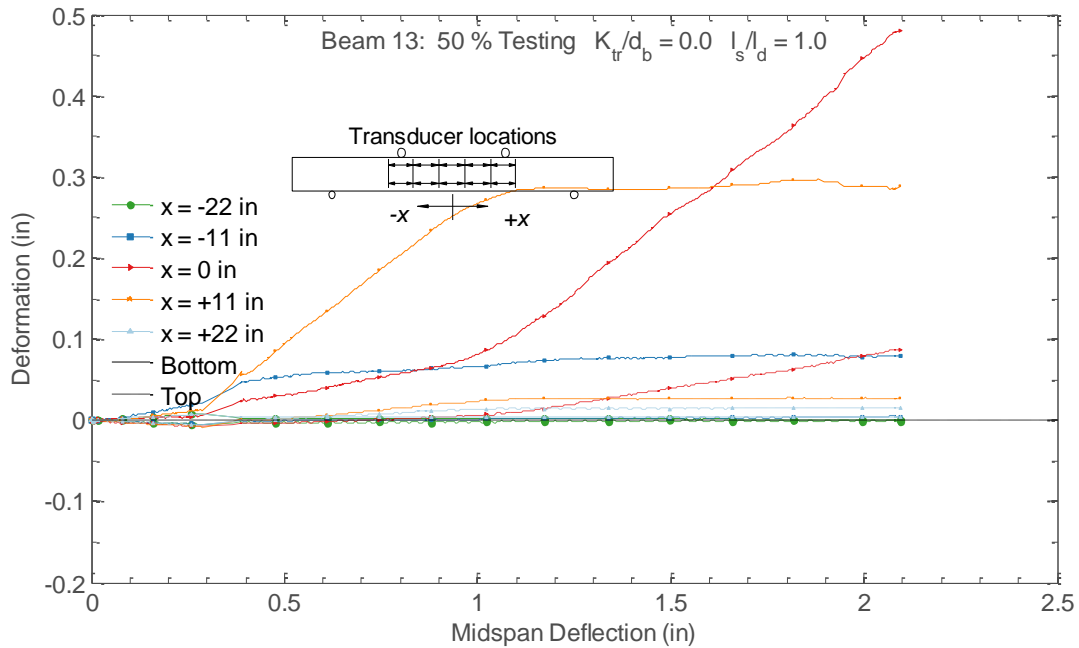
Figure C.51. Measured section deformations for Beam 13

178
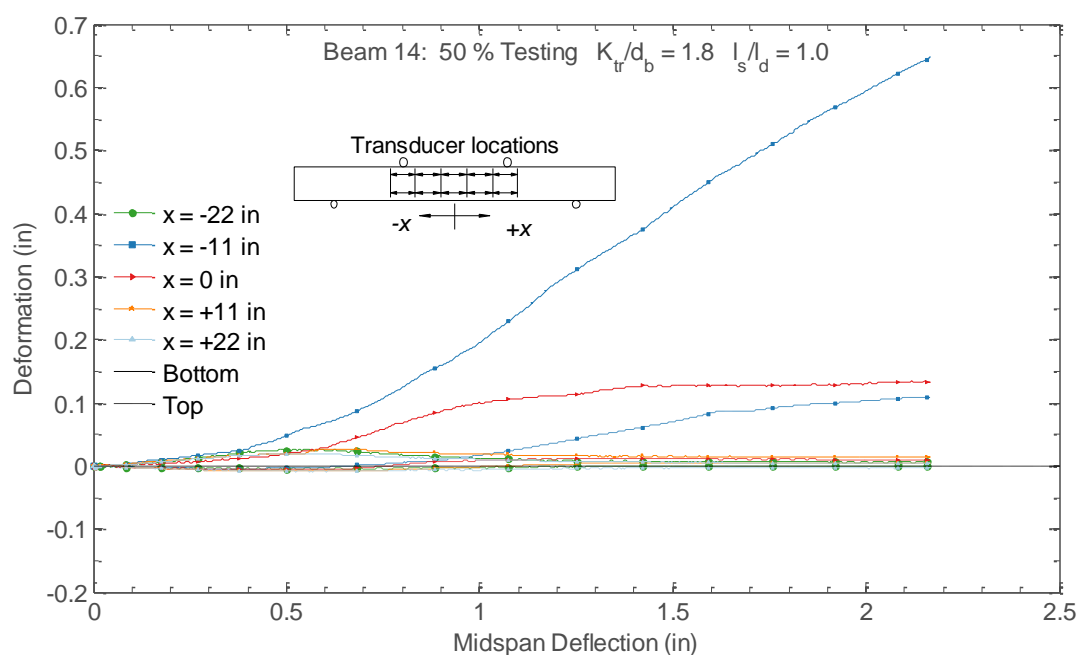
Figure C.52. Measured section deformations for Beam 14
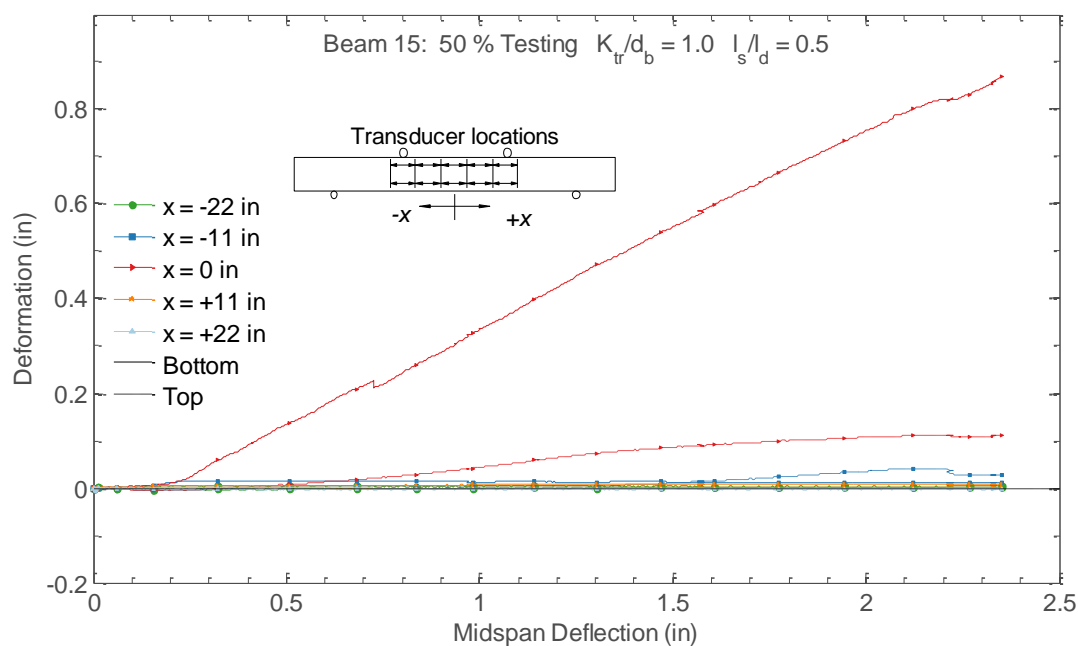
Figure C.53. Measured section deformations for Beam 15

179
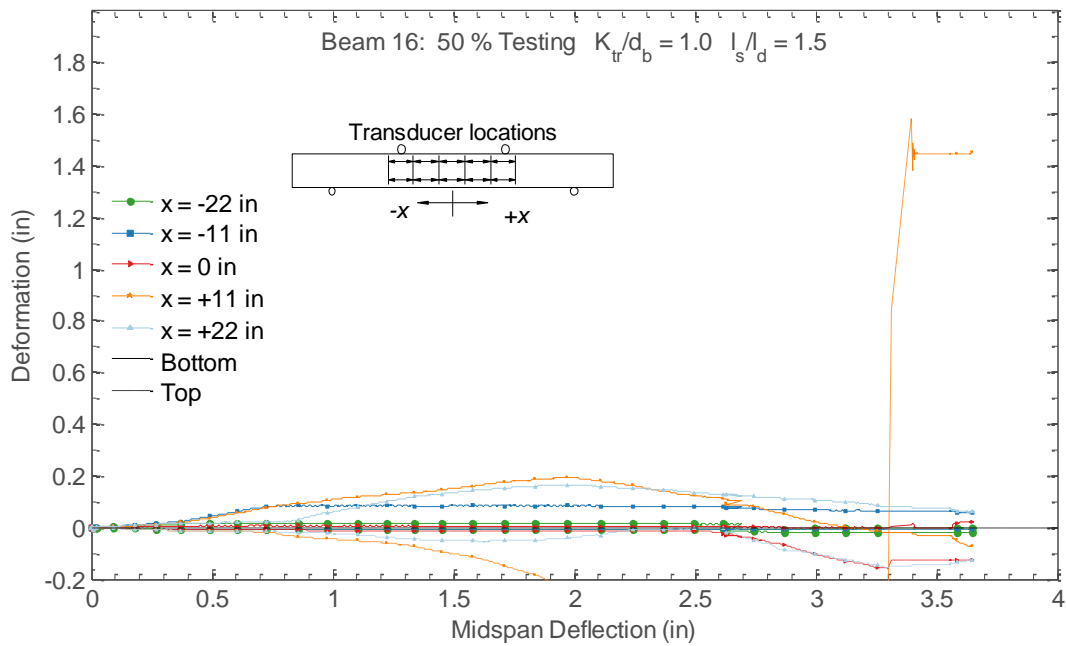
Figure C.54. Measured section deformations for Beam 16
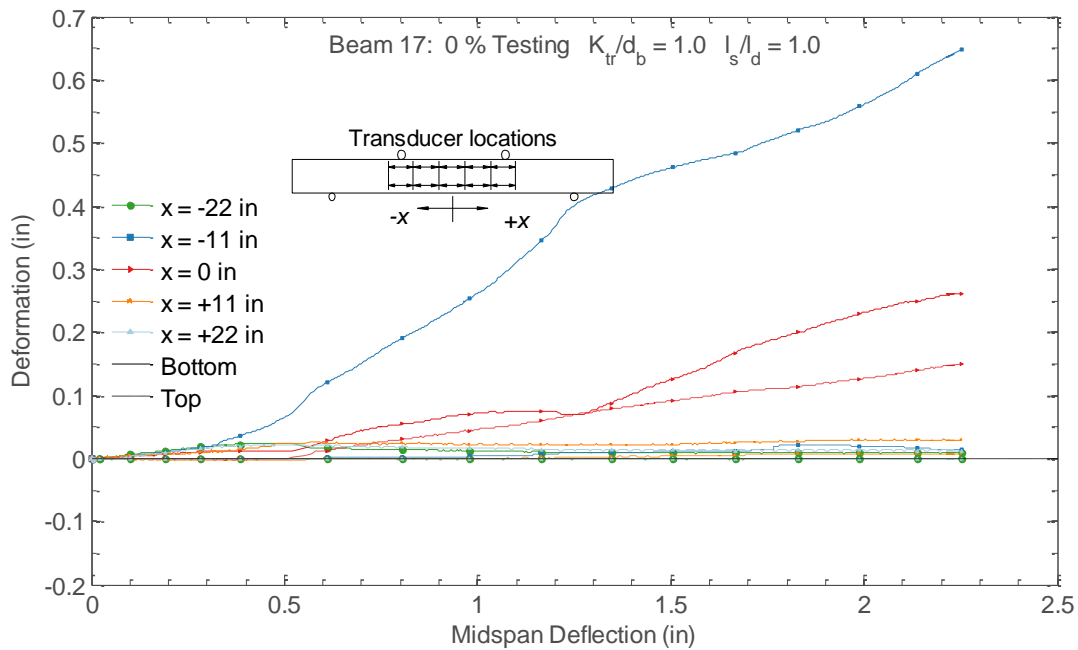
Figure C.55. Measured section deformations for Beam 17

180
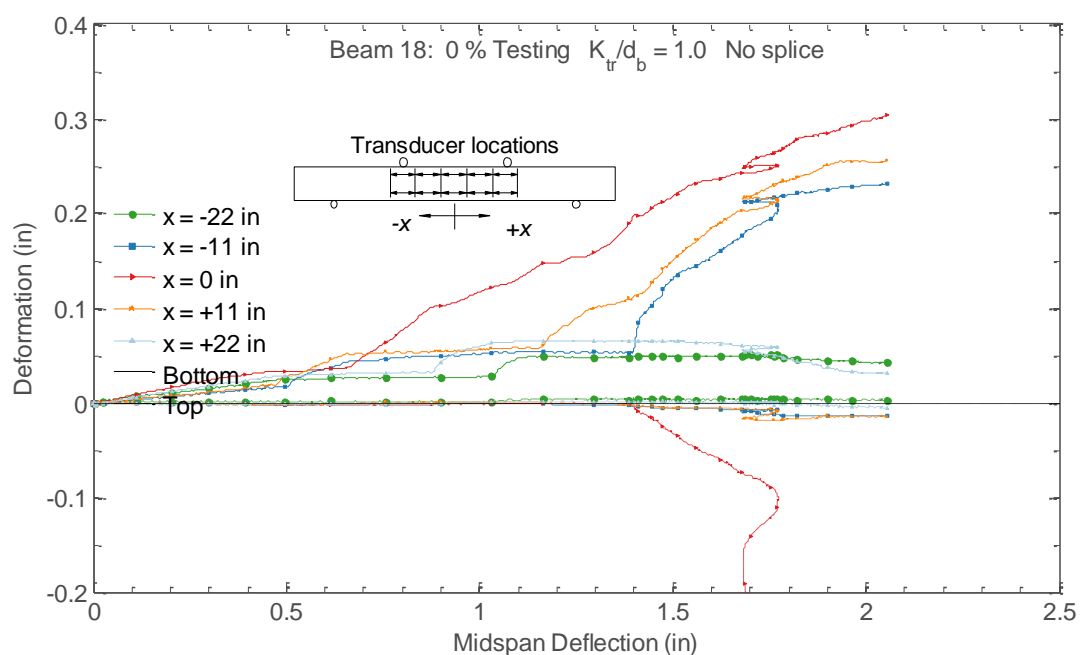
Figure C.56. Measured section deformations for Beam 18
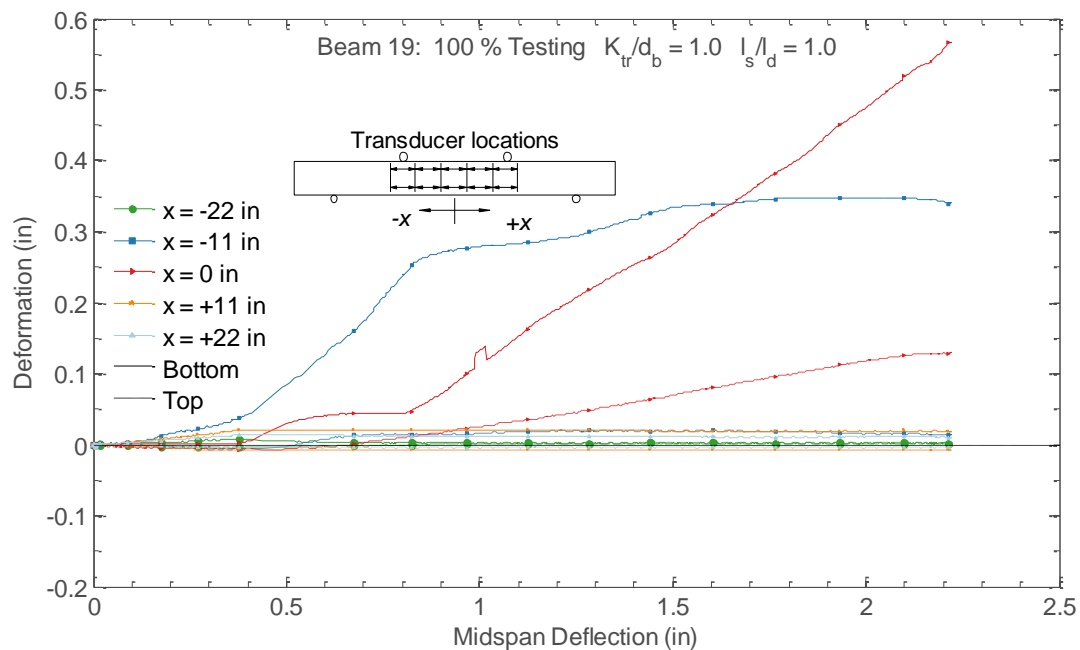
Figure C.57. Measured section deformations for Beam 19

181

Section Rotation

The figures below show the computed rotations at the five measurement locations for the beam specimens. Section rotations were computed by dividing the difference between the top and bottom deformation measurements by the average separation between the instruments using Equation 4.1.
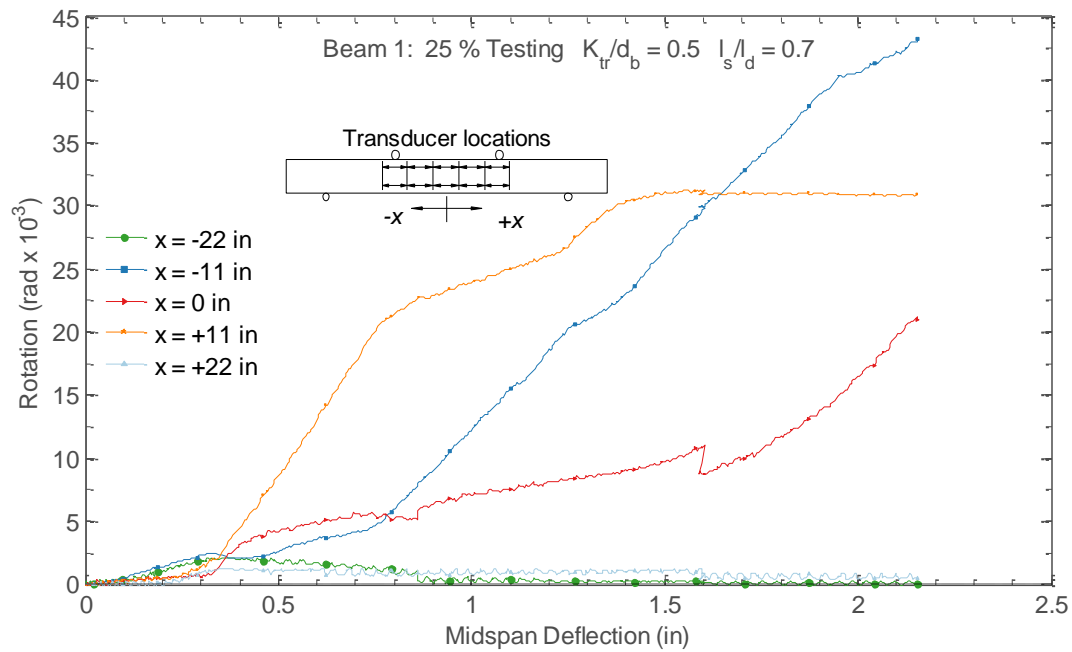
Figure C.58. Computed section rotations for Beam 1
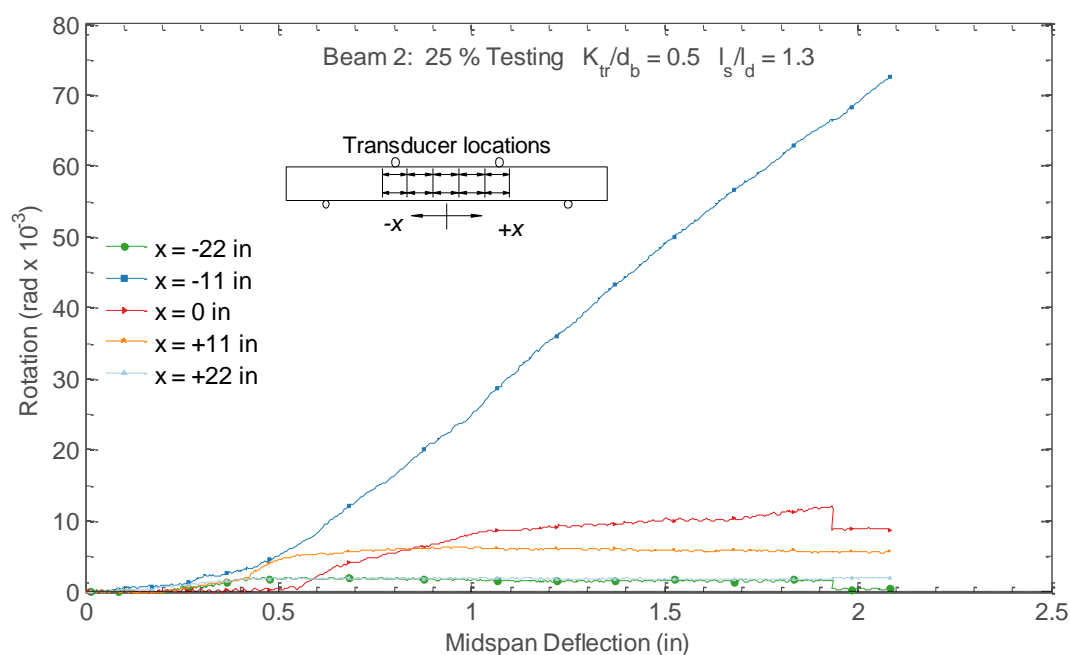
Figure C.59. Computed section rotations for Beam 2
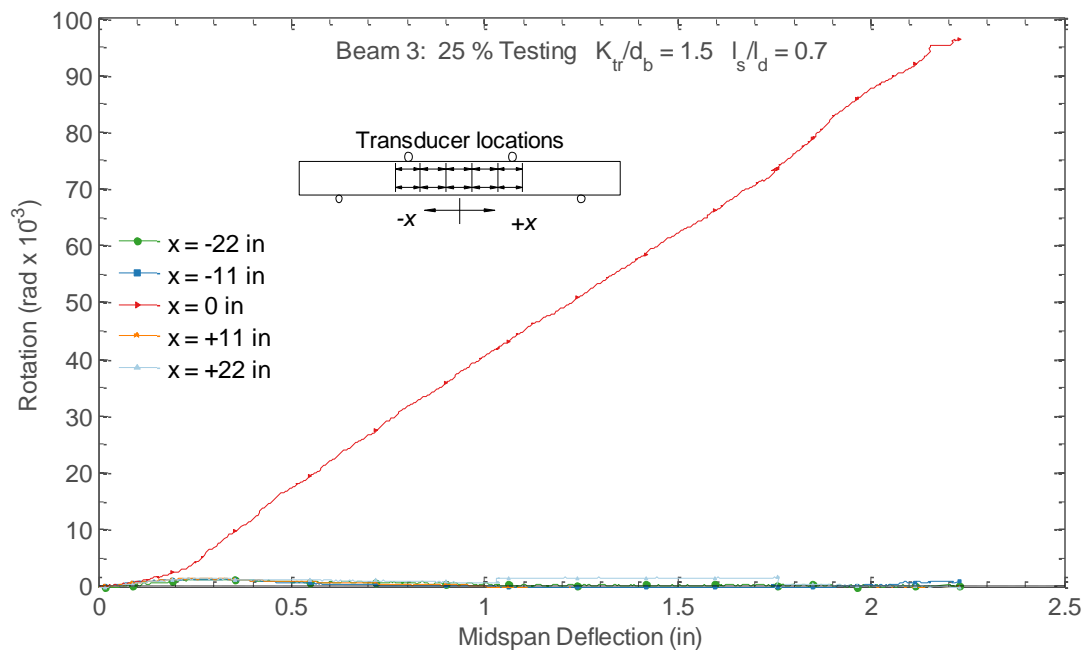
Figure C.60. Computed section rotations for Beam 3
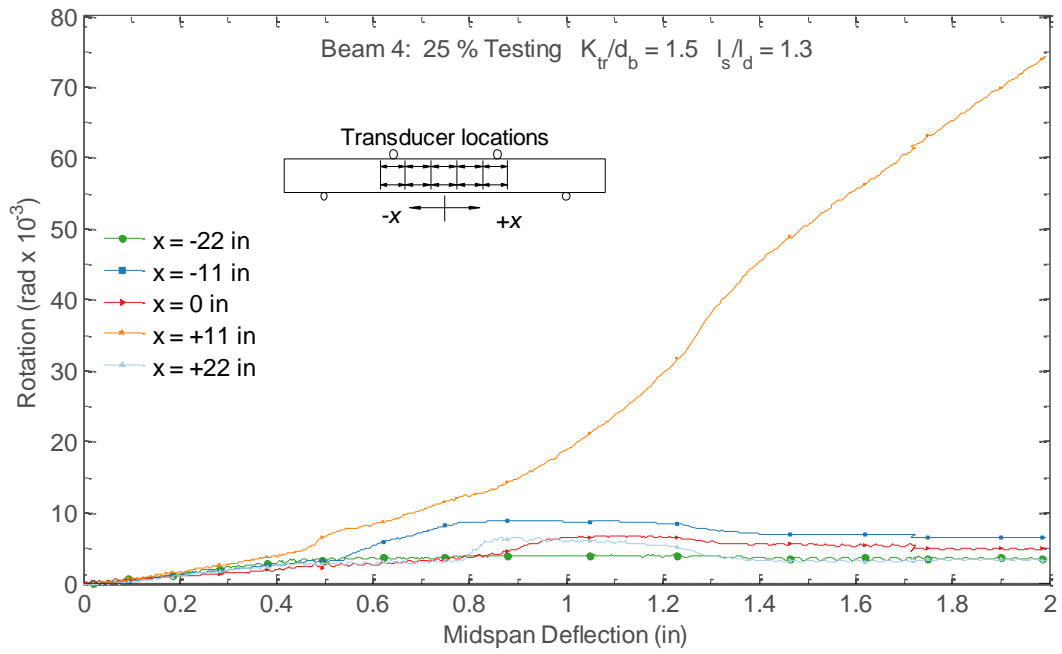
Figure C.61. Computed section rotations for Beam 4
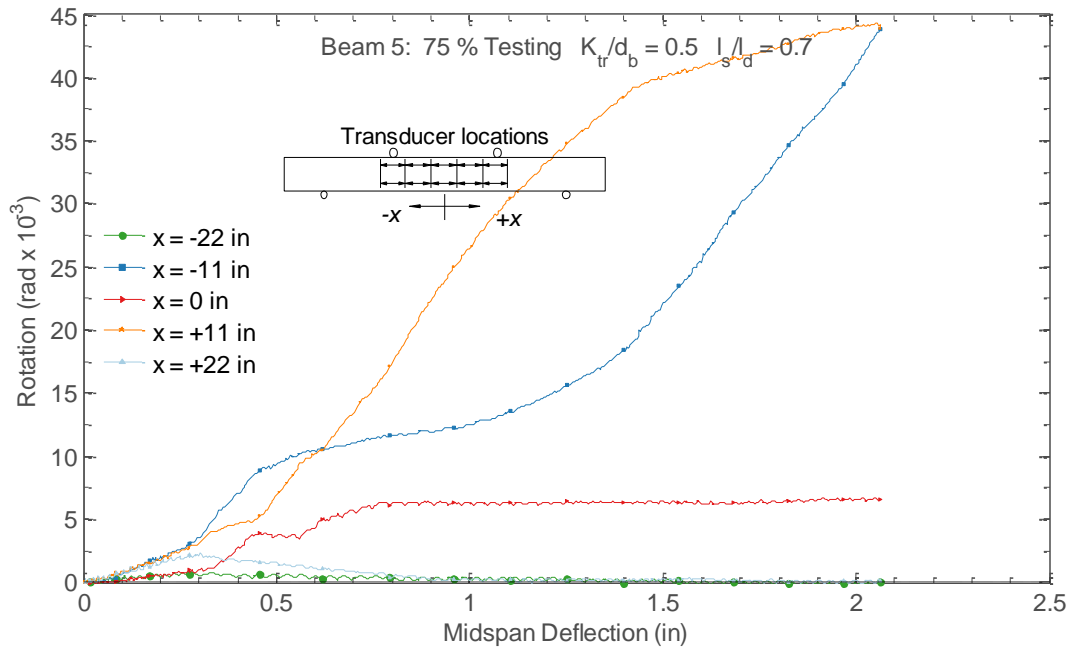
Figure C.62. Computed section rotations for Beam 5

184
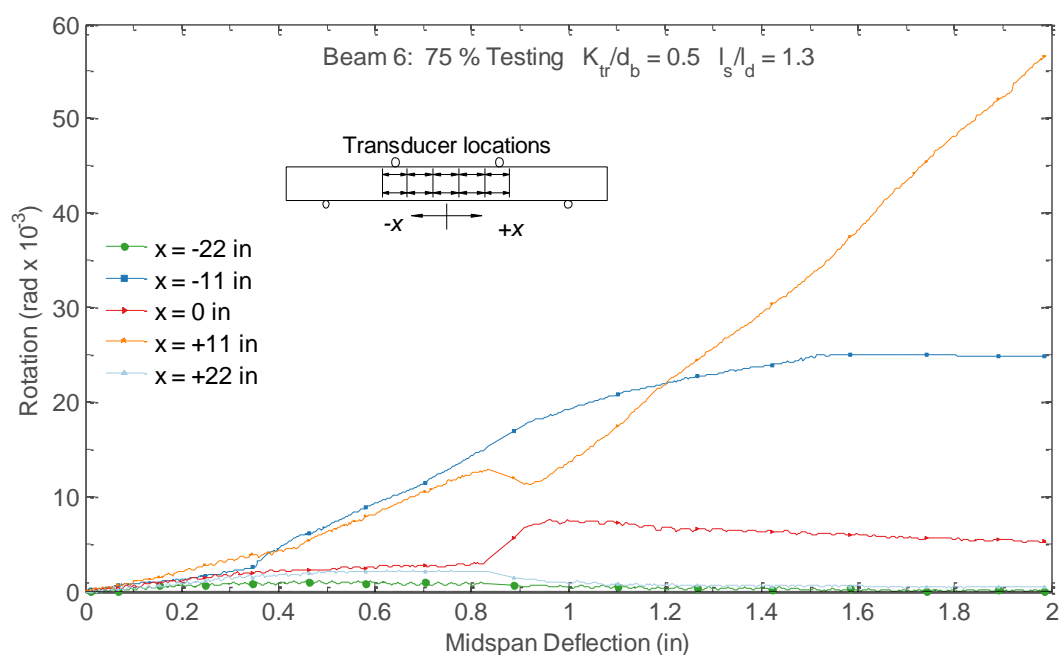
Figure C.63. Computed section rotations for Beam 6
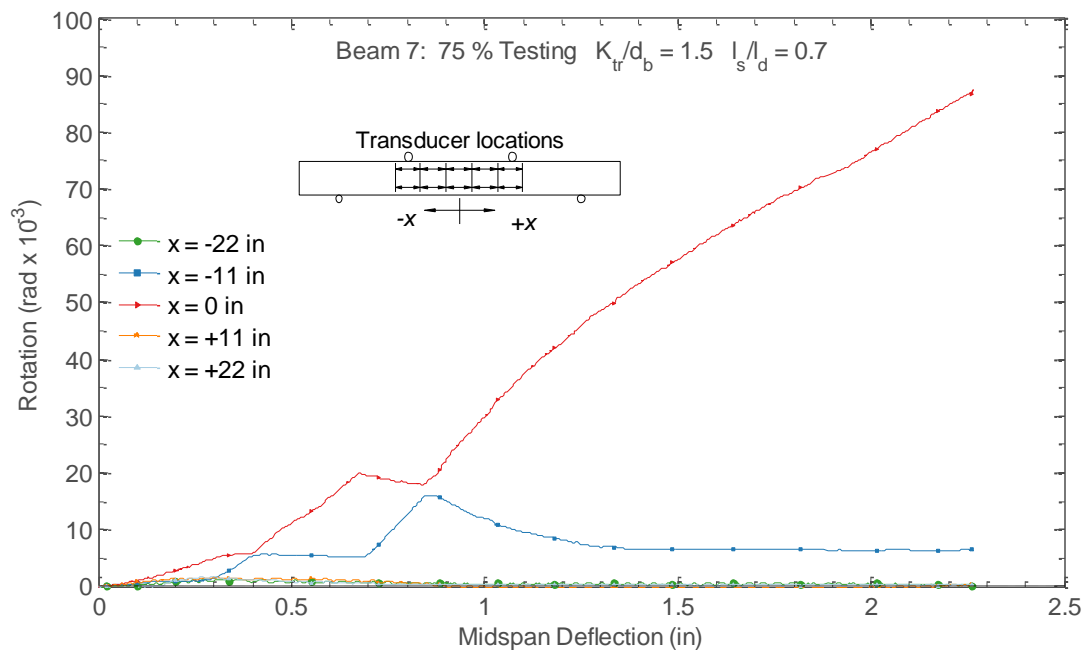
Figure C.64. Computed section rotations for Beam 7

185
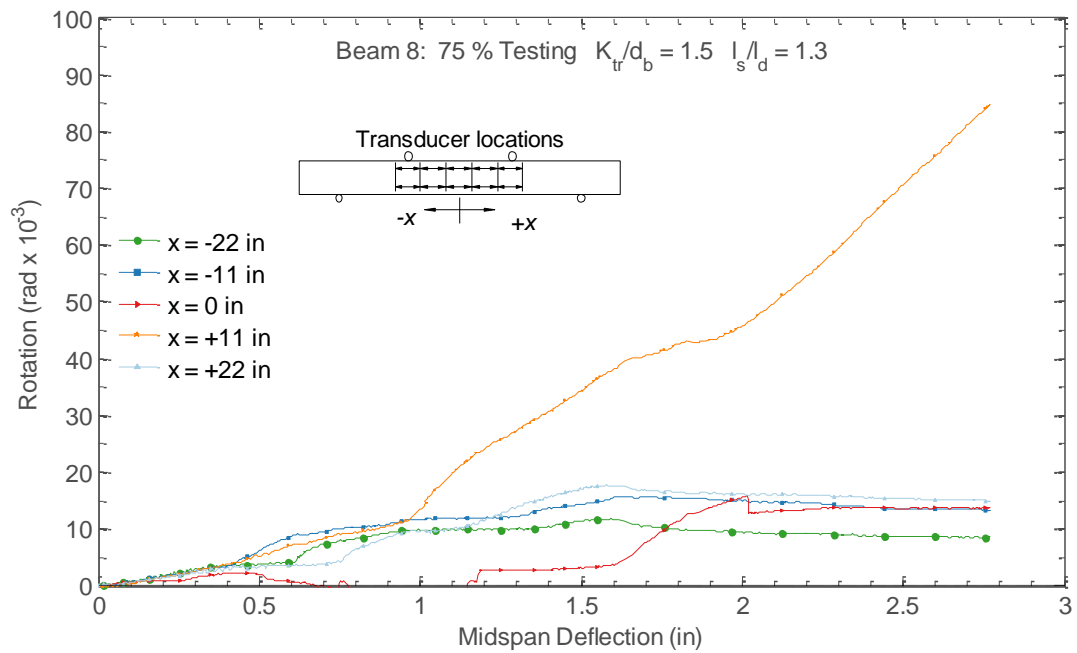
Figure C.65. Computed section rotations for Beam 8
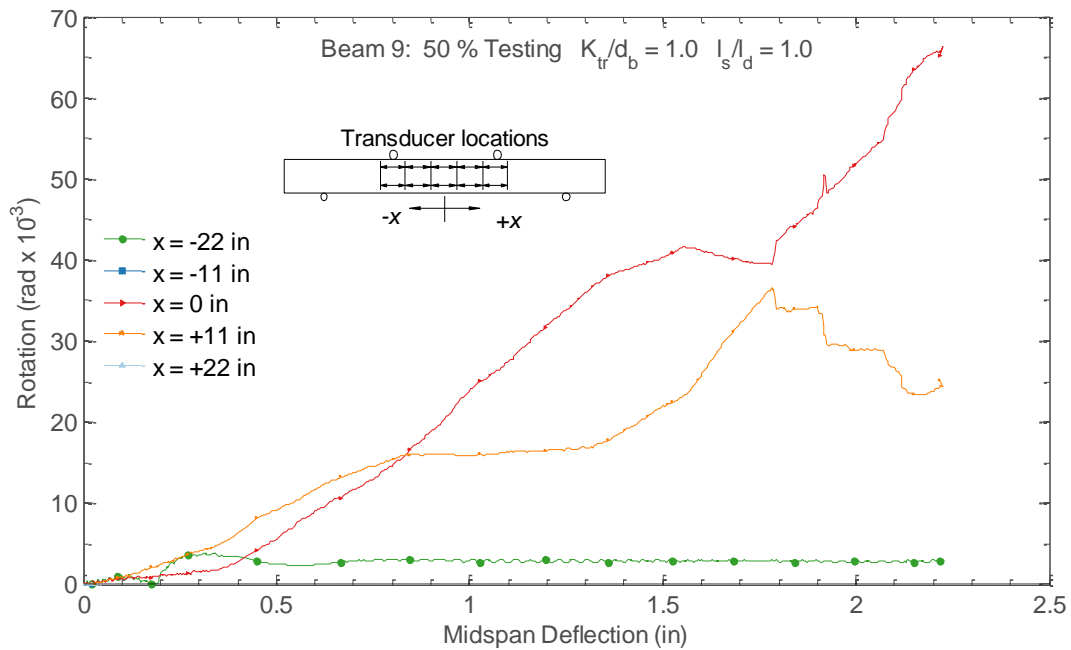
Figure C.66. Computed section rotations for Beam 9

186
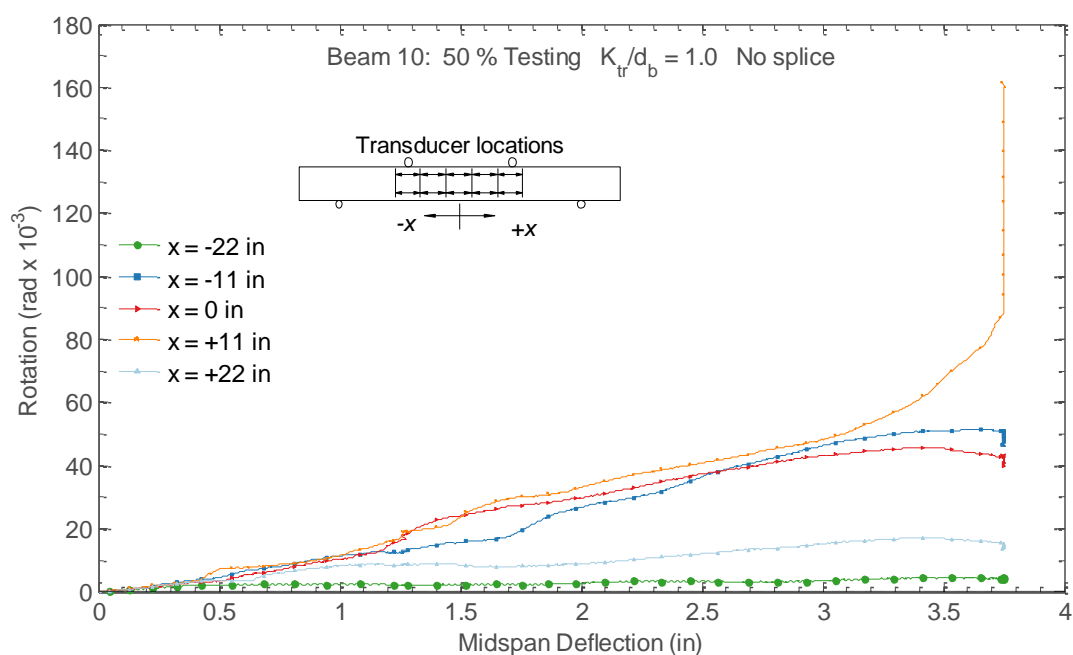
Figure C.67. Computed section rotations for Beam 10
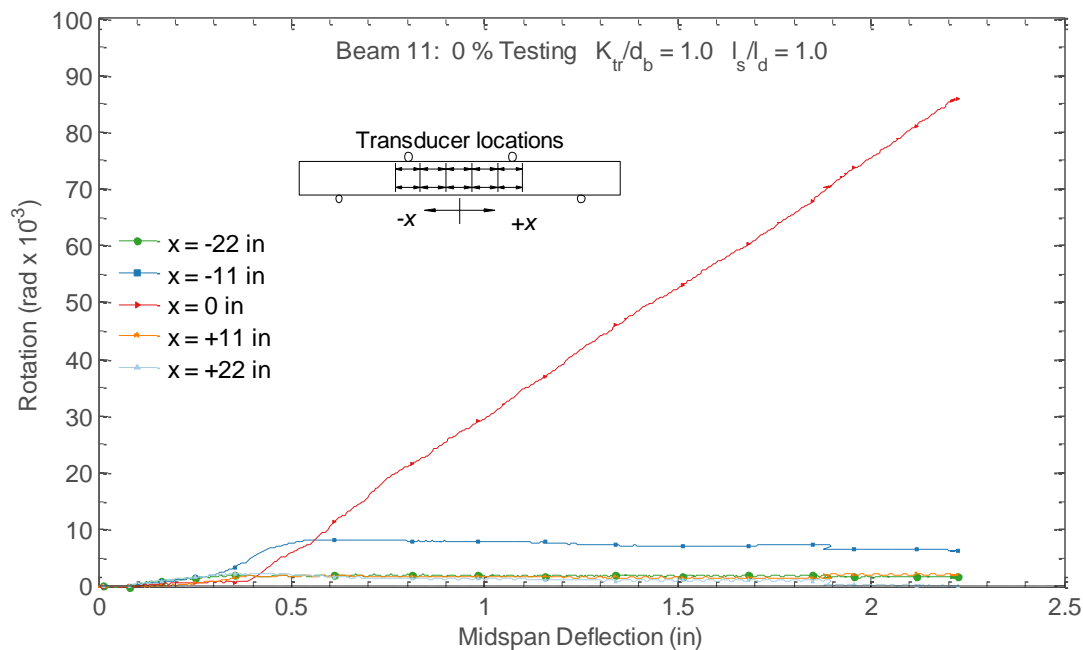
Figure C.68. Computed section rotations for Beam 11

187
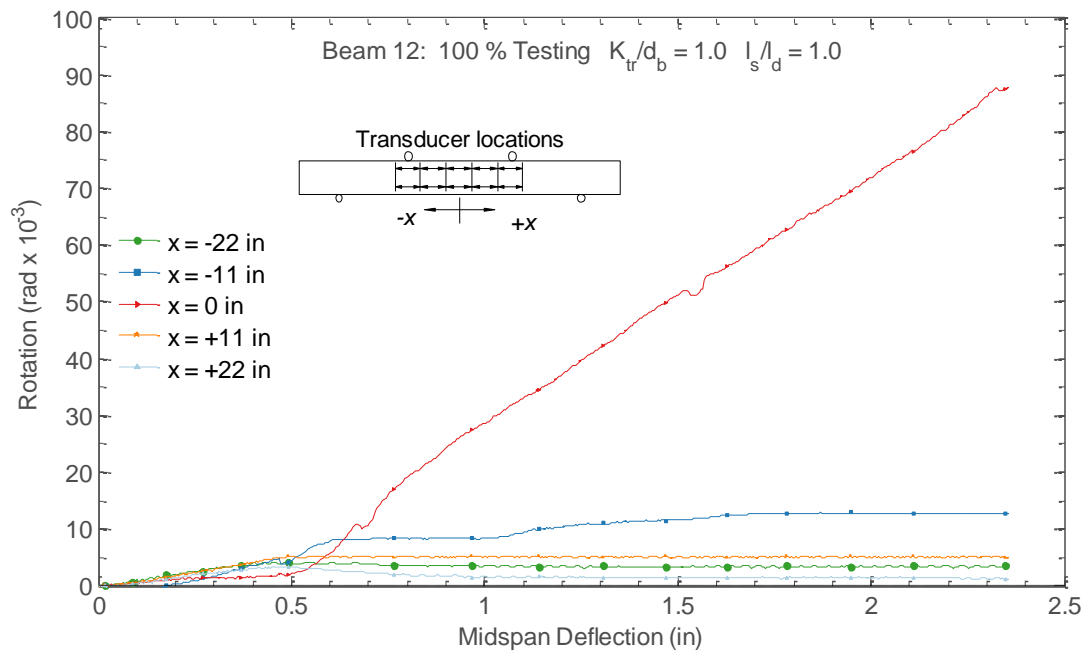
Figure C.69. Computed section rotations for Beam 12
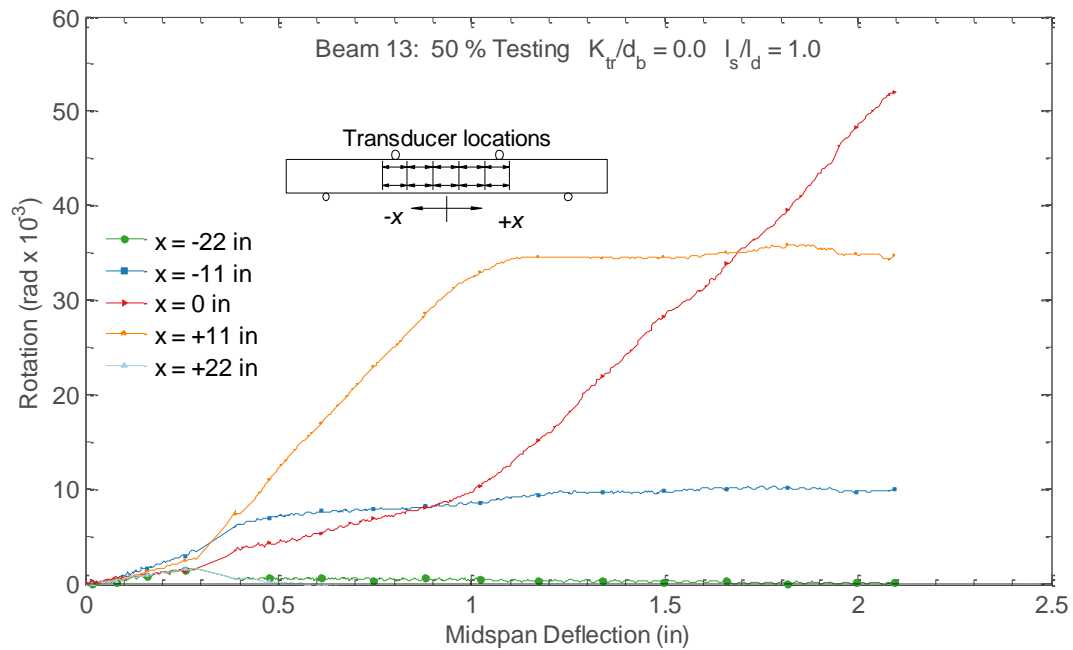
Figure C.70. Computed section rotations for Beam 13
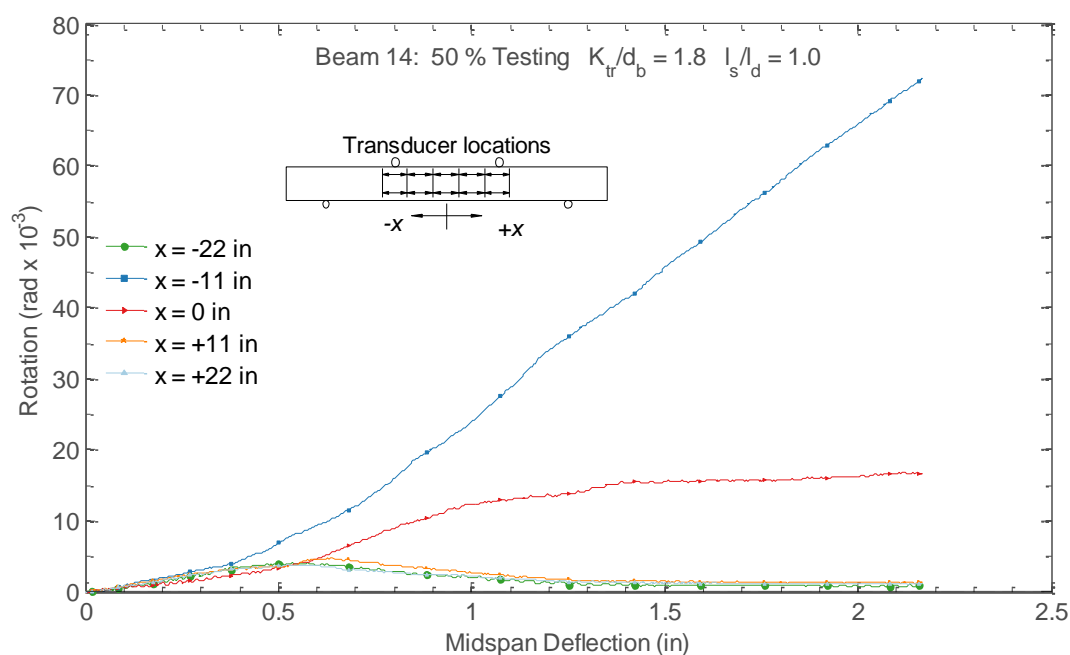
Figure C.71. Computed section rotations for Beam 14
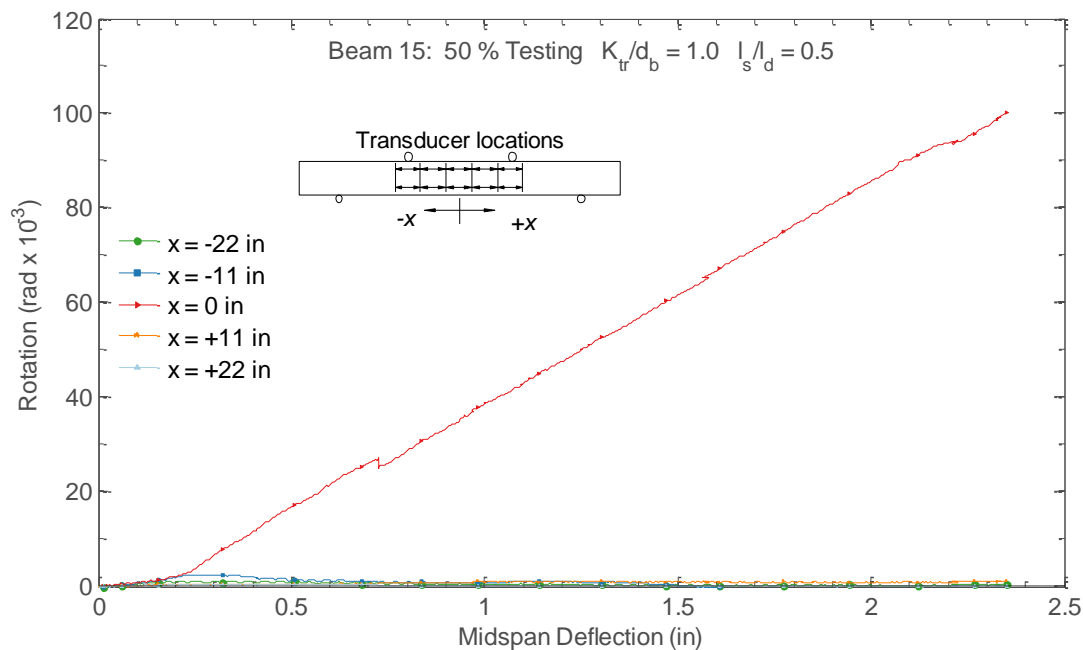
Figure C.72. Computed section rotations for Beam 15

189
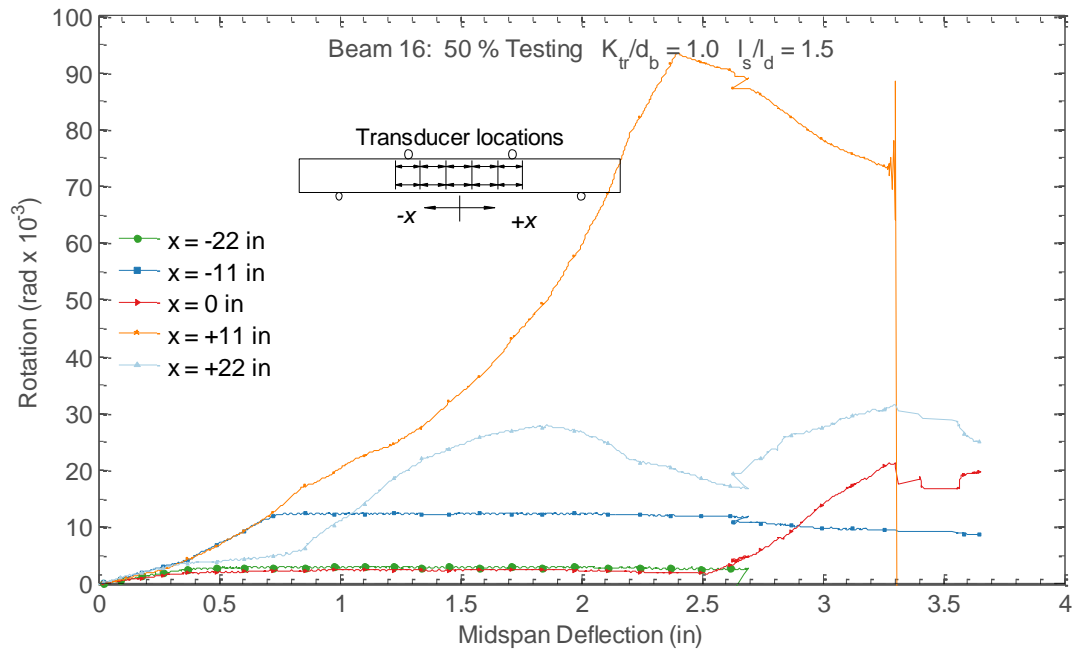
Figure C.73. Computed section rotations for Beam 16
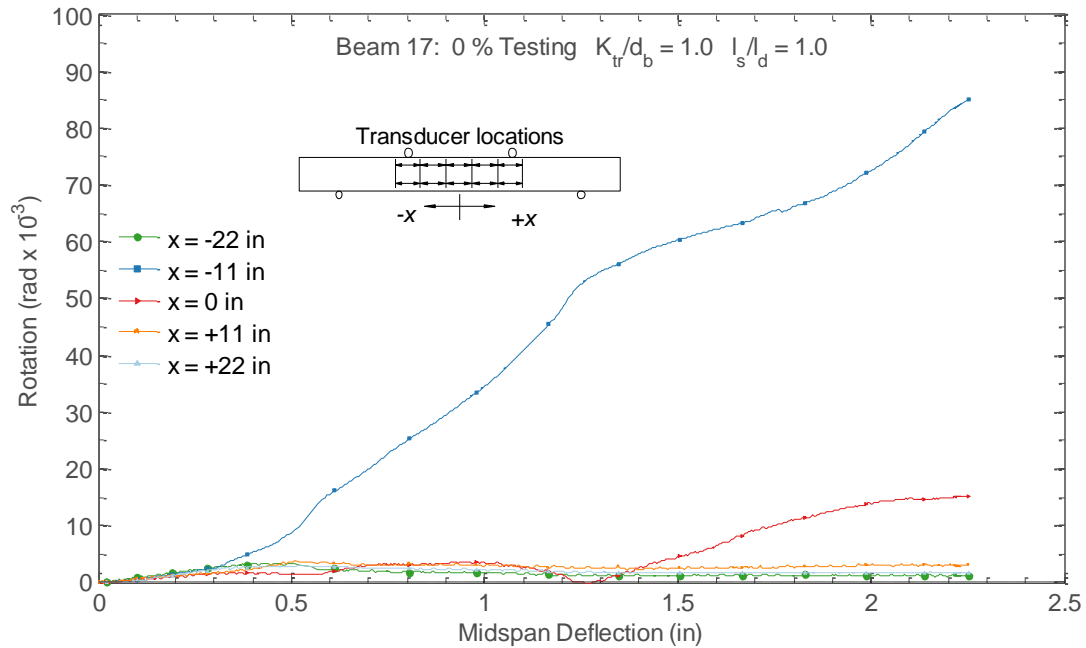
Figure C.74. Computed section rotations for Beam 17

190
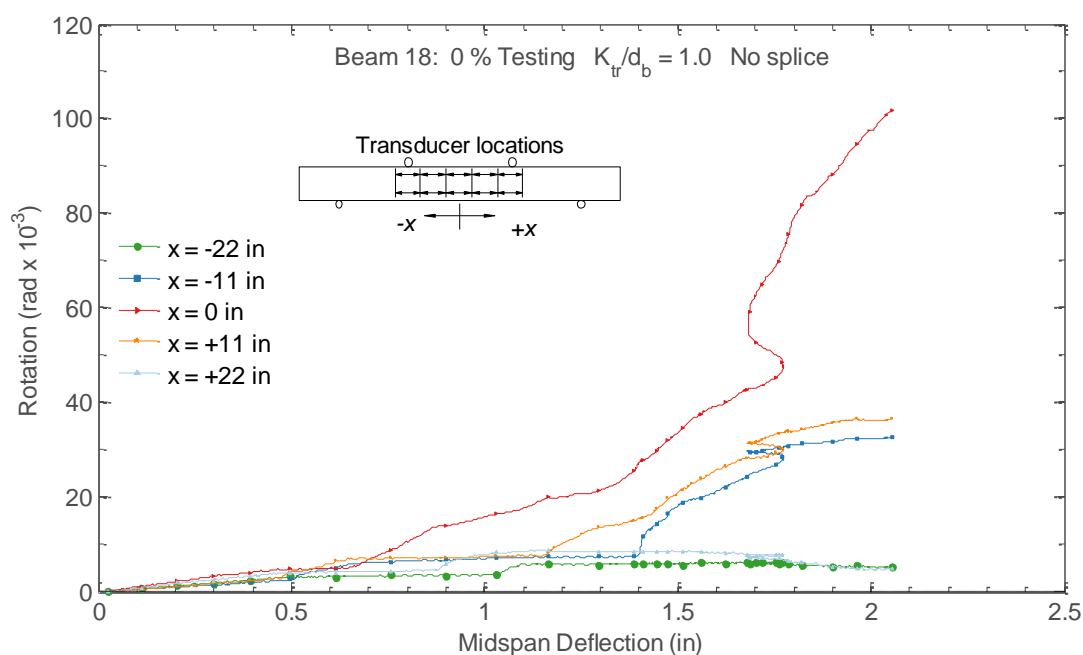
Figure C.75. Computed section rotations for Beam 18
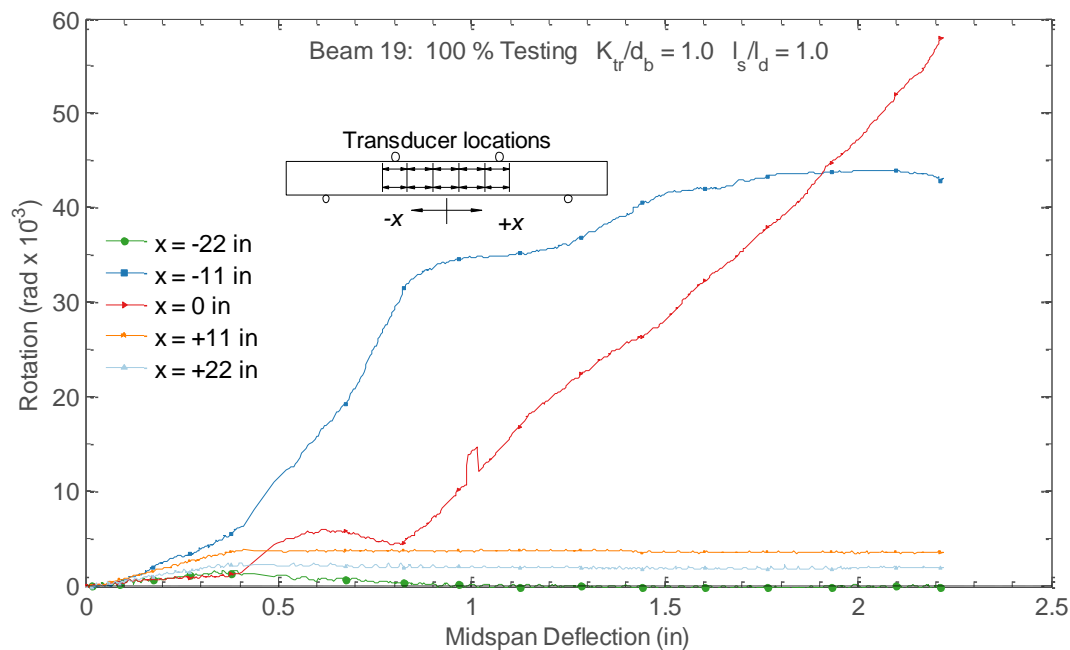
Figure C.76. Computed section rotations for Beam 19

191

Section Rotation Profile

The figures below show the distribution of rotation along the beam's length for the beam specimens. The rotation distributions are shown at the maximum moment strength and at several intermediate levels of applied moment corresponding to fractions of the ACI nominal moment strength of the beam.
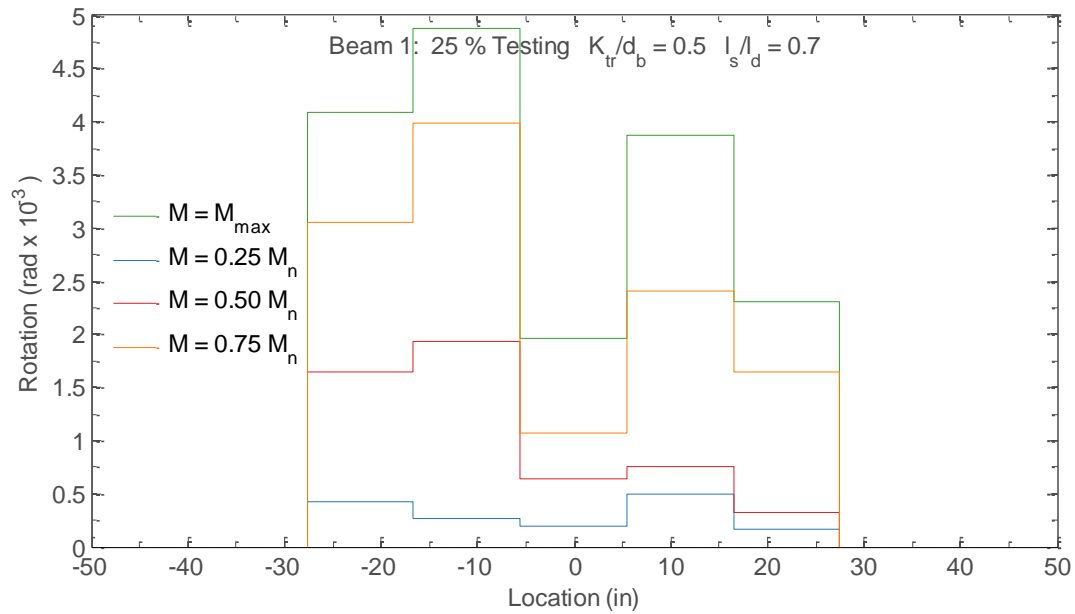
Figure C.77. Measured section rotation profiles for Beam 1
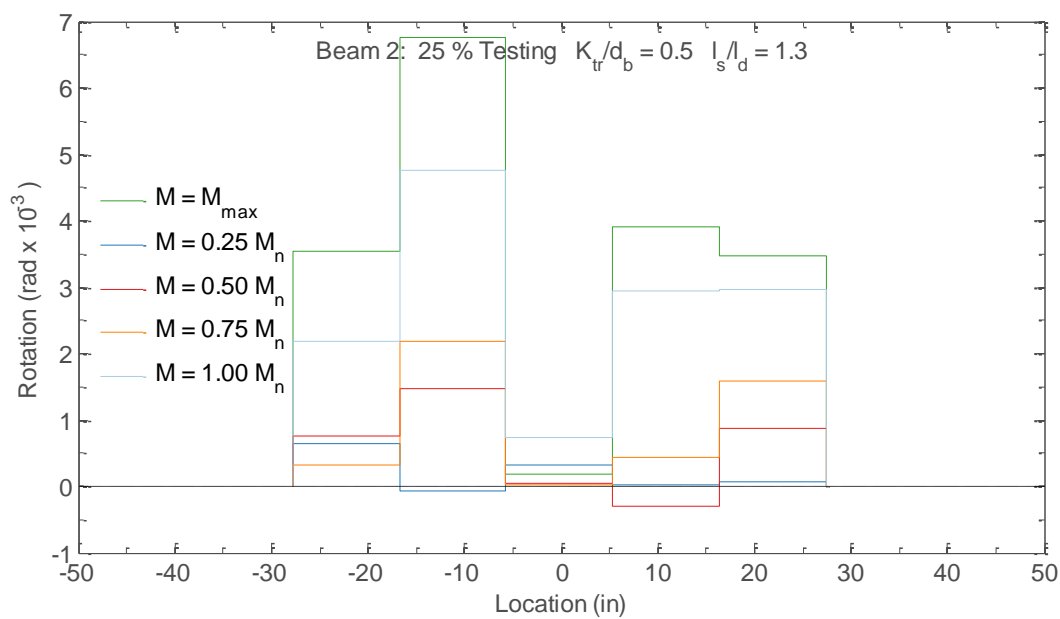
Figure C.78. Measured section rotation profiles for Beam 2
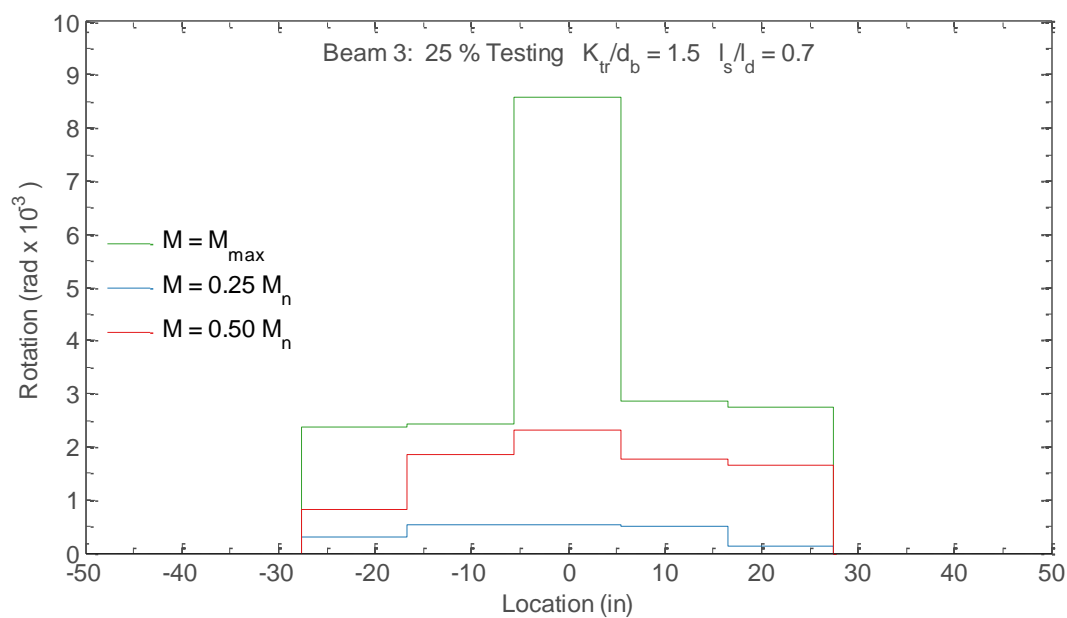
Figure C.79. Measured section rotation profiles for Beam 3
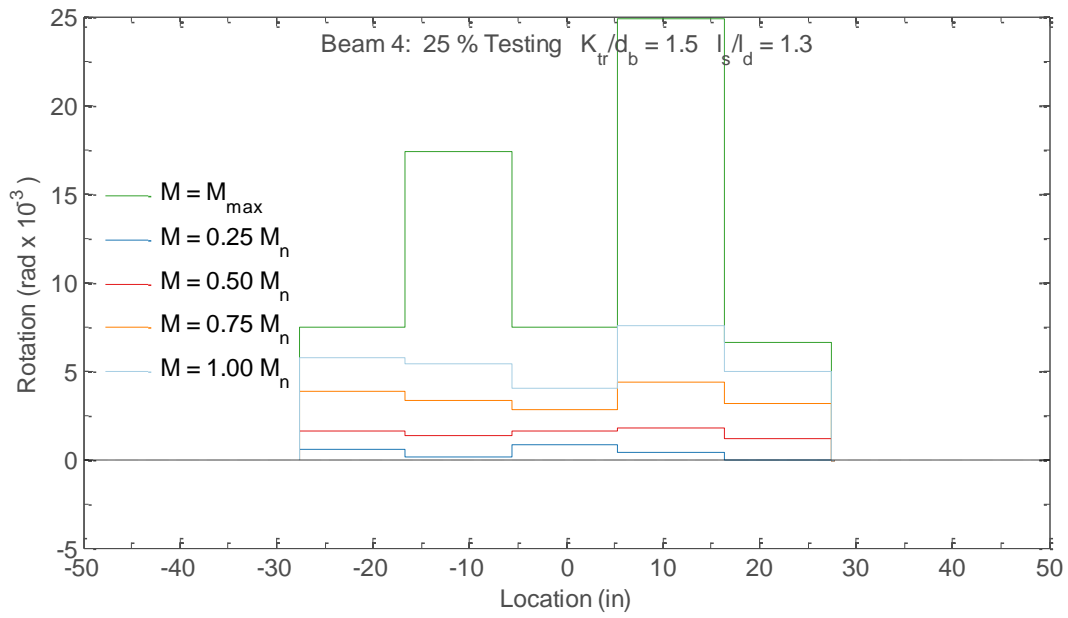
Figure C.80. Measured section rotation profiles for Beam 4
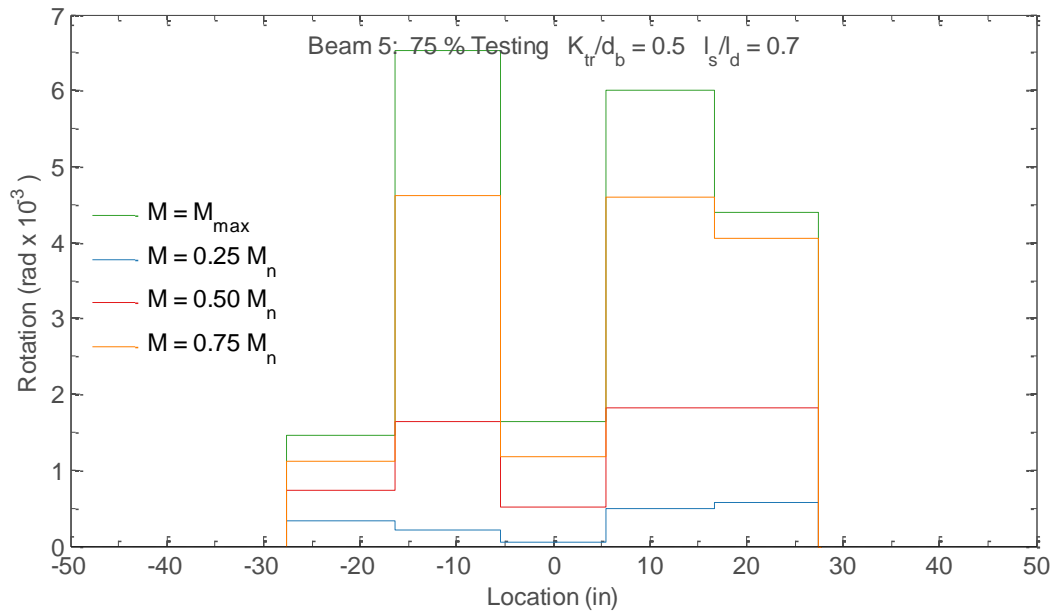
Figure C.81. Measured section rotation profiles for Beam 5
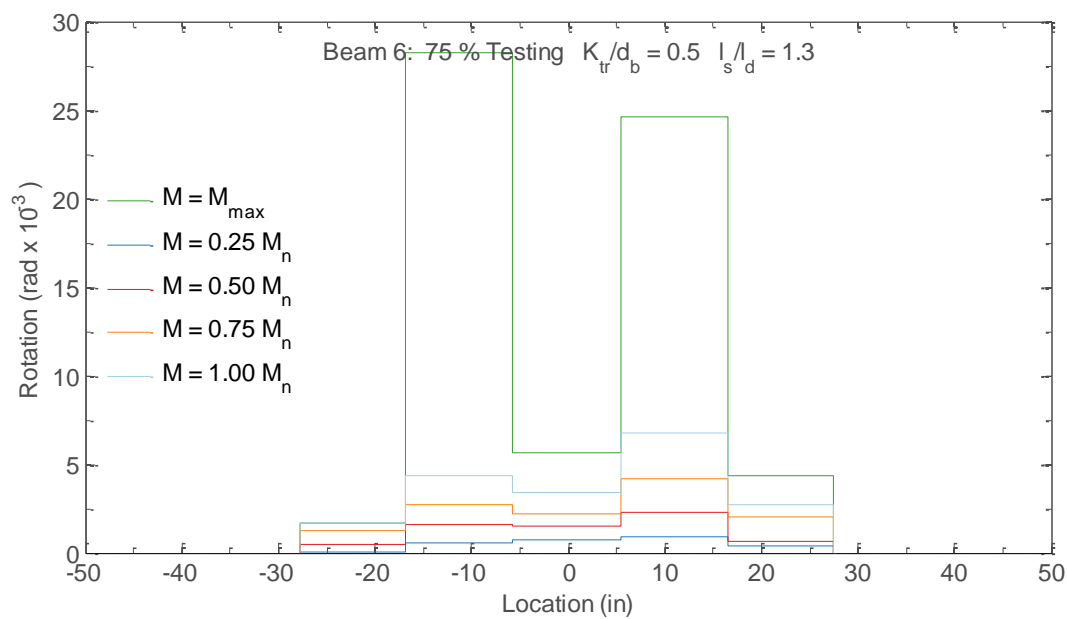
Figure C.82. Measured section rotation profiles for Beam 6
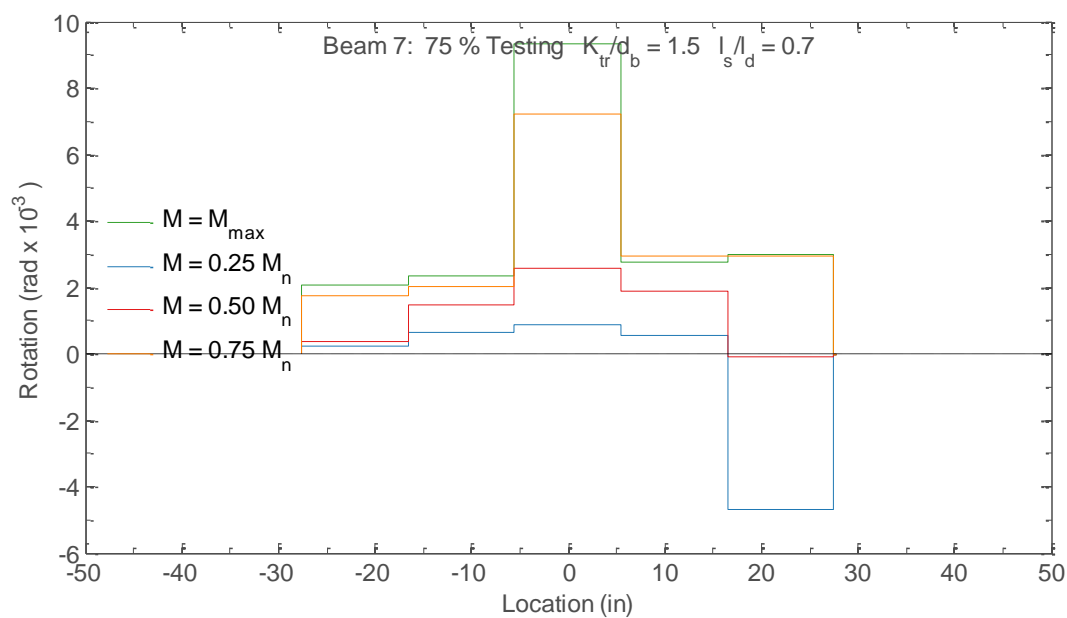
Figure C.83. Measured section rotation profiles for Beam 7

195
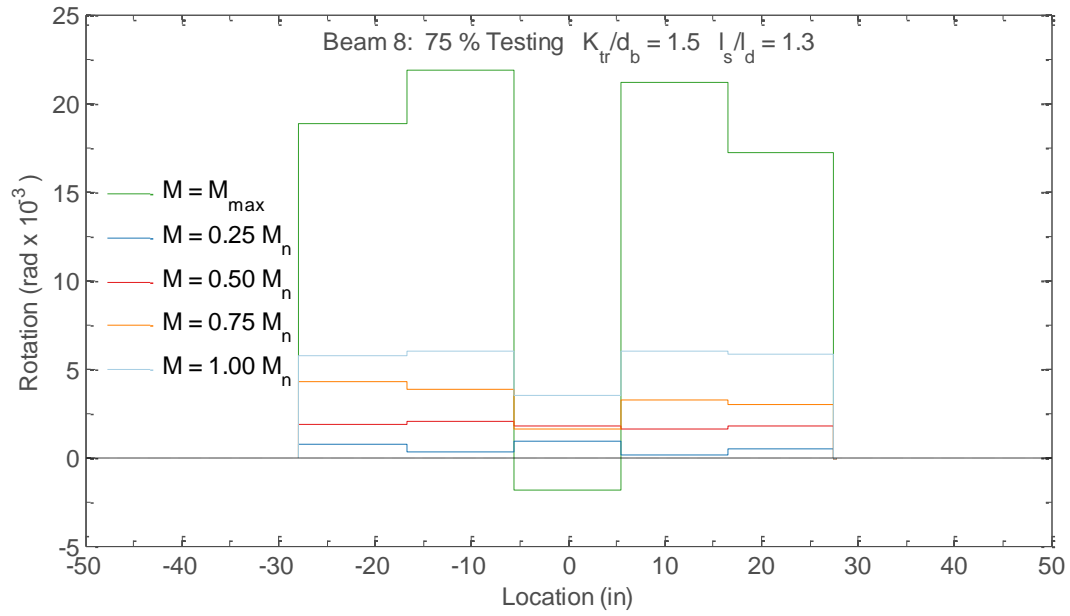
Figure C.84. Measured section rotation profiles for Beam 8
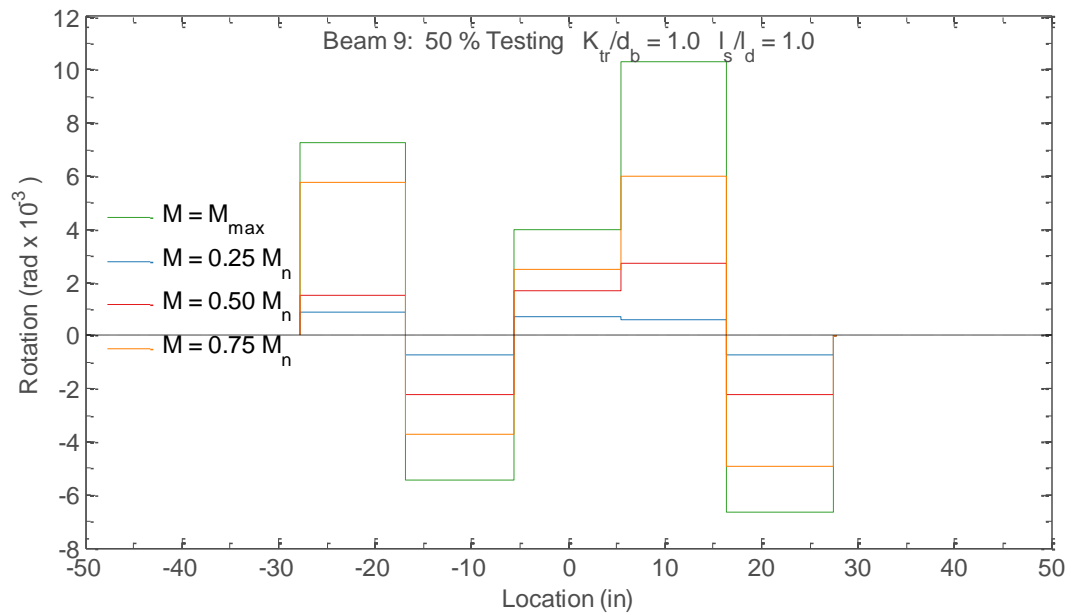
Figure C.85. Measured section rotation profiles for Beam 9
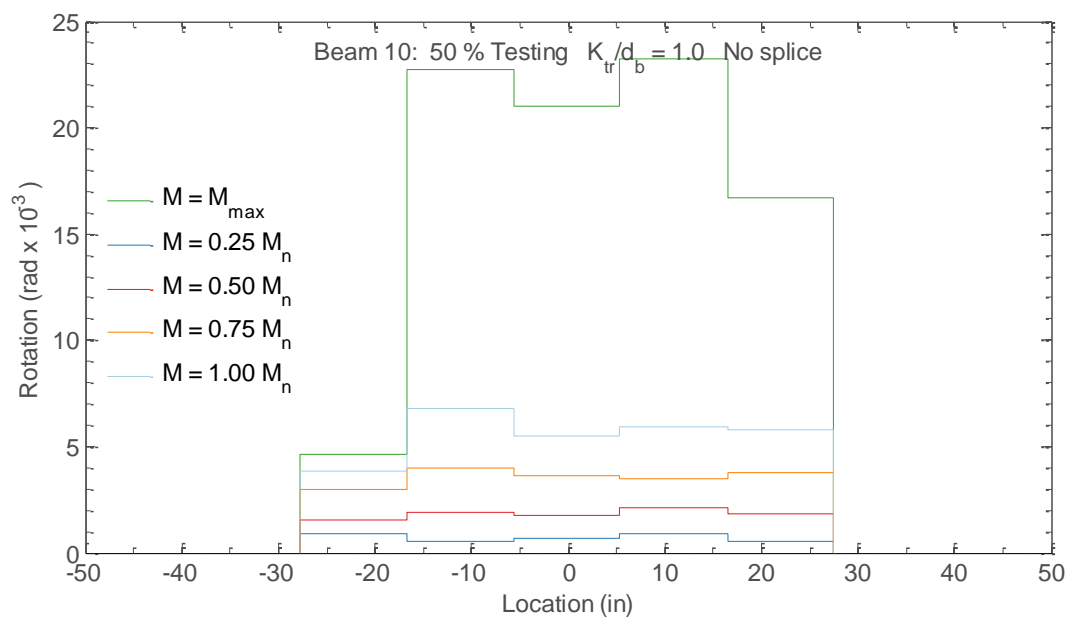
Figure C.86. Measured section rotation profiles for Beam 10
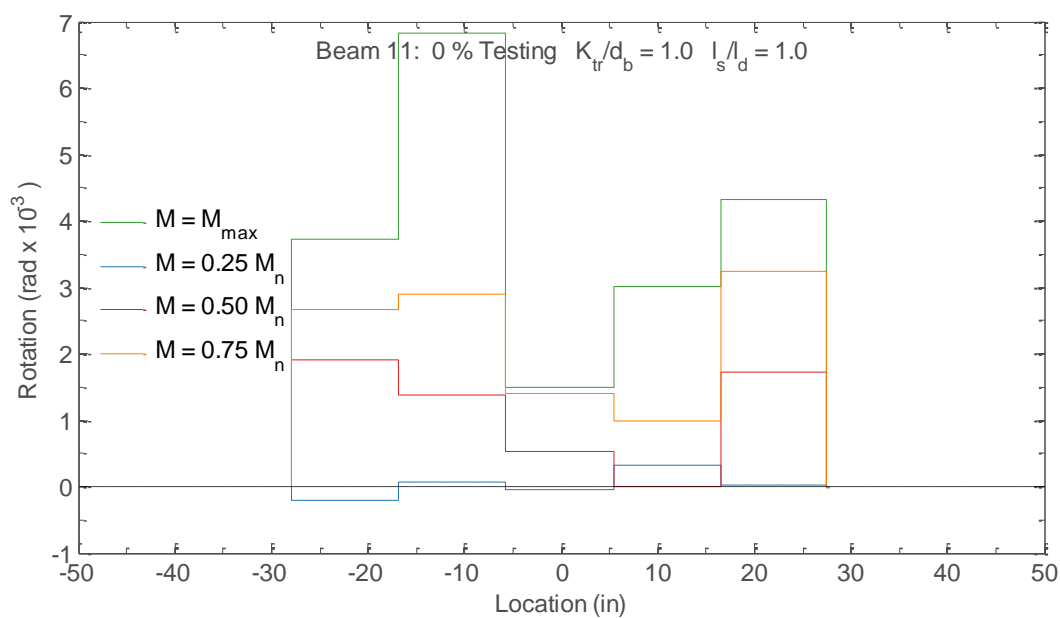
Figure C.87. Measured section rotation profiles for Beam 11
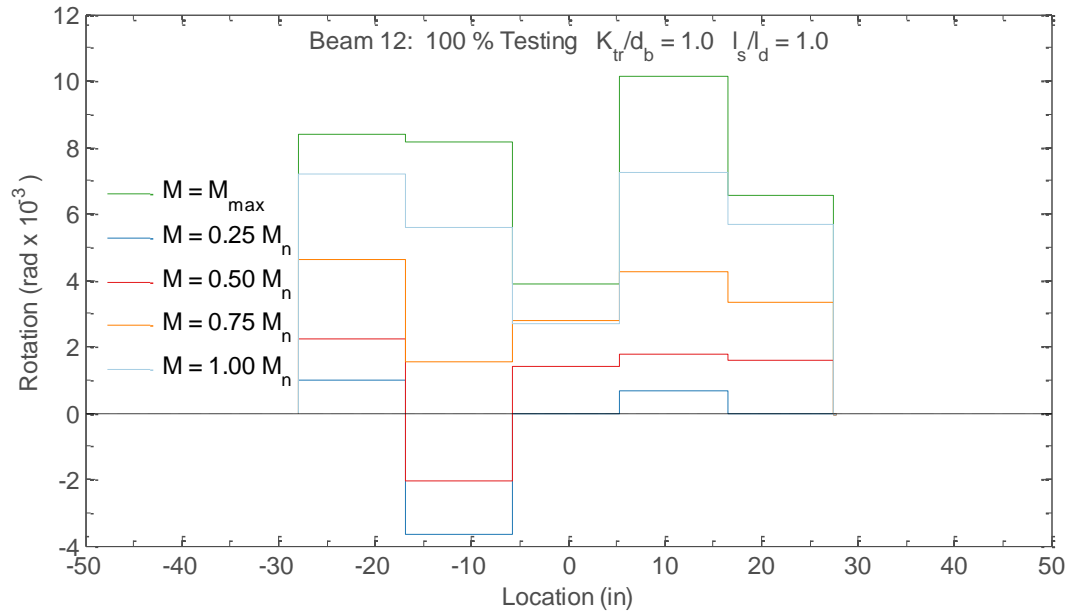
Figure C.88. Measured section rotation profiles for Beam 12
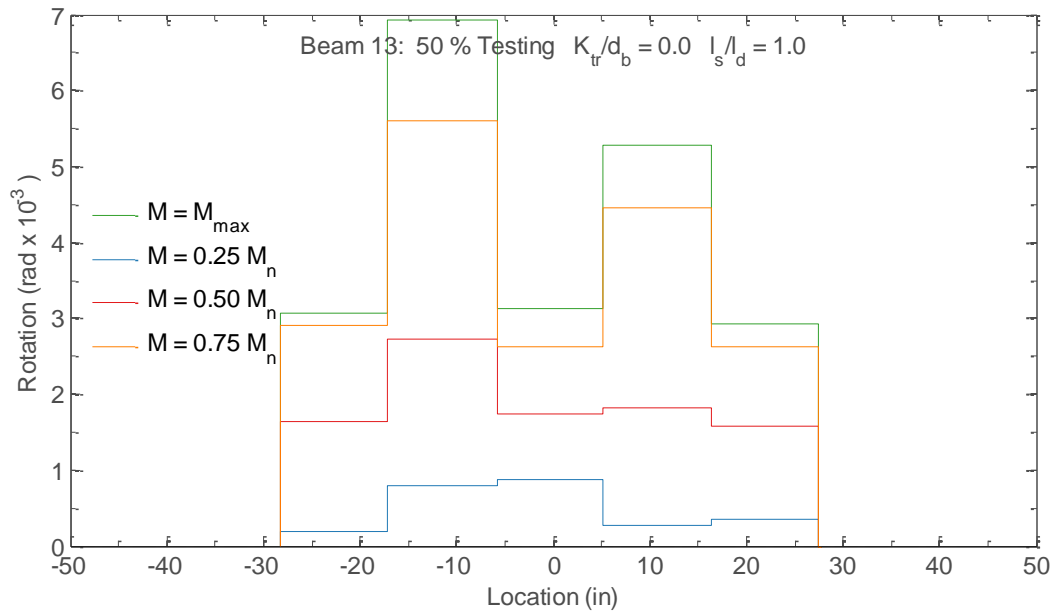
Figure C.89. Measured section rotation profiles for Beam 13
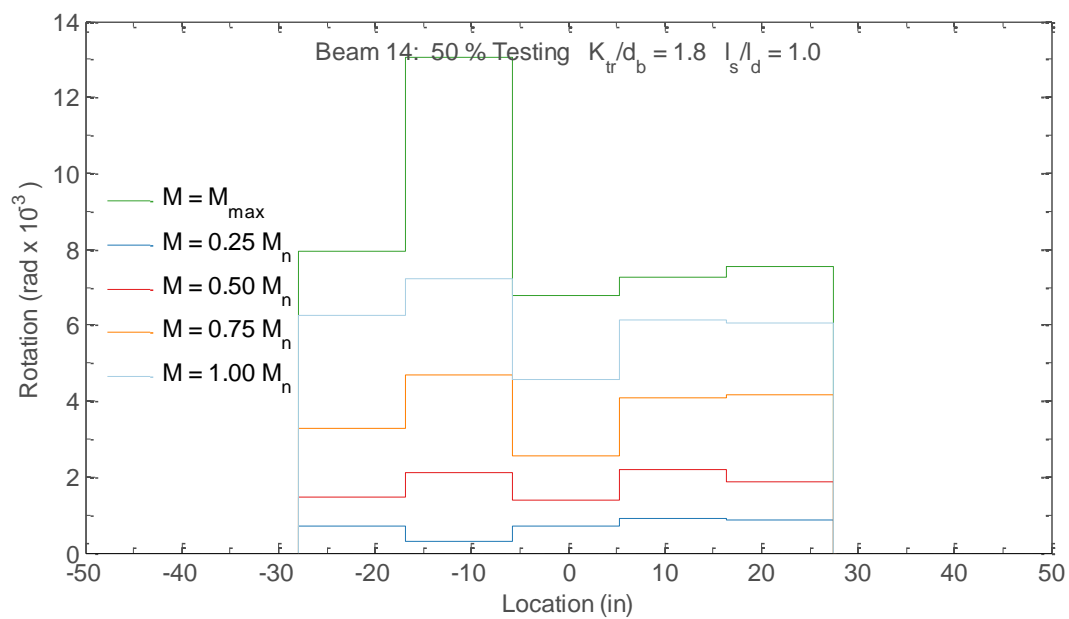
Figure C.90. Measured section rotation profiles for Beam 14
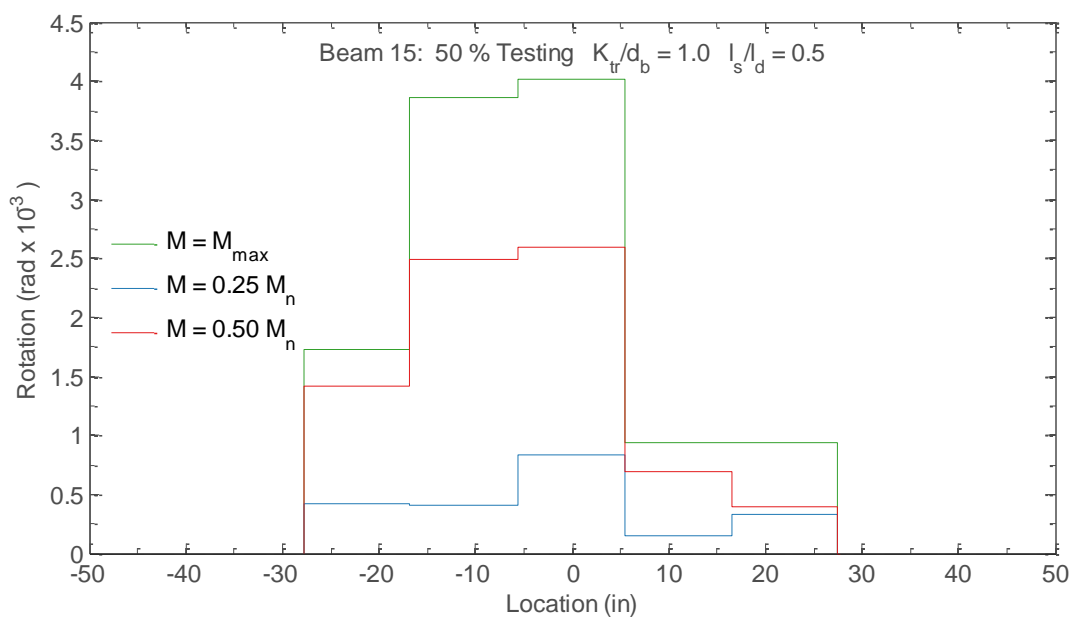
Figure C.91. Measured section rotation profiles for Beam 15
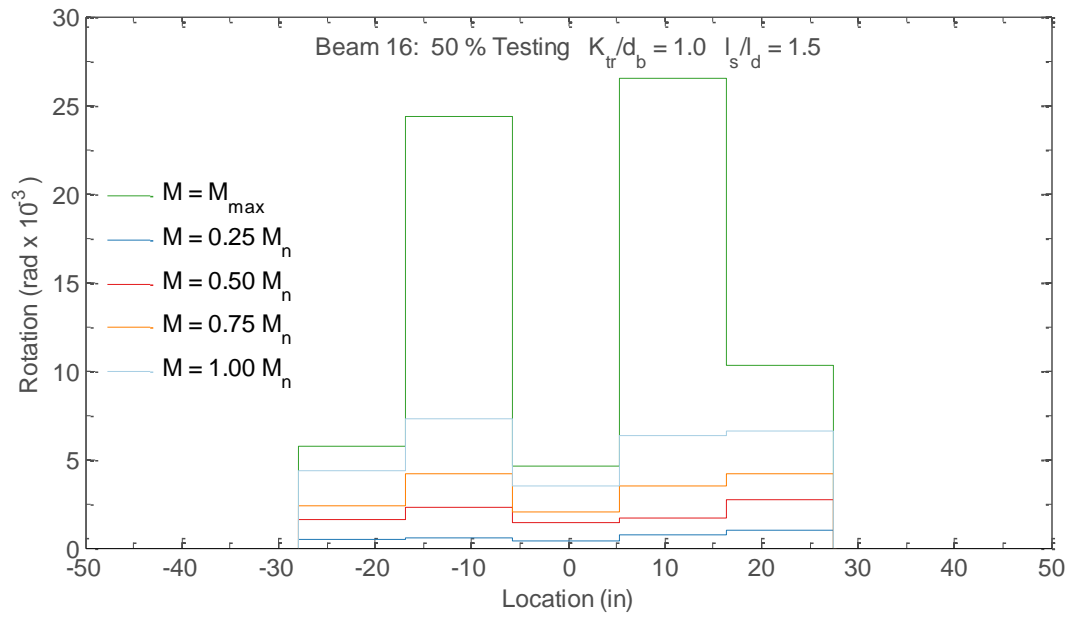
Figure C.92. Measured section rotation profiles for Beam 16
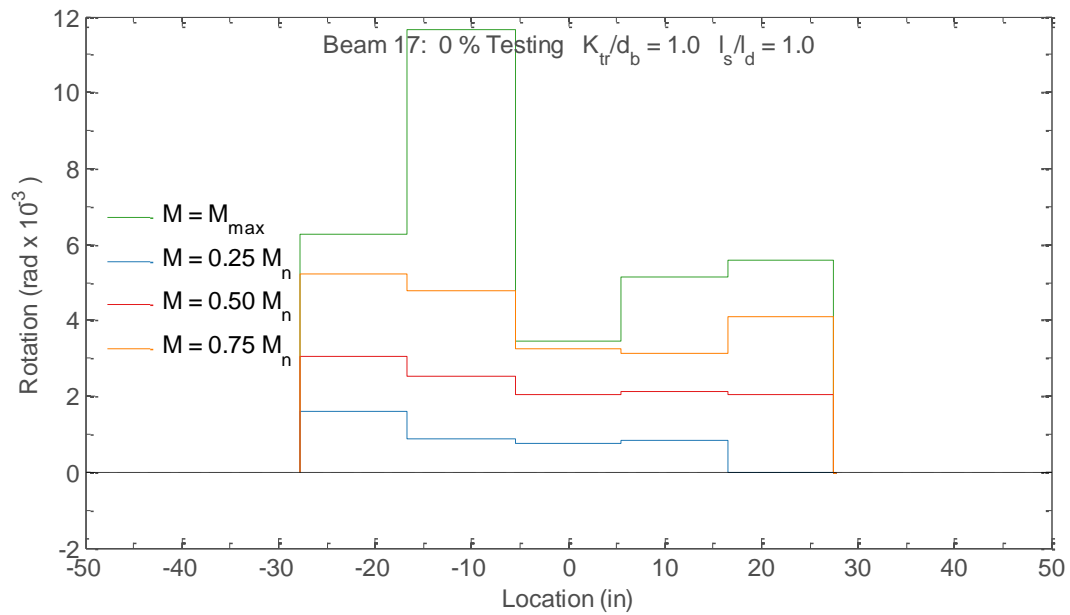
Figure C.93. Measured section rotation profiles for Beam 17
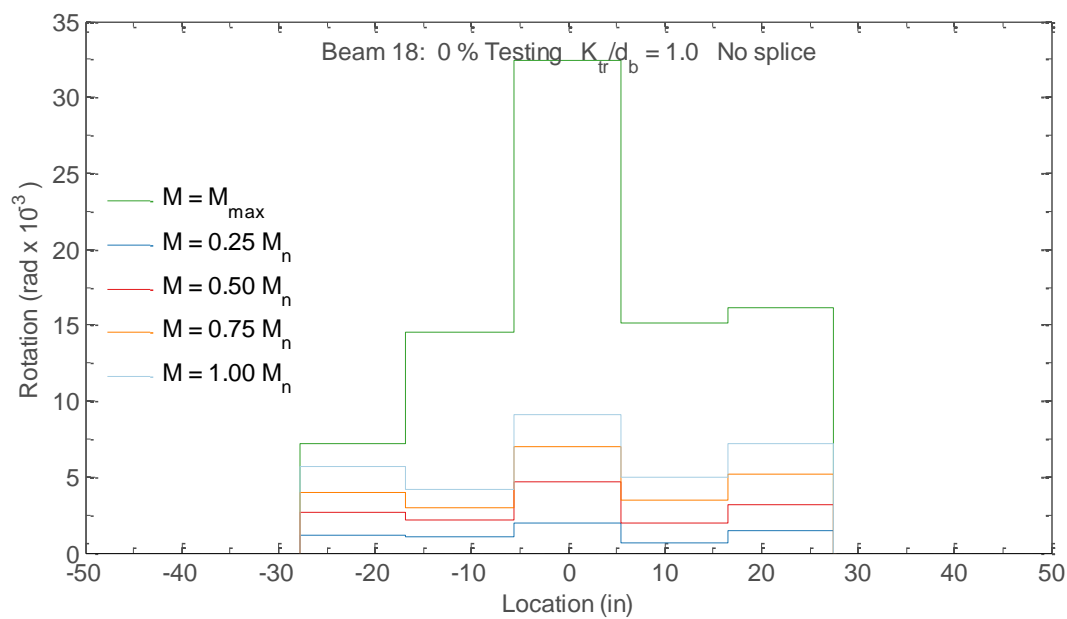
Figure C.94. Measured section rotation profiles for Beam 18
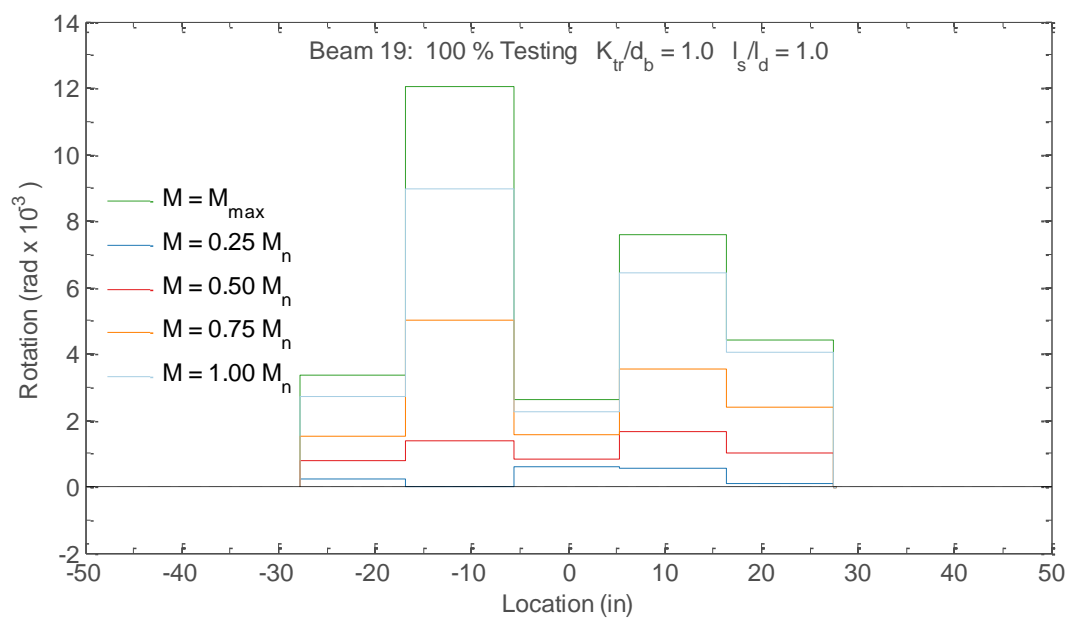
Figure C.95. Measured section rotation profiles for Beam 19

End Rotations

The figures below show the beam end rotation, with respect to a horizontal axis, measured over the supports at mid-height of the beam for the beam specimens. Rotations were roughly symmetric, especially at smaller vertical midspan deflections. Measured rotations were consistent with the deflections measured halfway between the supports and loading points.
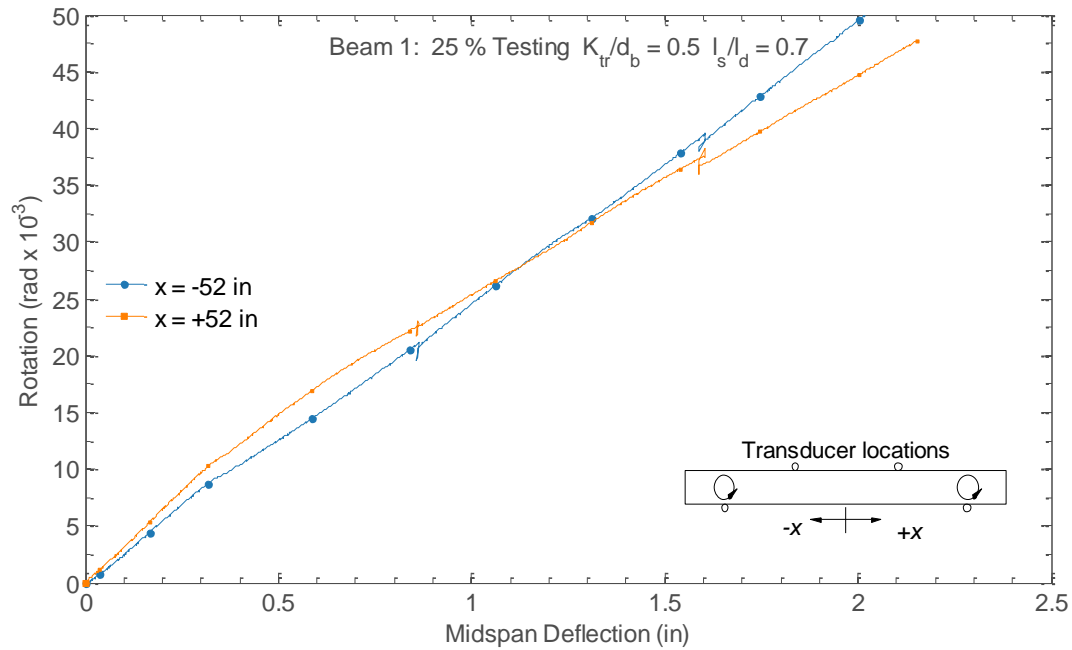
Figure C.96. Measured end rotations for Beam 1
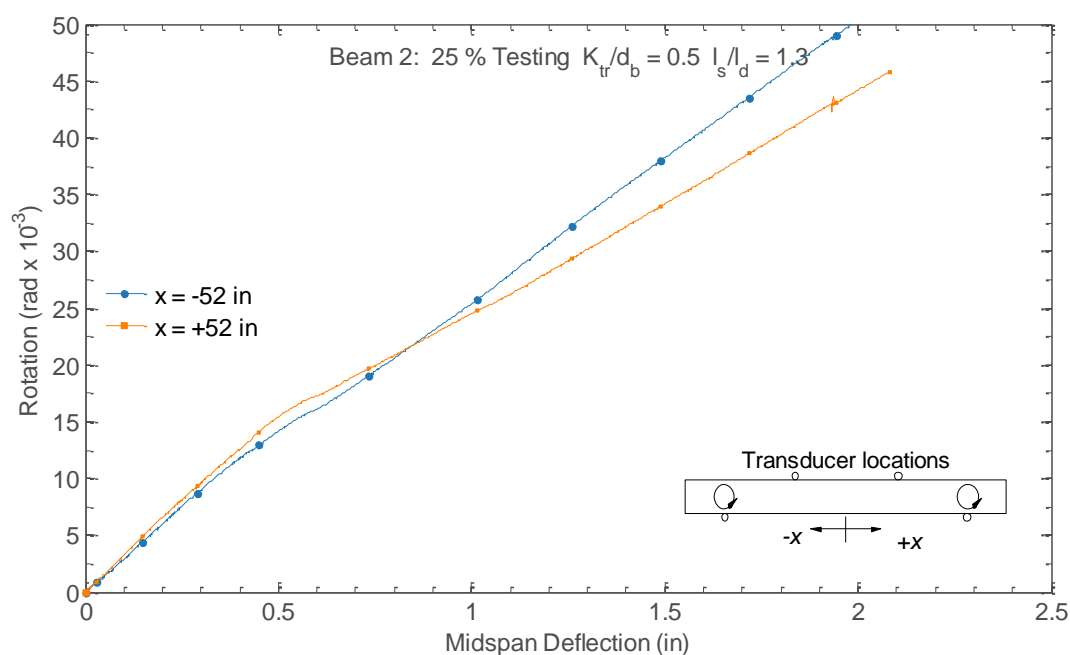
Figure C.97. Measured end rotations for Beam 2
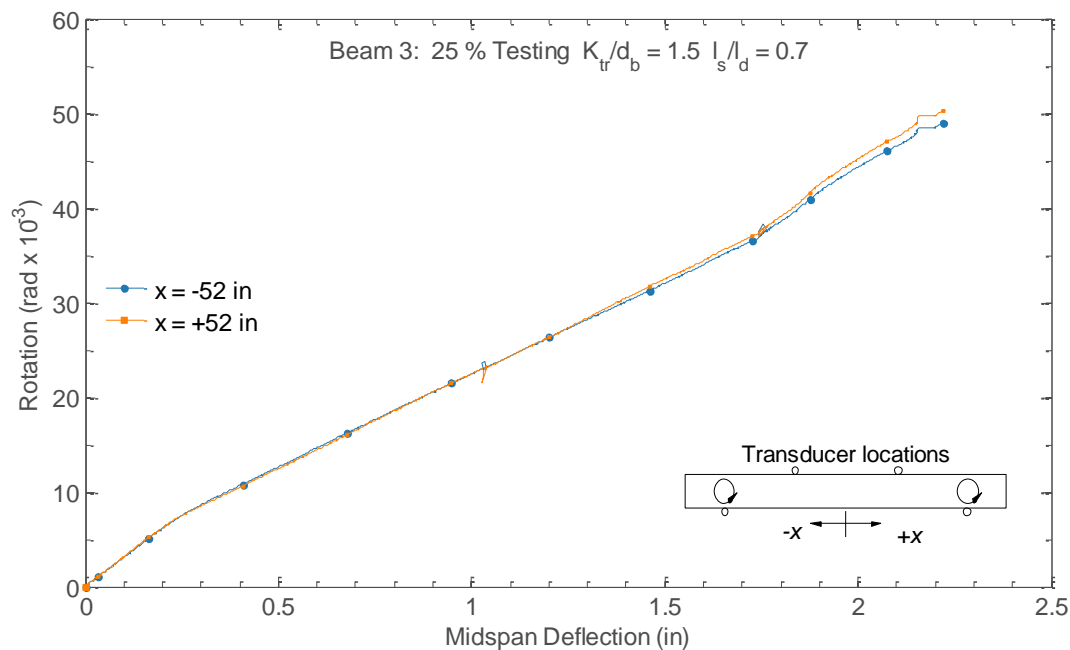
Figure C.98. Measured end rotations for Beam 3

203
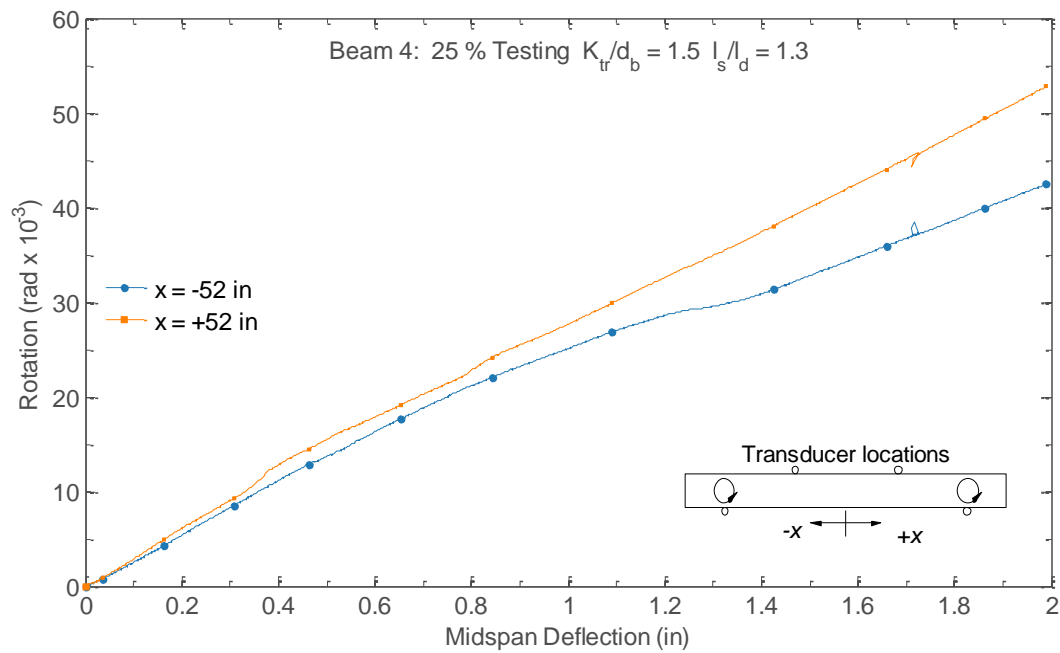
Figure C.99. Measured end rotations for Beam 4
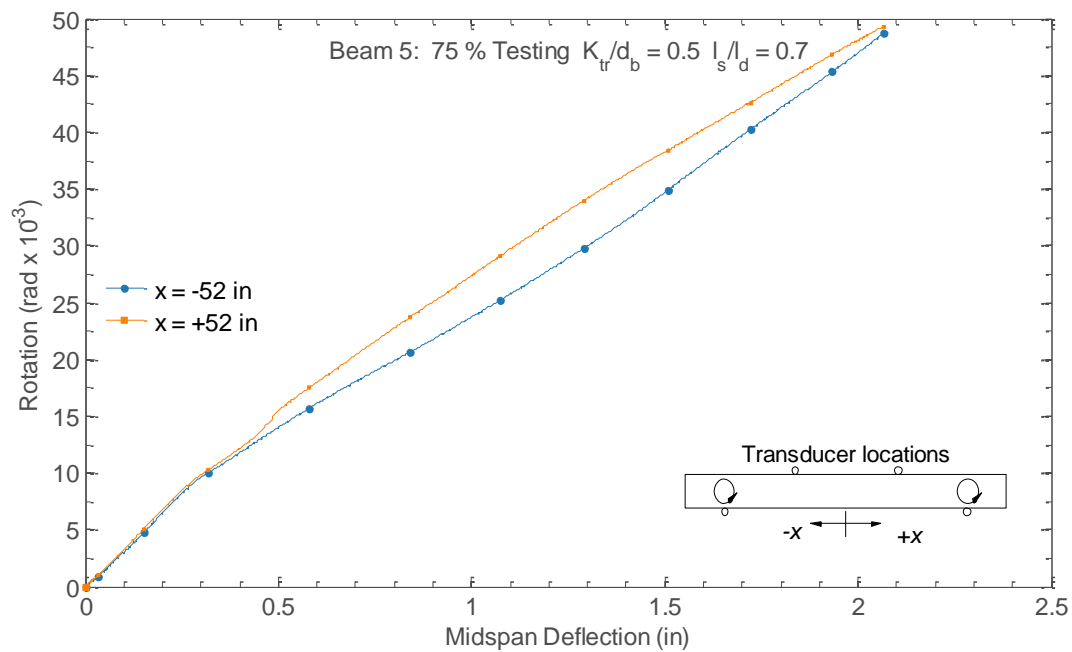
Figure C.100. Measured end rotations for Beam 5

204
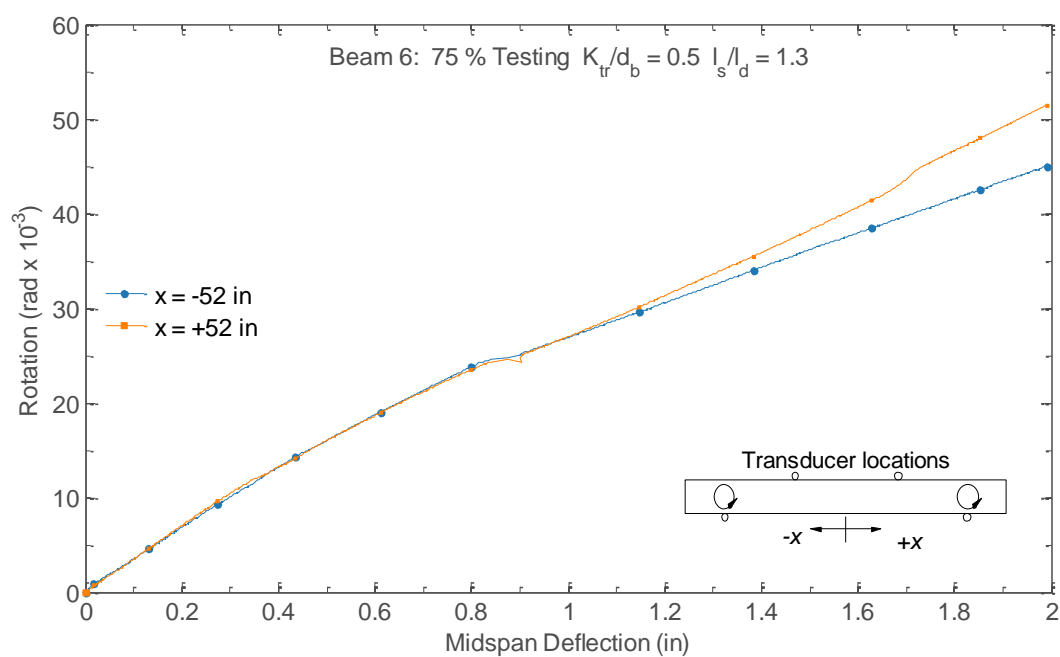
Figure C.101. Measured end rotations for Beam 6
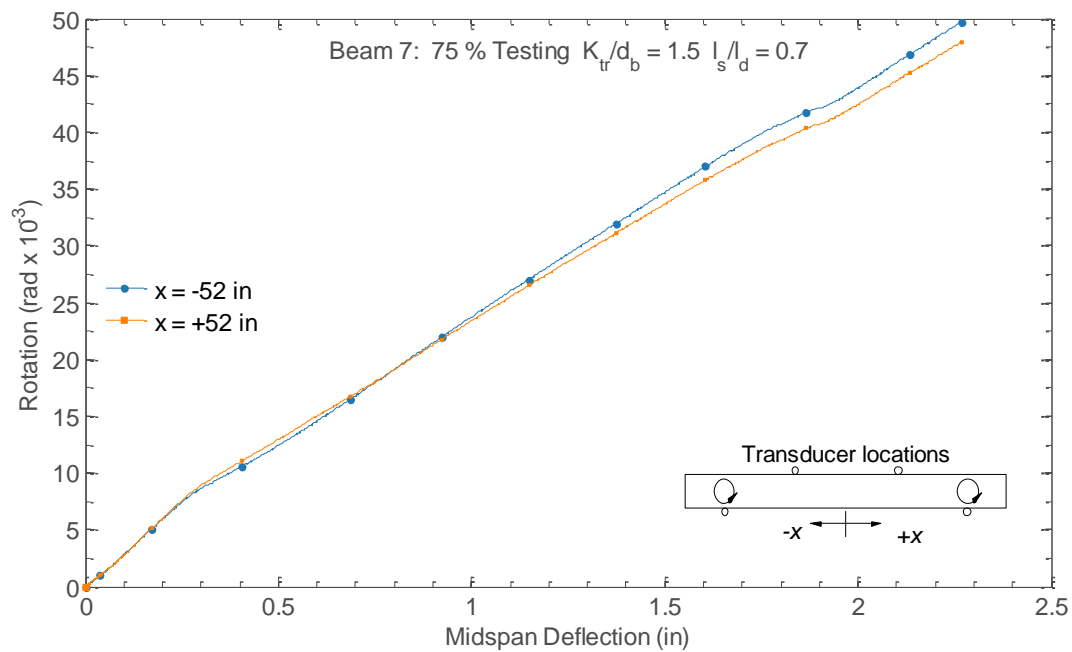
Figure C.102. Measured end rotations for Beam 7

205
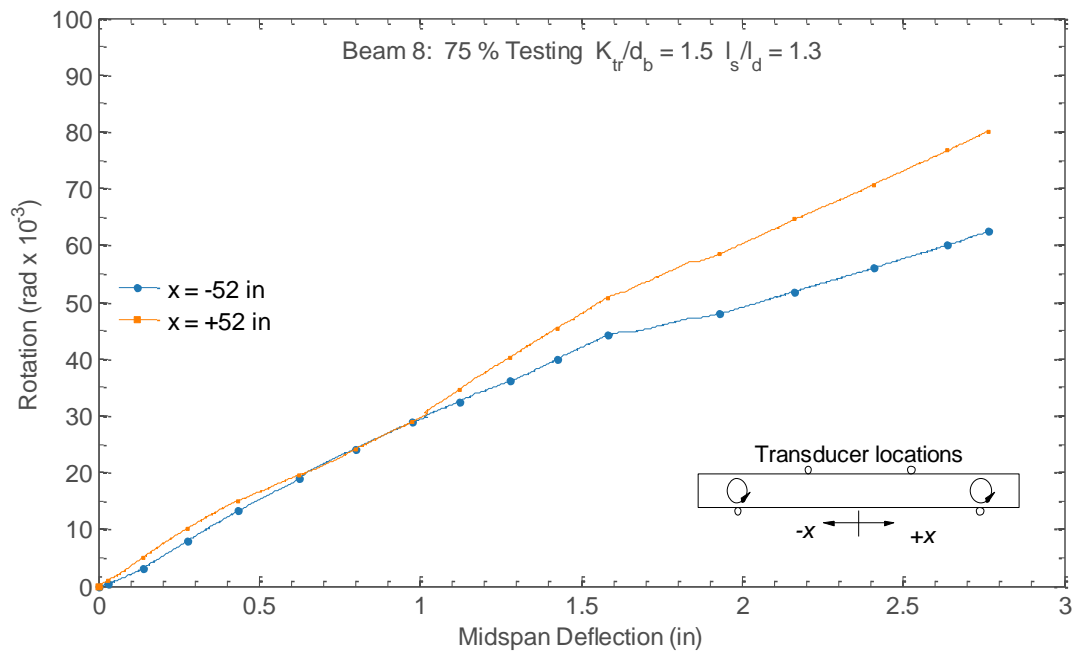
Figure C.103. Measured end rotations for Beam 8
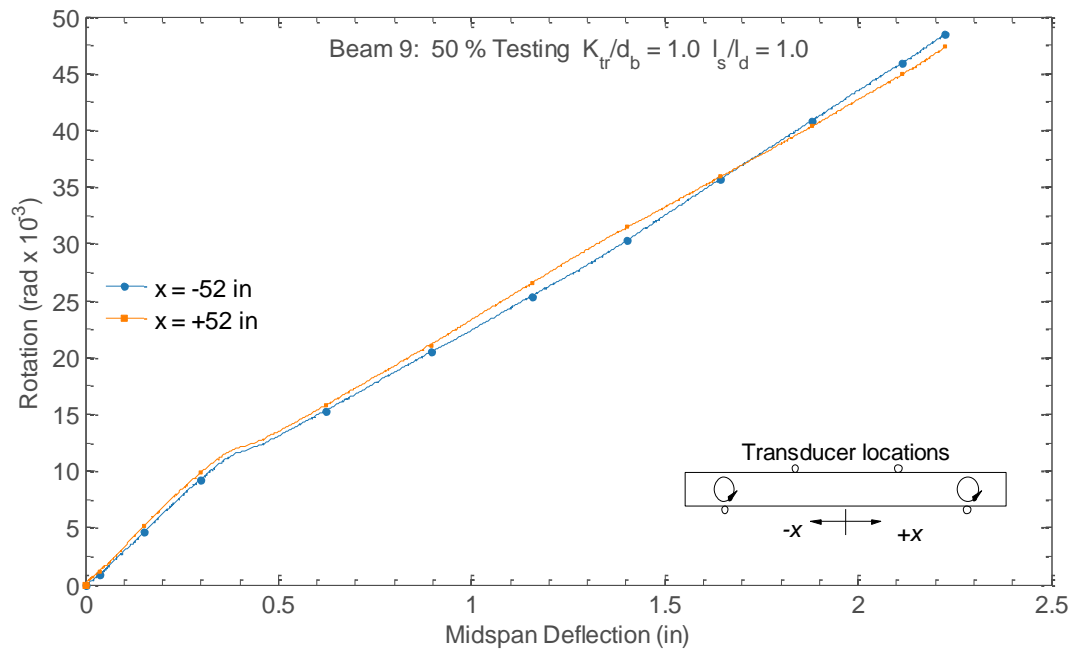
Figure C.104. Measured end rotations for Beam 9

206
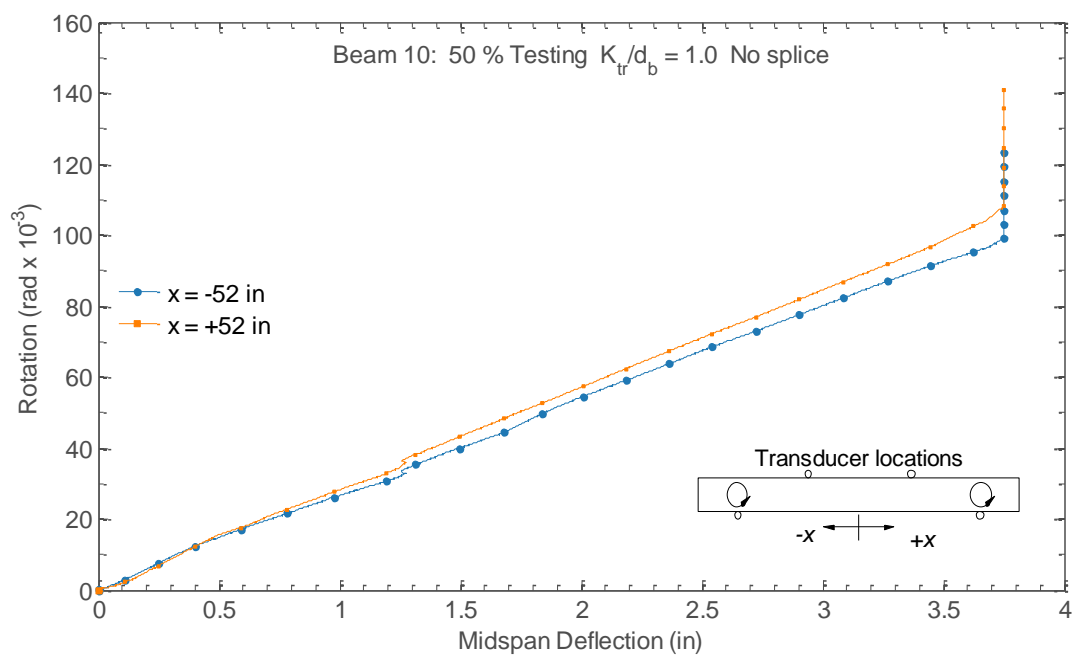
Figure C.105. Measured end rotations for Beam 10
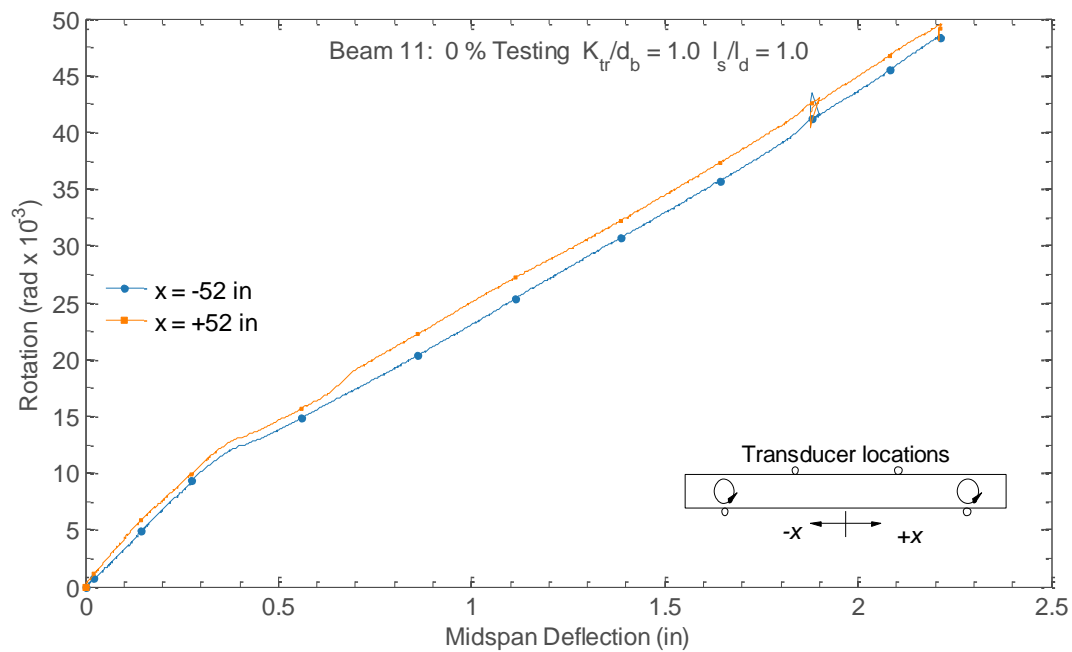
Figure C.106. Measured end rotations for Beam 11

207
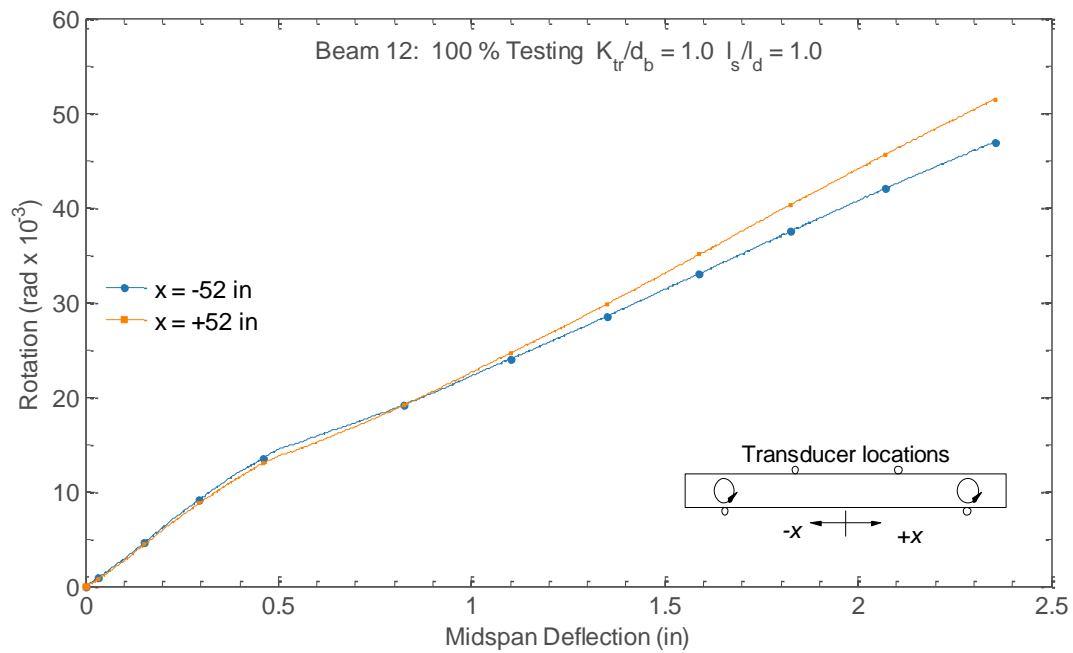
Figure C.107. Measured end rotations for Beam 12
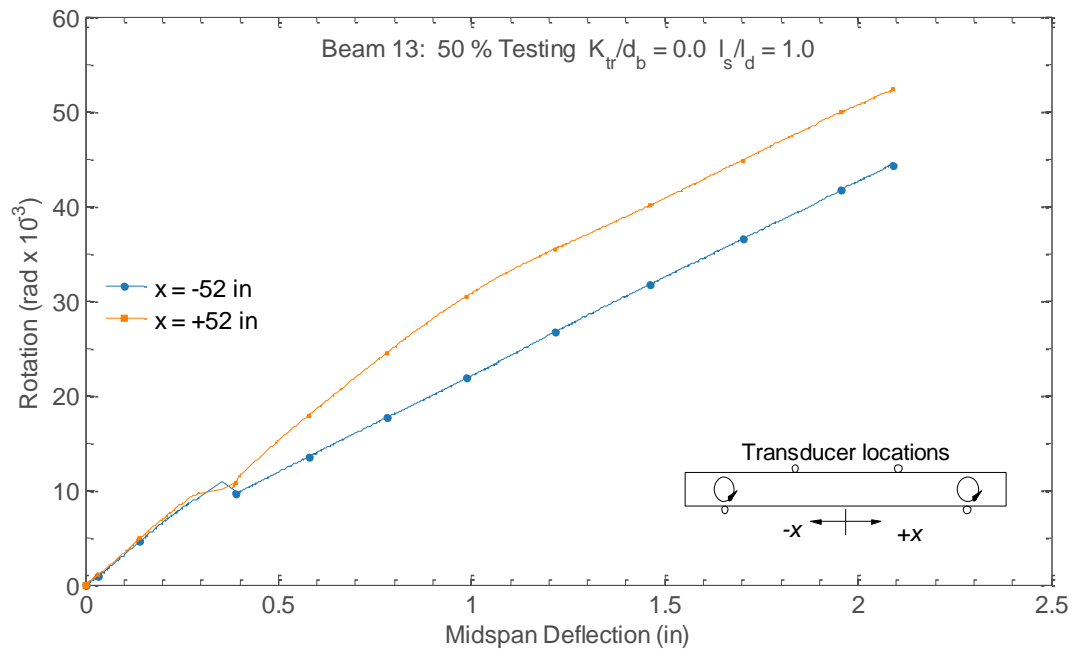
Figure C.108. Measured end rotations for Beam 13

208
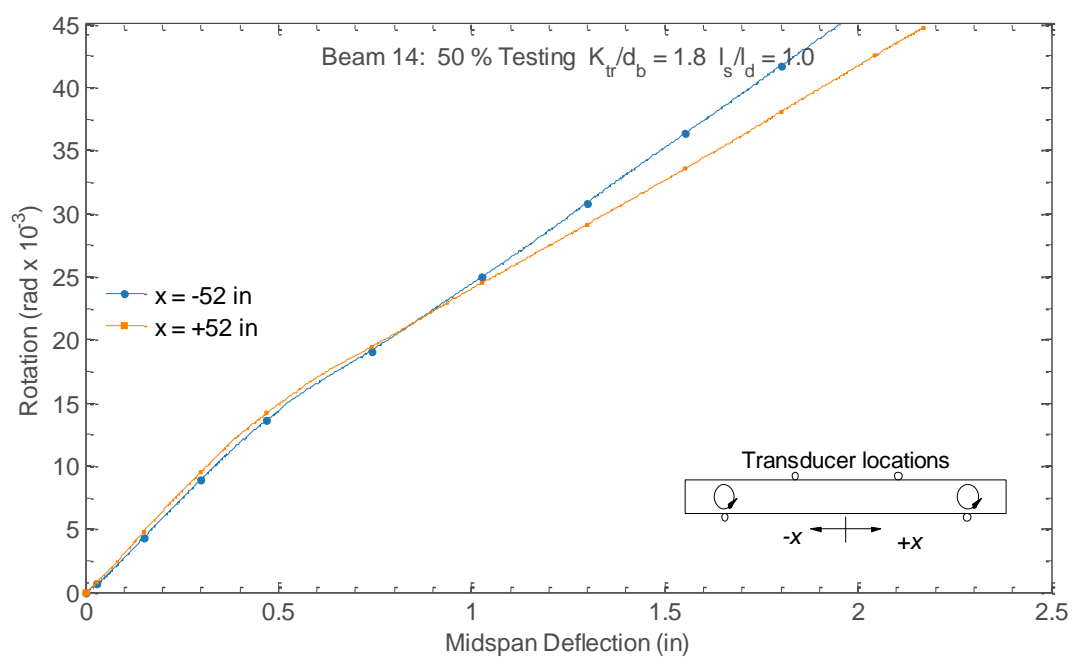
Figure C.109. Measured end rotations for Beam 14
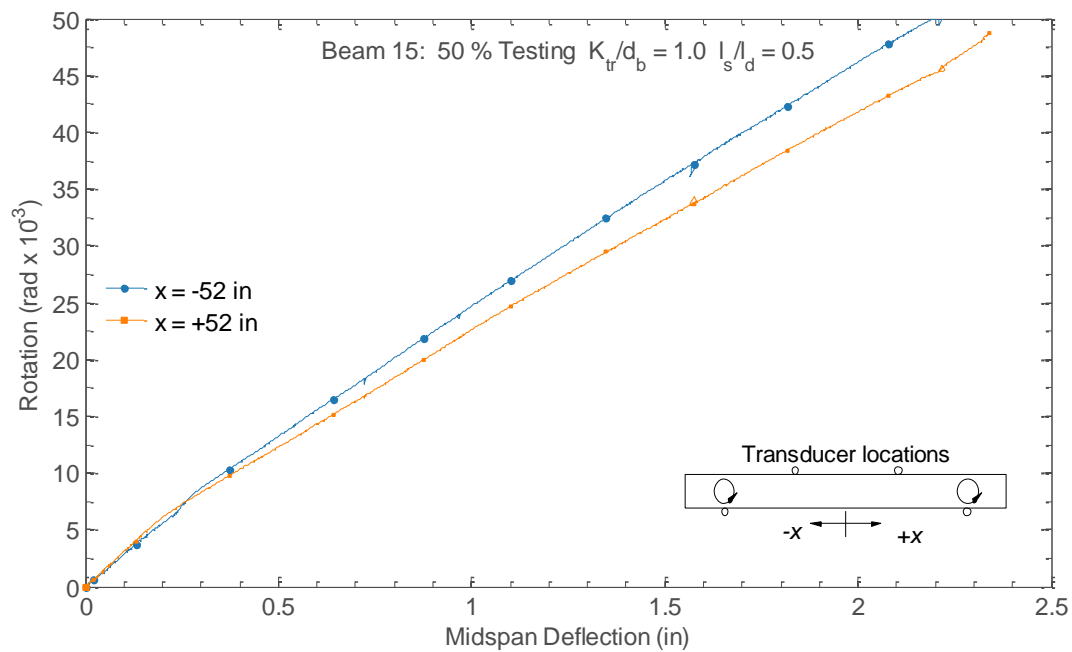
Figure C.110. Measured end rotations for Beam 15
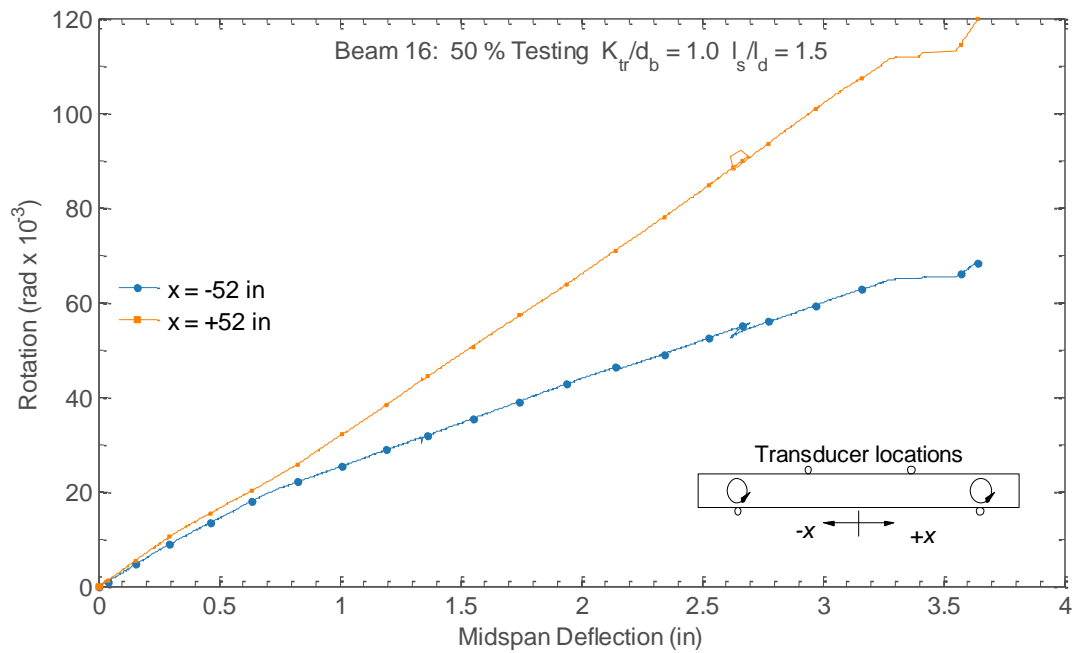
Figure C.111. Measured end rotations for Beam 16
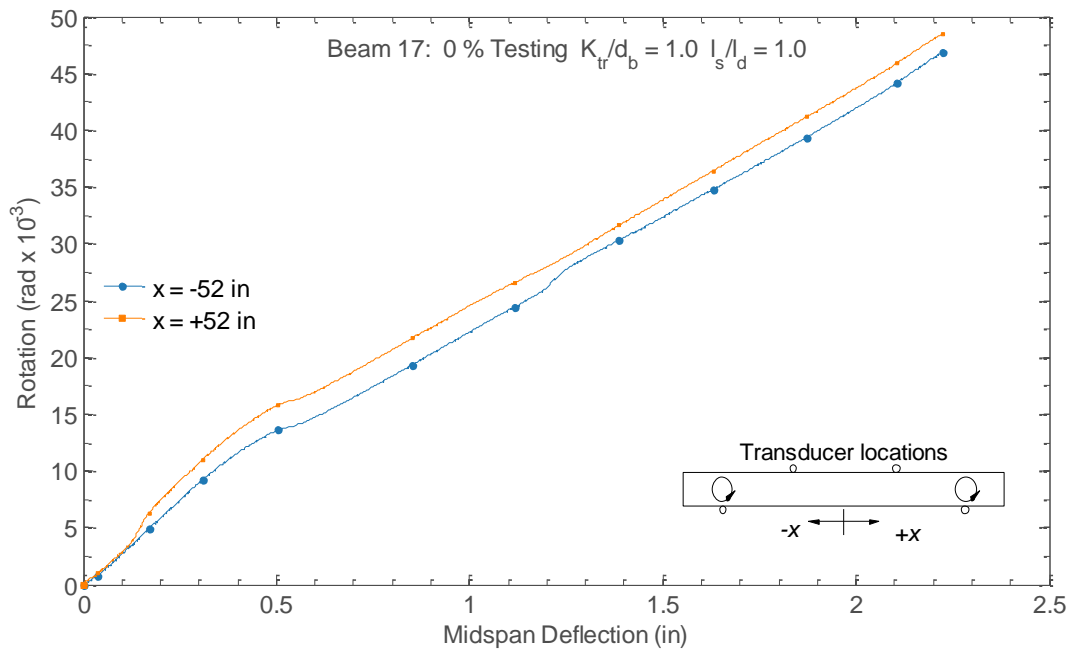
Figure C.112. Measured end rotations for Beam 17
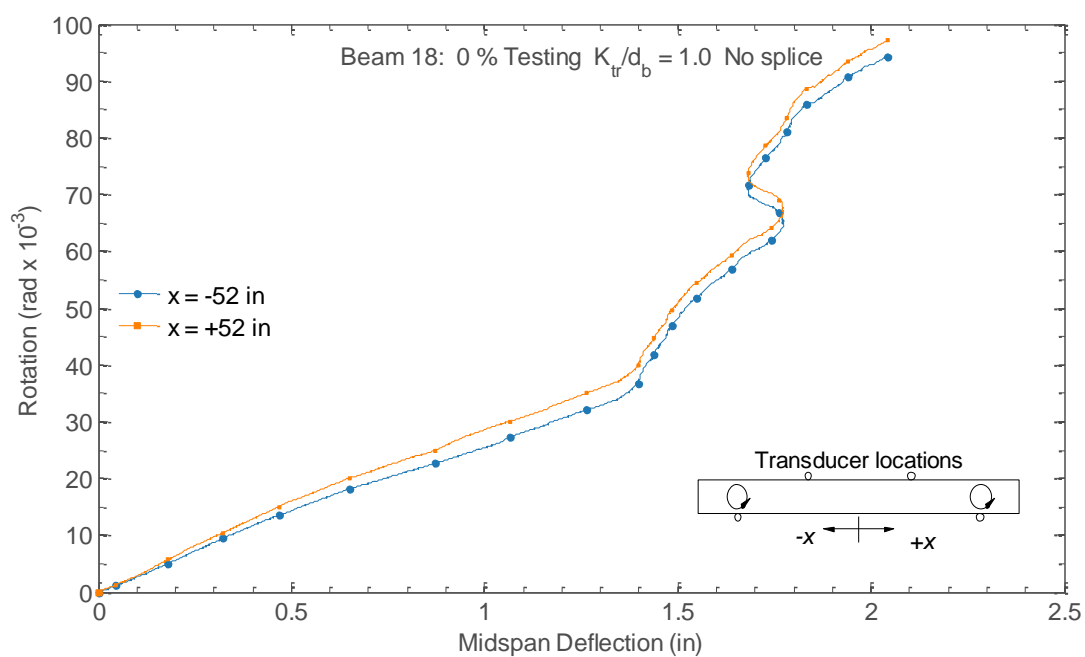
Figure C.113. Measured end rotations for Beam 18
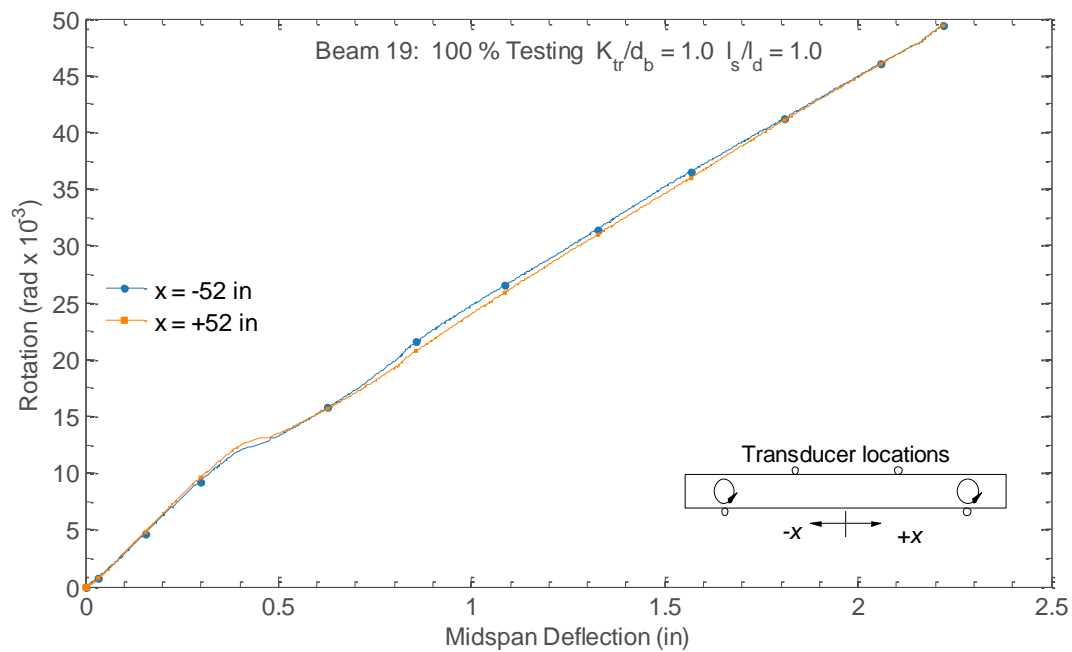
Figure C.114. Measured end rotations for Beam 19

211

Strain Increments in the Tensile Reinforcement

The figures below present the measured midspan moment as a function of the measured longitudinal strain increments in the tensile reinforcement during testing for the beam specimens. The strain increments are shown here, separating strains caused by expansion and structural loads. The strain histories for the instruments have been truncated at the location of the beam's peak moment strength or when the gages failed during testing, whichever occurred first. The measurement location within the splice region is designated in the figures by color. In the figures, the marker is positioned at the average value of the strains for each gage location, while the error band at each time corresponds to expanded uncertainty based on the individual measurements.

Also plotted in the figures is the predicted strain development based on an elastic section analysis using the nominal (28-day) material properties and both the transformed and cracked section properties. While the reduction in the elastic modulus measured during the test period (roughly 50 %) resulted in only a small change to the strain development assuming cracked properties (roughly 5 %), it resulted in a significant change to the strain development assuming transformed properties (decreases slope by 50 %) due to the change in the modular ratio.
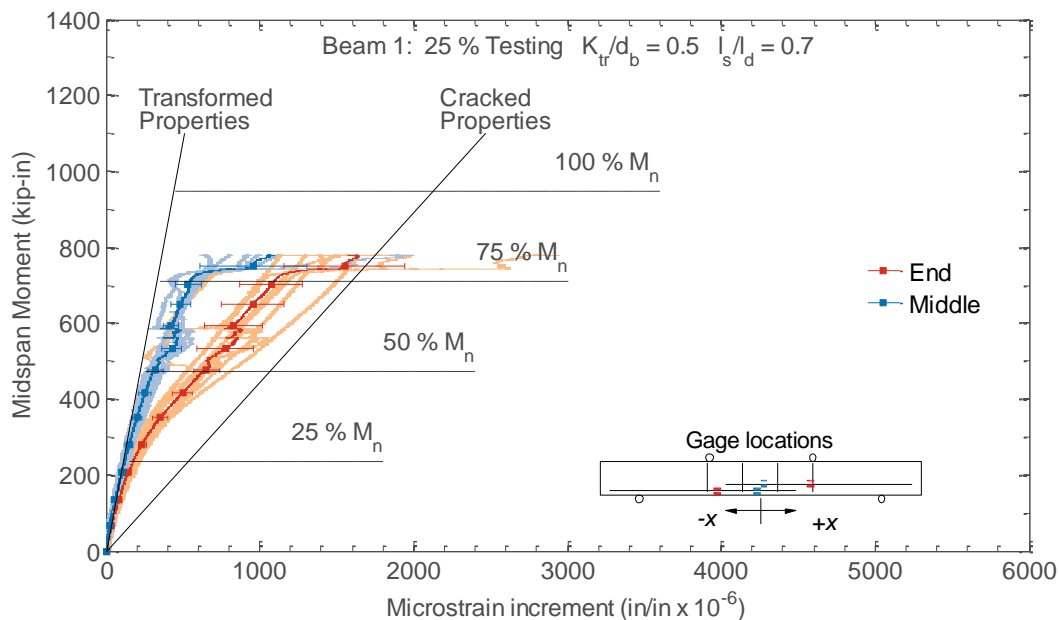
Figure C.115. Measured strain increment in the tensile reinforcement for Beam 1
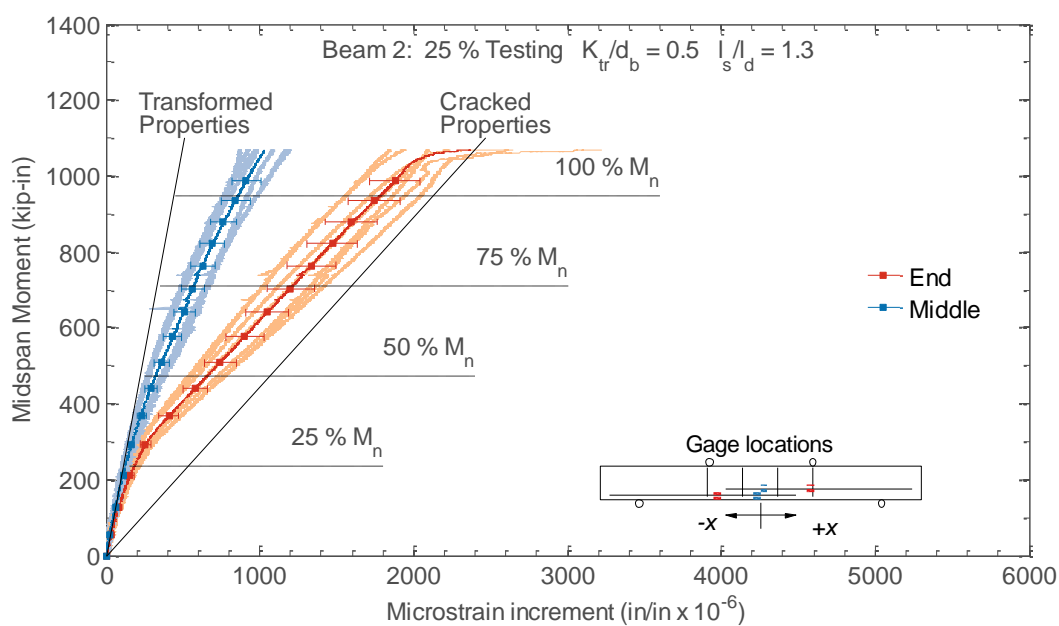
Figure C.116. Measured strain increment in the tensile reinforcement for Beam 2
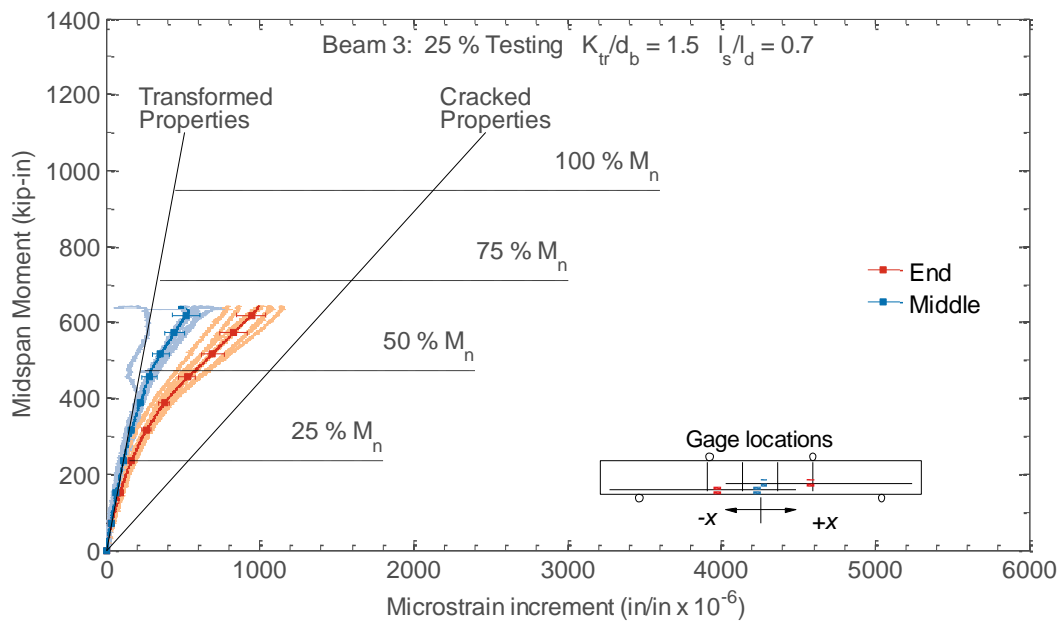
Figure C.117. Measured strain increment in the tensile reinforcement for Beam 3
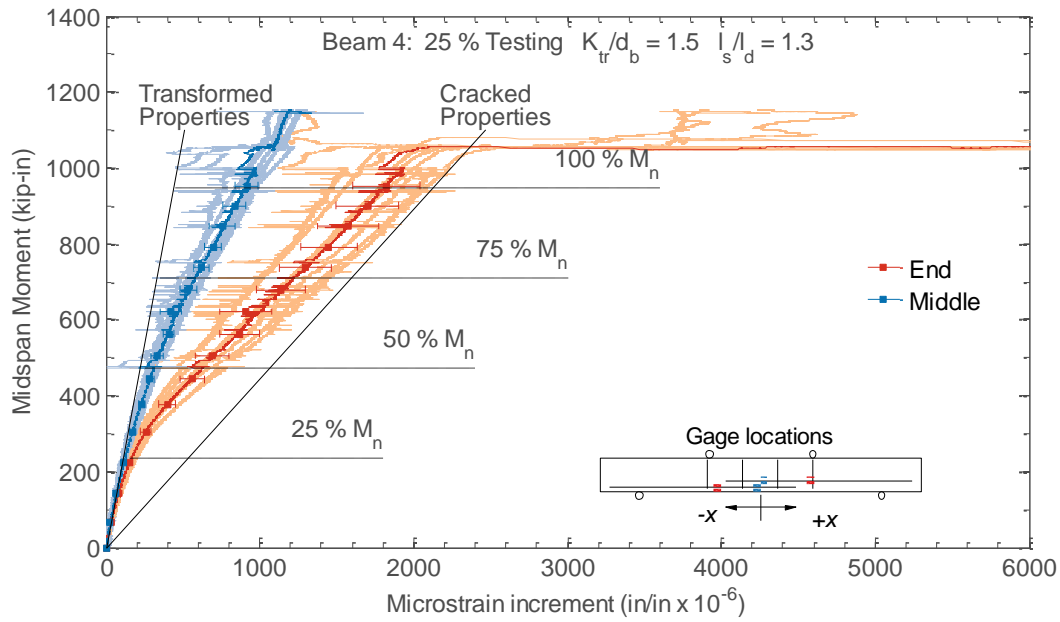
Figure C.118. Measured strain increment in the tensile reinforcement for Beam 4
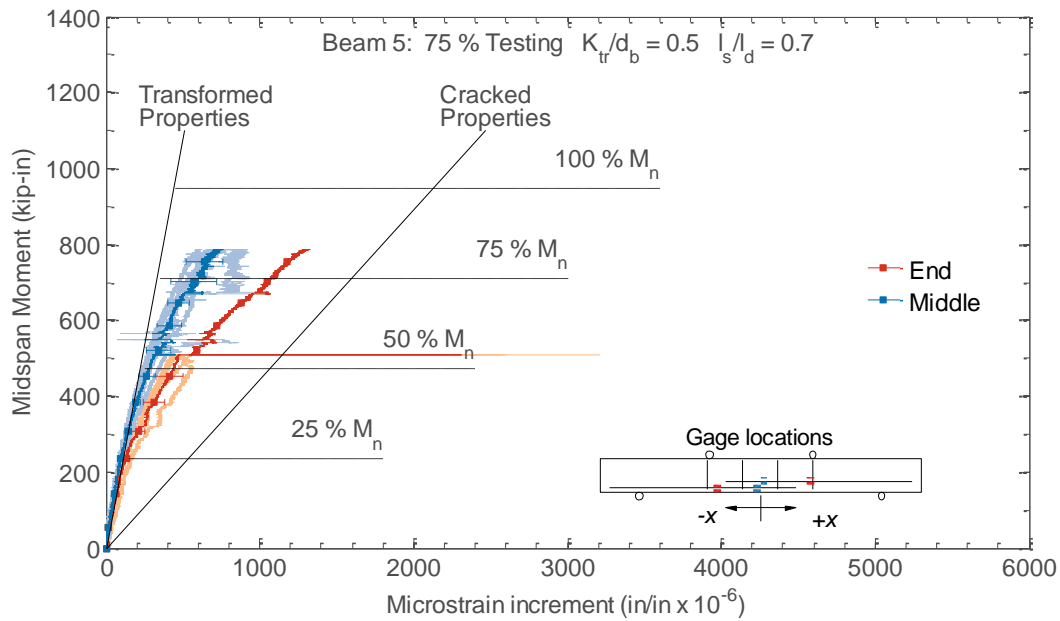
Figure C.119. Measured strain increment in the tensile reinforcement for Beam 5
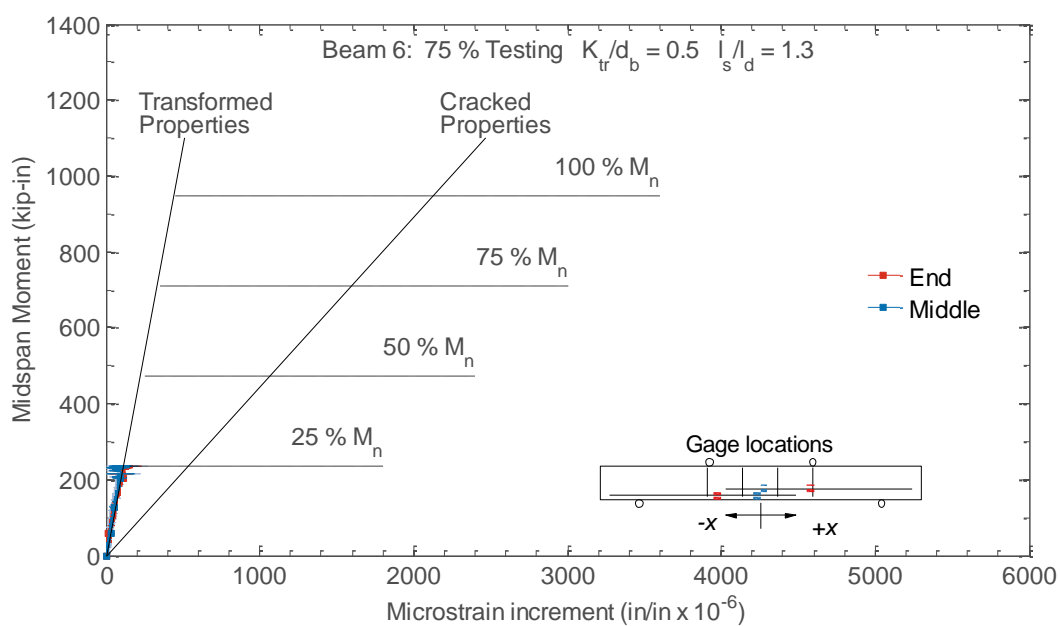
Figure C.120. Measured strain increment in the tensile reinforcement for Beam 6
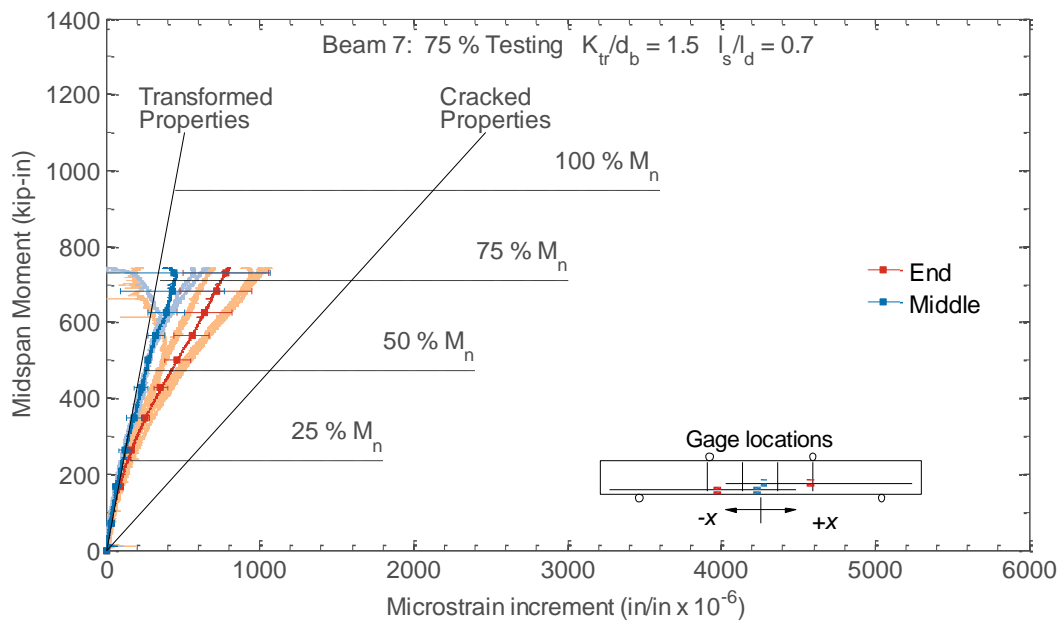
Figure C.121. Measured strain increment in the tensile reinforcement for Beam 7

215
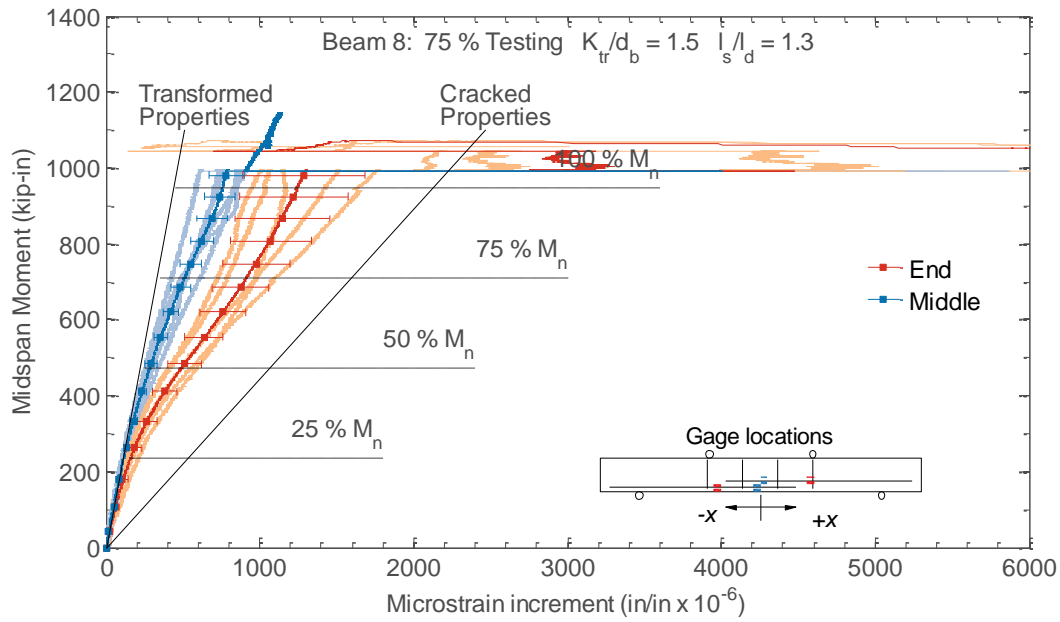
Figure C.122. Measured strain increment in the tensile reinforcement for Beam 8
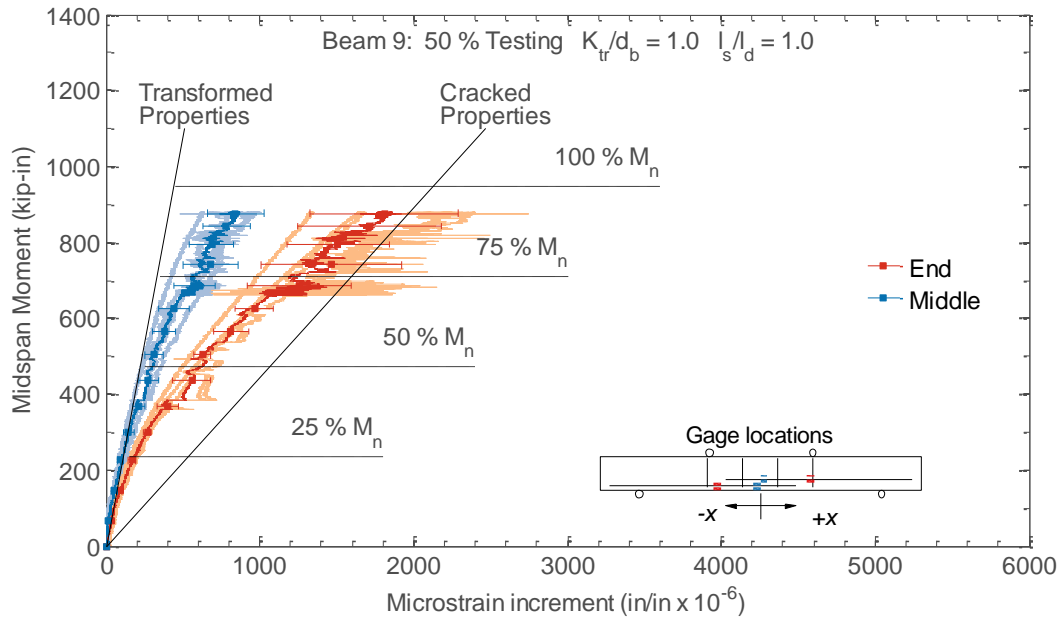
Figure C.123. Measured strain increment in the tensile reinforcement for Beam 9
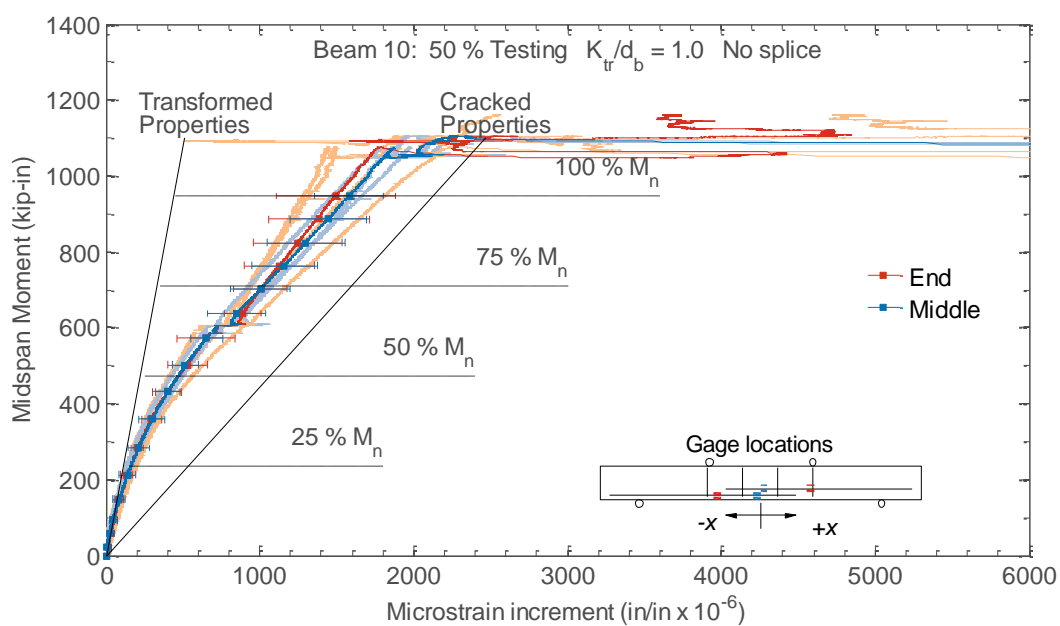
Figure C.124. Measured strain increment in the tensile reinforcement for Beam 10
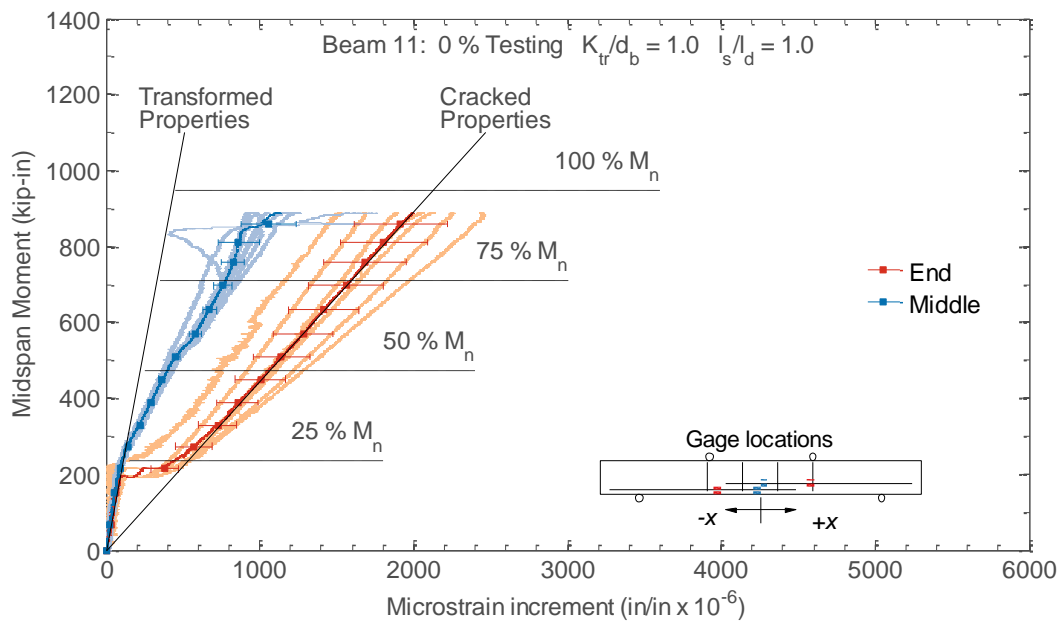
Figure C.125. Measured strain increment in the tensile reinforcement for Beam 11
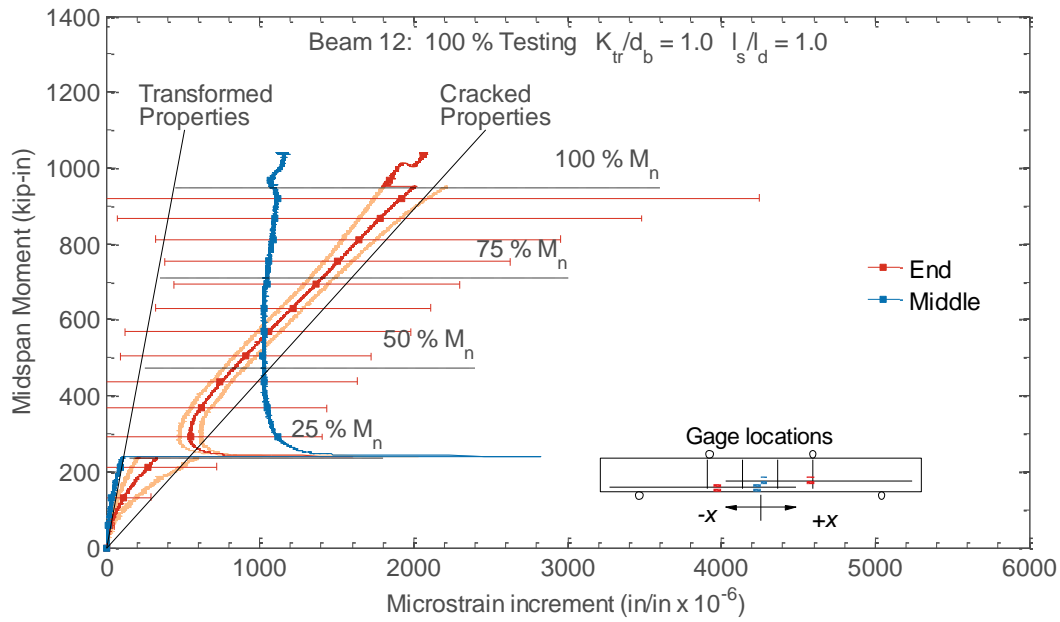
Figure C.126. Measured strain increment in the tensile reinforcement for Beam 12
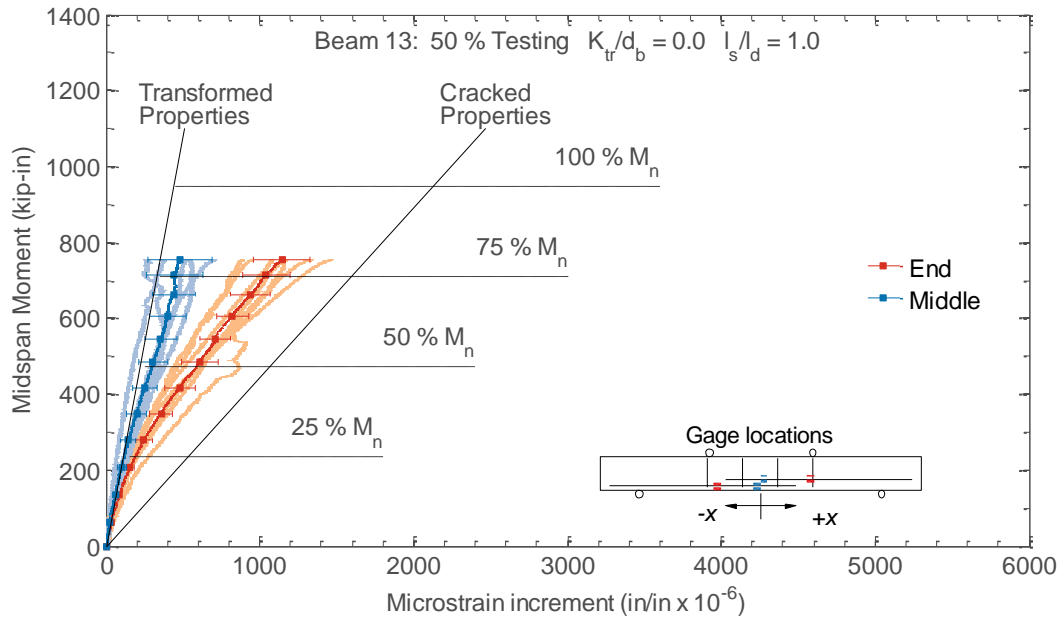
Figure C.127. Measured strain increment in the tensile reinforcement for Beam 13
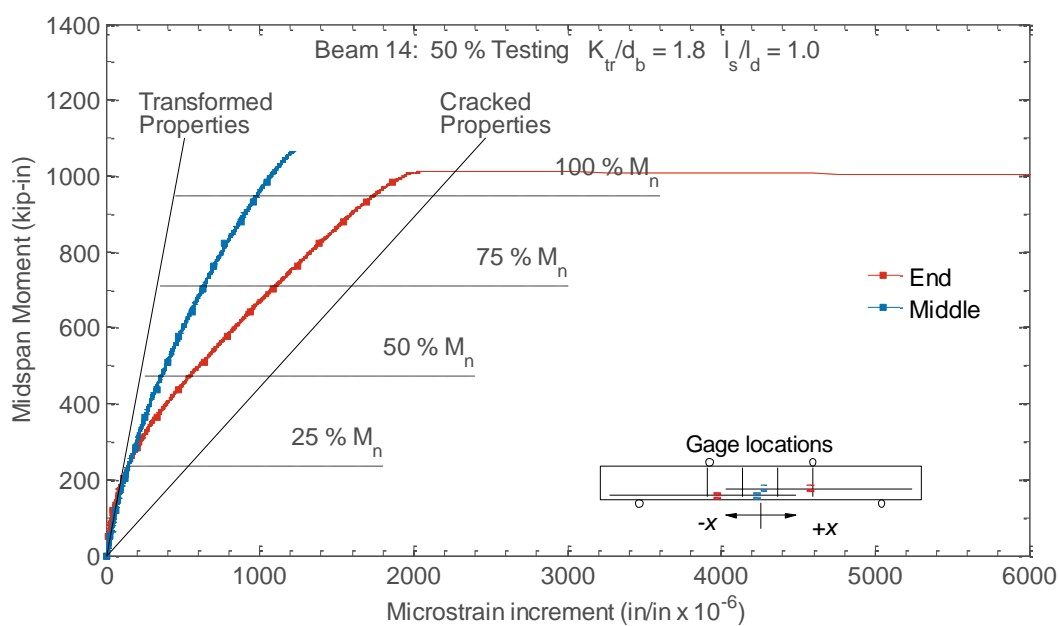
Figure C.128. Measured strain increment in the tensile reinforcement for Beam 14
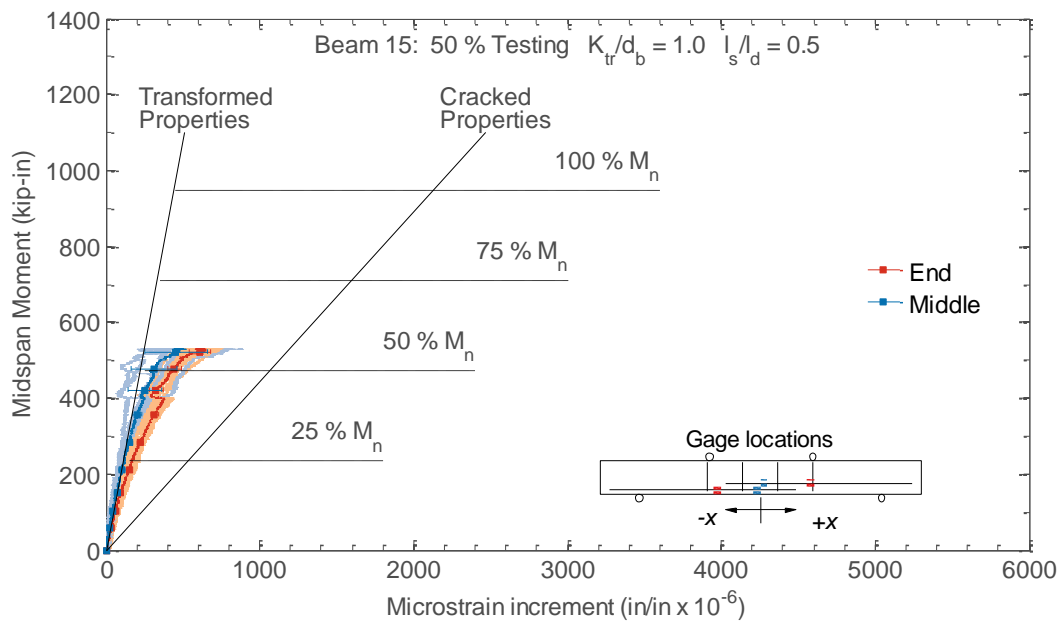
Figure C.129. Measured strain increment in the tensile reinforcement for Beam 15
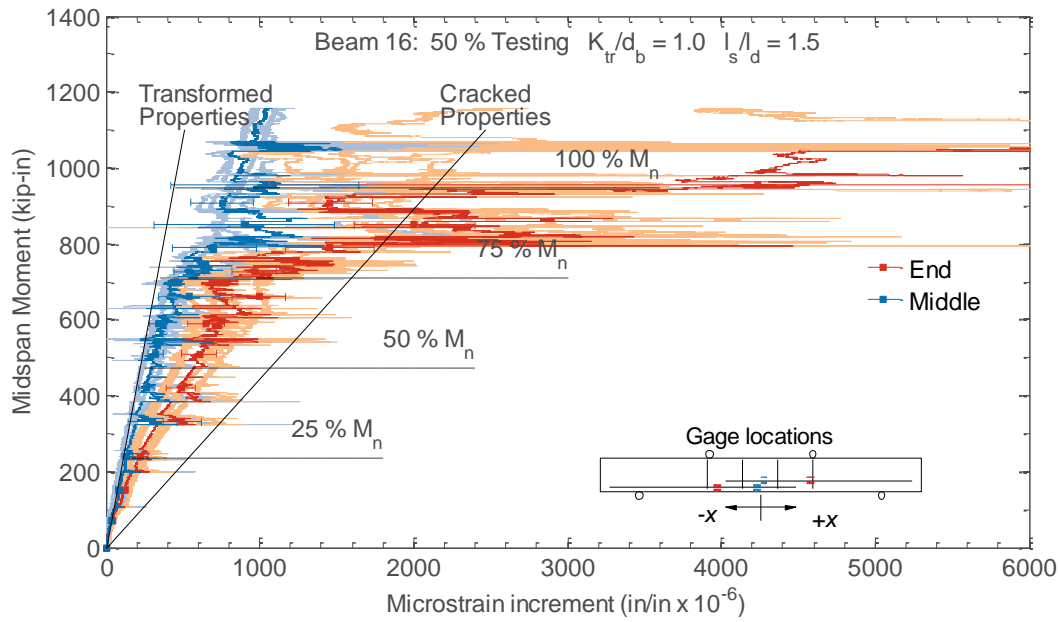
Figure C.130. Measured strain increment in the tensile reinforcement for Beam 16
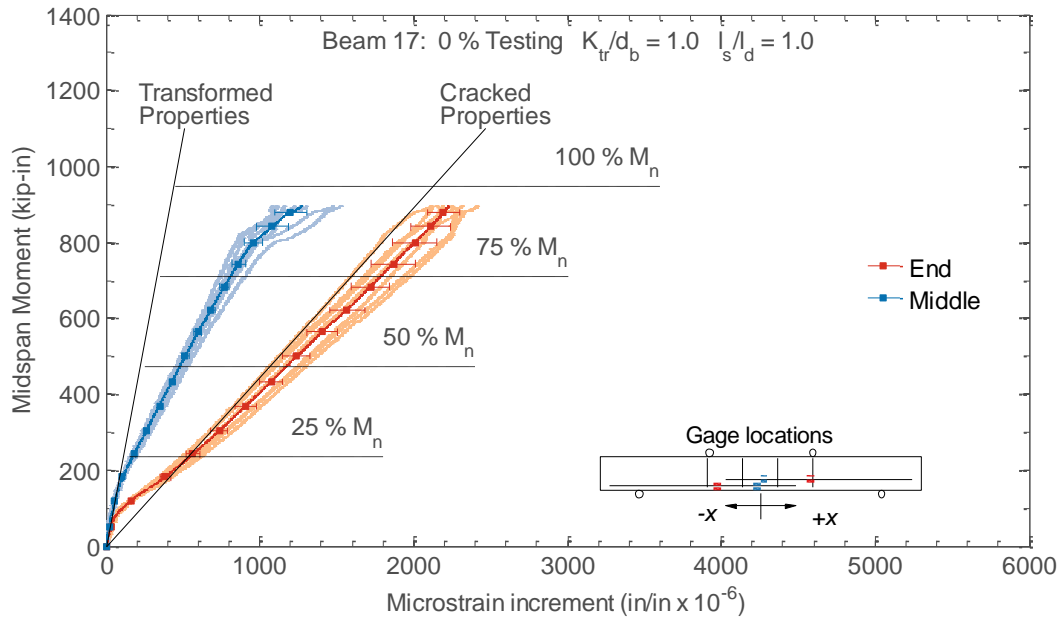
Figure C.131. Measured strain increment in the tensile reinforcement for Beam 17
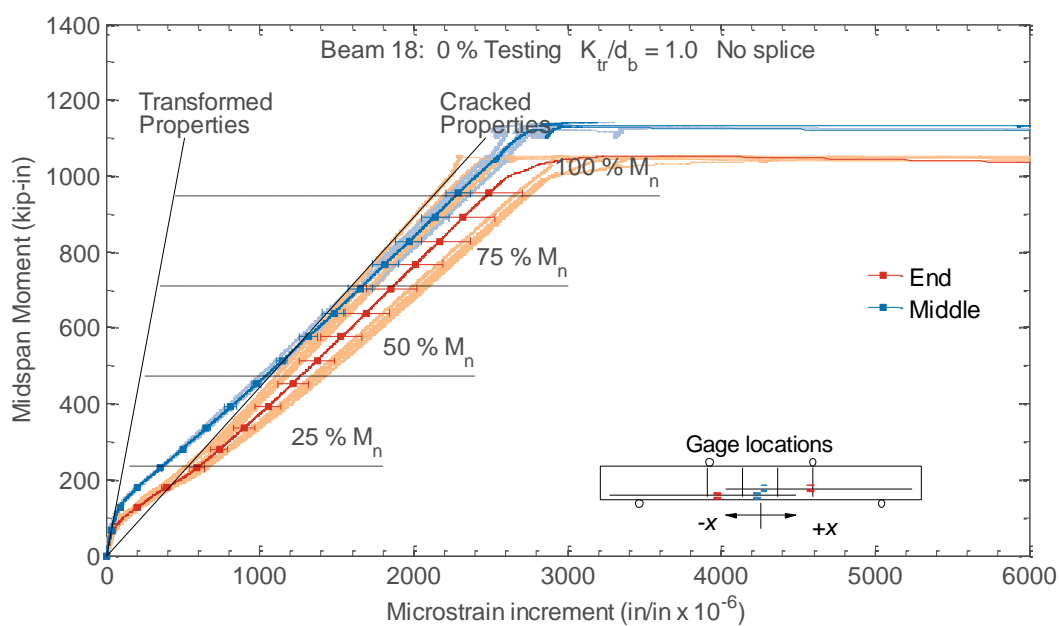
Figure C.132. Measured strain increment in the tensile reinforcement for Beam 18
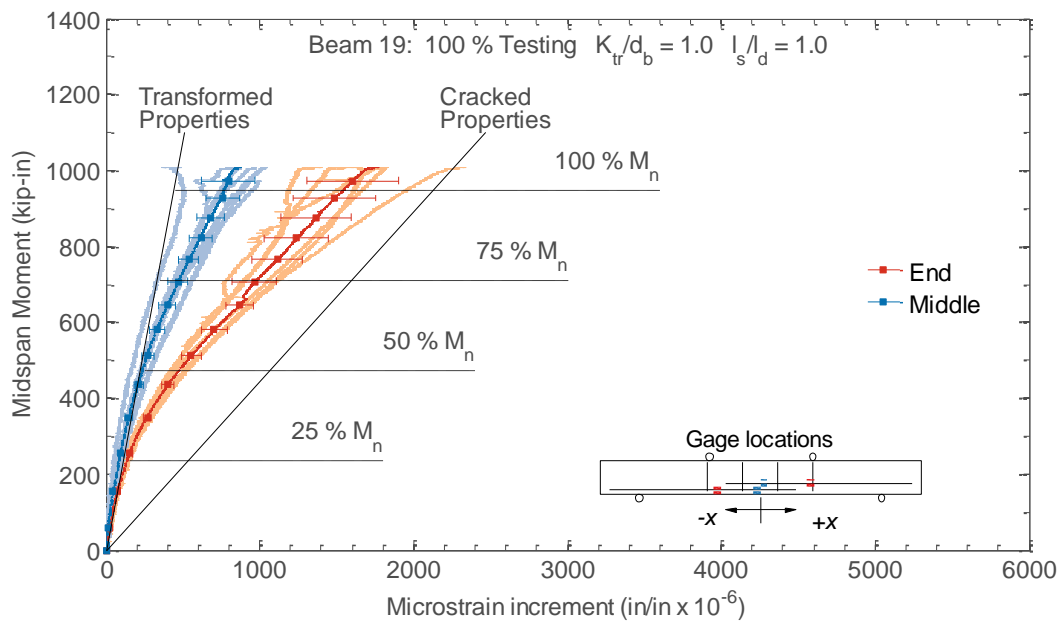
Figure C.133. Measured strain increment in the tensile reinforcement for Beam 19

Strain Increments in the Stirrups

The figures below present the measured midspan moment as a function of the measured strain increments in the stirrups during testing of the beam specimens. The strain increments are shown here, to separate strains caused by expansion and structural loads. The strain histories for the instruments have been truncated at the location of the beam's peak moment strength or when the gages failed during testing, whichever occurred first. The measurement location on the stirrups is designated in the figure by color.
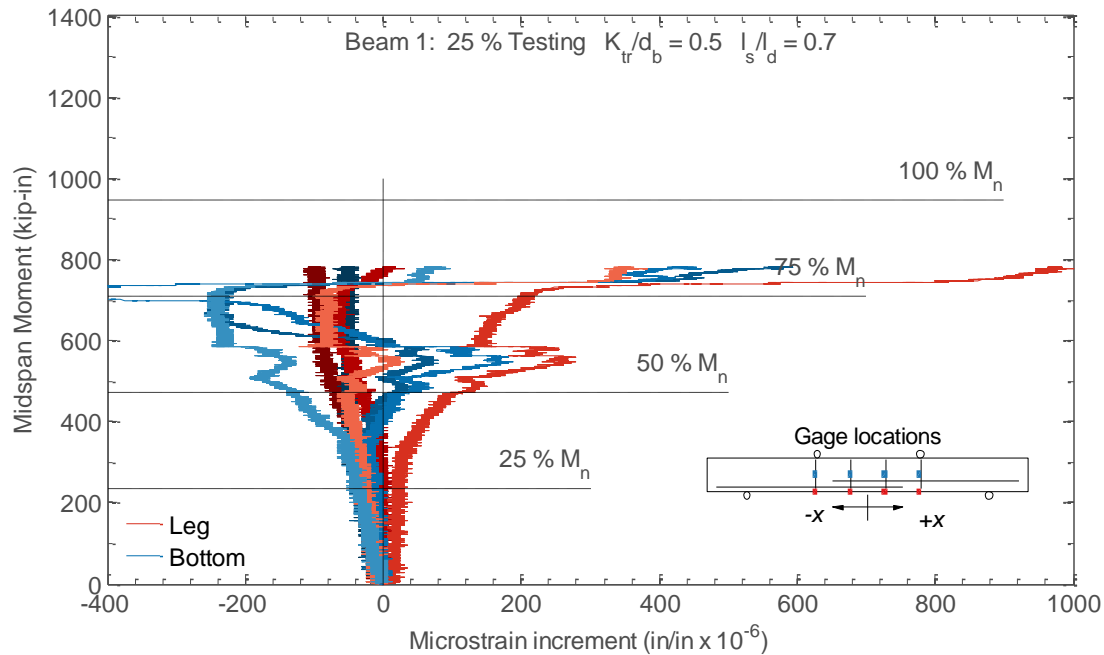
Figure C.134. Measured strain increment in the stirrups for Beam 1
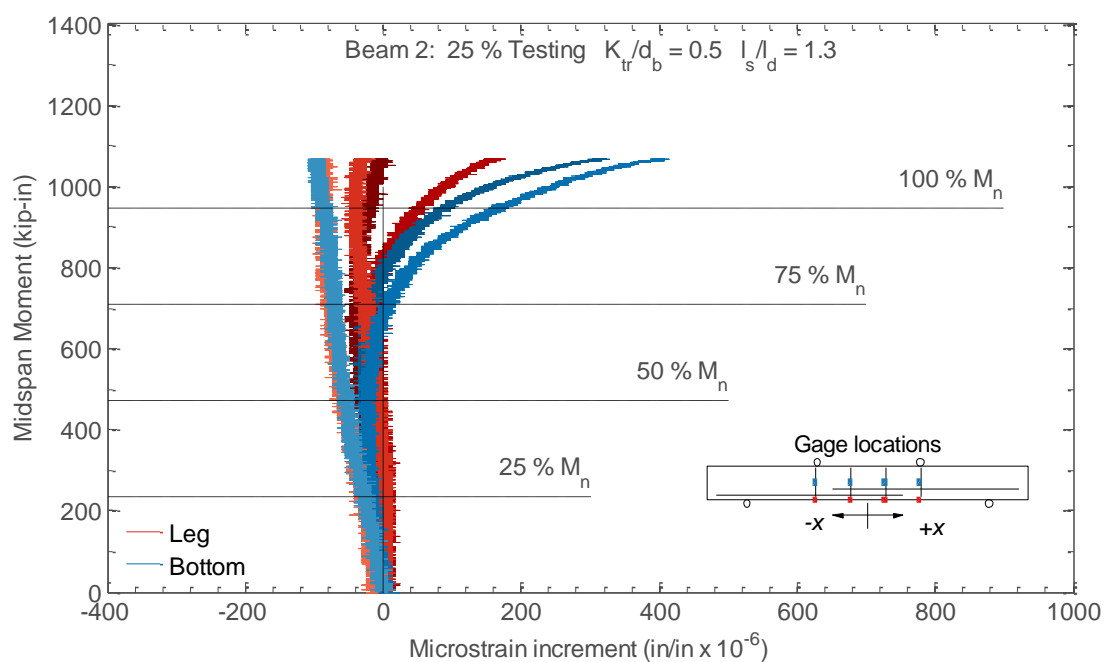
Figure C.135. Measured strain increment in the stirrups for Beam 2
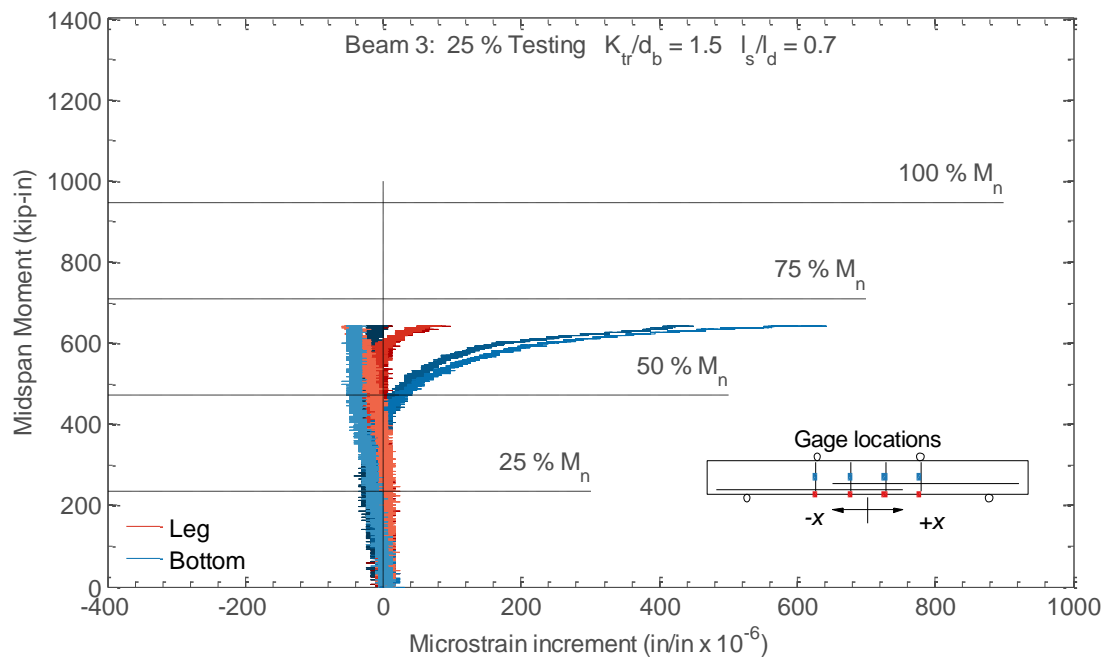
Figure C.136. Measured strain increment in the stirrups for Beam 3

223
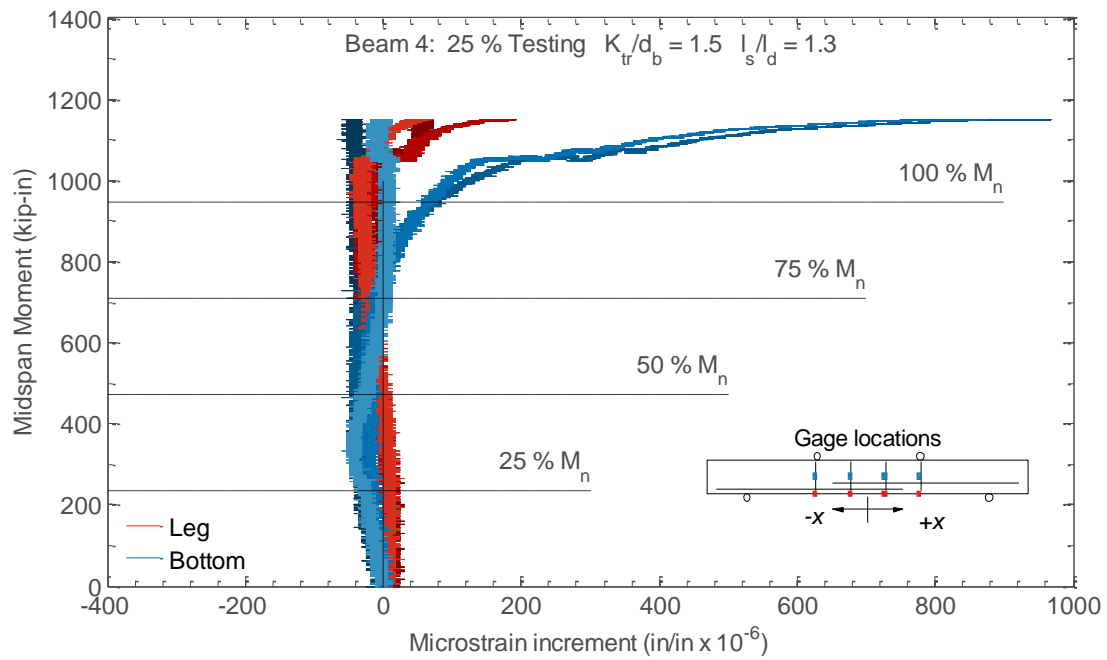
Figure C.137. Measured strain increment in the stirrups for Beam 4
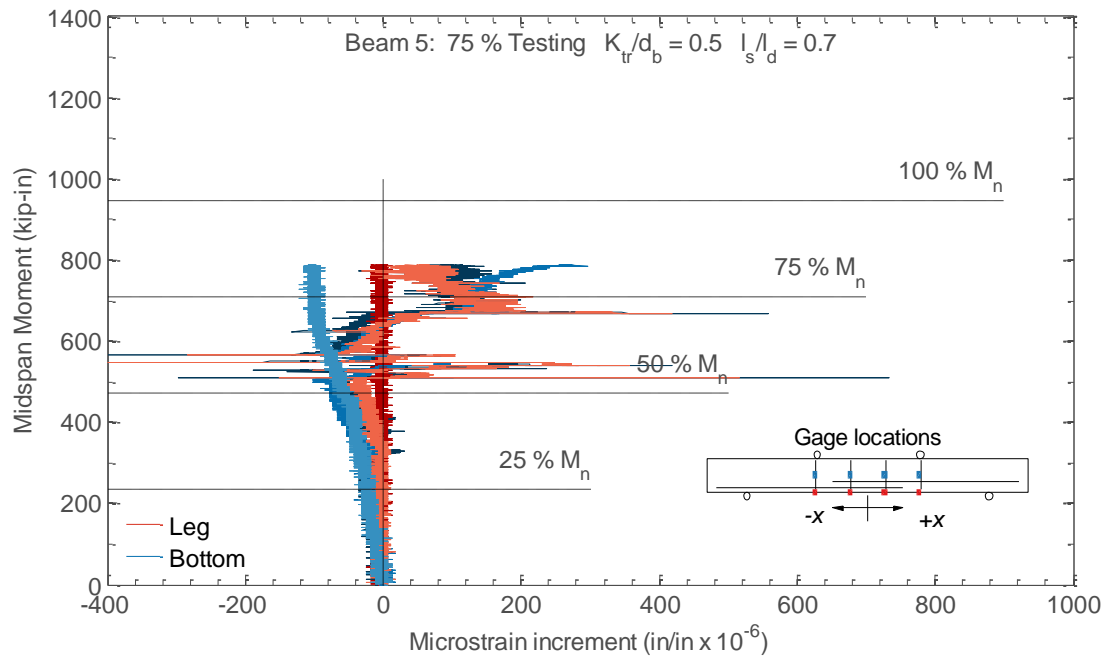
Figure C.138. Measured strain increment in the stirrups for Beam 5

224
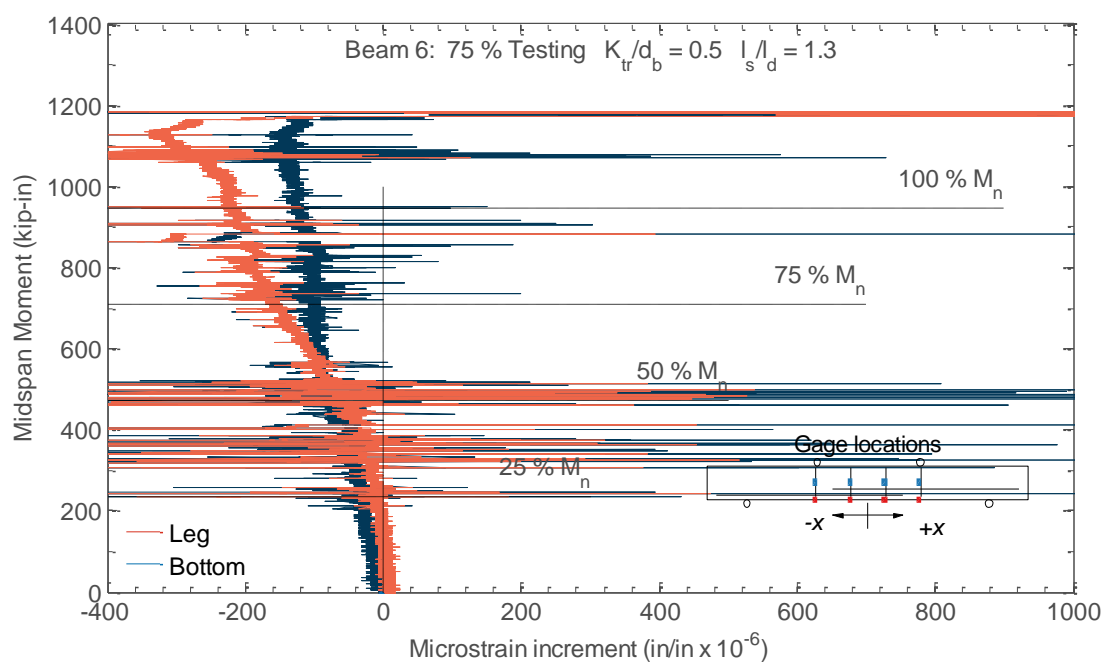
Figure C.139. Measured strain increment in the stirrups for Beam 6
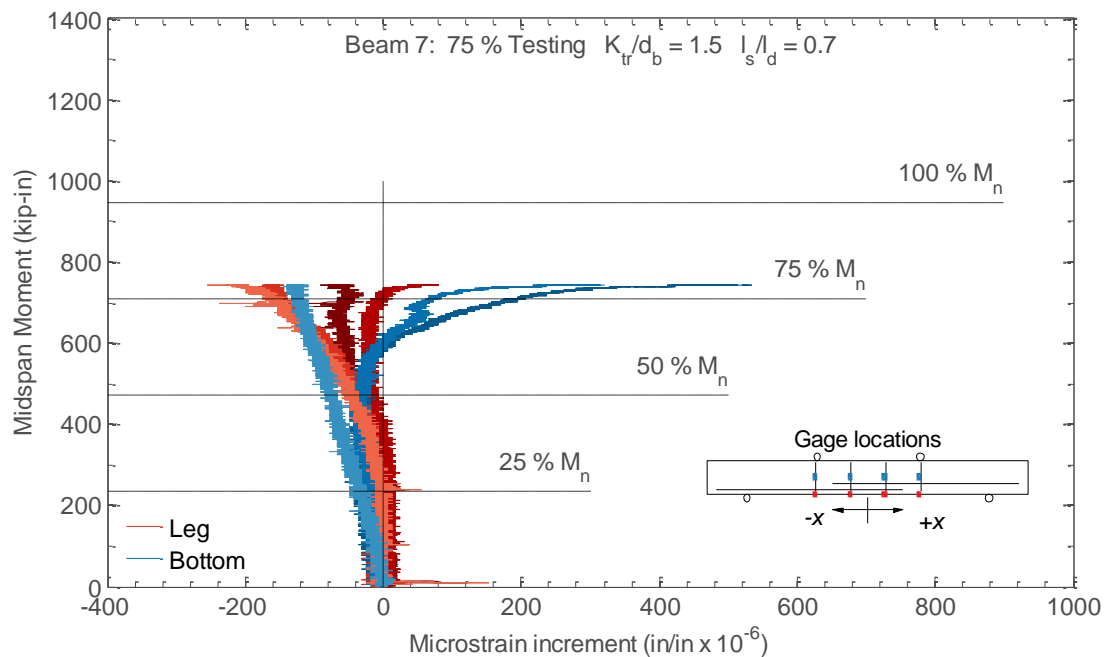
Figure C.140. Measured strain increment in the stirrups for Beam 7

225
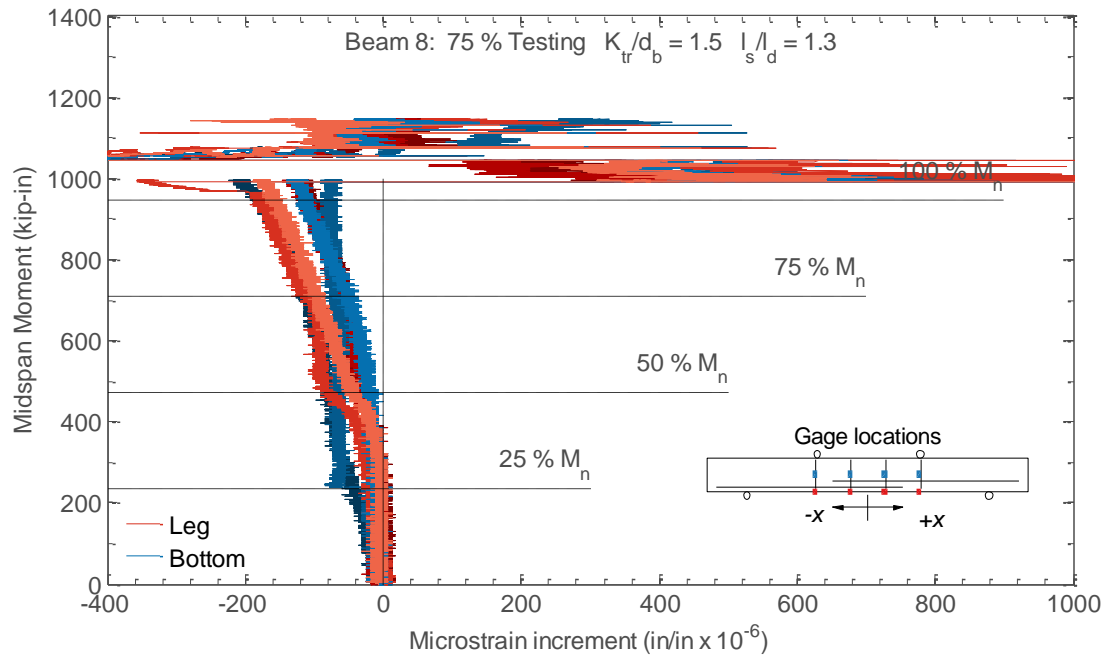
Figure C.141. Measured strain increment in the stirrups for Beam 8
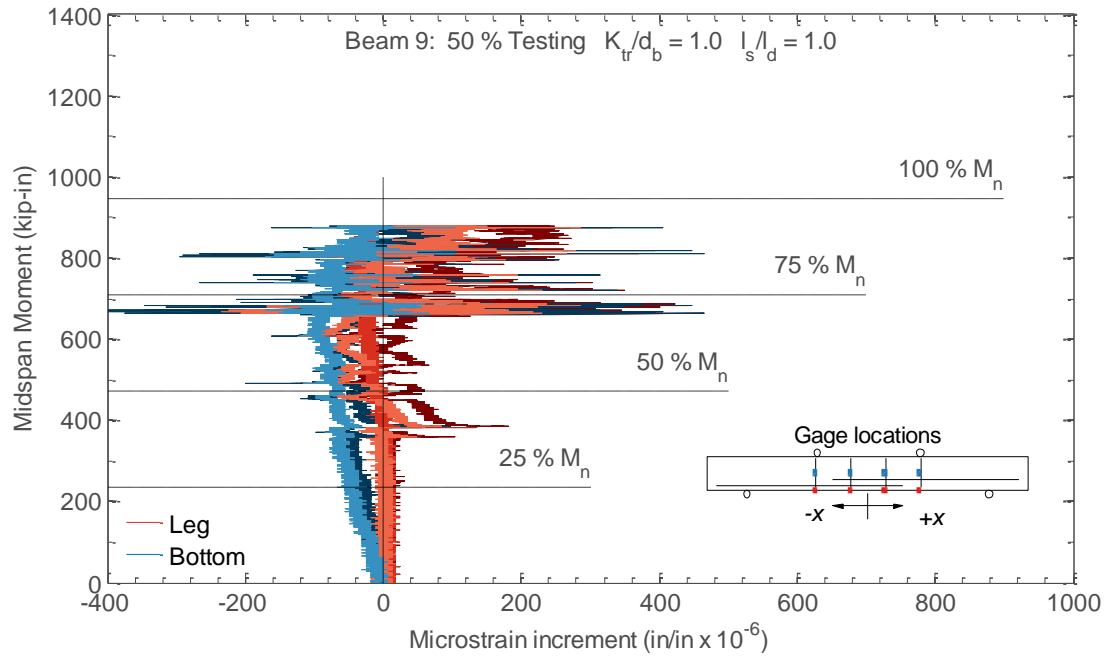
Figure C.142. Measured strain increment in the stirrups for Beam 9
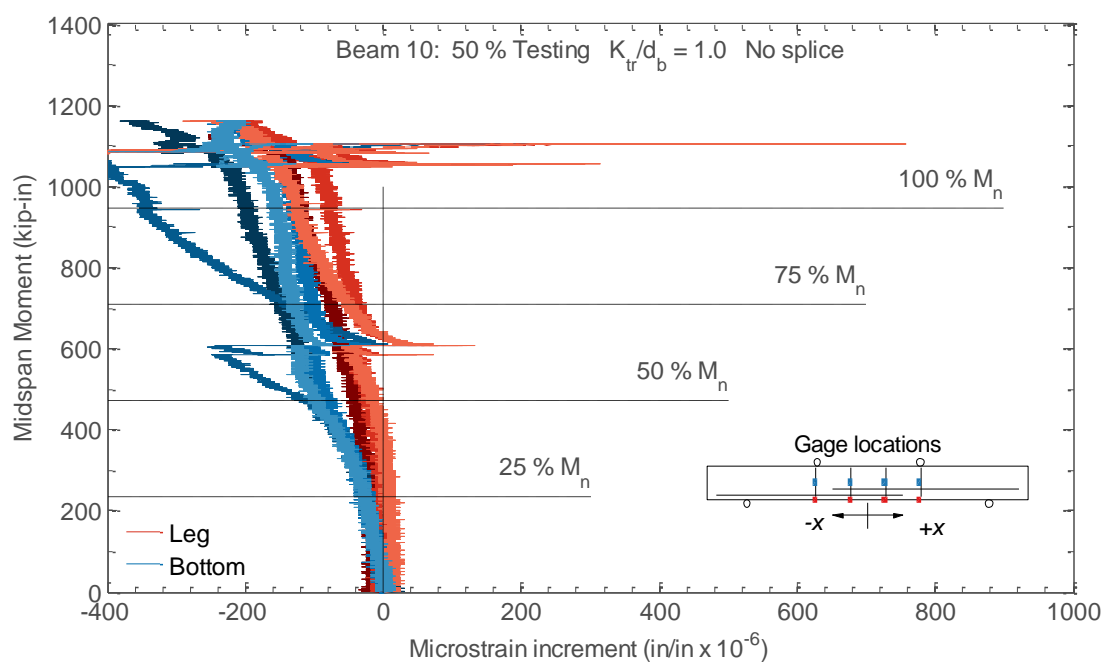
Figure C.143. Measured strain increment in the stirrups for Beam 10
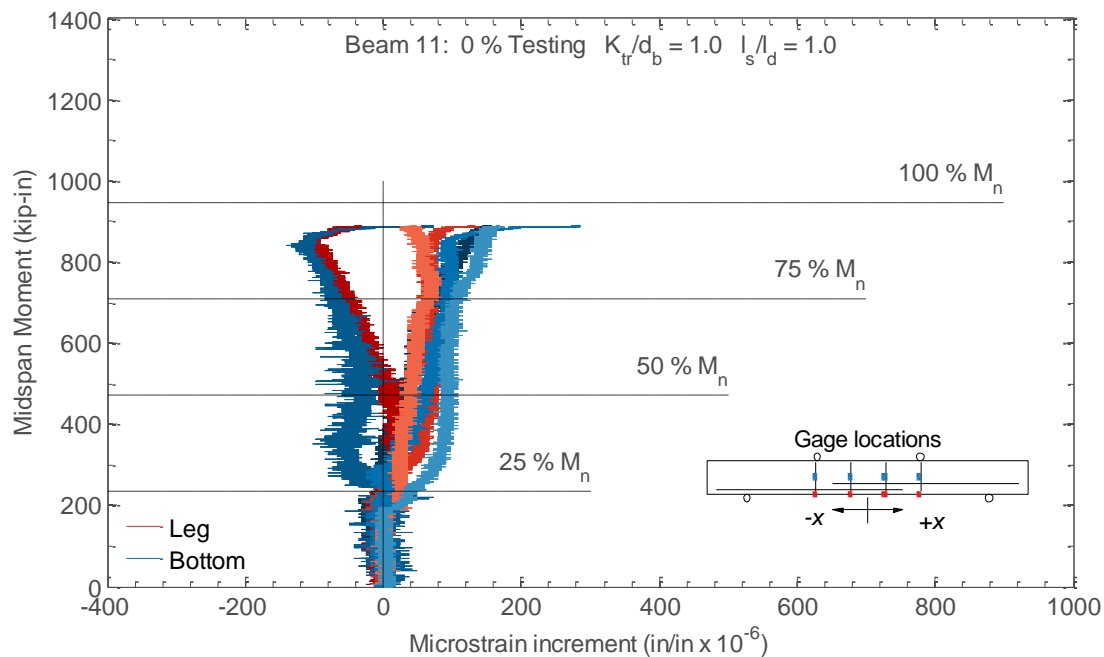
Figure C.144. Measured strain increment in the stirrups for Beam 11
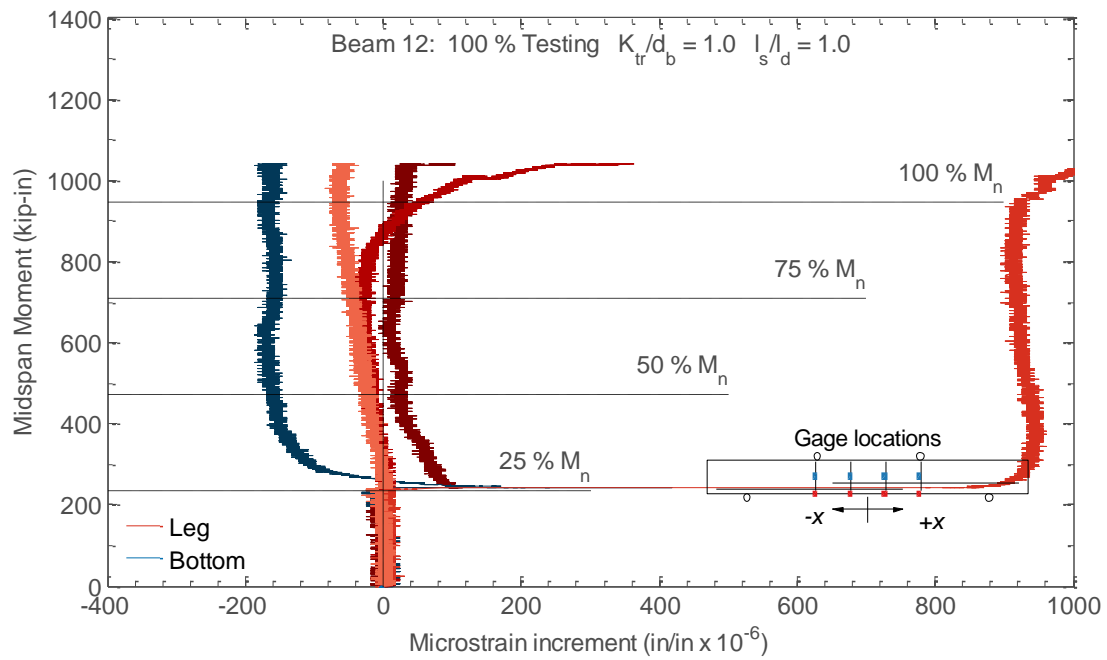
Figure C.145. Measured strain increment in the stirrups for Beam 12
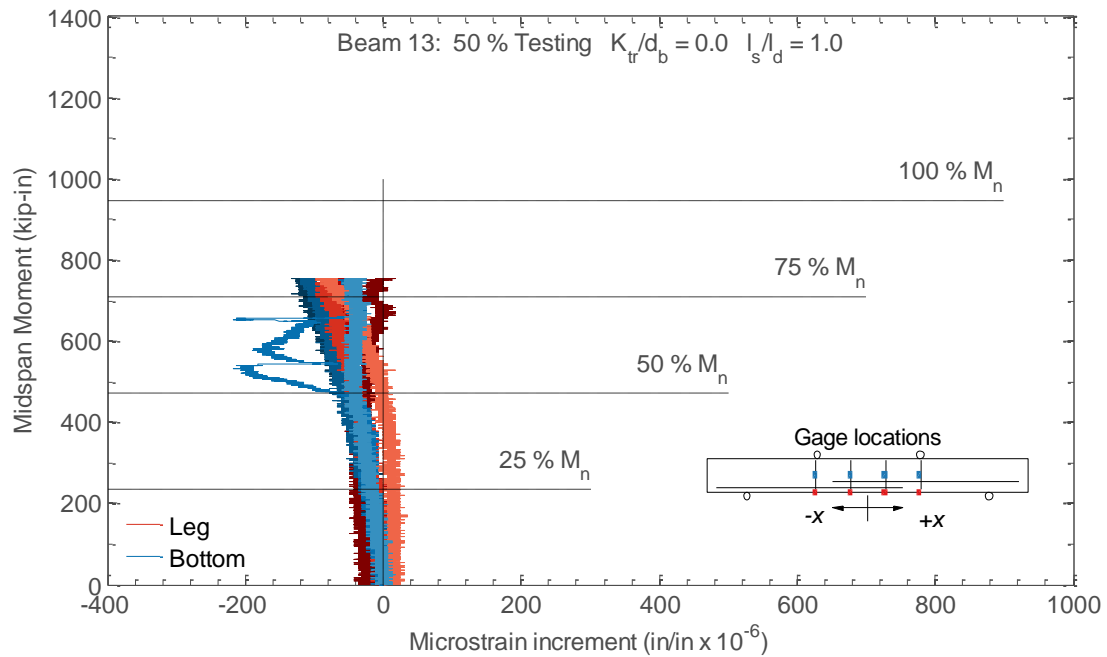
Figure C.146. Measured strain increment in the stirrups for Beam 13
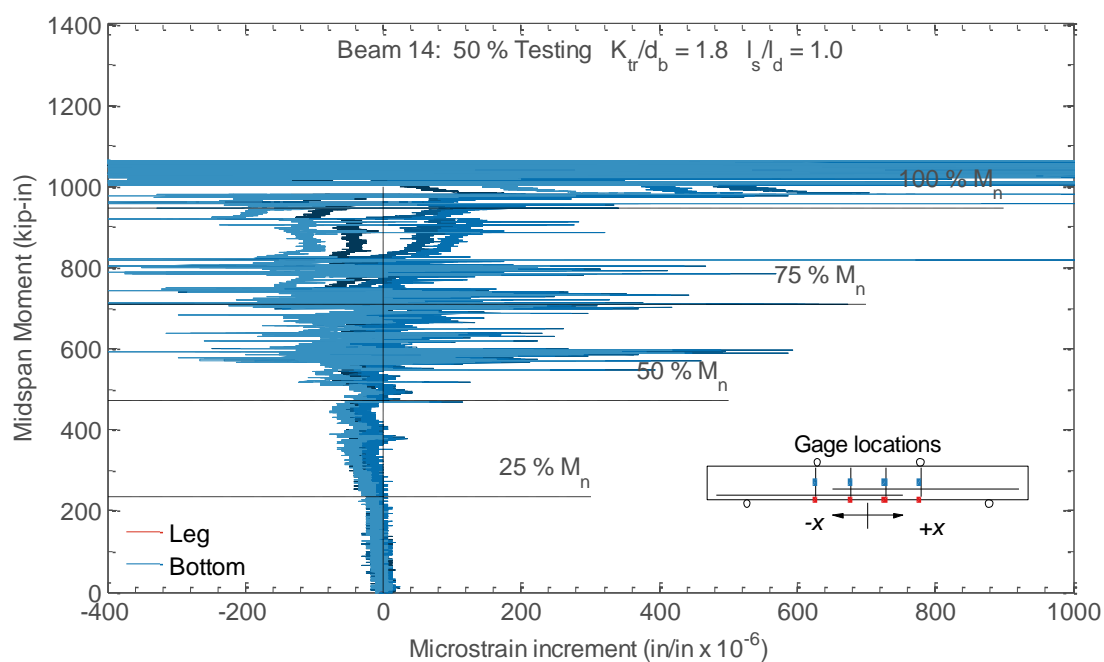
Figure C.147. Measured strain increment in the stirrups for Beam 14
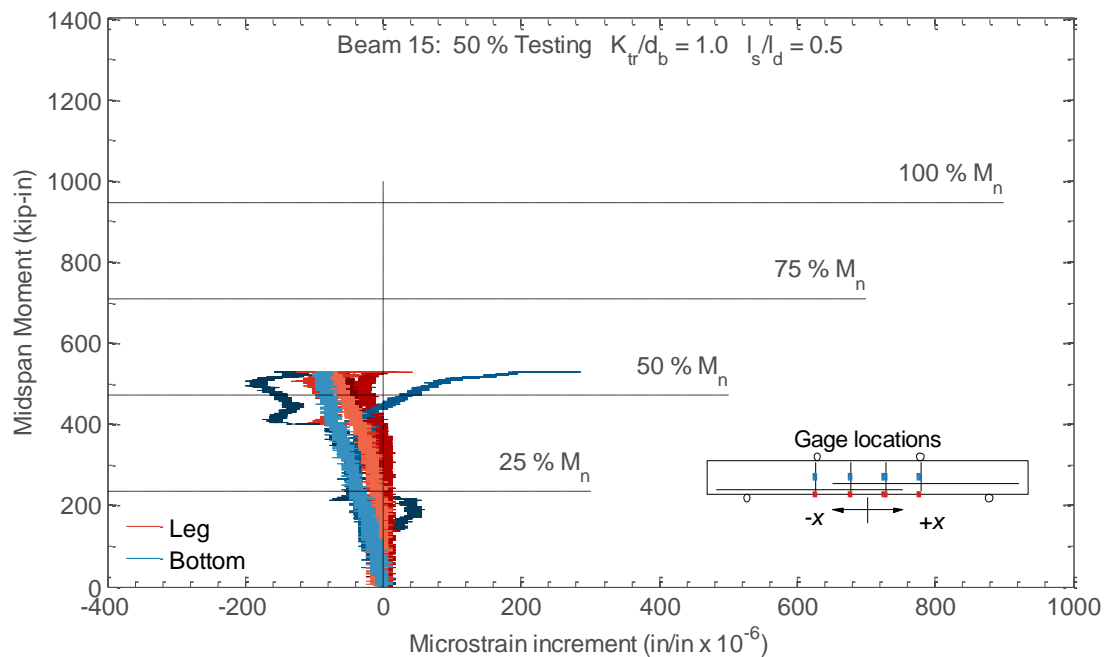
Figure C.148. Measured strain increment in the stirrups for Beam 15

229
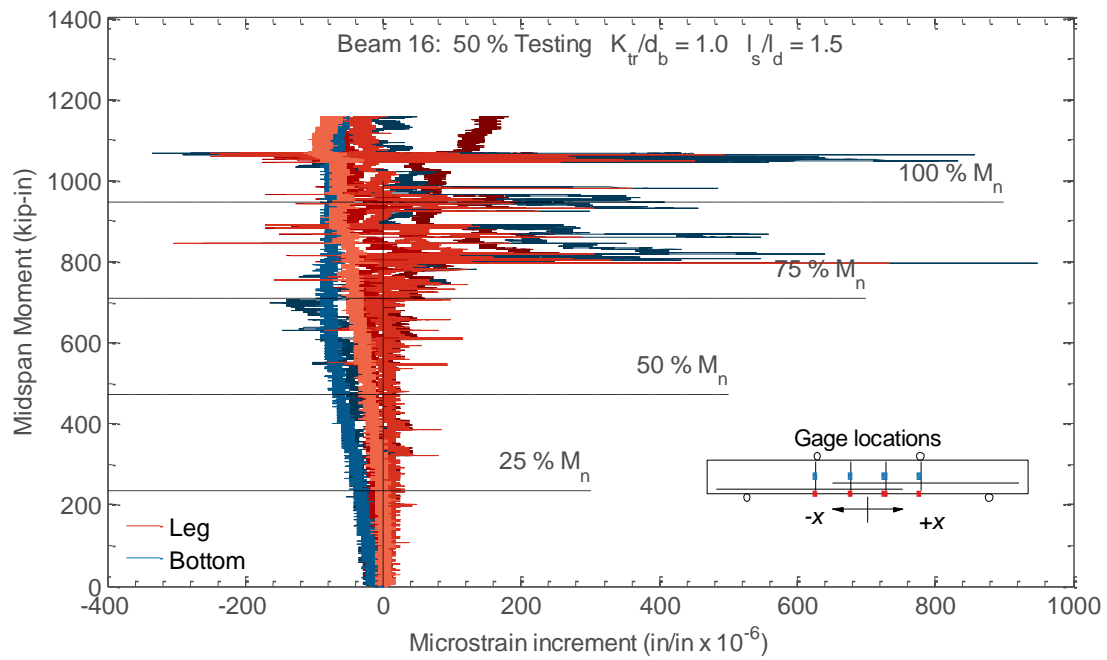
Figure C.149. Measured strain increment in the stirrups for Beam 16
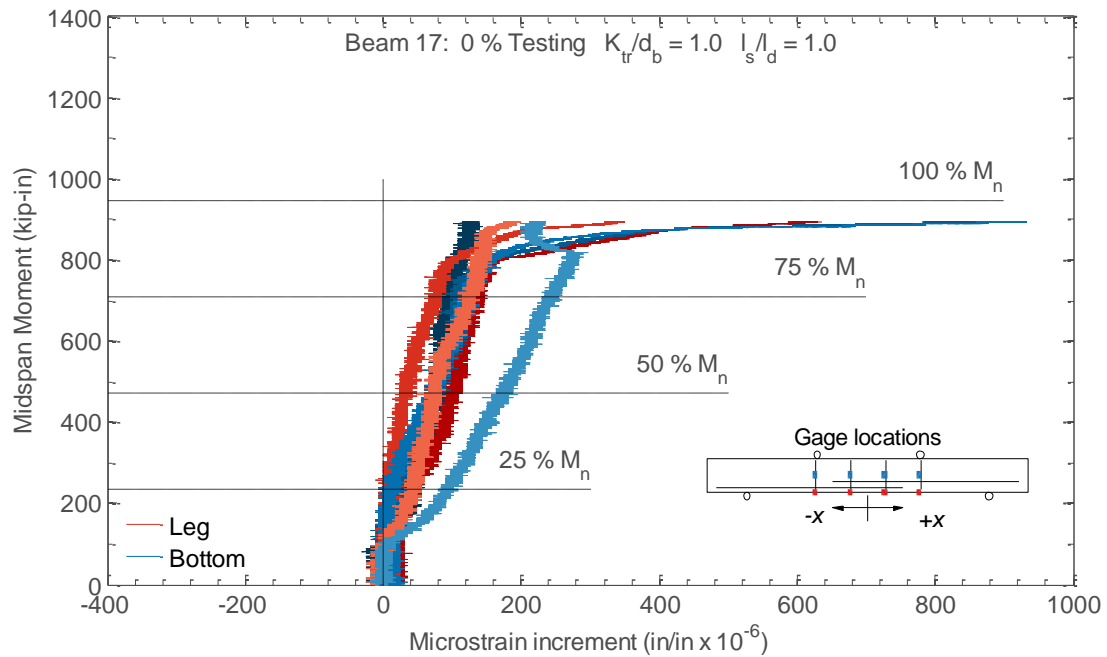
Figure C.150. Measured strain increment in the stirrups for Beam 17
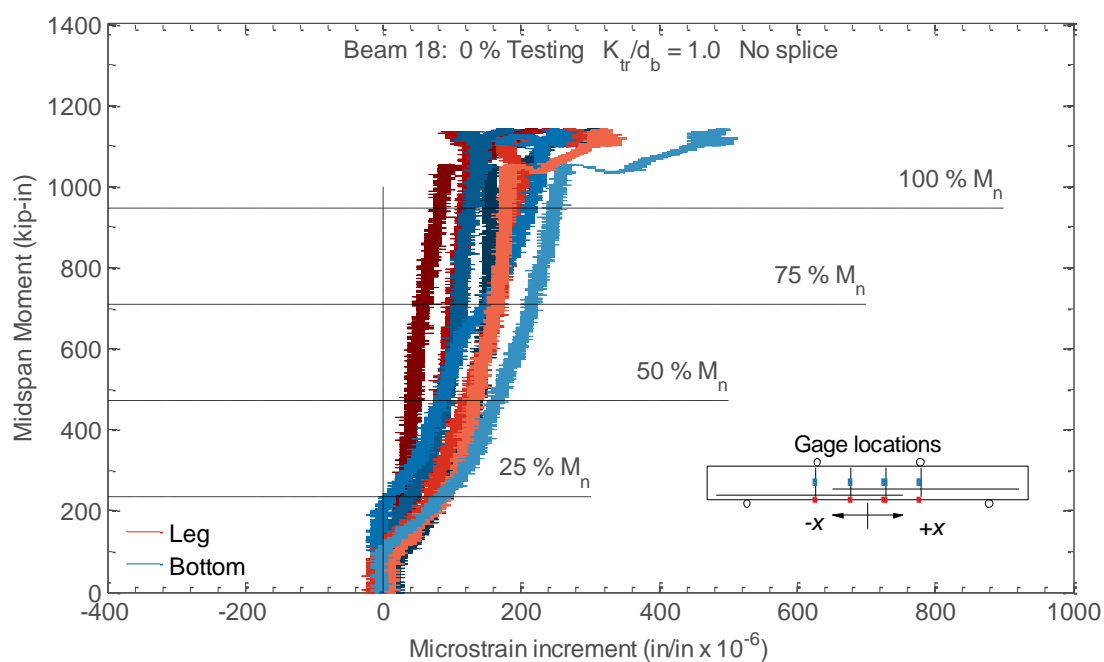
Figure C.151. Measured strain increment in the stirrups for Beam 18
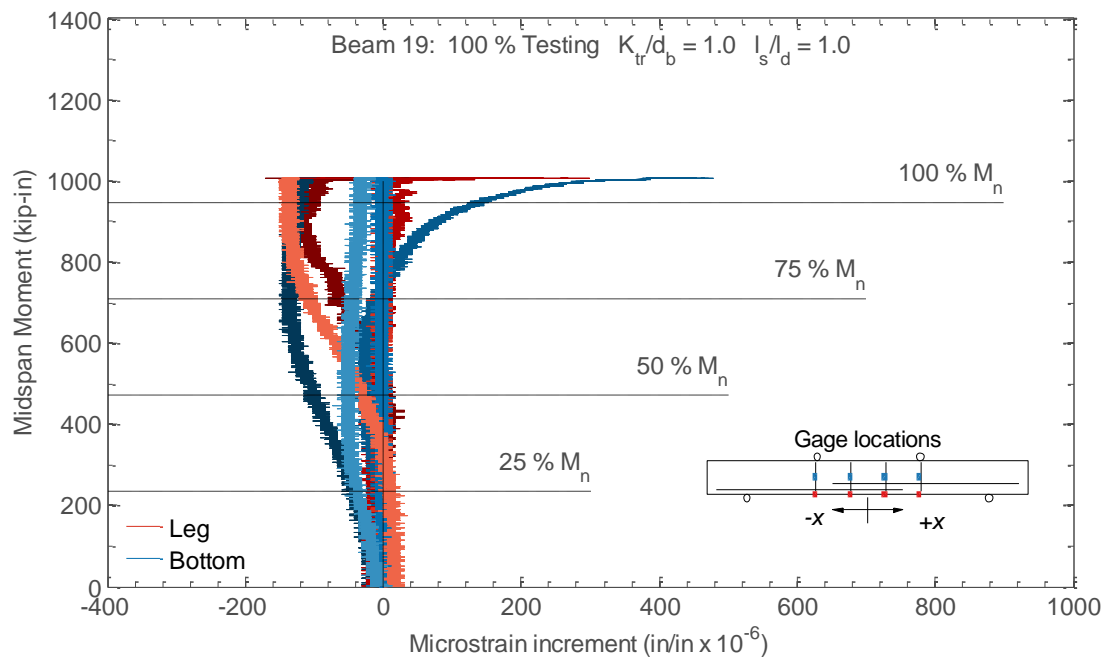
Figure C.152. Measured strain increment in the stirrups for Beam 19

231

Strain Distribution in the Splice Region

The figures below show the normalized strain increment as a function of normalized length along the tensile reinforcement splice for two representative beam specimens at the maximum midspan moment during testing and at several fractions of the nominal moment strength. Along the x-axis, 0.0 represents the free end of the splice and 1.0 represents one development length away from the free end. The y-axis represents the measured strain increment at the specified midspan moment values, divided by the yield strain. The lightly colored circles in the figures indicate individual measurements, and square marks and error bars indicate the average value and the expanded uncertainty in the mean, respectively. Also plotted in the figures is a reference line from a normalized strain increment of 0.0 at the free end to a normalized strain increment of 1.0 at ℓ/ℓ_d = 1.0, corresponding to the code specified development length.
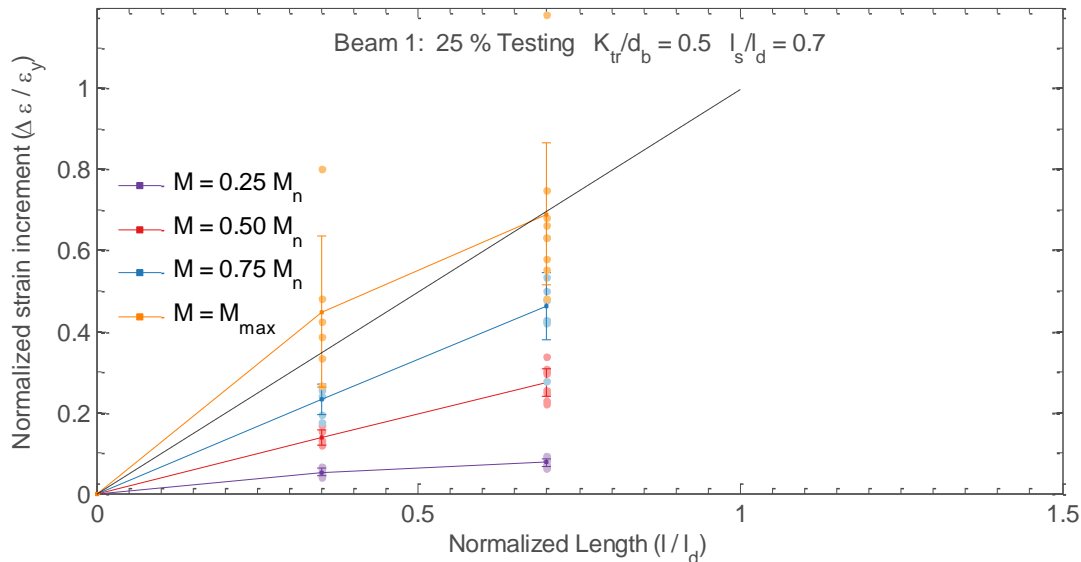
Figure C.153. Distribution of strain increment in the tensile reinforcement for Beam 1
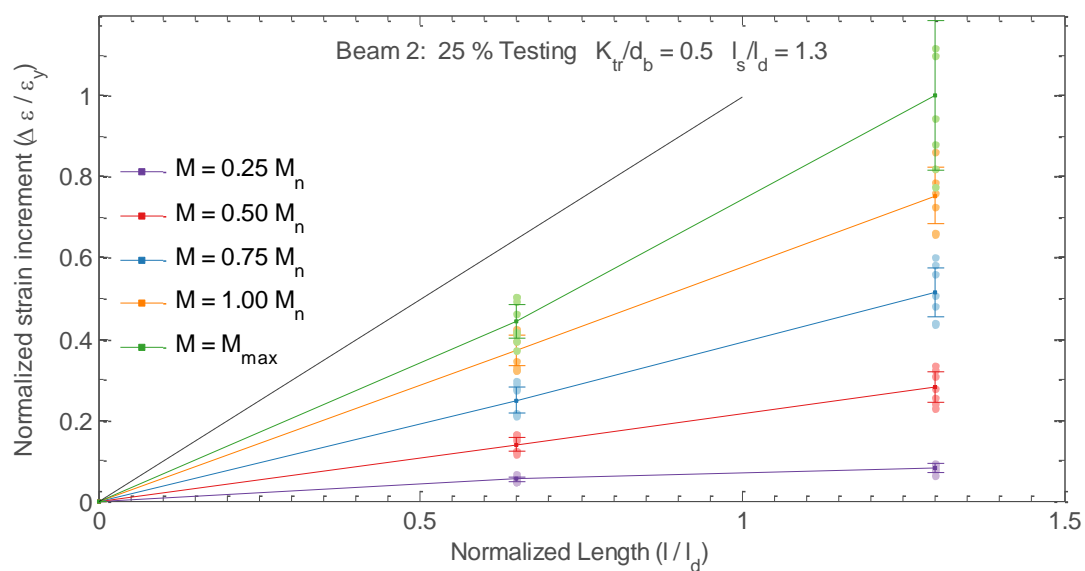
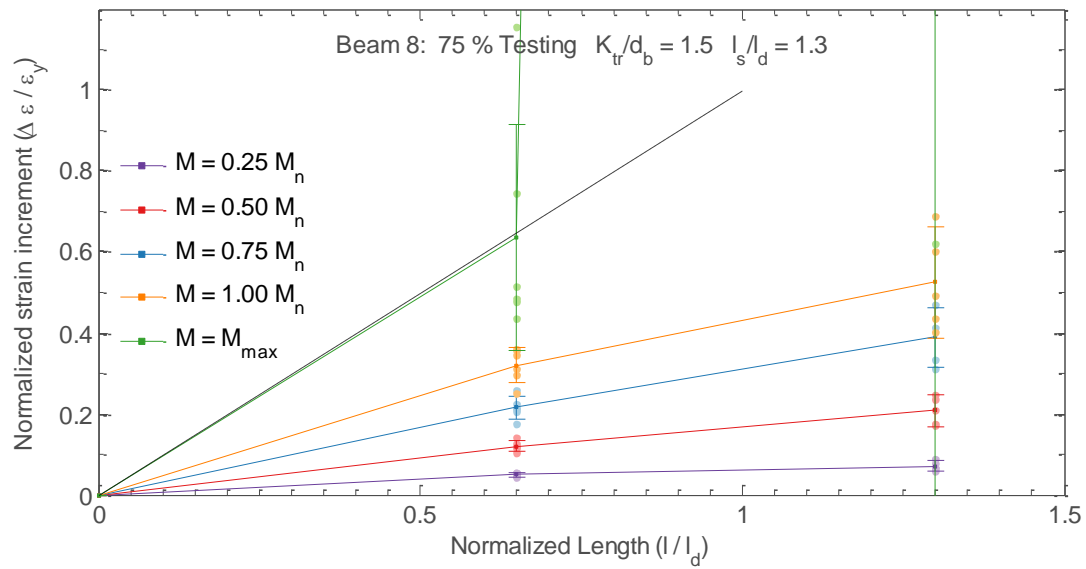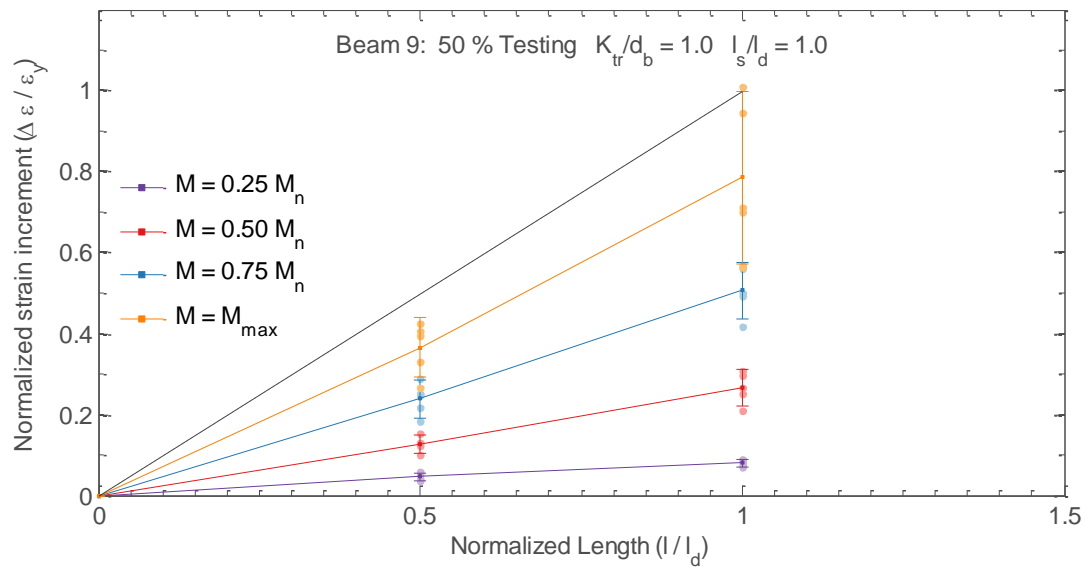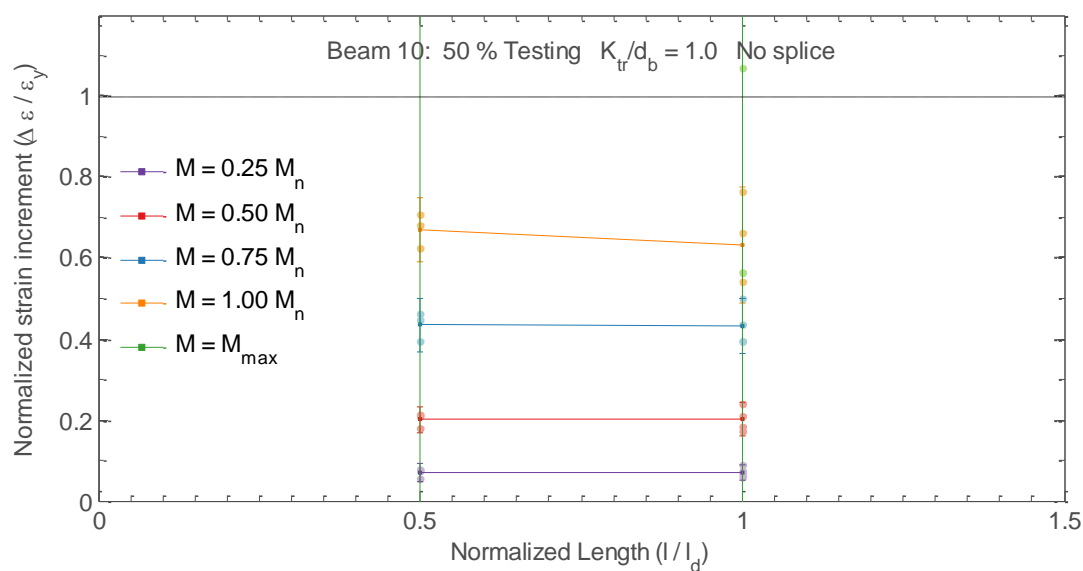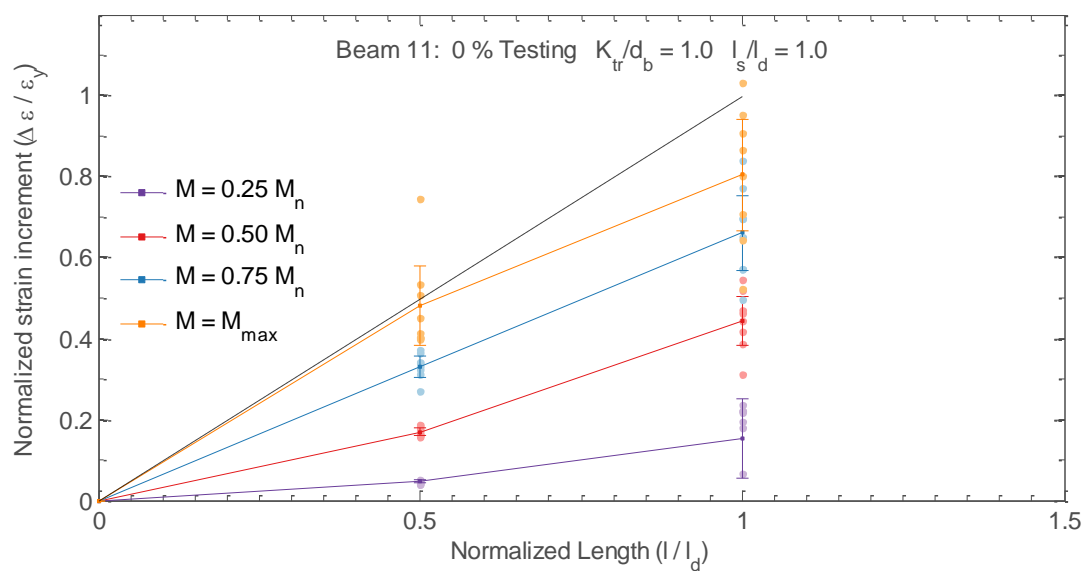**Figure C.154. Distribution of strain increment in the tensile reinforcement for Beam 2**
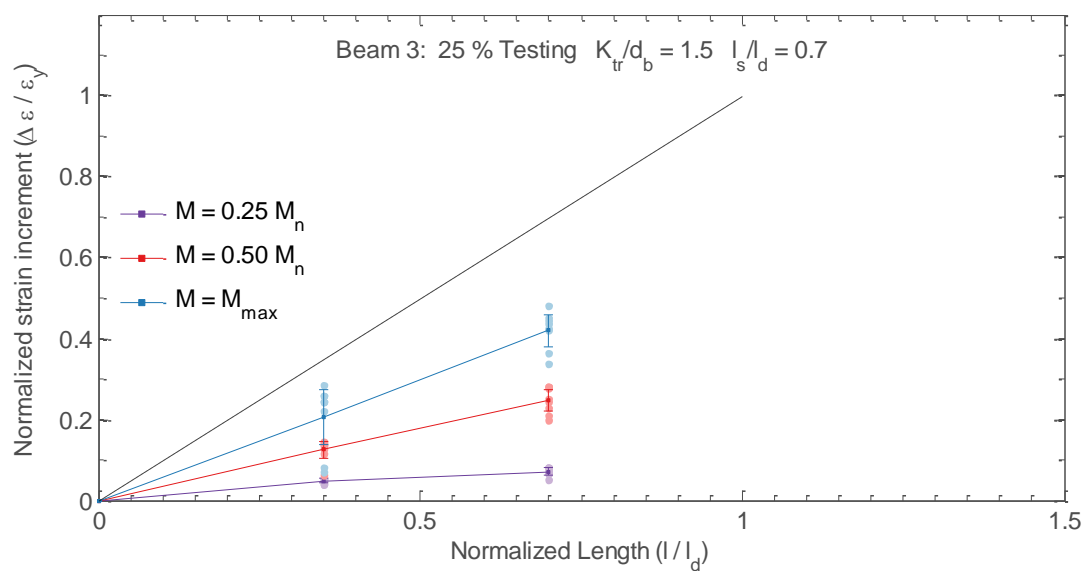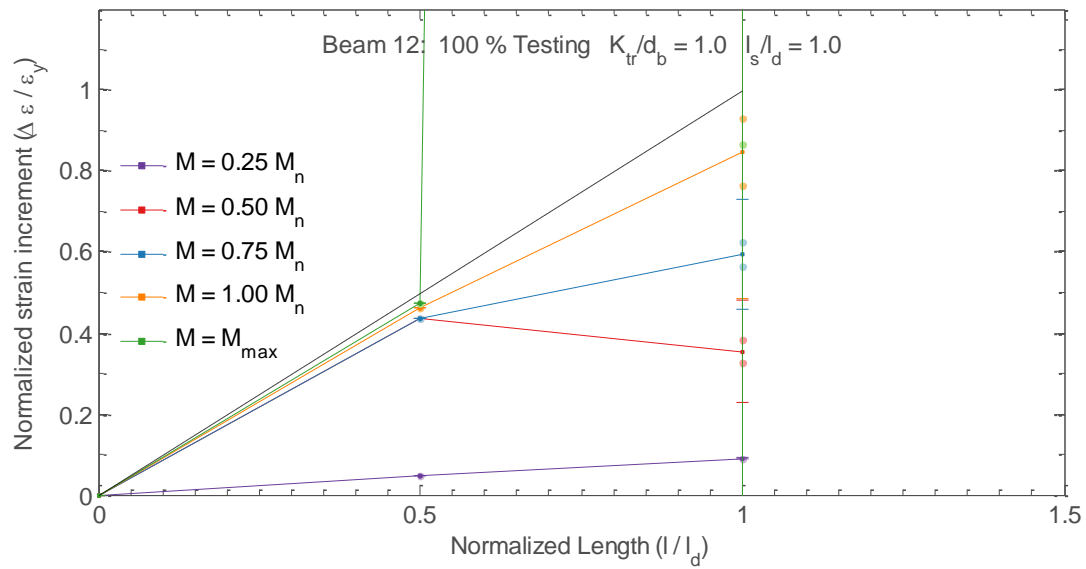

Figure C.155. Distribution of strain increment in the tensile reinforcement for Beam 3

233
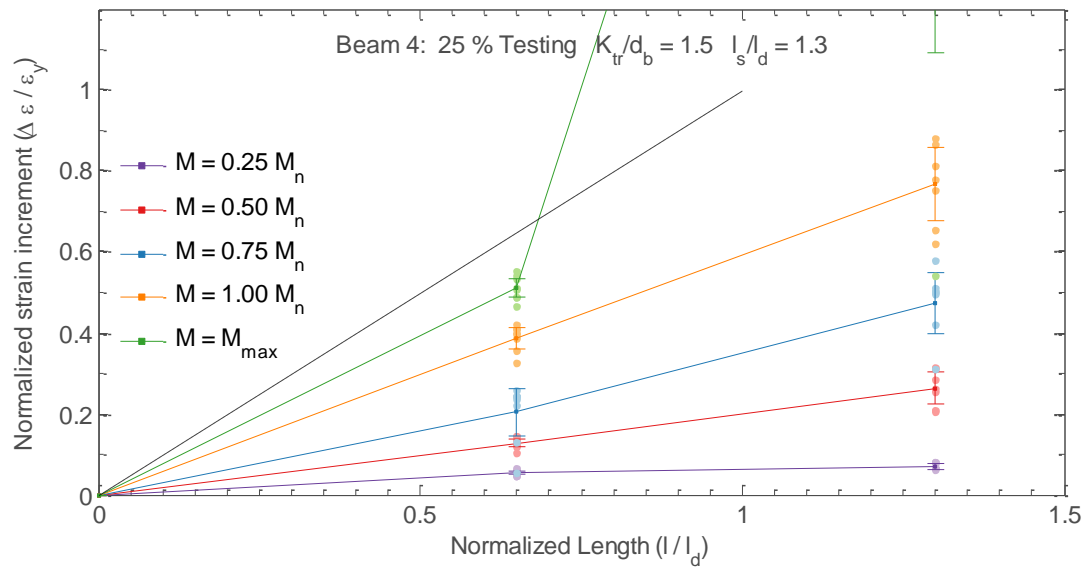
Figure C.156. Distribution of strain increment in the tensile reinforcement for Beam 4
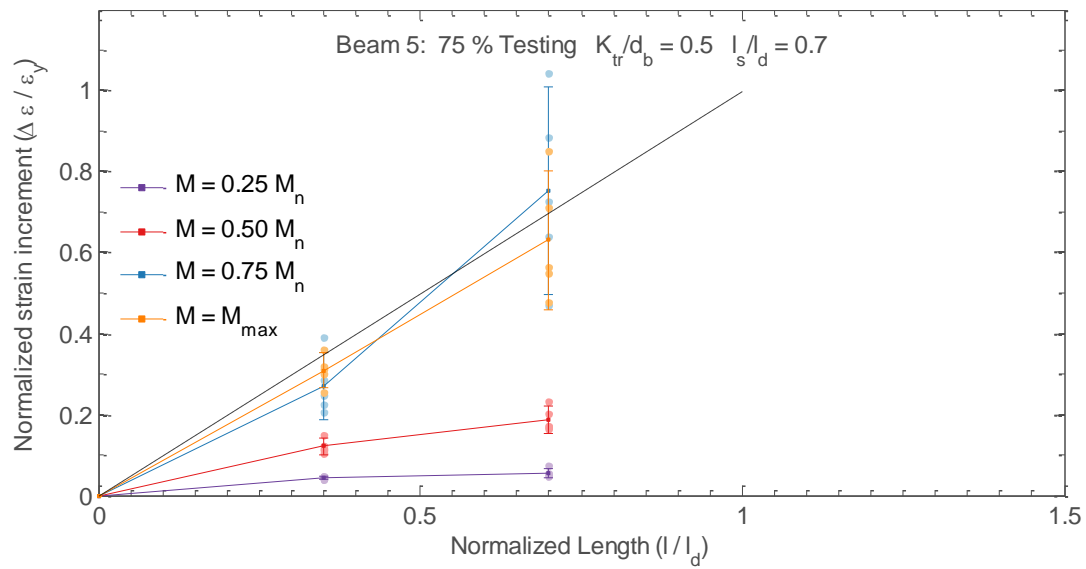
Figure C.157. Distribution of strain increment in the tensile reinforcement for Beam 5
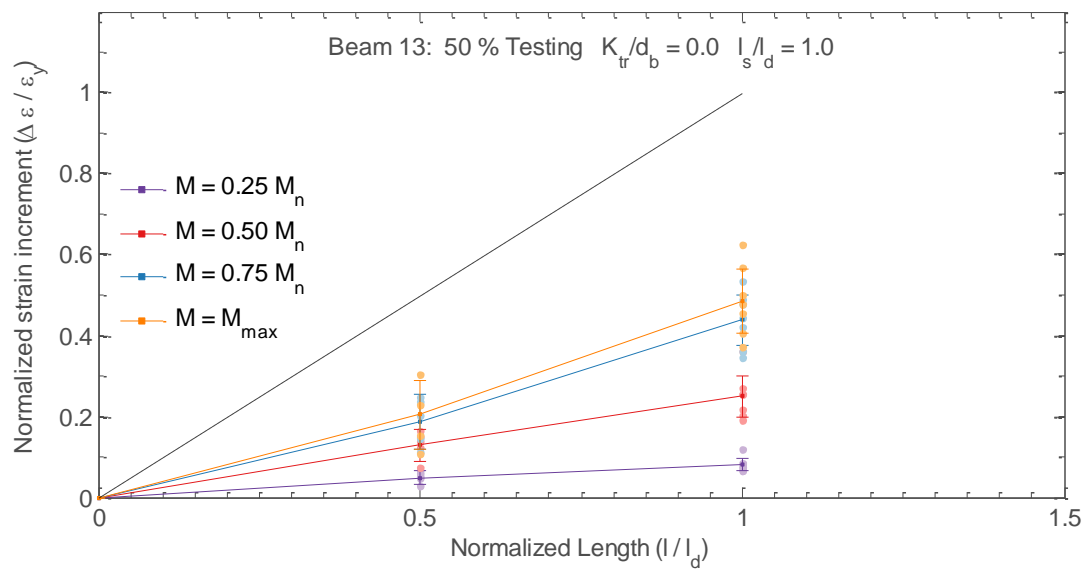
234
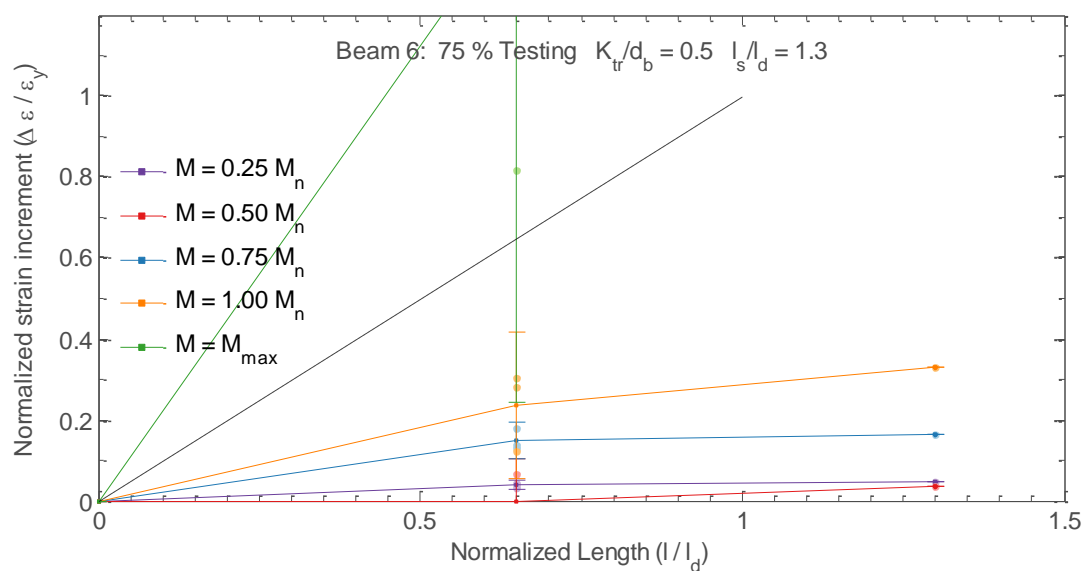
Figure C.158. Distribution of strain increment in the tensile reinforcement for Beam 6
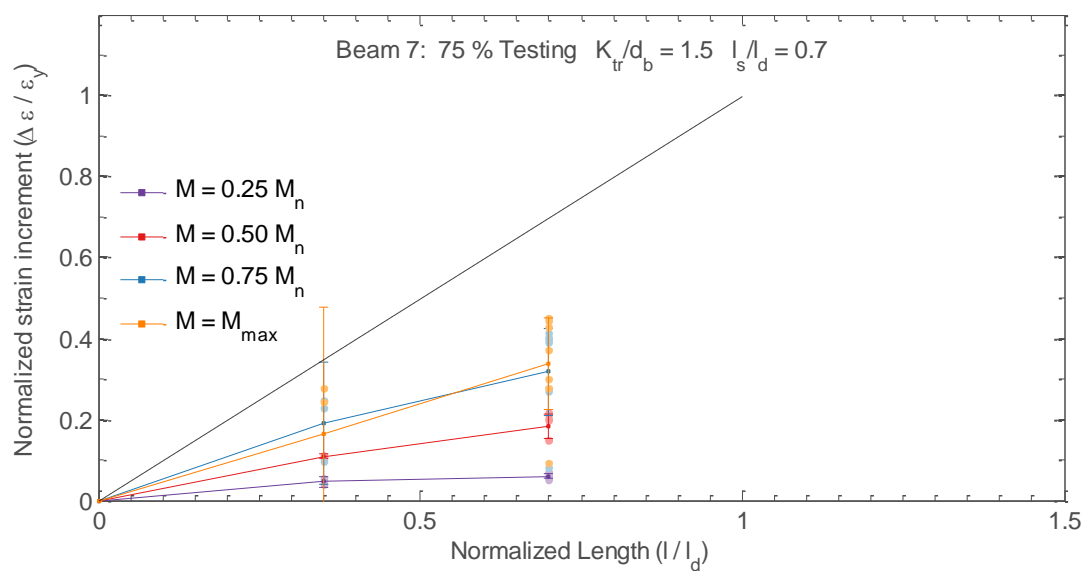
Figure C.159. Distribution of strain increment in the tensile reinforcement for Beam 7
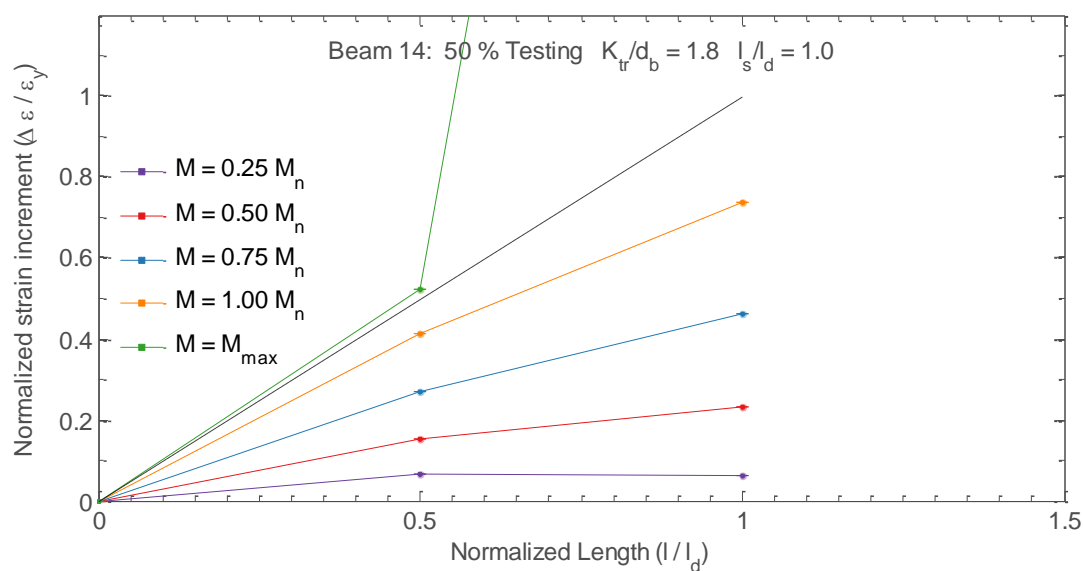
Figure C.160. Distribution of strain increment in the tensile reinforcement for Beam 8

Figure C.161. Distribution of strain increment in the tensile reinforcement for Beam 9

Figure C.162. Distribution of strain increment in the tensile reinforcement for Beam 10
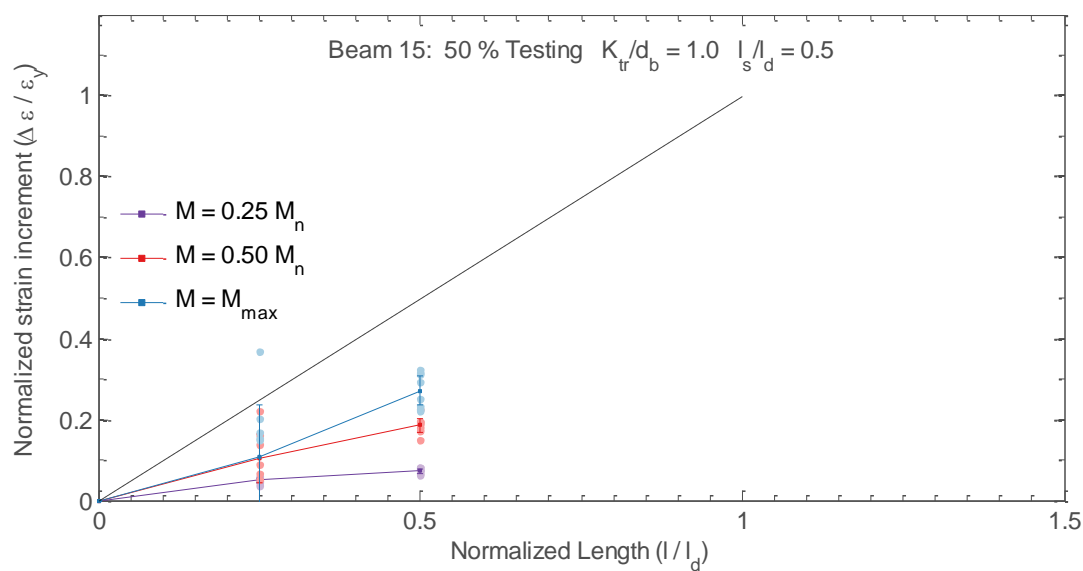

Figure C.163. Distribution of strain increment in the tensile reinforcement for Beam 11

237

Figure C.164. Distribution of strain increment in the tensile reinforcement for Beam 12

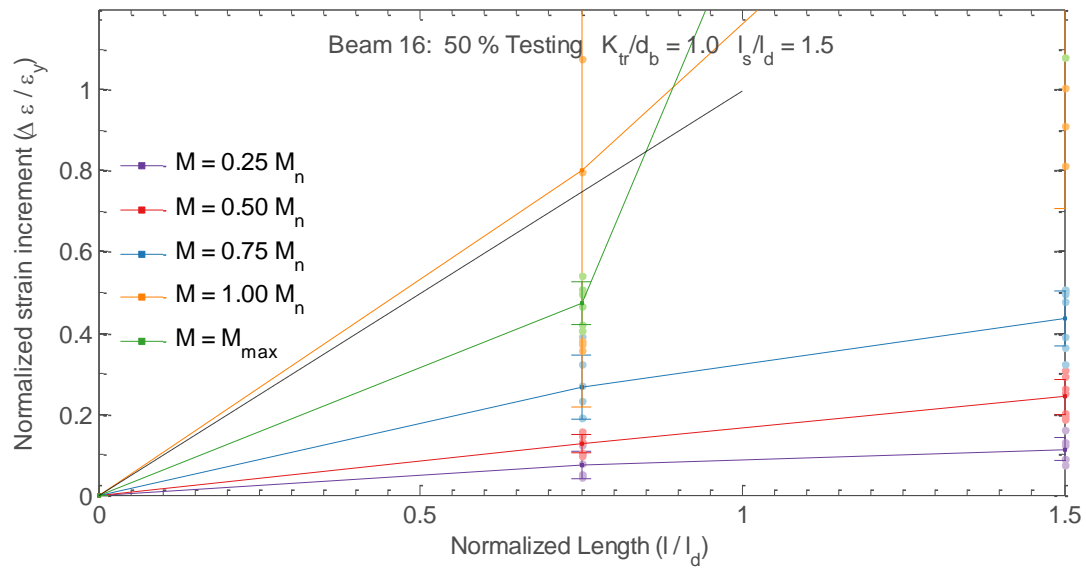**Figure C.165. Distribution of strain increment in the tensile reinforcement for Beam 13**
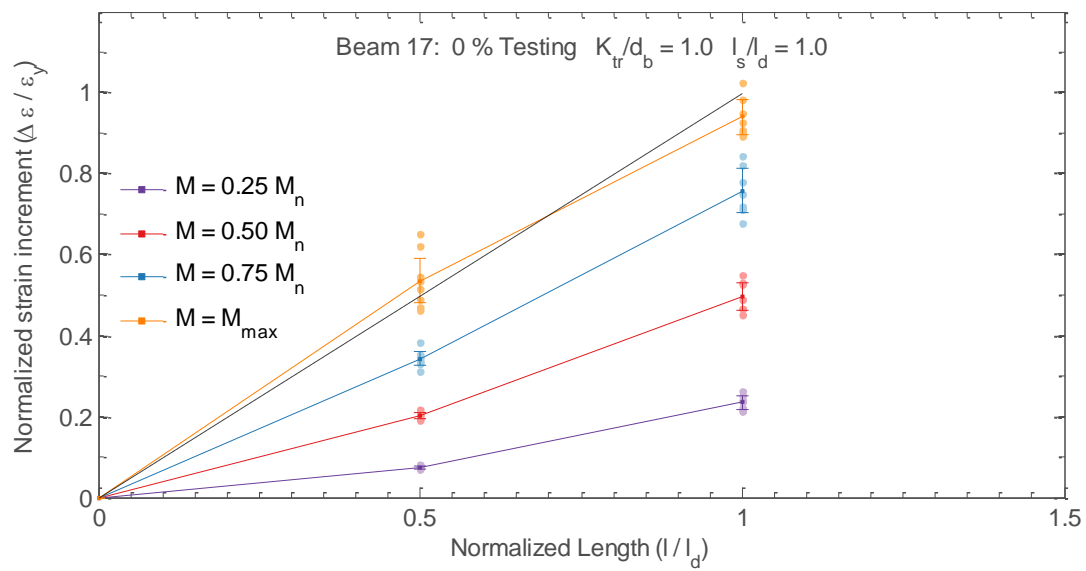
Figure C.166. Distribution of strain increment in the tensile reinforcement for Beam 14

Figure C.167. Distribution of strain increment in the tensile reinforcement for Beam 15

239

Figure C.168. Distribution of strain increment in the tensile reinforcement for Beam 16

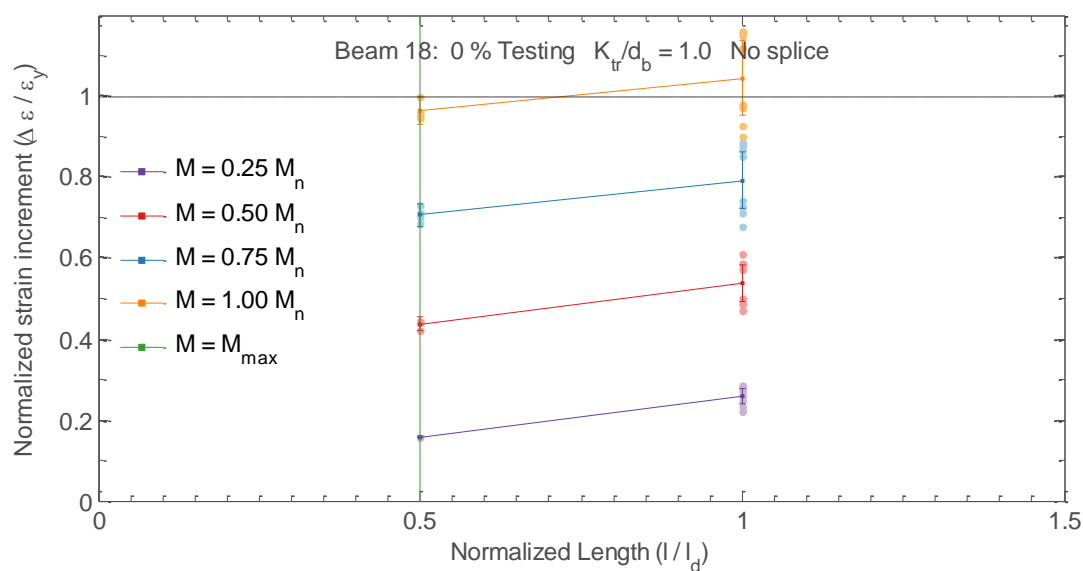**Figure C.169. Distribution of strain increment in the tensile reinforcement for Beam 17**

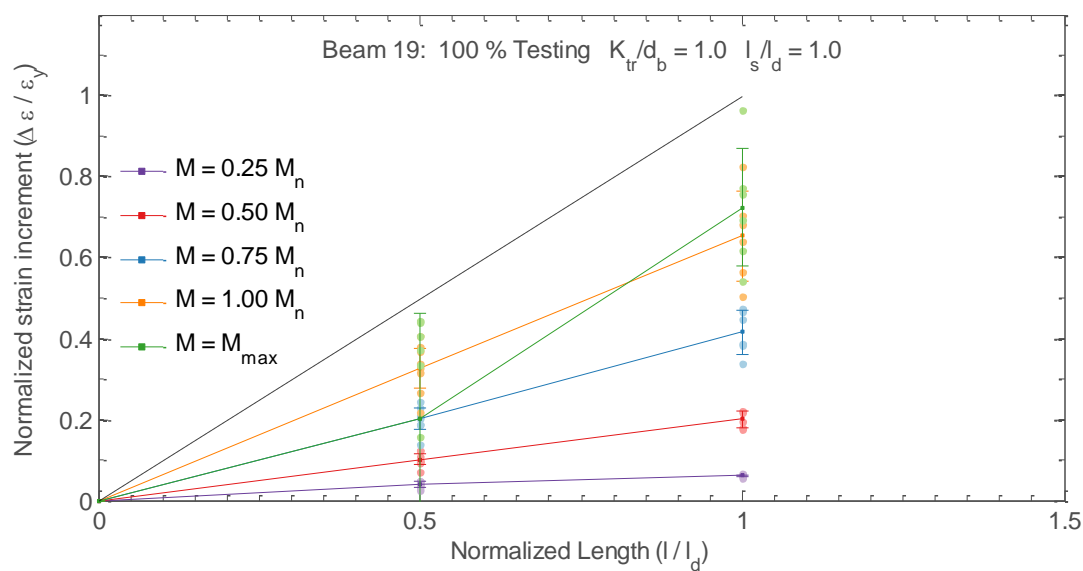**Figure C.170. Distribution of strain increment in the tensile reinforcement for Beam 18**

FigureC.171. Distribution of strain increment in the tensile reinforcement for Beam 19